UNIVERSITY OF LEEDS

Fog and aerosols over central Greenland

by

Heather Guy

Submitted in accordance with the requirements for the degree of Doctor of Philosophy

The University of Leeds
School of Earth and Environment

December 2022

Declaration of authorship

The candidate confirms that the work submitted is her own, except where work which has formed part of jointly authored publications has been included. The contribution of the candidate and the other authors to this work has been explicitly indicated below. The candidate confirms that appropriate credit has been given within the thesis where reference has been made to work of others.

Guy, H., Brooks, I.M., Carslaw, K.S., Murray, B.J., Walden, V.P., Shupe, M.D., Pettersen, C., Turner, D.D., Cox, C.J., Neff, W.D. and Bennartz, R., 2021. Controls on surface aerosol particle number concentrations and aerosol-limited cloud regimes over the central Greenland Ice Sheet. ***Atmospheric Chemistry and Physics*****, 21(19), pp.15351-15374. DOI: 10.5194/acp-21-15351-2021**

For this publication (Chapter 2) I led the data collection and curation of ICECAPS-ACE aerosol data (supervised by RN and IB), and I led the analysis with contributions and feedback from RN, IB, BM, CP, MS, KC, WN and CC. I prepared the text and figures, and all coauthors provided feedback and suggestions for improvements.

Guy, H., Turner, D.D., Walden, V.P., Brooks, I.M. and Neely, R.R., 2022. Passive ground-based remote sensing of radiation fog. ***Atmospheric Measurement Techniques*****, pp.1-31.DOI: 10.5194/amt-15-5095-2022**

This publication (Chapter 3) was conceived by DT, who developed and ran the TROPoe retrieval algorithm, processed the MWR data, and calculated the T_b bias correction. I led the data analysis (with contributions from DT and RN), wrote the text, and prepared all figures apart from Fig. A1 which was contributed by DT. VW prepared the PAERI data, DT and VW contributed to the text, and all coauthors provided feedback and suggestions for improvements.

Observations of fog-aerosol interactions over central Greenland. Guy H., Brooks, I. M., Turner, D. D., Cox, C. J., Rowe, P. R., Shupe, M. D., Walden,

V. P., and Neely, R. R ***In preparation for submission to: J. Geophys. Res.-Atmos.***

Chapter 4 is prepared in the template ready for submission to the Journal of Geophysical Research: Atmospheres. I conceived this study and prepared the aerosol data with feedback from RN and IB, I ran the MIXCRA algorithm in consultation with DT, performed the analysis, generated all figures, and wrote the text. DT wrote the MIXCRA algorithm and provided valuable guidance on its operation, and also generated the TROPoe retrievals required to run MIXCRA as part of Chapter 3. PR provided the temperature dependent SSPs of supercooled water. VW prepared the AERI data. CC quantified the uncertainties in the FM100 measurements. All co-authors provided feedback and suggestions for improvement.

Acknowledgements

Many people have contributed to the completion of this thesis beyond what is already acknowledged in the individual chapters. Ryan Neely and Ian Brooks have provided unwavering support and guidance in all aspects of my PhD, and I am extremely privileged to have had the opportunity to learn from them both. I am also grateful to Ken Carslaw for his valuable feedback and suggestions, and to the wider ICECAPS community for welcoming me and supporting my work. In particular I have learnt a lot from Dave Turner, Von Walden, Claire Pettersen, Chris Cox, Matthew Shupe, Eric Olsen, and Penny Rowe. In Leeds I am grateful for the support of the NCAS Atmospheric Measurement and Observation Facility and especially to Barbara Brooks and James Groves for providing instrument and technological support, and also to Tony Windross and Stephen Burgess in the School of Earth and Environment Instrument workshop.

I am hugely grateful to the staff and management at Summit Station and Polar Field Services, who not only accommodated the installation of our instruments, but who have worked alongside me to make improvements, made my time at Summit enjoyable, and gave me the opportunity to spend additional time there working as a science technician. Thank you to Bethany Wyld, Angela White, and Jennie Mowatt, who helped with the initial installation of the ICECAPS-ACE instruments, and to all the science technicians at Summit who have ensured their continued successful operation. Particular thanks are due to Sam Dorsi for continuously supporting my work at Summit, and to Nate Bowker and Jennie Mowatt who inducted me as a science technician.

Finally thank you to Baker Perry, for his continued support and faith in me; to Sarah Barr, whom I would be lost without after 12 years of friendship and adjacent career paths; and to John Howarth for engineering and CAD support, for never objecting to me going away on fieldwork, and for making tacos.

This PhD was funded by the NERC DTP SPHERES (grant no. NE/L002574/1), and ICECAPS-ACE was funded by the NSFGEO-NERC grant no. 1801477.

Abstract

The Greenland Ice Sheet (GrIS) is losing mass at an accelerating rate and is the largest single contributor to global sea level rise. To understand the future of the ice sheet, we must understand the processes that drive the ice sheet surface energy budget (SEB). The central GrIS experiences strong radiative cooling that drives a stable boundary layer, dynamically isolating the lowest ∼100 m of the atmosphere. Fog regularly forms within this layer and can be difficult to detect. The particles that make up fog absorb and scatter radiation, with potentially large impacts on the SEB. The formation of these fog particles, whether they be liquid or ice, is related the population of aerosol particles, but our understanding of the role of aerosols in fog and cloud formation over central Greenland is limited by a lack of observations.

In this thesis I use new and existing measurements, collected at Summit Station, to advance our understanding of surface aerosol concentrations, fog properties, and fog-aerosol interactions over central Greenland. Firstly, I show that aerosol particle number concentrations are controlled by both local and synoptic processes, and that extremely low number concentrations can occur in all seasons. Secondly, I use ground-based infrared remote sensing to detect and characterise fog events, showing that some instruments that are often used to detect liquid water are not sufficiently sensitive to detect the optically thin shallow fogs that are common at Summit. Finally, by combining the results of these two studies, I present observational evidence supporting the hypotheses that (a) low surface aerosol particle number concentrations can limit fog liquid water path, (b) fog can act to increase near-surface aerosol particle number concentrations through enhanced mixing, and (c) multiple fog events in quiescent periods gradually deplete near-surface aerosol particle number concentrations.

This thesis demonstrates the importance of dedicated instrumentation to monitor fog and the thermodynamic structure of the boundary layer over the ice sheet and highlights the need for vertical profiles of aerosol properties to better understand the relationship between aerosols, clouds, and the ice sheet SEB.

Contents

List of Figures

List of Tables

Abbreviations

N_{CCN} number concentration of cloud condensation nuclei (CCN), cm^{-3}

N_{INP} number concentration of ice nucleating particles (INP), cm^{-3}

a.g.l above ground level

a.s.l above sea level

AERI Atmospheric Emitted Radiance Interferometer

CBH cloud base height

CCN cloud condensation nuclei

CPC Condensation Particle Counter

FLEXPART flexible particle dispersion model

GISP2 The Greenland Ice Sheet Project 2 (Mayewski et al., 1994)

GrIS Greenland Ice Sheet

HATPRO Humidity and Temperature Profiler

ICECAPS Integrated Characterization of Energy, Clouds, Atmospheric state and Precipitation at Summit

ICECAPS-ACE ICECAPS- Aerosol Cloud Experiment

INP ice nucleating particles

LES large-eddy simulations

LT local time

LWP liquid water path

MIXCRA mixed-phase cloud property retrieval algorithm

MMCR Millimetre cloud radar

MWR microwave radiometer

NOAA National Oceanic and Atmospheric Administration

NWP numerical weather prediction

OPC Optical Particle Counter

POPS Portable Optical Particle Counter

POSS Precipitation Occurrence Sensor System

RMSE root mean squared error

SEB surface energy budget

SMPS Scanning Mobility Particle Sizer

SSP single scattering properties

TKE Turbulent kinetic energy

UAV unmanned aerial vehicle

UTC coordinated universal time

VOC Volatile organic compound

Chapter 1.

Introduction

1. Climate change in the Arctic

The Arctic is warming up to four times faster than the global average due to a combination of positive feedback processes (Rantanen et al. 2022); for example, the reduction in snow and ice cover associated with atmospheric warming results in a lower surface albedo and increased absorption of solar radiation at the surface (e.g. Box et al. 2012; Dai et al. 2019). Differences in temperature and the vertical distribution of temperature in the Arctic atmosphere compared to lower latitudes also contributes to the amplification of surface warming (Pithan and Mauritsen 2014; Stuecker et al. 2018), as do changes in meridional heat transport (e.g. Graversen and Burtu 2016), and feedbacks associated with changes in cloud properties (e.g. Taylor et al. 2013).

The rapid warming of the Arctic has ramifications for ecosystems and communities both within the Arctic (e.g. Vincent et al. 2011; Ford et al. 2021), and globally, for example from the release of additional greenhouse gases due to melting permafrost (Natali et al. 2021), and from global sea level rise caused by the melting of Arctic glaciers and land-ice (Box et al. 2018). The annual reduction in Arctic sea-ice is opening up new opportunities for shipping and industrial development in the Arctic (e.g. Smith and Stephenson 2013), which will modify local aerosol and greenhouse gas emissions, with the potential to change how some Arctic climate feedbacks behave in the future (Stephenson et al. 2018). Understanding how the Arctic climate is going to change in the future requires an understanding of how all these feedback processes interact and will respond to future changes.

One of the important questions from an adaptation perspective is: How quickly will sea levels rise? (Nicholls 2018). The single largest contributor to global (barystatic)

sea level rise is the Greenland Ice Sheet (GrIS) (Van den Broeke et al. 2016; Bamber et al. 2018; Slater et al. 2020), which covers approximately 1,710,000 km^2 and holds water equivalent to 7.4 m of global sea level rise (Morlighem et al. 2017). Near-surface temperatures over central Greenland increased by 0.09 ± 0.01 °C $year^{-1}$ between 1982 to 2011, which is six times the global average (McGrath et al. 2013). At the same time, the GrIS is losing mass at an accelerating rate; between 2012 and 2017 the GrIS lost on average 244 Gt yr^{-1} of ice, compared to just 26 Gt yr^{-1} between 1992 and 1997 (Rignot et al. 2011; IMBIE 2020).

Eventually, the GrIS will cross a 'tipping-point' beyond which the current ice sheet configuration becomes unstable and further melting becomes inevitable. Recent studies estimate we are close to a GrIS 'tipping-point' if we have not already crossed one (e.g. Robinson et al. 2012; Boers and Rypdal 2021; Armstrong McKay et al. 2022). However, projections of how quickly sea levels will rise are limited by large inter-model differences in the contribution from the GrIS (Hofer et al. 2019; Goelzer et al. 2020).

2. The Greenland Ice Sheet surface energy budget

More than half of the current GrIS mass loss results from increased surface melt and runoff (Van den Broeke et al. 2016; IMBIE 2020) that is controlled by the net flux of energy at the ice sheet surface, the surface energy budget (SEB). Climate and glacier mass balance models require an accurate representation of the processes that control the GrIS SEB to make projections of future GrIS melt, but currently, differences in the representation of these processes between different models result in a factor of 1.85 difference in 2100 total GrIS melt projections, which is larger than the difference between low and high greenhouse gas emission scenarios (a factor of 1.75; Hofer et al. 2019). Therefore, improving our understanding of the controls on the GrIS SEB is critical for reducing the uncertainty in future projections of sea level rise.

The SEB can be separated into contributions from longwave and shortwave radiative fluxes, sensible and latent heat fluxes, and the flux of energy coming from below the surface (the ground heat flux). The most important drivers of the SEB over the GrIS are changes in downwelling radiative fluxes and sensible heat flux, with the other components responding to, and often compensating for, these changes (Miller et al. 2017; Hofer et al. 2017). In the ablation zone around the edge of the GrIS, which experiences annual melt, there are large fluctuations in the surface albedo (0.2 to 0.9, e.g. Moustafa et al. 2015). When the surface albedo is low (< 0.5) a greater percentage of downwelling

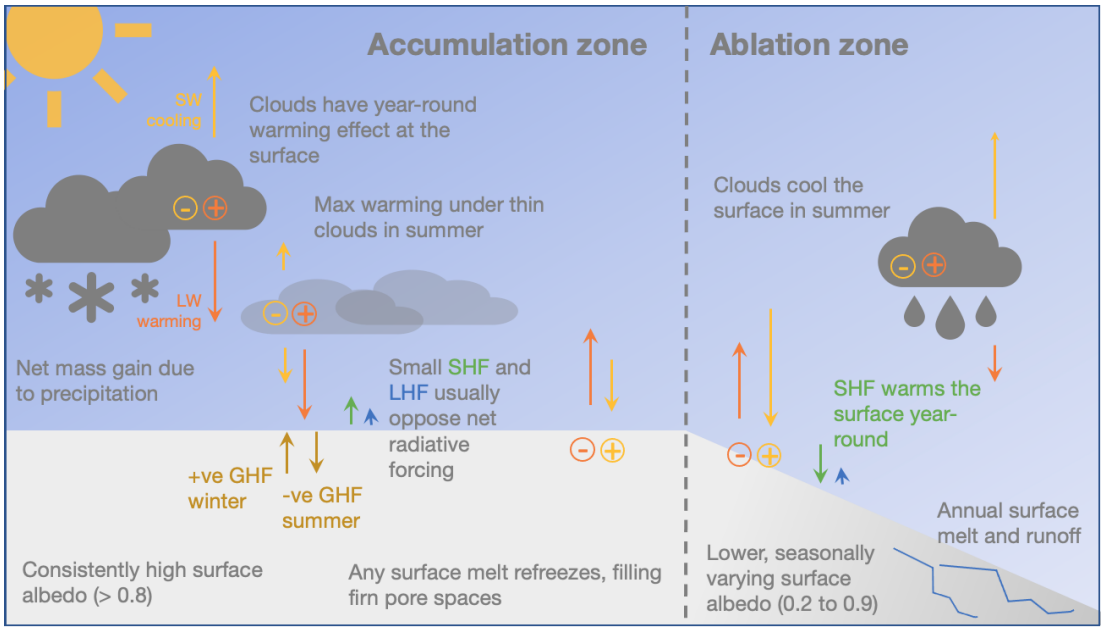

Figure 1.1.: Schematic illustrating the controls on the SEB in the accumulation and ablation zones of the GrIS. Arrows indicate the net direction of heat transfer from each component. Note that shortwave (SW) radiative effects (yellow) are only relevant in the summer, whereas longwave (LW) radiative effects are present year-round. Typical directions of sensible heat flux (SHF), latent heat flux (LHF) and ground heat flux (GHF) are indicated in green, blue and brown respectively.

shortwave radiation is absorbed at the surface, and changes in downwelling shortwave radiation, along with the sensible heat flux, become the most important controls on the SEB (Van den Broeke et al. 2011a; Wang et al. 2021). In contrast, in the accumulation zone, the central part of the GrIS where changes to the surface albedo throughout the year are small (Box et al. 2012; Miller et al. 2018), and the magnitude of the sensible heat flux is usually < 20 W m^{-2} (Cohen et al. 2007; Miller et al. 2017), changes in net downwelling longwave radiation become more important (e.g. Miller et al. 2015). Figure 1.1 illustrates some of the key drivers of the GrIS SEB and how they differ between the accumulation and ablation zones.

Downwelling longwave radiation is controlled by the temperature and emissivity profile of the atmosphere whereas downwelling shortwave radiation is controlled by solar output, solar zenith angle, and atmospheric transmittance. Both quantities are extremely sensitive to the presence and type of clouds (fig. 1.1), which can reflect incoming solar (shortwave) radiation and emit longwave radiation towards the surface (Shupe and Intrieri 2004; Miller et al. 2015). Hence, the occurrence, vertical structure, and temperature of clouds are important controls on the GrIS SEB and subsequently surface

melt (e.g. Van den Broeke et al. 2016; Hofer et al. 2017; Niwano et al. 2019). Over central Greenland, clouds can increase downwelling longwave radiation at the surface relative to clear skies by 40 to 60 W m^{-2} year-round and reduce downwelling shortwave radiation by similar amounts in the summer months (Miller et al. 2015).

3. The role of aerosol particles

Particles suspended in the atmosphere (atmospheric aerosol) can also absorb and scatter radiation and therefore impact downwelling radiative fluxes at the surface. Globally, the direct effect of atmospheric aerosol at the surface is a net cooling due to scattering of incoming solar radiation (Bellouin et al. 2020). But this effect is minimised over high albedo surfaces like those in central Greenland since most of the downwelling solar radiation is reflected (e.g. Di Biagio et al. 2012), and is partly offset by thermal emission from atmospheric aerosols that can act to increase downwelling longwave radiation at the surface. At coastal Arctic sites, atmospheric aerosol can increase downwelling longwave radiation at the surface by 2.99 to 4.66 W m^{-2} relative to clear sky conditions (Ritter et al. 2005), and can reduce downwelling shortwave radiation by up to 10 W m^{-2} during the summer months (Di Biagio et al. 2012).

Although the direct radiative forcing of atmospheric aerosol is small compared to that of clouds, aerosol particles are also an important control on cloud properties. Cloud particles form on aerosol, and the characteristics of atmospheric aerosol (number concentration, size distribution and chemical composition) can control both cloud microphysical properties and lifetime (e.g. Fan et al. 2016 and references therein). This means that the aerosol population is a direct control on the magnitude of cloud radiative forcing, and correctly representing this indirect radiative effect of atmospheric aerosol in models is important for modelling cloud microphysical properties and their impact on the SEB. Limited case studies in the Arctic have demonstrated that atmospheric aerosols can be responsible for changes in cloud radiative forcing of -11 to +3.4 W m^{-2} (Lubin and Vogelmann 2006, 2010), and up to a magnitude of 70 W m^{-2} in situations where the aerosol population is a critical control on cloud lifetime (Mauritsen et al. 2011; Stevens et al. 2018). However, where and how often these effects are important is poorly constrained, largely due to a lack of observations (e.g. Schmale et al. 2021).

3.a. Aerosol cloud interactions

The mechanisms through which atmospheric aerosol can modify cloud radiative forcing for liquid and mixed-phase clouds are illustrated in Table 1.1. Liquid droplets form on cloud condensation nuclei (CCN); a subset of the aerosol population that can provide a surface for cloud droplet activation at a given supersaturation. The ability of a particle to act as a CCN at a given supersaturation is a function of particle size and hygroscopicity (which is dependent on particle composition). For the supersaturations observed in typical shallow clouds (0.1 to 0.4%), CCN particles range from 50-200 nm diameter (Carslaw 2022), but in clean Arctic environments supersaturations can reach higher values, and particles as small as 20 nm diameter can act as CCN (Leaitch et al. 2016; Baccarini et al. 2020).

Table 1.1.: Mechanisms through which atmospheric aerosol can modify cloud radiative forcing. The pathway describes the difference in cloud microphysical properties relative to an equivalent cloud without the stated modification. Impacts shaded blue (red) result in reduced (increased) downwelling radiation at the surface. Impacts related to cloud lifetime can either increase or decrease downwelling radiation at the surface as explained in the text.

	Aerosol modification	Pathway			Impact
Liquid cloud	Increase N_{CCN}	More, smaller cloud droplets	Higher reflectivity		Reduced ↓SW (summer)
			Higher emissivity (optically thin clouds only)		Increased ↓LW (optically thin clouds)
			Reduced sedimentation rates	Reduced precipitation efficiency	Increased cloud lifetime
			Increased cloud top cooling	Increased entrainment of overlying air: Dry air entrainment	Reduced cloud LWP and lifetime
				Increased entrainment of overlying air: Moist air entrainment	Increased cloud LWP and lifetime
	Remove almost all CCN	Fewer, larger droplets	Reduced emissivity		Reduced ↓LW
			Reduced reflectivity		increased ↓SW (summer)
			Increased precipitation efficiency, initiates positive feedback loop that removes remaining CCN		Reduced cloud lifetime
Mixed-phase cloud	Increase N_{INP}	Cloud glaciation	Larger particle sizes	Increased precipitation efficiency	Reduced cloud lifetime
				Reduced emissivity (optically thin clouds)	Reduced ↓LW (optically thin clouds)
			Smaller particle number concentration	Reduced reflectivity	Increased ↓SW (summer)
	Increase N_{CCN}	More, smaller cloud droplets	Reduced riming efficiency	Reduced precipitation efficiency	Increased cloud lifetime
			Inhibits ice formation		Increased cloud lifetime

The number concentration of CCN, cm^{-3} (N_{CCN}) determines the number concentration of cloud droplets; hence in environments with high N_{CCN}, a cloud will contain a larger number of smaller droplets than in a cloud with the same liquid water content but lower N_{CCN} (Twomey 1977). This impacts the radiative properties of the cloud, since higher

droplet number concentrations result in a greater shortwave reflectivity (Twomey 1991), and for optically thin clouds smaller droplets result in increased longwave emissivity (Garrett and Zhao 2006). For a cloud with a fixed liquid water content, the change in cloud albedo as a function of the increase in aerosol number concentration can be up to 0.01 cm^3 (Twomey 1991), and for a cloud with a liquid water path < 25 g m^{-2}, the change in cloud emissivity as a function of increased CCN concentrations can exceed 0.01 cm^3 (Garrett and Zhao 2006). Both of these effects have a larger impact when the original N_{CCN} is small (< 50 cm^{-3}).

An increase in cloud emissivity due to increased N_{CCN} also increases cloud top cooling; Williams and Igel (2021) showed that for a cloud with a fixed liquid water content, maximum cloud top radiative cooling increases by ∼50% if cloud droplet number concentration increases from 10 to 1,000 cm^{-3}, due to the smaller droplet sizes at cloud top. The increased cloud top cooling enhances mixing and entrainment that, depending on the humidity of the overlying air, can either reduce or increase cloud water content (Ackerman et al. 2004; Small et al. 2009; Williams and Igel 2021). In Arctic regions, moisture inversions at cloud top are common and increased entrainment of moist air from above can prolong cloud lifetime (e.g. Solomon et al. 2011), moisture inversions have also been observed over central Greenland (Shupe et al. 2013).

Smaller cloud droplets associated with higher N_{CCN} result in reduced sedimentation rates which can also act to increase cloud liquid water and lifetime (Albrecht 1989; Suzuki et al. 2013). The relative importance of these different aerosol-cloud interactions varies regionally and is difficult to quantify due to their dependence on local meteorology (Gryspeerdt et al. 2019). For example, over the Arctic Ocean, the response of cloud liquid water to increased N_{CCN} depends on lower tropospheric stability and humidity; in stable conditions, and when specific humidity is high, increased N_{CCN} is correlated with increased cloud liquid water, whereas for neutral or unstable atmospheres and low specific humidities, increases in N_{CCN} result in reduced cloud liquid water (Murray-Watson and Gryspeerdt 2022). The relative importance of these processes over the GrIS is unknown, but the high static stability of the lower troposphere over central Greenland suggests that a positive relationship between N_{CCN} and cloud liquid water is likely to dominate.

If N_{CCN} is exceptionally low ($< \sim 10$ cm^{-3}), clouds can exist in an aerosol-limited regime, where all CCN activate and droplets grow to relatively large sizes (> 20 μm diameter, Mauritsen et al. 2011). The lack of CCN allows higher supersaturations to be reached, potentially activating smaller particles that would not otherwise act as CCN; the activation of particles as small as 20 nm diameter has been observed in clean Arctic

environments (Leaitch et al. 2016; Baccarini et al. 2020; Bulatovic et al. 2021). The larger droplet sizes result in higher sedimentation rates, which act as a sink for CCN, generating a positive feedback effect that can result in cloud dissipation in as little as two hours (Sterzinger et al. 2022). This aerosol-limited regime has been observed over the Arctic Ocean (Mauritsen et al. 2011; Stevens et al. 2018), and over central Greenland (Sterzinger et al. 2022).

The processes described above can also occur in mixed-phase clouds, but ice particles generate additional complexity. Primary ice formation relies on the presence of ice nucleating particles (INPs); a subset of the aerosol population that can catalyse ice formation (e.g. Kanji et al. 2017). When the atmosphere is supersaturated with respect to ice, ice can form directly on INPs (via deposition nucleation), but more commonly in low-level clouds (with temperatures > -30°C) ice forms from liquid droplets either through immersion freezing (the freezing of a cloud droplet containing an INP) or contact freezing (the freezing of a cloud droplet that makes contact with an INP) (Ansmann et al. 2008; De Boer et al. 2011; Westbrook and Illingworth 2013; Kanji et al. 2017).

In mixed-phase clouds, ice crystals are usually larger than liquid droplets; for example, the effective radius of ice crystals in mixed-phase clouds during the SHEBA campaign was 18±15 μm, compared to 9±4 μm for liquid droplets (Turner 2005). Due to the differences in size distributions, phase partitioning in mixed-phase clouds can have important radiative effects; observational studies demonstrate that the magnitude of both longwave and shortwave radiative forcing in mixed-phase clouds is closely related to changes in liquid water path (e.g. Shupe and Intrieri 2004; Miller et al. 2015). In an environment where the air becomes sub-saturated with respect to water but supersaturated with respect to ice, ice particles will grow at the expense of liquid droplets, causing the liquid droplets to evaporate (e.g. Korolev 2007). Increasing the number concentration of INP, cm^{-3} (N_{INP}) can result in the rapid glaciation of a mixed-phase cloud through this process, resulting in increased precipitation due to the higher fall speed of the larger ice particles, and a reduction in cloud lifetime (Morrison et al. 2011).

Changes in N_{CCN} can also impact the phase partitioning in mixed-phase clouds; observations and laboratory studies show that riming efficiency decreases for smaller liquid droplets and approaches zero for droplets < 10 μm diameter (Borys et al. 2003; Lohmann 2004; Norgren et al. 2018). A reduction in riming efficiency reduces ice precipitation rates, since unrimed ice crystals have slower fall speeds (< 0.8 m s^{-1}) compared to rimed crystals (> 1m s^{-1}, Yau and Rogers 1996). There is also observational evi-

dence that smaller cloud droplets freeze less readily, and so smaller droplets associated with higher N_{CCN} might inhibit ice formation (Lance et al. 2011), with both processes acting to prolong cloud lifetime.

Aerosol induced changes in cloud lifetime might result in either an increase or a decrease in the net radiative flux at the surface, depending on whether the net effect of the cloud would have been surface cooling or warming without the aerosol induced modification. Over central Greenland, clouds act to warm the surface year-round (due to the high surface albedo, Miller et al. 2015), and so a reduction in cloud lifetime would a have a cooling effect at the surface (an overall reduction in the net radiative flux at the surface). Understanding the impact of aerosol cloud interactions on the GrIS SEB requires knowledge of the spatial and temporal distribution of N_{CCN} and N_{INP} in addition to thermodynamic profiles of the atmosphere.

3.b. Observations of aerosol over Greenland

There are very few observations of aerosol properties over central Greenland, and those that do exist are limited to the summer season (Flyger et al. 1976; Hogan et al. 1984; Davidson et al. 1993; Bergin et al. 1994, 1995; Ziemba et al. 2010). Over the Arctic more generally, there is a well-established seasonal cycle in tropospheric aerosol associated with Arctic haze (Shaw 1995). This cycle is characterised by a build-up of anthropogenic pollutants in the winter when the polar front migrates southwards and wet deposition is at a minimum, followed by lower aerosol particle number concentrations and smaller particle sizes in the summer associated with local marine sources and enhanced wet deposition (e.g. Shaw 1995; Quinn et al. 2002; Freud et al. 2017). Although Arctic haze is observed along the north coast of Greenland (Nguyen et al. 2016), there is no evidence that this anthropogenic pollution reaches the central GrIS (Dibb 2007; Schmeisser et al. 2018). In contrast, indirect measurements (from snowpits, and aerosol optical properties) indicate that aerosol particle concentrations over the central GrIS are at a minimum during the winter and increase rapidly (over $\sim$1 month) to a maximum in April before declining steadily over the summer and autumn (Drab et al. 2002; Dibb 2007; Schmeisser et al. 2018). The difference in the seasonal cycle of aerosol particle concentrations over the central GrIS compared to other Arctic locations is due to the high elevation and associated differences in circulation and aerosol transport pathways (Stohl 2006; Hirdman et al. 2010). Hence, aerosol measurements from coastal and central Arctic regions are not representative of those over the central GrIS.

Compared to five other Arctic research stations spanning the circumference of the Arctic Ocean, Summit Station (Summit, see section 5) in central Greenland has the lowest annual mean aerosol scattering coefficient (1.74 Mm^{-1}) and the lowest annual mean absorption coefficient (0.12 Mm^{-1}), both of which are directly dependent on aerosol particle amount (Schmeisser et al. 2018). The mean annual scattering Ångström exponent, which is inversely related to aerosol size, is highest at Summit (1.80) suggesting that the average size of aerosols that make it to central Greenland are smaller than in other areas of the Arctic (Schmeisser et al. 2018). The lower particle concentrations and lack of larger particles at Summit implies a long transport pathway, where large particles are deposited or scavenged before they reach central Greenland. This also suggest that N_{CCN} over central Greenland could be especially low, since CCN are typically larger particles ($>$ 80 nm diameter).

Direct measurements of N_{CCN} over the central GrIS (100 to 300 km from the coast) are limited to summertime aircraft campaigns (4,000 to 5,000 m a.s.l) in 1971 and 1973 that found CCN concentrations of 0-17 cm^{-3} (at 1% supersaturation, Flyger et al. 1973, 1976). Size resolved measurements of surface aerosol particle number concentrations ($>$ 10 nm) are also only available from limited summer campaigns, which show that total particle number concentrations typically range from 10 to 1000 cm^{-3} with a high temporal variability that depends on both synoptic conditions and local meteorology (Hogan et al. 1984; Bergin et al. 1994, 1995; Ziemba et al. 2010). The concentrations of larger aerosol particles (diameters $>$ 0.5 μm) are extremely low ($<$ 5 cm^{-3}, Bergin et al. 1994, 1995). Each of these findings supports the idea that N_{CCN} over central Greenland could be low enough to limit cloud formation (as described in Mauritsen et al. 2011), but the lack of long-term and year-round measurements of aerosol particle concentrations over central Greenland limits our ability to understand the importance of the aerosol-limited cloud regime over Greenland, and to generate realistic model parameterisations of aerosol properties and aerosol-cloud interactions.

4. Fog over the ice sheet

Fog consists of suspended water droplets or ice crystals in the atmosphere that reduce the horizontal visibility at the surface (Gultepe et al. 2007). Like clouds, the formation of fog particles is closely related to the aerosol population and can impact the SEB by modifying net downwelling radiation. Fog over central Greenland has a net warming effect at the surface year-round due to the increase in downwelling longwave radiation (Cox et al. 2019). The presence of supercooled liquid fogs at Summit results in an

average increase in net surface radiation of 26.1 W m^{-2} compared to equivalent clear sky days, with some cases increasing net surface radiation by > 60 W m^{-2} (Cox et al. 2019).

Fog forms when the near-surface air reaches saturation, either through cooling or through a moistening process such as evaporation/sublimation or moist air advection (Gultepe et al. 2007), and CCN or INP activate to form fog particles. Near surface cooling can result from the advection of a cold air mass or a warmer air mass over a cold surface, through orographic effects such as mechanical lifting, or through the direct radiative cooling of the surface (which forms radiation fog). Radiation fog commonly forms over central Greenland due to longwave cooling at the ice sheet surface (Hoch et al. 2007; Berkelhammer et al. 2016).

Daily meteorological reports (at 00, 12, and 18 UTC) from Summit between 2010 and 2020 indicate that freezing fog in the absence of drifting or blowing snow (defined as fog that reduces horizontal visibility to < 800 m) occurs 8.3% of the time, and mist (horizontal visibility reduced to < 5,000 m but > 800 m) occurs 11% of the time (fig. 1.2). This is consistent with two years of dedicated fog measurements at Summit that detected fog 10 to 20% of the time year-round (Cox et al. 2019). Fogbows are regularly reported and photographed at Summit (see front page), suggesting that fogs are often optically thin and contain liquid droplets.

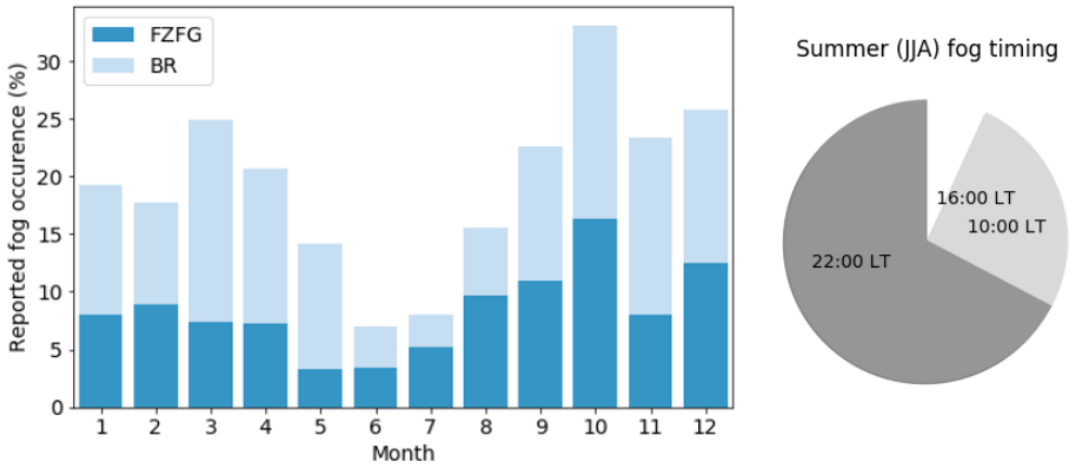

Figure 1.2.: Left: Monthly occurrence of freezing fog (FZFG, surface visibility < 800 m) and mist (BR, surface visibility > 800 m) reported daily at (00, 12, and 18 UTC) by observers at Summit 2010-2020. Right: Percentage occurrence of FZFG reports at 00 UTC (22 LT), 12 UTC (10 LT), and 18 UTC (16 LT) in summer months (JJA).

Radiation fog can exist in two states; in a shallow (usually < 50 m) stable layer where

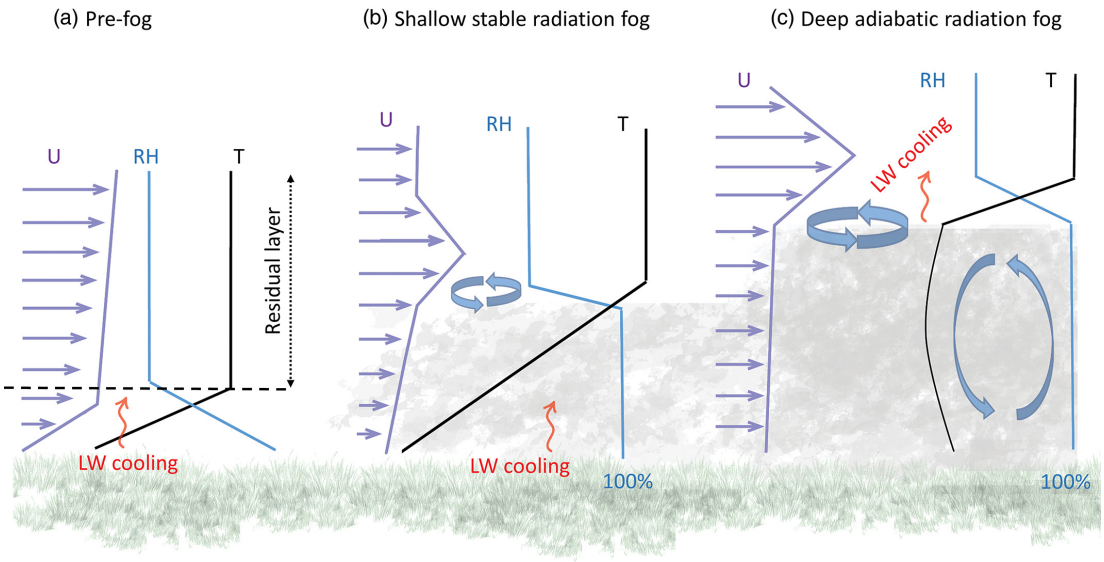

Figure 1.3.: Schematic taken from Smith et al. (2018) that illustrates the typical structure of a radiation fog and how it changes as the fog transitions to a well-mixed adiabatic fog. The red arrows show the location of the strongest longwave cooling, the curved blue arrows represent turbulent mixing, U is the wind speed, T is the temperature, and RH is the relative humidity.

the fog geometric thickness and LWP are limited by the radiative cooling rate and absolute humidity in the isolated surface layer, or as a well-mixed adiabatic fog that can be > 100 m thick and interacts with the atmosphere above fog top through turbulent mixing (fig. 1.3, Price 2011; Smith et al. 2018). Initially, radiation fog particles form near the surface where radiative cooling is the strongest (Hoch et al. 2007). As the fog becomes optically thicker, the location of maximum longwave cooling transitions from the surface to the fog top (fig. 1.3), this transition takes place rapidly ($\sim$2 hours) and occurs on average 3.4 hours after fog initiation (Price 2011). The cooling at fog top generates a thermodynamic instability that drives mixing and acts to thicken the fog layer (Boutle et al. 2018; Smith et al. 2018, fig. 1.3). This process drives the transition from an optically thin fog in a stable boundary layer, that normally dissipates after $\sim$5 hours, to a thick well-mixed fog that can persist for > 8 hours (Price 2011; Boutle et al. 2018).

The transition from a stable to an adiabatic radiation fog can result in an increase in longwave radiative forcing at the surface by > 60 W m^{-2} over central Greenland due to the associated increase in LWP (Cox et al. 2019), and the impact on the SEB is further enhanced by the longer average lifetime of adiabatic fog. More commonly, fogs over central Greenland have a longwave radiative forcing of 10-20 W m^{-2} (Cox et al. 2019), suggesting that the transition to an adiabatic fog is relatively rare. Whether or not

this transition occurs is extremely sensitive to the vertical wind and thermodynamic profiles in the boundary layer (Haeffelin et al. 2013; Smith et al. 2018) and to the properties of the aerosol population (Boutle et al. 2018); suggesting that the surface aerosol population at Summit could play a key role in fog radiative forcing.

4.a. Fog-aerosol interactions

When the near-surface air cools to the point when it is saturated with respect to water, liquid and mixed-phase fogs form initially by the activation and subsequent growth of CCN into liquid droplets (e.g. Gultepe et al. 2007). Ice fogs can form either from homogeneous freezing of liquid droplets when temperatures fall below $\sim$ -35°C, heterogeneous glaciation of supercooled liquid fog involving contact or immersion nucleation of INP, or by the deposition nucleation of INP when the air becomes supersaturated with respect to ice (Gultepe et al. 2015, 2017). In all fogs, fog particles will continue to grow as long as supersaturation is maintained (either by further cooling or moistening), and new fog particles will continue to form as long as there are sufficient CCN (or INP) at the current supersaturation (or temperature). In this way, N_{CCN} and N_{INP} can modulate fog lifetime and microphysical properties (phase partitioning, droplet size distribution) in the same way as in clouds (Table 1.1, e.g. Maalick et al. 2016).

The properties of the aerosol population modulate fog top radiative cooling by dictating the fog emissivity associated with the fog particle size distribution and number concentration. This means that changes to the aerosol population can also impact if, and when, a fog event makes the transition from an optically thin fog in a stable boundary layer to a well-mixed fog with a longer lifetime and larger radiative impact at the surface (Maalick et al. 2016; Poku et al. 2019).

The occurrence of fog can also modify the aerosol population (e.g. Eck et al. 2012; Ervens 2015). In central Greenland, the number concentration of aerosol particles $>$ 0.5 μm diameter decreases to near zero during fog events (Bergin et al. 1994, 1995), suggesting that all large aerosol particles are either activated into, or scavenged by, fog droplets. The flux of aerosol chemical species to the ice sheet surface is up to twice as high during fog events compared to dry deposition alone (Bergin et al. 1995), this means that fog can act as a sink for CCN and INP particles, which could potentially impact fog and/or cloud formation later in time.

Fog can also facilitate mixing in the boundary layer which is otherwise almost always stably stratified over central Greenland (Miller et al. 2013). The mixing of air from

higher in the atmosphere down to the surface by either wind-shear or buoyancy driven mixing at fog top (e.g. fig. 1.3) could act to transport aerosol particles into the boundary layer, a process that is important in low-level Arctic stratocumulus clouds (Solomon et al. 2014; Igel et al. 2017). This process could also be important over the GrIS, since early studies of radionuclide tracers collected using filter samples suggest that aerosol species at Summit are depleted during extended stable periods and replenished during periods of increased vertical mixing (Dibb 1990; Dibb et al. 1992). The processing of aerosol particles in fog/cloud droplets can also modify aerosol chemistry and size distributions, with the combined effect of chemical reactions and the coagulation of interstitial aerosol particles with droplets resulting in an increase in the size of aerosol particles after droplet evaporation (e.g. Noble and Hudson 2019). The relative importance of these processes in fogs over GrIS is unknown.

Fogs are often not considered in studies of aerosol-cloud interactions (in part because of the difficulties associated with fog detection, see section 4.b) and existing long-term observational studies that have focused on fog over Greenland do not include aerosol measurements (Cox et al. 2019). The lack of observations of fog-aerosol interactions has been highlighted as a key deficiency in our understanding of aerosol-cloud-climate feedbacks over Greenland (Schmale et al. 2021).

4.b. Fog detection

One of the reasons that there are so few studies of fog over the GrIS is that fog can be extremely difficult to detect, particularly over ice-covered surfaces. Ground-based active remote sensing instruments such as radar and lidar underestimate fog occurrence, since fog can occur below the lowest range-gate of the instrument ($\sim$ 50-100 m, e.g. Nowak et al. 2008; Newsom et al. 2020). Satellite retrievals of fog over polar ice are also challenging; detection of fog based on visible light is not possible during winter and is difficult in summer since the difference in albedo between fog and ice is small. Satellite infrared detection of fog relies on accurately differentiating between the surface temperature and the fog top temperature (Yi et al. 2019), which can be subject to large uncertainties (Østby et al. 2014; Shuman et al. 2014). Uncertainties in surface elevation (especially over snow- and ice-covered surfaces) mean that a fog-top echo from space-borne lidar can be indistinguishable from a surface echo (Guzman et al. 2017). These uncertainties, combined with sparse in-situ observations, suggest that fog occurrence is likely to be underestimated over the GrIS.

Climate models tend to underestimate the occurrence of optically thin clouds over cen-

tral Greenland, especially in the summer and near the surface, and hence underestimate downwelling longwave radiation (Lacour et al. 2018; Taylor et al. 2019). Fog occurrence is likely to be underestimated in reanalysis and long-term observations due to difficulties in the remote sensing of fog over ice, yet can be an important control on downwelling longwave radiation at the surface, and on the surface aerosol population. Together this demonstrates a need for improvements in continuous long-term fog detection over Greenland, and for improved understanding of the processes controlling fog formation, lifetime, and microphysical properties.

5. Summit Station

Summit Station (72.58°N, 38.45°W; 3250 m a.s.l) is the only year-round research station located in the accumulation zone of the GrIS (fig. 1.4) and has been a focal point for measurement campaigns in central Greenland since the GISP2 ice coring project took place in 1989. Summit is over 400 km from the coast in each direction, and atmospheric conditions at Summit are representative of the high central plateau area of the ice sheet (> 2,000 m a.s.l, > 70° N), where there is very little topographic relief and the surface albedo is high year-round (Ettema et al. 2010; Box et al. 2012; Alexander et al. 2014). This is the region where cloud radiative forcing has a net annual warming effect at the surface (Miller et al. 2015; Wang et al. 2019), and where the surface aerosol population is more sensitive to long range transport and characterised by lower aerosol scattering and absorption coefficients compared to coastal Arctic sites (Hirdman et al. 2010; Schmeisser et al. 2018). Note that measurements collected at Summit are not representative of the ablation zone around the ice sheet edge (fig. 1.1), where there are steep elevation gradients, regular melt, and a distinctive annual cycle in surface albedo (Van den Broeke et al. 2011b; Ryan et al. 2022).

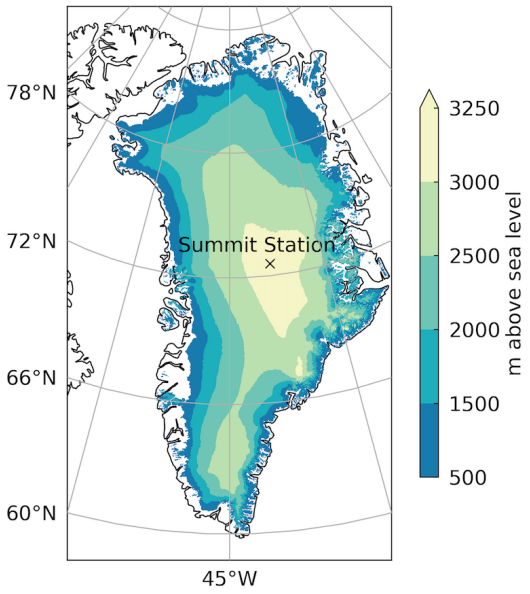

Figure 1.4.: The location of Summit Station at the highest point on the Greenland Ice Sheet, taken from Guy et al. (2021). Ice elevation contours are from the Greenland Ice Mapping Project (Howat et al. 2017).

The structure of the atmospheric boundary layer over this central part of the ice sheet is driven by the annual and diurnal cycles of solar radiation (Cohen et al. 2007), by large-scale circulation that advects different air masses over the ice sheet (e.g. Gallagher et al. 2018), and is modified by the presence of clouds (e.g. Miller et al. 2017). Under quiescent conditions (clear skies, light winds), longwave radiative cooling at the surface due to the high emissivity of the ice sheet and relatively low clear-sky downwelling longwave radiation (Hoch et al. 2007) drives persistent surface-based temperature inversions, which occur over 80% of the time between October and April and over 25% of the time between May and September (Miller et al. 2013).

Boundary layer depths for stable and neutral conditions in the spring and summer average 156 m at Summit (Cohen et al. 2007). The stable stratification and shallow boundary layer depths encourage the formation of shallow radiation fog and limit turbulent exchange of moisture and aerosol particles (e.g. Dibb 2007). This means that atmospheric properties measured near the surface (e.g. temperature, water vapor, and aerosol properties) are unlikely to be representative of those at cloud height (Berkelhammer et al. 2016), and even within fog layers, there can be strong thermodynamic gradients. This can explain some unique characteristics observed in fog events at Summit; for example, radiation fogs tend to form in a slightly elevated layer (2 to 10 m a.g.l) due to the water vapor mixing ratio gradient near the surface (Berkelhammer et al. 2016; Cox et al. 2019), and fogs containing liquid droplets can be present even when the 2 m air temperature is below the homogeneous freezing point of water ($< \sim$ -35°C), with the liquid droplets present in a warmer layer a few meters higher up (Cox et al. 2019).

5.a. Instrumentation at Summit

The Integrated Characterization of Energy, Clouds, Atmospheric state and Precipitation at Summit (ICECAPS) project has collected year-round measurements of atmospheric properties at Summit since 2010 (Shupe et al. 2013). The ICECAPS instrument suite consists of ground-based remote sensing instruments (radar, lidar, microwave and infrared radiometers), as well as twice-daily radiosonde launches, to monitor clouds, precipitation, and atmospheric structure above Summit, and has contributed the data from which much of our current understanding of atmospheric processes and their role in the SEB over central Greenland has been derived (e.g. Shupe et al. 2013; Bennartz et al. 2013; Miller et al. 2013, 2015, 2017; Cox et al. 2014, 2015; Pettersen et al. 2018, 2022; Gallagher et al. 2018).

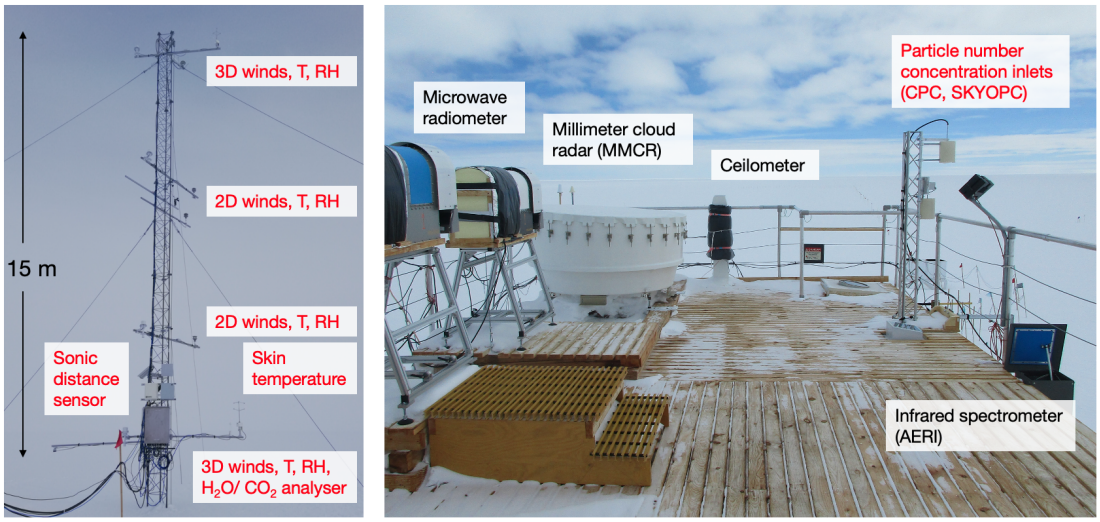

Figure 1.5.: Instrumentation used in this thesis, installed as part of the ICECAPS project at Summit. Instruments labelled in red were installed by the author in 2019 as part of ICECAPS-ACE.

In 2019, ICECAPS received an additional three years of funding to continue operations at Summit and to expand the instrument suite to include measurements of aerosol particle number concentrations and SEB components, with the purpose of enabling investigations into aerosol-cloud interactions over the ice sheet and how they impact the SEB. This extension was called ICECAPS- Aerosol Cloud Experiment (ICECAPS-ACE), and the measurements collected as part of ICECAPS-ACE (from the instruments shown in fig. 1.5) form the basis of this thesis. Notably, ICECAPS-ACE collected the first year-round measurements of surface aerosol particle number concentrations over central Greenland.

The NOAA Global Monitoring Laboratory measurements of surface meteorology and aerosol optical properties at Summit, as well as summer campaign measurements of aerosol particle number concentrations (Bergin et al. 1994, 1995), provide a long-term context for the ICECAPS-ACE measurements. Complementary multi-year observations of fog and SEB components at Summit provide additional background information, including year-round in-situ measurements of fog particle size distributions, which were not available during ICECAPS-ACE (Hoch et al. 2007; Cohen et al. 2007; Berkelhammer et al. 2016; Cox et al. 2019). The presence of the existing measurement platform, alongside complementary and historical measurements of aerosol, cloud, and fog properties, make Summit an ideal location to study fog and aerosol processes and their interaction with the SEB over the rapidly changing central plateau of the GrIS.

6. Objective and outline

The overall goal of this thesis is to combine new measurements of aerosol particle number concentrations and boundary layer meteorology from ICECAPS-ACE with existing ground-based remote sensing measurements at Summit to improve our understanding of the controls on the surface aerosol population and the interactions between fog and aerosol particles that might be important for the GrIS SEB.

Although the initial objective of ICECAPS-ACE was to study aerosol-cloud interactions, aerosol particle number concentrations measured near the surface are unlikely to be representative of those at cloud level ($>$ 150 m a.g.l) due to the persistent stable stratification of the boundary layer at Summit (e.g. Cohen et al. 2007). However, fog forms within this stable surface layer and interacts directly with the near-surface aerosol population. Fog at Summit shares some characteristics of typical low-level Arctic clouds, for example, there is evidence that fogs can be 'mixed-phase', consisting of a liquid layer above settling ice crystals (Cox et al. 2019). Also, fogs are not necessarily coupled to the ice surface itself; Berkelhammer et al. (2016) show that in the spring and summer, condensation preferentially occurs just above the surface at Summit, and fogs forming under these conditions rely on a moisture source from above, a process that can also act to sustain mixed-phase Arctic clouds (e.g. Solomon et al. 2014). Hence, in addition to being an important topic of study due to a lack of existing observations and difficulties associated with fog detection over the ice sheet, the study of fog-aerosol interactions at Summit can provide motivation and direction for future studies of vertical profiles of aerosol properties and their interaction with clouds over the ice sheet.

The main body of this thesis is organised into three chapters, each of which is a standalone publication. Chapter 2 presents the first full annual cycle of surface aerosol particle number concentrations (particles greater than 20 nm diameter, N_{20}) measured at Summit and explores the local and synoptic drivers of variability in N_{20}. Although direct measurements of N_{CCN} and N_{INP} are unavailable, N_{20} provides useful information about the cloud-relevant aerosol population. Existing observations indicate that N_{CCN} and N_{INP} particles in the Arctic are $>$ 20 nm diameter and make up only a subset of the total particle number concentration (Leaitch et al. 2016; Baccarini et al. 2020; Creamean et al. 2022), therefore N_{20} provides an upper bound to N_{CCN} and N_{INP}. The objective of Chapter 2 is to answer the following questions:

(i) What is the seasonal cycle in N_{20} at Summit?

(ii) What are the key drivers of intra-annual and intra-seasonal variability in N_{20}?

(iii) Are aerosol particle number concentrations ever low enough to critically limit cloud or fog formation at Summit?

The answers to these three questions will enable future studies to investigate how the aerosol population over the GrIS might change in the future with projected changes in atmospheric circulation and climate over the GrIS, and how important such changes might be for the GrIS SEB and future melt.

To use the measurements presented in Chapter 2 to study fog-aerosol interactions, we need to be able to detect fog events at Summit and determine the characteristics of the fog that might impact, or be impacted by, the aerosol population (i.e. phase partitioning, fog particle effective radius, optical depth, and the thermodynamic and turbulent structure of the fog). Chapter 3 is concerned with the first part of this problem; the detection of radiation fog at Summit in the absence of dedicated fog detection or visibility sensors. This chapter introduces a radiative definition of fog that is more appropriate for the studying the impact of fog on the SEB than traditional visibility-based definitions and shows that fog can have a detectable impact on downwelling longwave radiation even when active remote sensing instruments (radar, lidar, ceilometer) and the microwave radiometer (traditionally used for liquid water path detection) struggle to detect it. The objective of Chapter 3 is to explore the sensitivity of spectrally resolved measurements of downwelling longwave radiation (8 to 20 μm) to shallow near-surface temperature inversions and small increases in liquid water path associated with radiation fog formation at Summit.

Continuous accurate profiles of boundary layer temperature are necessary for the retrieval of fog microphysical properties (phase and particle size distributions) from spectrally resolved downwelling longwave radiation (e.g. Turner 2005). A further objective of Chapter 3 is to quantify the uncertainties in the boundary layer temperature profile retrievals so that they can be used in Chapter 4 to retrieve fog microphysical properties. The first half of Chapter 4 then explores the potential to use spectrally resolved downwelling longwave radiation to retrieve fog optical depth, phase, and particle size distributions. The second half of Chapter 4 combines the retrievals of fog microphysical properties with the surface aerosol particle measurements across twelve case studies of radiation fog during the summer of 2019. This final section discusses the observational evidence for aerosol controls on fog lifetime and microphysical properties, and for modifications of the aerosol population induced by the fog over the central GrIS.

This thesis presents novel observations of surface aerosol properties over central Greenland, and the first application of ground-based infrared remote sensing for the detection

and retrieval of fog microphysical properties in cases of optically thin radiation fog. As an observational study, a goal of this thesis is to provide measurements, case studies, and direction for future process-based modelling studies, model evaluation, and the development of improved parameterisations of aerosol and fog properties over the GrIS that might ultimately reduce the uncertainty in future projections of the GrIS SEB. In addition, the results of this thesis have broader implications for the detection of radiation fog outside of Greenland, highlight important deficiencies in existing measurements, and raise new questions that might direct future studies. Chapter 5 discusses all these points and provides a summary of the main conclusions.

References

Ackerman, A. S., Kirkpatrick, M. P., Stevens, D. E., and Toon, O. B.: The impact of humidity above stratiform clouds on indirect aerosol climate forcing, Nature, 432, 1014–1017, 2004.

Albrecht, B. A.: Aerosols, cloud microphysics, and fractional cloudiness, Science, 245, 1227–1230, 1989.

Alexander, P., Tedesco, M., Fettweis, X., Van De Wal, R., Smeets, C., and Van Den Broeke, M.: Assessing spatio-temporal variability and trends in modelled and measured Greenland Ice Sheet albedo (2000–2013), The Cryosphere, 8, 2293–2312, 2014.

Ansmann, A., Tesche, M., Althausen, D., Müller, D., Seifert, P., Freudenthaler, V., Heese, B., Wiegner, M., Pisani, G., and Knippertz, P.: Influence of Saharan dust on cloud glaciation in southern Morocco during the Saharan Mineral Dust Experiment, Journal of Geophysical Research: Atmospheres, 113, 2008.

Armstrong McKay, D. I., Staal, A., Abrams, J. F., Winkelmann, R., Sakschewski, B., Loriani, S., Fetzer, I., Cornell, S. E., Rockström, J., and Lenton, T. M.: Exceeding 1.5 °C global warming could trigger multiple climate tipping points, Science, 377, 2022.

Baccarini, A., Karlsson, L., Dommen, J., Duplessis, P., Vüllers, J., Brooks, I. M., Saiz-Lopez, A., Salter, M., Tjernström, M., Baltensperger, U., et al.: Frequent new particle formation over the high Arctic pack ice by enhanced iodine emissions, Nature communications, 11, 1–11, 2020.

Bamber, J., Tedstone, A., King, M., Howat, I., Enderlin, E., Van Den Broeke, M., and Noel, B.: Land ice freshwater budget of the Arctic and North Atlantic Oceans: 1. Data, methods, and results, Journal of Geophysical Research: Oceans, 123, 1827–1837, 2018.

Bellouin, N., Quaas, J., Gryspeerdt, E., Kinne, S., Stier, P., Watson-Parris, D., Boucher, O., Carslaw, K. S., Christensen, M., Daniau, A.-L., et al.: Bounding global aerosol radiative forcing of climate change, Reviews of Geophysics, 58, 2020.

Bennartz, R., Shupe, M. D., Turner, D. D., Walden, V., Steffen, K., Cox, C. J., Kulie, M. S., Miller, N. B., and Pettersen, C.: July 2012 Greenland melt extent enhanced

by low-level liquid clouds, Nature, 496, 83–86, 2013.

Bergin, M., Jaffrezo, J., Davidson, C., Caldow, R., and Dibb, J.: Fluxes of chemical species to the Greenland Ice Sheet at Summit by fog and dry deposition, Geochimica et cosmochimica acta, 58, 3207–3215, 1994.

Bergin, M., Jaffrezo, J.-L., Davidson, C., Dibb, J. E., Pandis, S., Hillamo, R., Maenhaut, W., Kuhns, H., and Makela, T.: The contributions of snow, fog, and dry deposition to the summer flux of anions and cations at Summit, Greenland, Journal of Geophysical Research: Atmospheres, 100, 16 275–16 288, 1995.

Berkelhammer, M., Noone, D. C., Steen-Larsen, H. C., Bailey, A., Cox, C. J., O'Neill, M. S., Schneider, D., Steffen, K., and White, J. W.: Surface-atmosphere decoupling limits accumulation at summit, Greenland, Science Advances, 2, 2016.

Boers, N. and Rypdal, M.: Critical slowing down suggests that the western Greenland Ice Sheet is close to a tipping point, Proceedings of the National Academy of Sciences, 118, 2021.

Borys, R. D., Lowenthal, D. H., Cohn, S. A., and Brown, W. O.: Mountaintop and radar measurements of anthropogenic aerosol effects on snow growth and snowfall rate, Geophysical Research Letters, 30, 2003.

Boutle, I., Price, J., Kudzotsa, I., Kokkola, H., and Romakkaniemi, S.: Aerosol–fog interaction and the transition to well-mixed radiation fog, Atmospheric Chemistry and Physics, 18, 7827–7840, 2018.

Box, J., Fettweis, X., Stroeve, J., Tedesco, M., Hall, D., and Steffen, K.: Greenland Ice Sheet albedo feedback: thermodynamics and atmospheric drivers, The Cryosphere, 6, 821–839, 2012.

Box, J. E., Colgan, W. T., Wouters, B., Burgess, D. O., O'Neel, S., Thomson, L. I., and Mernild, S. H.: Global sea-level contribution from Arctic land ice: 1971–2017, Environmental Research Letters, 13, 2018.

Bulatovic, I., Igel, A. L., Leck, C., Heintzenberg, J., Riipinen, I., and Ekman, A. M.: The importance of Aitken mode aerosol particles for cloud sustenance in the summertime high Arctic–a simulation study supported by observational data, Atmospheric Chemistry and Physics, 21, 3871–3897, 2021.

Carslaw, K. S.: Aerosol processes, in: Aerosols and Climate, pp. 135–185, Elsevier,

2022.

Cohen, L., Helmig, D., Neff, W. D., Grachev, A. A., and Fairall, C. W.: Boundary-layer dynamics and its influence on atmospheric chemistry at Summit, Greenland, Atmospheric Environment, 41, 5044–5060, 2007.

Cox, C. J., Walden, V. P., Compo, G. P., Rowe, P. M., Shupe, M. D., and Steffen, K.: Downwelling longwave flux over Summit, Greenland, 2010–2012: Analysis of surface-based observations and evaluation of ERA-Interim using wavelets, Journal of Geophysical Research: Atmospheres, 119, 12–317, 2014.

Cox, C. J., Walden, V. P., Rowe, P. M., and Shupe, M. D.: Humidity trends imply increased sensitivity to clouds in a warming Arctic, Nature communications, 6, 1–8, 2015.

Cox, C. J., Noone, D. C., Berkelhammer, M., Shupe, M. D., Neff, W. D., Miller, N. B., Walden, V. P., and Steffen, K.: Supercooled liquid fogs over the central Greenland Ice Sheet, Atmospheric Chemistry and Physics, 19, 7467–7485, 2019.

Creamean, J. M., Barry, K., Hill, T. C., Hume, C., DeMott, P. J., Shupe, M. D., Dahlke, S., Willmes, S., Schmale, J., Beck, I., et al.: Annual cycle observations of aerosols capable of ice formation in central Arctic clouds, Nature communications, 13, 1–12, 2022.

Dai, A., Luo, D., Song, M., and Liu, J.: Arctic amplification is caused by sea-ice loss under increasing CO_2, Nature communications, 10, 1–13, 2019.

Davidson, C. I., Jaffrezo, J.-L., Small, M. J., Summers, P. W., Olson, M. P., and Borys, R. D.: Trajectory analysis of source regions influencing the south Greenland Ice Sheet during the Dye 3 Gas and Aerosol Sampling Program, Atmospheric Environment. Part A. General Topics, 27, 2739–2749, 1993.

De Boer, G., Morrison, H., Shupe, M., and Hildner, R.: Evidence of liquid dependent ice nucleation in high-latitude stratiform clouds from surface remote sensors, Geophysical Research Letters, 38, 2011.

Di Biagio, C., di Sarra, A., Eriksen, P., Ascanius, S. E., Muscari, G., and Holben, B.: Effect of surface albedo, water vapour, and atmospheric aerosols on the cloud-free shortwave radiative budget in the Arctic, Climate dynamics, 39, 953–969, 2012.

Dibb, J. E.: Beryllium-7 and Lead-210 in the atmosphere and surface snow over the

Greenland Ice Sheet in the summer of 1989, Journal of Geophysical Research: Atmospheres, 95, 22 407–22 415, 1990.

Dibb, J. E.: Vertical mixing above Summit, Greenland: Insights into seasonal and high frequency variability from the radionuclide tracers 7Be and 210Pb, Atmospheric Environment, 41, 5020–5030, 2007.

Dibb, J. E., Jaffrezo, J., and Legrand, M.: Initial findings of recent investigations of air-snow relationships in the Summit region of the Greenland Ice Sheet, Journal of atmospheric chemistry, 14, 167–180, 1992.

Drab, E., Gaudichet, A., Jaffrezo, J., and Colin, J.: Mineral particles content in recent snow at Summit (Greenland), Atmospheric Environment, 36, 5365–5376, 2002.

Eck, T. F., Holben, B. N., Reid, J., Giles, D., Rivas, M., Singh, R. P., Tripathi, S., Bruegge, C., Platnick, S., Arnold, G., et al.: Fog-and cloud-induced aerosol modification observed by the Aerosol Robotic Network (AERONET), Journal of Geophysical Research: Atmospheres, 117, 2012.

Ervens, B.: Modeling the processing of aerosol and trace gases in clouds and fogs, Chemical reviews, 115, 4157–4198, 2015.

Ettema, J., Van den Broeke, M., Van Meijgaard, E., and Van de Berg, W.: Climate of the Greenland Ice Sheet using a high-resolution climate model–Part 2: Near-surface climate and energy balance, The Cryosphere, 4, 529–544, 2010.

Fan, J., Wang, Y., Rosenfeld, D., and Liu, X.: Review of aerosol–cloud interactions: Mechanisms, significance, and challenges, Journal of the Atmospheric Sciences, 73, 4221–4252, 2016.

Flyger, H., Hansen, K., Megaw, W., and Cox, L.: The background level of the summer tropospheric aerosol over Greenland and the North Atlantic Ocean, Journal of Applied Meteorology and Climatology, 12, 161–174, 1973.

Flyger, H., Heidam, N., Hansen, K., Megaw, W., Walther, E., and Hogan, A.: The background level of the summer tropospheric aerosol, sulphur dioxide and ozone over Greenland and the North Atlantic Ocean, Journal of Aerosol Science, 7, 103–140, 1976.

Ford, J. D., Pearce, T., Canosa, I. V., and Harper, S.: The rapidly changing Arctic and its societal implications, Wiley Interdisciplinary Reviews: Climate Change, 12,

e735, 2021.

Freud, E., Krejci, R., Tunved, P., Leaitch, R., Nguyen, Q. T., Massling, A., Skov, H., and Barrie, L.: Pan-Arctic aerosol number size distributions: seasonality and transport patterns, Atmospheric Chemistry and Physics, 17, 8101–8128, 2017.

Gallagher, M. R., Shupe, M. D., and Miller, N. B.: Impact of atmospheric circulation on temperature, clouds, and radiation at Summit Station, Greenland, with self-organizing maps, Journal of Climate, 31, 8895–8915, 2018.

Garrett, T. J. and Zhao, C.: Increased Arctic cloud longwave emissivity associated with pollution from mid-latitudes, Nature, 440, 787–789, 2006.

Goelzer, H., Nowicki, S., Payne, A., Larour, E., Seroussi, H., Lipscomb, W. H., Gregory, J., Abe-Ouchi, A., Shepherd, A., Simon, E., et al.: The future sea-level contribution of the Greenland Ice Sheet: a multi-model ensemble study of ISMIP6, The Cryosphere, 14, 3071–3096, 2020.

Graversen, R. G. and Burtu, M.: Arctic amplification enhanced by latent energy transport of atmospheric planetary waves, Quarterly Journal of the Royal Meteorological Society, 142, 2046–2054, 2016.

Gryspeerdt, E., Goren, T., Sourdeval, O., Quaas, J., Mülmenstädt, J., Dipu, S., Unglaub, C., Gettelman, A., and Christensen, M.: Constraining the aerosol influence on cloud liquid water path, Atmospheric Chemistry and Physics, 19, 5331–5347, 2019.

Gultepe, I., Tardif, R., Michaelides, S. C., Cermak, J., Bott, A., Bendix, J., Müller, M. D., Pagowski, M., Hansen, B., Ellrod, G., et al.: Fog research: A review of past achievements and future perspectives, Pure and applied geophysics, 164, 1121–1159, 2007.

Gultepe, I., Zhou, B., Milbrandt, J., Bott, A., Li, Y., Heymsfield, A. J., Ferrier, B., Ware, R., Pavolonis, M., Kuhn, T., et al.: A review on ice fog measurements and modeling, Atmospheric Research, 151, 2–19, 2015.

Gultepe, I., Heymsfield, A. J., Gallagher, M., Ickes, L., and Baumgardner, D.: Ice fog: The current state of knowledge and future challenges, Meteorological Monographs, 58, 4–1, 2017.

Guy, H., Brooks, I., Carslaw, K., Murray, B., Walden, V., Shupe, M., Pettersen, C.,

Turner, D., Cox, C., Neff, W., et al.: Controls on surface aerosol number concentrations and aerosol-limited cloud regimes over the central Greenland Ice Sheet, Atmospheric Chemistry and Physics, 21, 1–36, 2021.

Guzman, R., Chepfer, H., Noel, V., Vaillant de Guélis, T., Kay, J., Raberanto, P., Cesana, G., Vaughan, M., and Winker, D.: Direct atmosphere opacity observations from CALIPSO provide new constraints on cloud-radiation interactions, Journal of Geophysical Research: Atmospheres, 122, 1066–1085, 2017.

Haeffelin, M., Dupont, J.-C., Boyouk, N., Baumgardner, D., Gomes, L., Roberts, G., and Elias, T.: A comparative study of radiation fog and quasi-fog formation processes during the ParisFog field experiment 2007, Pure and Applied Geophysics, 170, 2283–2303, 2013.

Hirdman, D., Burkhart, J. F., Sodemann, H., Eckhardt, S., Jefferson, A., Quinn, P. K., Sharma, S., Ström, J., and Stohl, A.: Long-term trends of black carbon and sulphate aerosol in the Arctic: changes in atmospheric transport and source region emissions, Atmospheric Chemistry and Physics, 10, 9351–9368, 2010.

Hoch, S., Calanca, P., Philipona, R., and Ohmura, A.: Year-round observation of longwave radiative flux divergence in Greenland, Journal of Applied Meteorology and Climatology, 46, 1469–1479, 2007.

Hofer, S., Tedstone, A. J., Fettweis, X., and Bamber, J. L.: Decreasing cloud cover drives the recent mass loss on the Greenland Ice Sheet, Science Advances, 3, e1700 584, 2017.

Hofer, S., Tedstone, A. J., Fettweis, X., and Bamber, J. L.: Cloud microphysics and circulation anomalies control differences in future Greenland melt, Nature Climate Change, 9, 523–528, 2019.

Hogan, A., Barnard, S., Kebschull, K., Townsend, R., and Samson, J.: Aerosol variation in the western hemisphere Arctic, Journal of aerosol science, 15, 13–33, 1984.

Howat, I., Negrete, A., and Smith, B.: The Greenland Ice Mapping Project (GIMP) Land Ice and Ocean Classification Mask, Version 1., NASA National Snow and Ice Data Center Distributed Active Archive Center., https://doi.org/https://doi.org/10.5067/B8X58MQBFUPA, 2017.

Igel, A. L., Ekman, A. M., Leck, C., Tjernström, M., Savre, J., and Sedlar, J.: The free troposphere as a potential source of arctic boundary layer aerosol particles,

Geophysical Research Letters, 44, 7053–7060, 2017.

IMBIE: Mass balance of the Greenland Ice Sheet from 1992 to 2018, Nature, 579, 233–239, 2020.

Kanji, Z. A., Ladino, L. A., Wex, H., Boose, Y., Burkert-Kohn, M., Cziczo, D. J., and Krämer, M.: Overview of ice nucleating particles, Meteorological Monographs, 58, 1–1, 2017.

Korolev, A.: Limitations of the Wegener–Bergeron–Findeisen mechanism in the evolution of mixed-phase clouds, Journal of the Atmospheric Sciences, 64, 3372–3375, 2007.

Lacour, A., Chepfer, H., Miller, N., Shupe, M., Noel, V., Fettweis, X., Gallee, H., Kay, J., Guzman, R., and Cole, J.: How well are clouds simulated over Greenland in climate models? Consequences for the surface cloud radiative effect over the ice sheet, Journal of Climate, 31, 9293–9312, 2018.

Lance, S., Shupe, M., Feingold, G., Brock, C., Cozic, J., Holloway, J., Moore, R., Nenes, A., Schwarz, J., Spackman, J. R., et al.: Cloud condensation nuclei as a modulator of ice processes in Arctic mixed-phase clouds, Atmospheric Chemistry and Physics, 11, 8003–8015, 2011.

Leaitch, W. R., Korolev, A., Aliabadi, A. A., Burkart, J., Willis, M. D., Abbatt, J. P., Bozem, H., Hoor, P., Köllner, F., Schneider, J., et al.: Effects of 20–100 nm particles on liquid clouds in the clean summertime Arctic, Atmospheric Chemistry and Physics, 16, 11 107–11 124, 2016.

Lohmann, U.: Can anthropogenic aerosols decrease the snowfall rate?, Journal of the atmospheric sciences, 61, 2457–2468, 2004.

Lubin, D. and Vogelmann, A.: Observational quantification of a total aerosol indirect effect in the Arctic, Tellus B: Chemical and Physical Meteorology, 62, 181–189, 2010.

Lubin, D. and Vogelmann, A. M.: A climatologically significant aerosol longwave indirect effect in the Arctic, Nature, 439, 453–456, 2006.

Maalick, Z., Kühn, T., Korhonen, H., Kokkola, H., Laaksonen, A., and Romakkaniemi, S.: Effect of aerosol concentration and absorbing aerosol on the radiation fog life cycle, Atmospheric Environment, 133, 26–33, 2016.

Mauritsen, T., Sedlar, J., Tjernström, M., Leck, C., Martin, M., Shupe, M., Sjogren,

S., Sierau, B., Persson, P., Brooks, I., et al.: An Arctic CCN-limited cloud-aerosol regime, Atmospheric Chemistry and Physics, 11, 165–173, 2011.

McGrath, D., Colgan, W., Bayou, N., Muto, A., and Steffen, K.: Recent warming at Summit, Greenland: Global context and implications, Geophysical Research Letters, 40, 2091–2096, 2013.

Miller, N., Turner, D., Bennartz, R., Shupe, M., Kulie, M., Cadeddu, M., and Walden, V. P.: Surface-based inversions above central Greenland, Journal of Geophysical Research: Atmospheres, 118, 495–506, 2013.

Miller, N. B., Shupe, M. D., Cox, C. J., Walden, V. P., Turner, D. D., and Steffen, K.: Cloud radiative forcing at Summit, Greenland, Journal of Climate, 28, 6267–6280, 2015.

Miller, N. B., Shupe, M. D., Cox, C. J., Noone, D., Persson, P. O. G., and Steffen, K.: Surface energy budget responses to radiative forcing at Summit, Greenland, The Cryosphere, 11, 497–516, 2017.

Miller, N. B., Shupe, M. D., Lenaerts, J. T., Kay, J. E., de Boer, G., and Bennartz, R.: Process-based model evaluation using surface energy budget observations in Central Greenland, Journal of Geophysical Research: Atmospheres, 123, 4777–4796, 2018.

Morlighem, M., Williams, C. N., Rignot, E., An, L., Arndt, J. E., Bamber, J. L., Catania, G., Chauché, N., Dowdeswell, J. A., Dorschel, B., et al.: BedMachine v3: Complete bed topography and ocean bathymetry mapping of Greenland from multibeam echo sounding combined with mass conservation, Geophysical research letters, 44, 11–051, 2017.

Morrison, H., Zuidema, P., Ackerman, A. S., Avramov, A., De Boer, G., Fan, J., Fridlind, A. M., Hashino, T., Harrington, J. Y., Luo, Y., et al.: Intercomparison of cloud model simulations of Arctic mixed-phase boundary layer clouds observed during SHEBA/FIRE-ACE, Journal of Advances in Modeling Earth Systems, 3, 2011.

Moustafa, S., Rennermalm, A., Smith, L., Miller, M., Mioduszewski, J., Koenig, L., Hom, M., and Shuman, C.: Multi-modal albedo distributions in the ablation area of the southwestern Greenland Ice Sheet, The Cryosphere, 9, 905–923, 2015.

Murray-Watson, R. J. and Gryspeerdt, E.: Stability-dependent increases in liquid water with droplet number in the Arctic, Atmospheric Chemistry and Physics, 22, 5743–5756, 2022.

Natali, S. M., Holdren, J. P., Rogers, B. M., Treharne, R., Duffy, P. B., Pomerance, R., and MacDonald, E.: Permafrost carbon feedbacks threaten global climate goals, Proceedings of the National Academy of Sciences, 118, 2021.

Newsom, R., Turner, D., Lehtinen, R., Münkel, C., Kallio, J., and Roininen, R.: Evaluation of a compact broadband differential absorption lidar for routine water vapor profiling in the atmospheric boundary layer, Journal of Atmospheric and Oceanic Technology, 37, 47–65, 2020.

Nguyen, Q. T., Glasius, M., Sørensen, L. L., Jensen, B., Skov, H., Birmili, W., Wiedensohler, A., Kristensson, A., Nøjgaard, J. K., and Massling, A.: Seasonal variation of atmospheric particle number concentrations, new particle formation and atmospheric oxidation capacity at the high Arctic site Villum Research Station, Station Nord, Atmospheric Chemistry and Physics, 16, 11 319–11 336, 2016.

Nicholls, R. J.: Adapting to sea-level rise, Resilience, pp. 13–29, 2018.

Niwano, M., Hashimoto, A., and Aoki, T.: Cloud-driven modulations of Greenland Ice Sheet surface melt, Scientific reports, 9, 1–8, 2019.

Noble, S. R. and Hudson, J. G.: Effects of continental clouds on surface Aitken and accumulation modes, Journal of Geophysical Research: Atmospheres, 124, 5479–5502, 2019.

Norgren, M. S., De Boer, G., and Shupe, M. D.: Observed aerosol suppression of cloud ice in low-level Arctic mixed-phase clouds, Atmospheric Chemistry and Physics, 18, 13 345–13 361, 2018.

Nowak, D., Ruffieux, D., Agnew, J. L., and Vuilleumier, L.: Detection of fog and low cloud boundaries with ground-based remote sensing systems, Journal of Atmospheric and Oceanic Technology, 25, 1357–1368, 2008.

Østby, T. I., Schuler, T. V., and Westermann, S.: Severe cloud contamination of MODIS Land Surface Temperatures over an Arctic ice cap, Svalbard, Remote Sensing of Environment, 142, 95–102, 2014.

Pettersen, C., Bennartz, R., Merrelli, A. J., Shupe, M. D., Turner, D. D., and Walden, V. P.: Precipitation regimes over central Greenland inferred from 5 years of ICECAPS observations, Atmospheric Chemistry and Physics, 18, 4715–4735, 2018.

Pettersen, C., Henderson, S. A., Mattingly, K. S., Bennartz, R., and Breeden, M. L.:

The Critical Role of Euro-Atlantic Blocking in Promoting Snowfall in Central Greenland, Journal of Geophysical Research: Atmospheres, 127, 2022.

Pithan, F. and Mauritsen, T.: Arctic amplification dominated by temperature feedbacks in contemporary climate models, Nature geoscience, 7, 181–184, 2014.

Poku, C., Ross, A., Blyth, A., Hill, A., and Price, J.: How important are aerosol–fog interactions for the successful modelling of nocturnal radiation fog?, Weather, 74, 237–243, 2019.

Price, J.: Radiation fog. Part I: observations of stability and drop size distributions, Boundary-layer meteorology, 139, 167–191, 2011.

Quinn, P., Miller, T., Bates, T., Ogren, J., Andrews, E., and Shaw, G.: A 3-year record of simultaneously measured aerosol chemical and optical properties at Barrow, Alaska, Journal of Geophysical Research: Atmospheres, 107, AAC–8, 2002.

Rantanen, M., Karpechko, A. Y., Lipponen, A., Nordling, K., Hyvärinen, O., Ruosteenoja, K., Vihma, T., and Laaksonen, A.: The Arctic has warmed nearly four times faster than the globe since 1979, Communications Earth & Environment, 3, 1–10, 2022.

Rignot, E., Velicogna, I., van den Broeke, M. R., Monaghan, A., and Lenaerts, J. T.: Acceleration of the contribution of the Greenland and Antarctic ice sheets to sea level rise, Geophysical research letters, 38, 2011.

Ritter, C., Notholt, J., Fischer, J., and Rathke, C.: Direct thermal radiative forcing of tropospheric aerosol in the Arctic measured by ground based infrared spectrometry, Geophysical research letters, 32, 2005.

Robinson, A., Calov, R., and Ganopolski, A.: Multistability and critical thresholds of the Greenland Ice Sheet, Nature Climate Change, 2, 429–432, 2012.

Ryan, J., Smith, L., Cooley, S., Pearson, B., Wever, N., Keenan, E., and Lenaerts, J.: Decreasing surface albedo signifies a growing importance of clouds for Greenland Ice Sheet meltwater production, Nature Communications, 13, 1–8, 2022.

Schmale, J., Zieger, P., and Ekman, A. M.: Aerosols in current and future Arctic climate, Nature Climate Change, 11, 95–105, 2021.

Schmeisser, L., Backman, J., Ogren, J. A., Andrews, E., Asmi, E., Starkweather, S., Uttal, T., Fiebig, M., Sharma, S., Eleftheriadis, K., et al.: Seasonality of aerosol

optical properties in the Arctic, Atmospheric Chemistry and Physics, 18, 11 599–11 622, 2018.

Shaw, G. E.: The Arctic haze phenomenon, Bulletin of the American Meteorological Society, 76, 2403–2414, 1995.

Shuman, C. A., Hall, D. K., DiGirolamo, N. E., Mefford, T. K., and Schnaubelt, M. J.: Comparison of near-surface air temperatures and MODIS ice-surface temperatures at Summit, Greenland (2008–13), Journal of Applied Meteorology and Climatology, 53, 2171–2180, 2014.

Shupe, M. D. and Intrieri, J. M.: Cloud radiative forcing of the Arctic surface: The influence of cloud properties, surface albedo, and solar zenith angle, Journal of climate, 17, 616–628, 2004.

Shupe, M. D., Turner, D. D., Walden, V. P., Bennartz, R., Cadeddu, M. P., Castellani, B. B., Cox, C. J., Hudak, D. R., Kulie, M. S., Miller, N. B., et al.: High and dry: New observations of tropospheric and cloud properties above the Greenland Ice Sheet, Bulletin of the American Meteorological Society, 94, 169–186, 2013.

Slater, T., Hogg, A. E., and Mottram, R.: Ice-sheet losses track high-end sea-level rise projections, Nature Climate Change, 10, 879–881, 2020.

Small, J. D., Chuang, P. Y., Feingold, G., and Jiang, H.: Can aerosol decrease cloud lifetime?, Geophysical Research Letters, 36, 2009.

Smith, D., Renfrew, I., Price, J., and Dorling, S.: Numerical modelling of the evolution of the boundary layer during a radiation fog event, Weather, 73, 310–316, 2018.

Smith, L. C. and Stephenson, S. R.: New Trans-Arctic shipping routes navigable by midcentury, Proceedings of the National Academy of Sciences, 110, E1191–E1195, 2013.

Solomon, A., Shupe, M. D., Persson, P., and Morrison, H.: Moisture and dynamical interactions maintaining decoupled Arctic mixed-phase stratocumulus in the presence of a humidity inversion, Atmospheric Chemistry and Physics, 11, 10 127–10 148, 2011.

Solomon, A., Shupe, M. D., Persson, O., Morrison, H., Yamaguchi, T., Caldwell, P. M., and de Boer, G.: The sensitivity of springtime Arctic mixed-phase stratocumulus clouds to surface-layer and cloud-top inversion-layer moisture sources, Journal of the Atmospheric Sciences, 71, 574–595, 2014.

Stephenson, S. R., Wang, W., Zender, C. S., Wang, H., Davis, S. J., and Rasch, P. J.: Climatic responses to future trans-Arctic shipping, Geophysical research letters, 45, 9898–9908, 2018.

Sterzinger, L. J., Sedlar, J., Guy, H., Neely III, R. R., and Igel, A. L.: Do Arctic mixed-phase clouds sometimes dissipate due to insufficient aerosol? Evidence from comparisons between observations and idealized simulations, Atmospheric Chemistry and Physics, 22, 8973–8988, 2022.

Stevens, R. G., Loewe, K., Dearden, C., Dimitrelos, A., Possner, A., Eirund, G. K., Raatikainen, T., Hill, A. A., Shipway, B. J., Wilkinson, J., et al.: A model intercomparison of CCN-limited tenuous clouds in the high Arctic, Atmospheric Chemistry and Physics, 18, 11 041–11 071, 2018.

Stohl, A.: Characteristics of atmospheric transport into the Arctic troposphere, Journal of Geophysical Research: Atmospheres, 111, 2006.

Stuecker, M. F., Bitz, C. M., Armour, K. C., Proistosescu, C., Kang, S. M., Xie, S.-P., Kim, D., McGregor, S., Zhang, W., Zhao, S., et al.: Polar amplification dominated by local forcing and feedbacks, Nature Climate Change, 8, 1076–1081, 2018.

Suzuki, K., Stephens, G. L., and Lebsock, M. D.: Aerosol effect on the warm rain formation process: Satellite observations and modeling, Journal of Geophysical Research: Atmospheres, 118, 170–184, 2013.

Taylor, P. C., Cai, M., Hu, A., Meehl, J., Washington, W., and Zhang, G. J.: A decomposition of feedback contributions to polar warming amplification, Journal of Climate, 26, 7023–7043, 2013.

Taylor, P. C., Boeke, R. C., Li, Y., and Thompson, D. W.: Arctic cloud annual cycle biases in climate models, Atmospheric Chemistry and Physics, 19, 8759–8782, 2019.

Turner, D. D.: Arctic mixed-phase cloud properties from AERI lidar observations: Algorithm and results from SHEBA, Journal of Applied Meteorology, 44, 427–444, 2005.

Twomey, S.: The influence of pollution on the shortwave albedo of clouds, Journal of the atmospheric sciences, 34, 1149–1152, 1977.

Twomey, S.: Aerosols, clouds and radiation, Atmospheric Environment. Part A. General Topics, 25, 2435–2442, 1991.

Van den Broeke, M., Smeets, C., and Van de Wal, R.: The seasonal cycle and interannual variability of surface energy balance and melt in the ablation zone of the west Greenland Ice Sheet, The Cryosphere, 5, 377–390, 2011a.

Van den Broeke, M., Smeets, C., and Van de Wal, R.: The seasonal cycle and interannual variability of surface energy balance and melt in the ablation zone of the west Greenland Ice Sheet, The Cryosphere, 5, 377–390, 2011b.

Van den Broeke, M. R., Enderlin, E. M., Howat, I. M., Kuipers Munneke, P., Noël, B. P., Van De Berg, W. J., Van Meijgaard, E., and Wouters, B.: On the recent contribution of the Greenland Ice Sheet to sea level change, The Cryosphere, 10, 1933–1946, 2016.

Vincent, W. F., Callaghan, T. V., Dahl-Jensen, D., Johansson, M., Kovacs, K. M., Michel, C., Prowse, T., Reist, J. D., and Sharp, M.: Ecological implications of changes in the Arctic cryosphere, Ambio, 40, 87–99, 2011.

Wang, W., Zender, C. S., van As, D., and Miller, N. B.: Spatial distribution of melt season cloud radiative effects over Greenland: Evaluating satellite observations, reanalyses, and model simulations against in situ measurements, Journal of Geophysical Research: Atmospheres, 124, 57–71, 2019.

Wang, W., Zender, C. S., van As, D., Fausto, R. S., and Laffin, M. K.: Greenland surface melt dominated by solar and sensible heating, Geophysical Research Letters, 48, 2021.

Westbrook, C. and Illingworth, A.: The formation of ice in a long-lived supercooled layer cloud, Quarterly Journal of the Royal Meteorological Society, 139, 2209–2221, 2013.

Williams, A. S. and Igel, A. L.: Cloud Top Radiative Cooling Rate Drives Non-Precipitating Stratiform Cloud Responses to Aerosol Concentration, Geophysical Research Letters, 48, 2021.

Yau, M. K. and Rogers, R. R.: A short course in cloud physics, Elsevier, 1996.

Yi, L., Li, K.-F., Chen, X., and Tung, K.-K.: Arctic fog detection using infrared spectral measurements, Journal of Atmospheric and Oceanic Technology, 36, 1643–1656, 2019.

Ziemba, L. D., Dibb, J. E., Griffin, R. J., Huey, L. G., and Beckman, P.: Observations of particle growth at a remote, Arctic site, Atmospheric Environment, 44, 1649–1657,

2010.

Chapter 2.

Controls on surface aerosol particle number concentrations and aerosol-limited cloud regimes over the central Greenland Ice Sheet

Published in *Atmospheric Chemistry and Physics* (2021)

Atmos. Chem. Phys., 21, 15351–15374, 2021
https://doi.org/10.5194/acp-21-15351-2021

Atmospheric Chemistry and Physics
Open Access
EGU

Controls on surface aerosol particle number concentrations and aerosol-limited cloud regimes over the central Greenland Ice Sheet

Heather Guy[1,2], Ian M. Brooks[2], Ken S. Carslaw[2], Benjamin J. Murray[2], Von P. Walden[3], Matthew D. Shupe[4,5], Claire Pettersen[6], David D. Turner[8], Christopher J. Cox[5], William D. Neff[4,5], Ralf Bennartz[6,7], and Ryan R. Neely III[1,2]

[1]National Centre for Atmospheric Science, Leeds, UK
[2]School of Earth and Environment, University of Leeds, Leeds, UK
[3]Department of Civil and Environmental Engineering, Laboratory for Atmospheric Research, Washington State University, Pullman, WA, USA
[4]Cooperative Institute for Research in Environmental Sciences, University of Colorado Boulder, Boulder, CO, USA
[5]Physical Sciences Laboratory, National Oceanic and Atmospheric Administration, Boulder, CO, USA
[6]Space Science and Engineering Center, University of Wisconsin–Madison, Madison, WI, USA
[7]Earth and Environmental Sciences, Vanderbilt University, Nashville, TN, USA
[8]Global Systems Laboratory, National Oceanic and Atmospheric Administration, Boulder, CO, USA

Correspondence: Heather Guy (heather.guy@ncas.ac.uk)

Received: 10 June 2021 – Discussion started: 29 June 2021
Revised: 10 September 2021 – Accepted: 14 September 2021 – Published: 14 October 2021

Abstract. This study presents the first full annual cycle (2019–2020) of ambient surface aerosol particle number concentration measurements (condensation nuclei > 20 nm, N_{20}) collected at Summit Station (Summit), in the centre of the Greenland Ice Sheet (72.58° N, −38.45° E; 3250 m a.s.l.). The mean surface concentration in 2019 was 129 cm^{-3}, with the 6 h mean ranging between 1 and 1441 cm^{-3}. The highest monthly mean concentrations occurred during the late spring and summer, with the minimum concentrations occurring in February (mean: 18 cm^{-3}). High-N_{20} events are linked to anomalous anticyclonic circulation over Greenland and the descent of free-tropospheric aerosol down to the surface, whereas low-N_{20} events are linked to anomalous cyclonic circulation over south-east Greenland that drives upslope flow and enhances precipitation en route to Summit. Fog strongly affects particle number concentrations, on average reducing N_{20} by 20 % during the first 3 h of fog formation. Extremely-low-N_{20} events (< 10 cm^{-3}) occur in all seasons, and we suggest that fog, and potentially cloud formation, can be limited by low aerosol particle concentrations over central Greenland.

1 Introduction

The Greenland Ice Sheet (GrIS) has been losing mass at an unprecedented and accelerating rate since the early 21st century (Rignot et al., 2008, 2011; van den Broeke et al., 2016; Fettweis et al., 2017; Trusel et al., 2018; The IMBIE Team, 2020) and, as a result, has become the largest single contributor to global sea level rise (van den Broeke et al., 2016; Bamber et al., 2018; Slater et al., 2020). The majority of this mass loss is due to changes in the ice sheet surface mass balance (Slater et al., 2020) and, in particular, increased surface melt and run-off (Enderlin et al., 2014; van den Broeke et al., 2016; The IMBIE Team, 2020). Clouds play a critical role in the ice sheet surface mass balance, both by providing mass input in the form of precipitation and by modulating the net radiation at the surface, thus influencing surface melt and run-off (Bennartz et al., 2013; Van Tricht et al., 2016; Hofer et al., 2017; Miller et al., 2017). To make accurate projections of the future contribution of the GrIS to sea level rise, models must correctly represent the properties of clouds and their interaction with the surface energy budget. Although circulation anomalies drive a larger proportion of surface melt, discrepancies in cloud microphys-

ical properties between different models currently result in larger uncertainties in future GrIS melt projections than the difference between low- and high-greenhouse-emission scenarios (Hofer et al., 2019). Amongst the largest uncertainties in cloud microphysical modelling are the type, concentration, and sources of aerosol particles (e.g. Seinfeld et al., 2016). Improving our understanding of aerosols and their relationship with cloud properties over the GrIS is therefore key to reducing the uncertainty in future projections of GrIS melt and global sea level rise.

Cloud properties are sensitive to the type and concentration of tropospheric aerosol particles (e.g. Twomey, 1977; Curry et al., 1996; Storelvmo, 2017). Mixed-phase clouds in particular, which contribute significantly to surface warming over the GrIS (Miller et al., 2015; Van Tricht et al., 2016), are sensitive to the number concentration of cloud condensation nuclei and ice-nucleating particles (e.g. Norgren et al., 2018; Solomon et al., 2018), where cloud condensation nuclei (CCN) are a subset of aerosol particles on which liquid droplets can form, and ice-nucleating particles (INPs) are a subset of aerosols that can catalyse the formation of ice crystals.

In ice-covered polar regions, CCN concentrations can be very low; surface CCN concentrations at 0.2 % supersaturation are usually less than $100\,\mathrm{cm}^{-3}$ and can regularly fall below $10\,\mathrm{cm}^{-3}$ in the high Arctic (e.g. Mauritsen et al., 2011; Leck and Svensson, 2015), compared to typical values of over $1000\,\mathrm{cm}^{-3}$ at rural mid-latitude sites (e.g. Schmale et al., 2018). In cases where CCN are extremely low ($< 10\,\mathrm{cm}^{-3}$), the small number of sites for droplet activation limits cloud droplet number concentration, and high supersaturations cause all available CCN to activate and grow to relatively large sizes, facilitating further growth by collision and coalescence and resulting in precipitation as drizzle (Mauritsen et al., 2011). This generates a positive feedback where the lack of CCN can result in total dissipation of the cloud (Mauritsen et al., 2011; Stevens et al., 2018). Thus, within this CCN-limited regime, the availability of CCN becomes a dominant control on cloud formation and longevity such that a small increase in concentration can lead to a decrease in droplet size that serves to reduce precipitation efficiency, leading to a relative increase in cloud liquid water path (LWP) (Mauritsen et al., 2011). The change in LWP in turn modulates the cloud longwave radiative effect (Mauritsen et al., 2011; Miller et al., 2015). Alternatively, the addition of CCN when a cloud is not in the CCN-limited regime can have a cooling effect at the surface in the summer due to the associated increase in cloud reflectivity of incoming solar radiation (Twomey, 1977; Intrieri et al., 2002). For optically thin clouds ($< 40\,\mathrm{g\,m}^{-2}$), which are common at Summit Station (Summit; Shupe et al., 2013b; Miller et al., 2015), the smaller droplet size associated with increased CCN results in higher cloud emissivity, increasing the downwelling longwave radiative flux and having a relative warming effect at the surface (Lubin and Vogelmann, 2006; Garrett and Zhao, 2006). Understanding when and where each of these processes dominates is extremely important for understanding cloud radiative forcing and the surface energy budget (Schmale et al., 2021).

The concentration of ice-nucleating particles (INPs) is also an important control on the longevity and radiative impact of clouds. INPs are required to form primary ice in supercooled liquid clouds that are warmer than the homogeneous freezing temperature (approximately $-38\,^{\circ}\mathrm{C}$) (e.g. Kanji et al., 2017). Because the low-level clouds that have the largest radiative effect at the Arctic surface usually have temperatures between $-38\,^{\circ}\mathrm{C}$ and $0\,^{\circ}\mathrm{C}$ (Shupe and Intrieri, 2004; Shupe et al., 2013b; Miller et al., 2015), INP concentrations are an important control on the ice and liquid water contents of these clouds. Clouds containing ice crystals are optically thinner than those containing only supercooled water droplets and therefore emit less longwave radiation towards the surface, having a relative cooling effect (e.g. Prenni et al., 2007). Even more importantly, once ice crystals are present in a supercooled cloud, the lower saturation vapour pressure of ice versus liquid water results in the preferential growth of ice crystals at the expense of liquid droplets when the environment is subsaturated with respect to water but supersaturated with respect to ice. This is known as the Wegener–Bergeron–Findeisen (WBF) process, the result of which is a decrease in LWP as droplets evaporate and an increase in precipitation due to the growth of relatively large ice crystals, ultimately leading to cloud dissipation (e.g. Lohmann and Feichter, 2005). INP concentrations are typically orders of magnitude lower than CCN concentrations and are particularly low in the Arctic based on limited existing measurements ($\sim 10^{-7}$ to $10^{-5}\,\mathrm{cm}^{-3}$, Wex et al., 2019). The lack of INPs in the Arctic may contribute to the unusual persistence of low-level mixed-phase stratocumulus clouds (Morrison et al., 2012), which are highly important for radiative forcing at the surface, and played a role in the anomalous GrIS surface melt event in 2012 (Bennartz et al., 2013).

Both CCN and INP concentrations are also important for precipitation accumulation. In liquid clouds, the increase in cloud droplet number concentration and associated decrease in cloud droplet size under high CCN concentrations reduces the opportunities for droplet collision and coalescence and hence reduces precipitation relative to equivalent situations with lower droplet concentrations (e.g. Lohmann and Feichter, 2005). In mixed-phase clouds this process is more complex, since changes in the cloud droplet size distribution can have both positive and negative effects on the efficiency of ice production (Cheng et al., 2010; Lance et al., 2011; Possner et al., 2017). Cloud phase partitioning is also important since ice phase clouds have markedly different precipitation characteristics to those containing super-cooled liquid water (Pettersen et al., 2018; McIlhattan et al., 2020). Model simulations generally overestimate precipitation accumulation over the GrIS (McIlhattan et al., 2017; Kay et al., 2018; Lenaerts et al., 2020) and in particular the contribu-

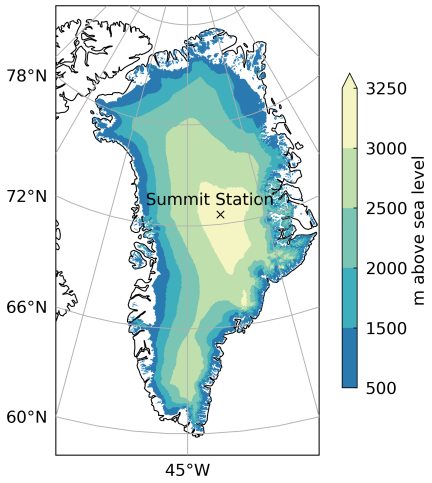

Figure 1. Location of Summit Station at the highest point on the Greenland Ice Sheet. Ice elevation contours are from the Greenland Ice Mapping Project (Howat et al., 2017).

tion from mixed-phase clouds. McIlhattan et al. (2017) find that the Community Earth System Model (CESM) overestimates snow frequency from mixed-phase clouds by 52 % and underestimates the occurrence frequency of liquid-bearing clouds by 21 % over the central GrIS. This is consistent with an overly active WBF process in the model – a process that is strongly controlled by INP concentrations.

To date, all observations of the CCN-limited regime (Mauritsen et al., 2011; Leaitch et al., 2016), and INP concentrations (Wex et al., 2019), in the Arctic are located at marine or coastal sites. However, the central GrIS is a distinct Arctic environment due to its high elevation (3250 m a.s.l. at its highest point, Fig. 1) and persistent ice cover (1.7×10^6 km^2) that results in a year-round high surface albedo. There are no substantial local sources of aerosol from the surface for over 400 km in any direction from the centre of the ice sheet. The year-round high surface albedo of the central GrIS (Box et al., 2012) results in unique seasonality in cloud radiative forcing. Most parts of the Arctic have less snow and ice cover in the summer and hence a lower albedo; during this time clouds can have a net cooling effect at the surface due their relatively high albedo (e.g. Shupe and Intrieri, 2004). In contrast, over the central GrIS the seasonal change in surface albedo is negligible and clouds have a net warming effect at the surface year-round (Miller et al., 2015; Van Tricht et al., 2016).

The high elevation and extreme radiative cooling from the centre of the GrIS drive low-level katabatic winds that radiate towards the ice sheet edge and, combined with synoptic and large-scale circulation patterns, support the formation of a persistent high-pressure system over Greenland (Heinemann and Klein, 2002; Hanna et al., 2016). For this reason, Greenland has been referred to as the "northern wind pole", where upper-level air currents driven by the Hadley circulation descend and return to lower latitudes (Hobbs, 1945; Heinemann and Klein, 2002). The descent of upper tropospheric air to the surface of the central GrIS results in a larger contribution of well-mixed free-tropospheric aerosol (Stohl, 2006). Hence, the transport processes and source regions controlling the concentrations of aerosol particles over the central GrIS are distinct from other Arctic sites (Hirdman et al., 2009; Backman et al., 2021).

The presumed insignificance of local aerosol sources at the surface of the GrIS suggests that both low CCN concentrations with the potential to limit cloud formation and low INP concentrations that can control cloud phase could certainly occur. The difference in aerosol transport pathways to the GrIS when compared to coastal or marine Arctic sites implies that the processes controlling aerosol-limited cloud regimes, and their frequency of occurrence, might differ substantially from other Arctic locations. Hence, a thorough analysis of the role of the aerosol-limited conditions over the GrIS is warranted, especially given the unique sensitivity of the GrIS to longwave cloud forcing.

Despite the potential for aerosol-limited clouds to affect the surface mass balance of the GrIS, and the large uncertainties in modelled cloud microphysical properties over Greenland (Hofer et al., 2019; Schmale et al., 2021), there are very few observations of aerosol particle number concentration over the central GrIS, and those that do exist are mostly limited to the summer season (Ziemba et al., 2010; Flyger et al., 1976; Hogan et al., 1984; Davidson et al., 1993; Bergin et al., 1994, 1995). This study presents the first full year of surface aerosol particle number concentration measurements from Summit Station, in the central GrIS, which can be used as a baseline for future modelling studies investigating the effect of cloud–aerosol interactions on the GrIS surface energy budget and mass balance. We assess local and synoptic controls on surface aerosol particle concentrations at Summit and present three case studies where extremely low total particle number concentrations (< 10 cm^{-3}) coincide with cloud dissipation, indicating that CCN-limited clouds occur over the central GrIS and could be an important contributor to the surface energy budget.

2 Measurements and methods

All observations in this study were made at Summit Station (Summit), a scientific research base funded by the US National Science Foundation. Summit is located at the highest point on the GrIS (3250 m a.s.l.), is over 400 km from the coast in the east and west directions, and is over 1000 km from the south-west and south-east coasts (Fig. 1). Aerosol, cloud, and atmospheric profile measurements were collected as part of the ICECAPS-ACE project: ICECAPS (Integrated Characterization of Energy, Clouds, Atmospheric State, and Precipitation at Summit) has been operating at Summit since 2010 and consists of a suite of ground-based remote sensing

Table 1. Measurements used in this study; references provide additional instrument information and methodologies for derived parameters.

Instrument	Measured/derived parameters (used in this study)	Data availability (used in this study)	Reference
Condensation particle counter (CPC)	Ambient condensation nuclei number concentration > 5 nm	Feb 2019–May 2020 (excluding 20 Jan)	Guy et al. (2020)
Alphasense optical particle counter (OPC-N3)	Aerosol particle size distribution 0.35 to 40 µm	Jun–Dec 2019	Crilley et al. (2018)
NOAA meteorological suite	10 m wind speed and direction, surface pressure	Feb 2019–May 2020	GMLMET (2021)
Vaisala HMP155 T/RH probe	2 m air temperature, 15 m air temperature	Jun–Oct 2019	Guy et al. (2020)
Precipitation occurrence sensor system (POSS), X-band (10.5 GHz)	Precipitation occurrence (POSS power unit)	Mar–Dec 2019	Sheppard and Joe (2008)
Millimeter cloud radar (MMCR) Ka band (35 GHz)	Radar reflectivity	Case studies only	Moran et al. (1998)
Radiosondes (00:00 and 12:00 UTC)	Vertical temperature and humidity profiles	Case studies only	Shupe et al. (2013b)
HATPRO and MWRHF microwave radiometers (23, 21, 90, and 150 GHz)	Liquid water path, precipitable water vapour	Case studies only	Turner et al. (2007) Shupe et al. (2013b)
Micropulse lidar (MPL)	Lidar depolarisation ratio	Case studies only	Flynna et al. (2007)

instrumentation and twice-daily radiosonde launches (Shupe et al., 2013b). The ACE (Aerosol Cloud Experiment) addition to ICECAPS began collecting data in February 2019 and includes measurements of surface aerosol particle number concentration and size distribution in addition to turbulent and radiative fluxes used to characterise the surface energy budget. This study uses a subset of ICECAPS-ACE data listed in Table 1, as well as meteorological measurements from the NOAA Global Monitoring Laboratory (GMLMET, 2021). The references in Table 1 provide additional information on the instruments and methodologies for the derived parameters. Section 2.1 provides the details of the aerosol particle number concentration sampling and quality control.

To investigate the effect of near-surface local processes that have the potential to modify surface aerosol particle concentrations, we look at four event types: fog, precipitation, blowing snow (BLSN), and strong surface-based temperature inversions (SBIs). For each type, we examine the change in aerosol particle concentrations across multiple events. To qualify, events of each type must last at least 60 min, and separate events of the same type must be at least 5 h apart. Sections 2.2 to 2.4 provide specific details about how each event type is defined.

To assess the synoptic controls on surface aerosol particle concentrations, we use ERA5 reanalysis data (Hersbach et al., 2020) made available by the European Centre for Medium-Range Weather Forecasts (ECMWF). ERA5 is the highest-resolution global reanalysis product to date, with $\sim$ 15 km horizontal resolution over Greenland, 137 pressure levels up to 80 km, and 1 h temporal resolution. We also use ERA5 reanalysis to drive the FLEXPART Lagrangian particle dispersion model (Pisso et al., 2019) to simulate aerosol transport pathways and surface emission sensitivities. Section 2.5 provides further details about the FLEXPART experimental design.

2.1 Surface aerosol particle number concentrations

A condensation particle counter (GRIMM CPC 5.400) measured the ambient number concentration of condensation nuclei at 1 Hz frequency. The omnidirectional conical inlet head was located $\sim$ 3 m above the surface (this varied slightly throughout the observation period with snow drifting and accumulation), and air was sampled with a flow rate of 0.3 L min^{-1}. The inlet was connected to the CPC via a 6 m length of conductive silicone tubing with an 8 mm inner diameter. Although the CPC is calibrated to measure condensation nuclei > 5 nm diameter, the addition of the long inlet results in a loss of particles inside the tubing. Figure 2 shows an estimation of the loss of aerosol particles inside the inlet generated by the Particle Loss Calculator (von der Weiden et al., 2009). Smaller particles are increasingly lost due to diffusion to the walls of the inlet, and larger particles are lost due to sedimentation and deposition. The Particle Loss Calculator does not account for the temperature gradient within the tubing; however, because the cold air in the inlet stream transitions into a warmer inlet (inside the heated building), this will act to reduce the loss of particles (von der Weiden et al., 2009). Also, because particle concentrations are small ($\ll 100\,000$ cm^{-3}), loss due to coagulation is negligible (von der Weiden et al., 2009). Based on these modelled inlet losses, the CPC measured condensation nuclei with diameters between 20 nm and 2.3 µm with over 50 % efficiency (Fig. 2). For this reason we henceforth refer to the CPC concentration measurements as N_{20}, indicating number concentrations of particles with diameter > 20 nm. Modelled inlet

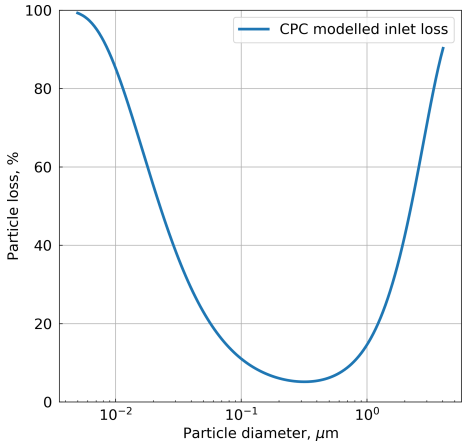

Figure 2. Modelled particle loss as a function of particle diameter in the CPC inlet, as estimated by the Particle Loss Calculator (von der Weiden et al., 2009).

losses are $< 15\,\%$ for particles with diameters between 0.08 and 1 µm, which is representative of the typical size range of CCN in clean Arctic environments (Hudson and Da, 1996; Leaitch et al., 2016).

Ziemba et al. (2010) made measurements of surface aerosol particle size distribution between 5.5 and 195 nm at Summit in May and June 2007. Their observations suggest that high concentrations of nucleation-mode particles (< 30 nm diameter) occur periodically during the summer at Summit. The reduced collection efficiency of our CPC between 20 and 40 nm would have resulted in an undercount of the total N_{20} by up to 27 % during the 2007 measurement period reported by Ziemba et al. (2010) but only 8 % in the accumulation mode (100 to 200 nm). The concentration of ultra-fine particles (< 100 nm diameter) at Summit likely varies seasonally as well as on shorter timescales. In the absence of year-round measurements of particle size distribution at Summit, it is not possible to fully quantify the uncertainties in N_{20} reported here.

To filter out data that may have been impacted by local station pollution, we omitted measurements collected when wind speeds are $< 1\,\mathrm{m\,s^{-1}}$ and when the wind direction is such that contaminated air from station operations may have advected across the inlet (between 270 and 360° from true north). A comparison between two OPC-N3 optical particle counters (described further in Sect. 2.2), located at the opposite sides of camp, confirmed that these criteria are sufficient to account for the impact of local station pollution (not shown). The removal of data associated with particular surface wind conditions may bias the dataset; however, during the measurement period considered in this study wind speeds $< 1\,\mathrm{m\,s^{-1}}$ only occur 3.4 % of the time and polluting wind directions only occur 9.1 % of the time.

2.2 Detection of fog

Supercooled liquid fog is common at Summit and occurs in all seasons, with a minimum occurrence in April and maximum in September (Cox et al., 2019). Fog droplets form on CCN and grow by condensation to typical diameters of 15 to 25 µm (Cox et al., 2019). Particles larger than ~ 3 µm cannot pass through the CPC inlet (Fig. 2); hence, during fog events, the CPC measures the interstitial aerosol particle concentration. In this way, fog can result in extremely low surface aerosol particle concentration measurements that are not representative of the aerosol population outside of the fog (Bergin et al., 1995). In the absence of an instrument designed specifically to detect fog at Summit, we use data from an Alphasense optical particle counter (OPC-N3, Crilley et al., 2018) located next to the CPC inlet to identify fog periods.

The OPC-N3 resolves particle size distribution in 24 bins between 0.35 and 40 µm diameter. Natural aerosol particles with diameters greater than 10 µm are highly unlikely to be present in central Greenland due to the large distance from the source of any coarse-mode aerosol particles and the large dry deposition velocity of such particles (Giorgi, 1986; Jaenicke, 1990). Under this assumption, particles detected by the OPC-N3 with diameters over 10 µm must be fog droplets or ice crystals. Real-time data monitoring at Summit and comparison with visual observations for 6 months confirm that the OPC-N3 detects particles within this size range during both fog and blowing snow. At Summit, 80 % of cases of drifting or blowing snow reported by on-site observers in 2019 occurred when the 3 h mean 10 m wind speed was $> 6\,\mathrm{m\,s^{-1}}$; we remove all cases with wind speeds above this threshold to separate fog events from possible blowing snow events. We classify fog events as when the total concentration of particles with diameters > 10 µm is greater than $0.1\,\mathrm{cm^{-3}}$. Figure 3 provides an example of the detection of fog using this methodology and the associated reduction in N_{20} measured by the CPC.

Comparing this OPC-N3 fog classification to manual on-site observations reported at 00:00, 12:00, and 18:00 UTC daily, the OPC-N3 does not detect fog when fog is reported by the observer (false negatives) in 35 out of 152 cases (23 %). Six of these cases can be attributed to inconsistent observer log entries or to logged issues with the OPC-N3; some others may result from discrepancies between the actual and reported observation time. However, false positive detection is rare, occurring in only 6 cases (1 %). Therefore, although some fog events might be missed by the OPC-N3 fog classification, it is an accurate indicator of fog presence. The OPC-N3 was in operation between June and December 2019, and during this time the data are 96 % complete.

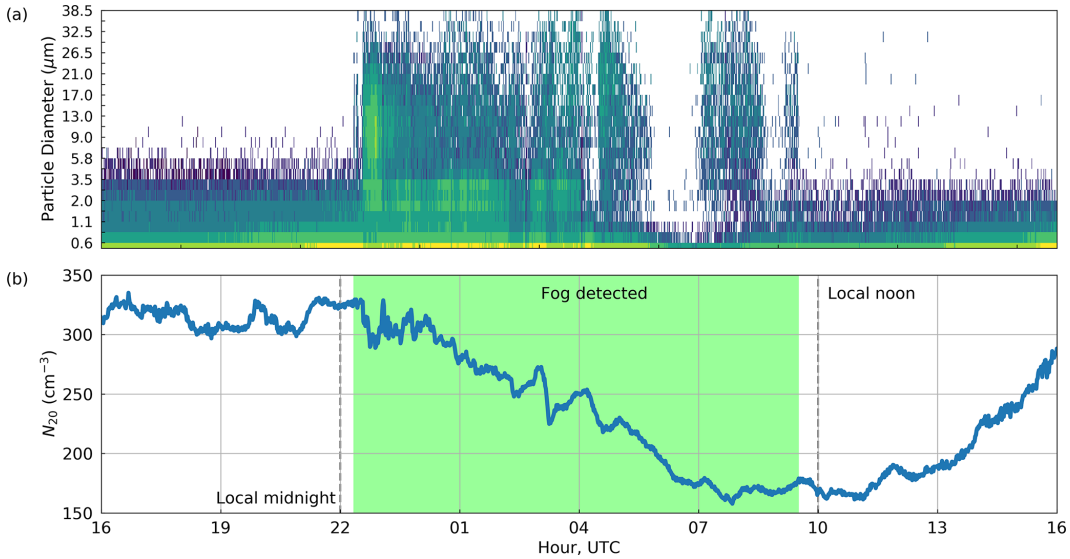

Figure 3. (a) Particle size distribution from the OPC-N3 from 31 July 2019 16:00 UTC to 1 August 2019 16:00 UTC (1 min averages). **(b)** N_{20} particle number concentration from the CPC during the same period (1 min averages). The duration of the fog event identified by the methodology described in Sect. 2.2 is shaded in green.

2.3 Detection of precipitation and blowing snow

Below-cloud wet scavenging during snowfall can also reduce surface aerosol particle concentrations (e.g. Martin et al., 1980; Paramonov et al., 2011). A precipitation occurrence sensor system (POSS) (Sheppard and Joe, 2008) located about 2 m a.g.l. at Summit measures the Doppler velocity spectrum of hydrometeors within a 1 m^3 sampling volume. Surface snowfall rate retrieved from the POSS agrees well with retrievals from the lowest reliable range gate of the millimeter cloud radar (MMCR) at Summit, with a root mean squared error of 0.08 mm h^{-1} (Castellani et al., 2015). The POSS power unit (the zeroth moment of the Doppler spectrum) can be used as a binary indicator of precipitation, and in this study we use a threshold of two POSS power units to identify precipitation events and exclude blowing snow, as per Pettersen et al. (2018). POSS data are 95 % complete between June and December 2019.

The wind speed threshold for blowing snow (BLSN) varies depending on temperature and the properties of surface snow (Schmidt, 1982; Mann et al., 2000). In Sect. 2.2 we used a 6 m s^{-1} threshold as a minimum to avoid cases of possible blowing snow. However, to positively identify BLSN events we use a 10 m wind speed threshold of ≥ 9 m s^{-1}. During 2019, on-site observers reported blowing or drifting snow 99 % of the time when the 3 h mean wind speed was above this threshold.

2.4 Detection of surface-based temperature inversions

Surface-based temperature inversions (SBIs) occur at Summit in all seasons due to strong and persistent radiative cooling of the surface. SBIs are most common in the winter (Oct–Mar) where they occur over 70 % of the time with a typical magnitude of ~ 5 °C between 10 and 2 m a.s.l. (Miller et al., 2013). In the summer (JJA), the amplitude of SBIs is weaker, and they only occur ~ 30 % of the time (Miller et al., 2013). SBIs limit the turbulent mixing of air (and aerosols) down to the surface, and as a result, aerosol particle concentrations measured at the surface may not be representative of concentrations at cloud level (Igel et al., 2017). To explore the effect of SBIs on surface aerosol particle concentrations in this study we classify SBI events where the 15 m minus the 2 m (above ground level) temperature difference is greater than 3 °C (> 0.23 °C m^{-1}). Detection of SBI events is limited to June through October 2019 due to outages in the 15 m temperature sensor, but during this time data were 97 % complete.

2.5 Aerosol source regions and transport pathways

The FLEXPART Lagrangian particle dispersion model (Pisso et al., 2019) is used to simulate aerosol transport pathways and surface emission sensitivities throughout 2019. FLEXPART simulations were run every 6 h and driven by reanalysis data from ERA5, at the same horizontal and vertical resolution as the input data. In each simulation, 40 000 particles were released at 100 m a.s.l. at Summit, and FLEXPART traced each particle back in time for 20 d. Particles follow the mean 3D wind field from ERA5 combined with a stochastic 3D turbulence field and parameterised convection (Forster et al., 2007). FLEXPART also simulates wet and dry deposition as linear decay constants based on a user input particle mean diameter, density, water, and ice nucle-

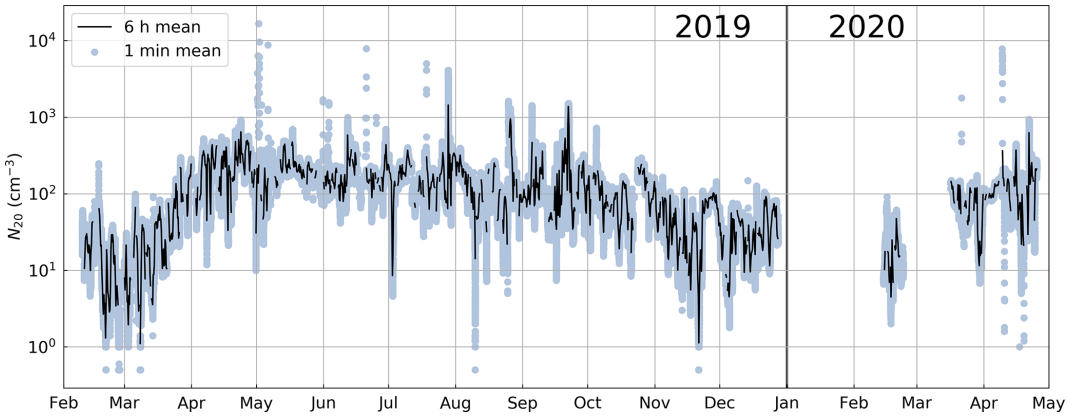

Figure 4. Surface N_{20} from the CPC at Summit from February 2019 until May 2020.

ation efficiency. In both cases deposition acts to reduce the total mass of each particle, and a particle's back trajectory stops when its mass reaches zero. Due to limited prior information about aerosols at Summit, we used the default aerosol tracer species, which assumes a particle mean diameter of 0.25 µm, density of 1400 kg m^{-3}, and water and ice nucleation efficiencies of 0.9 and 0.1, respectively. Particles of 0.25 µm diameter are efficiently measured by the CPC at Summit (Fig. 2), fall within the typical size range of Arctic CCN (e.g. Jung et al., 2018), and have the relatively long atmosphere lifetimes necessary for advection over the GrIS (> 10 d in the middle-upper troposphere; Jaenicke, 1990). FLEXPART outputs gridded emission sensitivity and supplementary back trajectory data that include the mean (centroid) back trajectory of all particles for each simulation, as well as the percentage of particles within the planetary boundary layer (PBL) at each time step. The surface emission sensitivity is proportional to the total amount of time that all particle back trajectories have spent near the surface (0–2000 m) during the simulation period, representing the probability that aerosol particles emitted from each grid cell would have been detected at Summit at the simulation start time. We plot surface emission sensitivity as a percentage of the maximum value to facilitate comparisons between figures.

3 Results

3.1 Surface aerosol particle number concentrations at Summit, 2019–2020

The mean surface N_{20} in 2019 was 129 cm^{-3}, with the 6 h mean ranging between 1 and 1441 cm^{-3} (Fig. 4). The minimum N_{20} in 2019 at Summit occurs in late February and early March, followed by a sharp increase of 2 orders of magnitude throughout March and April (Fig. 4). Between May and October, concentrations are fairly consistent and on the order of 100 cm^{-3} before decreasing again between October and December. Although data in early 2020 are limited, a similar increase in concentrations between February and May is apparent (Fig. 4).

3.2 The effect of local surface processes on aerosol particle concentrations

The OPC-N3 identified 48 distinct fog events whilst it was operational between June and December 2019. The longest cumulative fog duration was in August (Fig. 5a) when fog was present for ∼ 23 % of the month, consistent with previous multi-year observations of supercooled liquid fogs at Summit (Cox et al., 2019). The mean duration of fog events was 3.3 h, and the longest event lasted 9.8 h.

SBI events were also present in all months and increased in total duration from summer to winter (Fig. 5b), again consistent with previous observations (Miller et al., 2013). The average duration of SBI events was 8.4 h, and the longest individual event lasted 5.8 d. SBI and fog events are not independent since fog condensate often forms due to surface cooling associated with the establishment of SBIs (e.g. Cox et al., 2019). Just under half of all detected SBI events also contained fog (Fig. 5b), although because fog events are typically shorter, this only accounted for 17 % of the total SBI duration.

Precipitation frequency and duration was highest in the summer and lowest in November and December (Fig. 5c). The average duration of precipitation events was 2.9 h, and the longest event lasted 14.1 h. In contrast, BLSN events occurred most frequently in November and December, with an average duration of 6.9 h (Fig. 5d). The seasonal distribution and duration of precipitation and BLSN events are also consistent with previous multi-year observations (Castellani et al., 2015; Pettersen et al., 2018; Bennartz et al., 2019; Cox et al., 2019). Fog was detected during 23 of the 54 precipitation events (Fig. 5c). Because the OPC-N3 does not distinguish between fog and BLSN, it is not possible to determine how often fog might have been present during BLSN events. However, because of the high concentrations of ice crystals

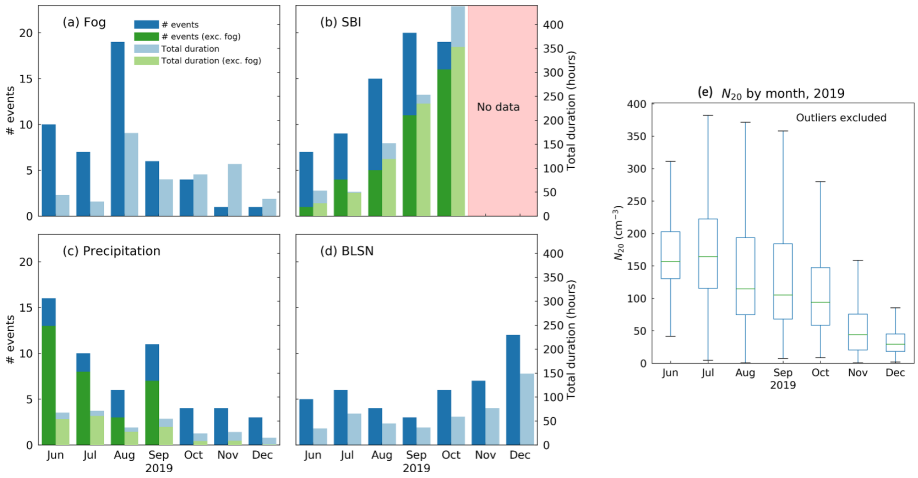

Figure 5. Frequency and duration of **(a)** fog events, **(b)** surface-based temperature inversion events, **(c)** precipitation events, and **(d)** blowing snow events, detected between June and December 2019 using the methodology described in Sects. 2.2–2.4. Blue bars include all events, and green bars show the change in distribution for SBI and precipitation events after the removal of events containing fog. **(e)** The distribution of N_{20} for the same months, excluding outliers.

during blowing snow events, any supercooled water droplets are likely to be removed either through riming or through the WBF process.

Figure 6 shows the median change in N_{20} during the first 3 h of each event type. Only during fog events is there a consistent change: after 3 h, the majority of fog events show a reduction in N_{20} by up to 35 % (Fig. 6a). For SBI events, there is very little discernible change in N_{20} during the first 2 h (Fig. 6b). After $\sim$ 140 min there is a small median reduction in N_{20} that is not present when events that contain fog are omitted. During both precipitation and BLSN events, the median change in N_{20} remains close to zero (Fig. 6c and d).

3.3 Synoptic controls on surface aerosol particle concentrations

Here we explore the general relationship between N_{20} and synoptic conditions during 2019. Because both N_{20} and variables that change on synoptic timescales (i.e. surface pressure, geopotential height) vary seasonally, this seasonal dependence is removed prior to analysis. To calculate N_{20} anomalies we subtract the monthly median value for 2019. For all other variables (from GML-MET, 2020, and ERA5) anomalies are calculated by subtracting the 10-year (2009–2019) monthly mean climatology. Generally throughout 2019 anomalous changes in the 3 d mean surface pressure are in phase with anomalous 3 d median N_{20}, with some exceptions (Fig. 7a). To look at typical synoptic conditions associated with anomalous N_{20} at Summit, we look at high- and low-N_{20} events, where the 3 d median N_{20} anomaly is greater than the 75th percentile or less than the 25th percentile, respectively. To avoid oversampling, any events separated by less than 4 d are combined into a single event. The resulting high- and low-N_{20} events are highlighted in Fig. 7a and are spread evenly throughout the annual cycle (15 high events and 14 low events).

On average, an increase in surface pressure anomaly precedes anomalously high-N_{20} events, with the maximum N_{20} coinciding with surface pressure anomalies levelling off (Fig. 7b). In contrast, a decrease in surface pressure anomaly precedes the majority of low-N_{20} events, with the minimum N_{20} coinciding with the minimum surface pressure anomaly on average (Fig. 7b). Averaged over all high-N_{20} events, 500 hPa geopotential heights are anomalously high (by over 75 m in central Greenland), and there is an anomalous anticyclonic circulation over the GrIS (Fig. 8a). In contrast, when averaged over the low-N_{20} events, there is a region of anomalously low geopotential heights and anomalous cyclonic circulation centred on south-east Greenland (Fig. 8b).

FLEXPART simulations of surface emission sensitivity during the high-N_{20} events show that sensitivity to surface emissions in the 20 d prior to detection at Summit outside of the ice sheet itself is rare (Fig. 9a), although there is some sensitivity to emissions from North America and Europe. Because there are no significant aerosol sources over the ice sheet itself, this implies that most of the simulated particles arriving at Summit during these events have been high in the atmosphere ($>$ 2000 m a.g.l.) for over 20 d prior to detection at Summit. This is supported by the low percentages of simulated particles in the planetary boundary layer and relatively high mean altitude of all simulated particles during the high-N_{20} events (Fig. 9a). In contrast, the surface emission sensitivity during the low-N_{20} events covers a broader area, encompassing coastal Greenland, Iceland, the Canadian Arctic, and the intervening north Atlantic Ocean (Fig. 9b). There is a much higher percentage of simulated particles in the boundary layer in the week preceding detection at Summit during

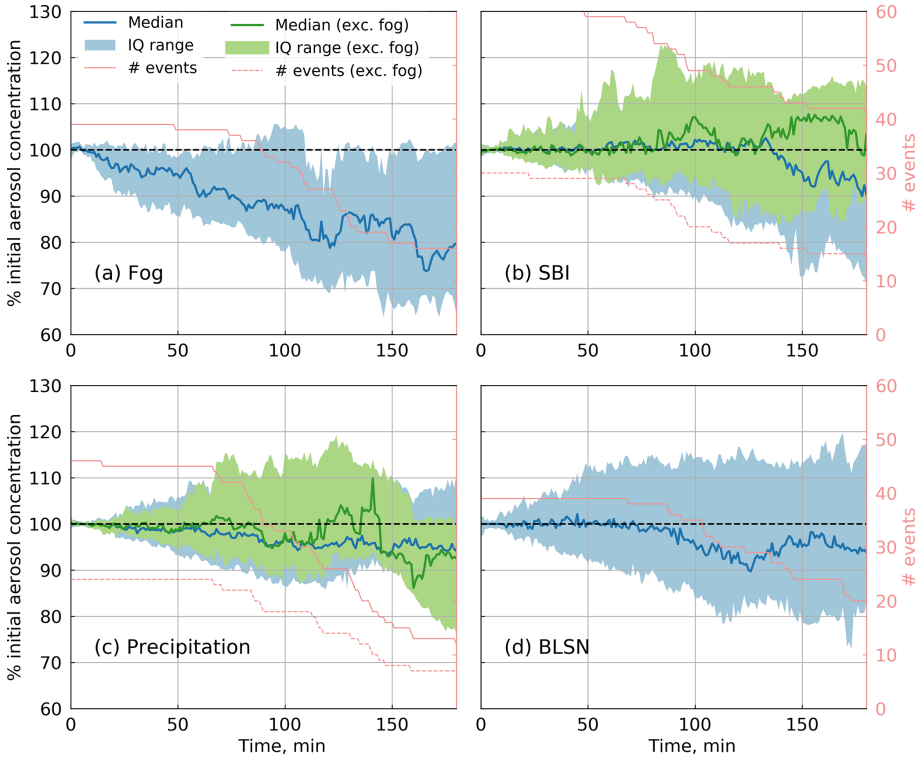

Figure 6. The change in surface aerosol particle concentration (%) over time during the first 3 h of each event for **(a)** fog, **(b)** surface-based temperature inversions, **(c)** precipitation, and **(d)** blowing snow events. The thick blue line and blue shading are the median and interquartile range of all events; the thick green line and green shading are the median and interquartile range for SBI and precipitation events that do not contain fog. The pink line indicates the total number of events at each time step for all events (solid) and excluding fog events (dashed).

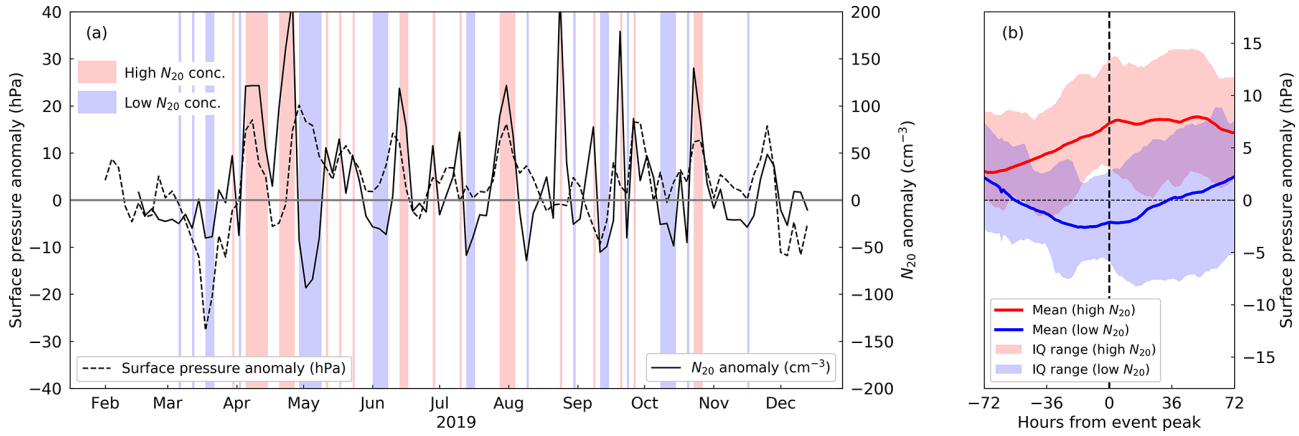

Figure 7. (a) Surface pressure anomaly (3 d mean, solid black line) and N_{20} anomaly (3 d median, dashed) during 2019. Red and blue shading highlight high- and low-aerosol-concentration events, respectively (high/low events are where the N_{20} anomaly is above the 75th/below the 25th percentile). **(b)** The mean and interquartile range in surface pressure anomaly across all high (red) and low (blue) N_{20} events, for the 72 h before and after the maximum (minimum) N_{20} for each high (low) event.

the low-N_{20} events than during the high-N_{20} events, and during the low-N_{20} events the simulated particles are transported up to the highest point of the ice sheet from lower elevations (Fig. 9b).

3.4 Case studies of potential aerosol-limited cloud regimes at Summit

Figure 4 demonstrates that N_{20} falls below 10 cm^{-3} in all seasons at Summit, suggesting that surface CCN concentra-

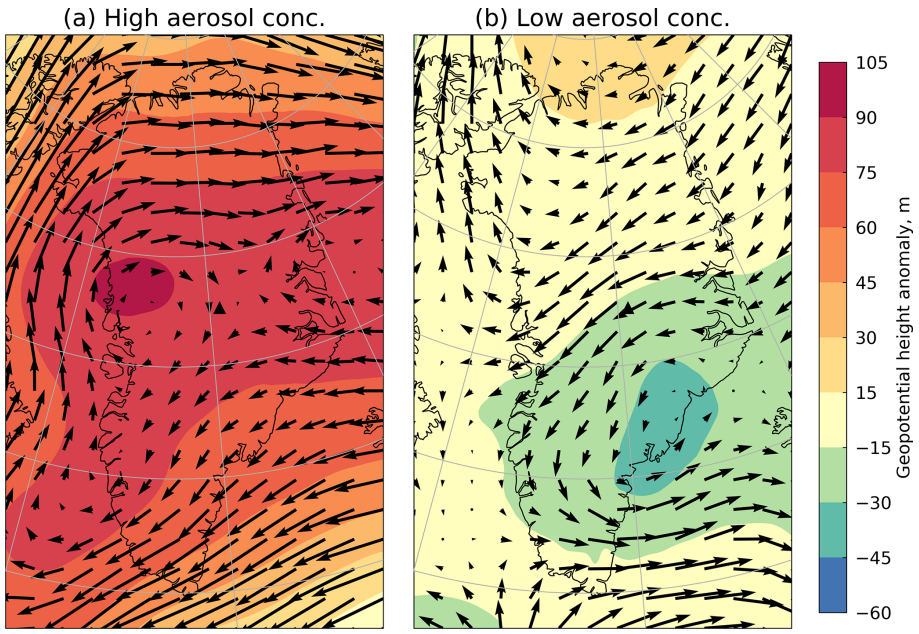

Figure 8. ERA5 mean 500 hPa geopotential height anomaly (shaded) and 500 hPa horizontal wind anomalies (barbed) for all high-N_{20} events **(a)** and low-N_{20} events **(b)**.

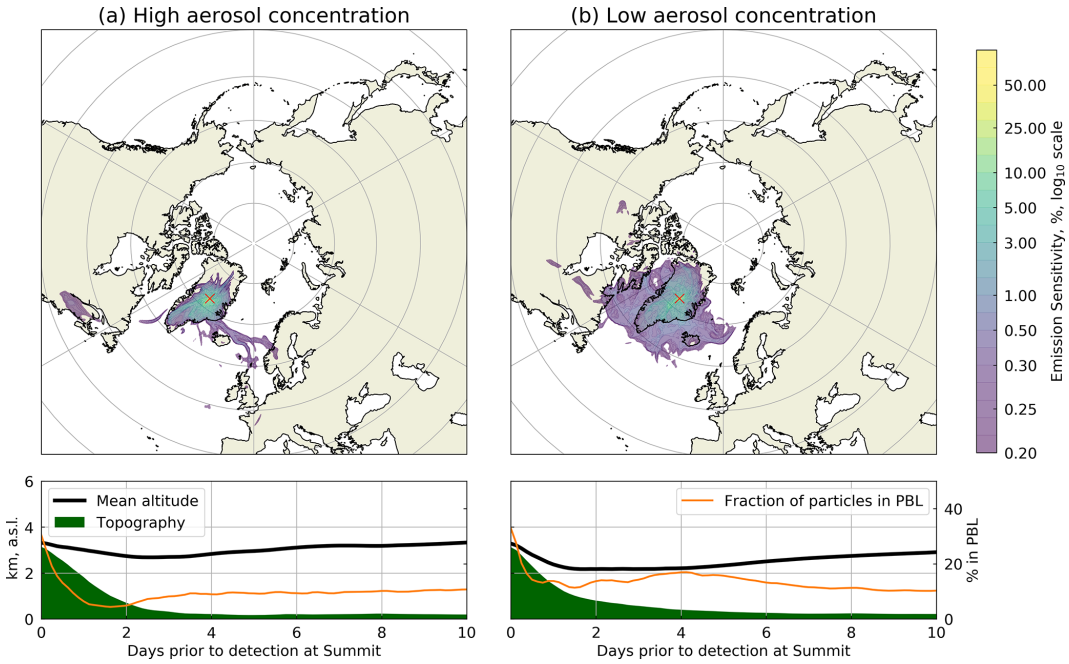

Figure 9. Results from FLEXPART back trajectory simulations averaged over the high-N_{20} events **(a)** and the low-N_{20} events **(b)**. Upper: surface emission sensitivity aggregated over 20 d prior to detection at Summit (as a percentage of the maximum value). Lower: mean altitude and fraction of particles within the planetary boundary layer (PBL) for all simulated particles over the 10 d prior to detection.

tions fall below this threshold even more frequently. Given the existing evidence that aerosol particle concentrations this low can limit cloud formation elsewhere in the Arctic (Mauritsen et al., 2011; Stevens et al., 2018), we hypothesise that fog formation can be limited by low CCN concentrations over central Greenland and, if there are occasions where the surface aerosol particle concentration is representative of concentration at cloud height, that cloud formation can be limited by low CCN concentrations too. In this section we look in detail at three events where extremely low aerosol

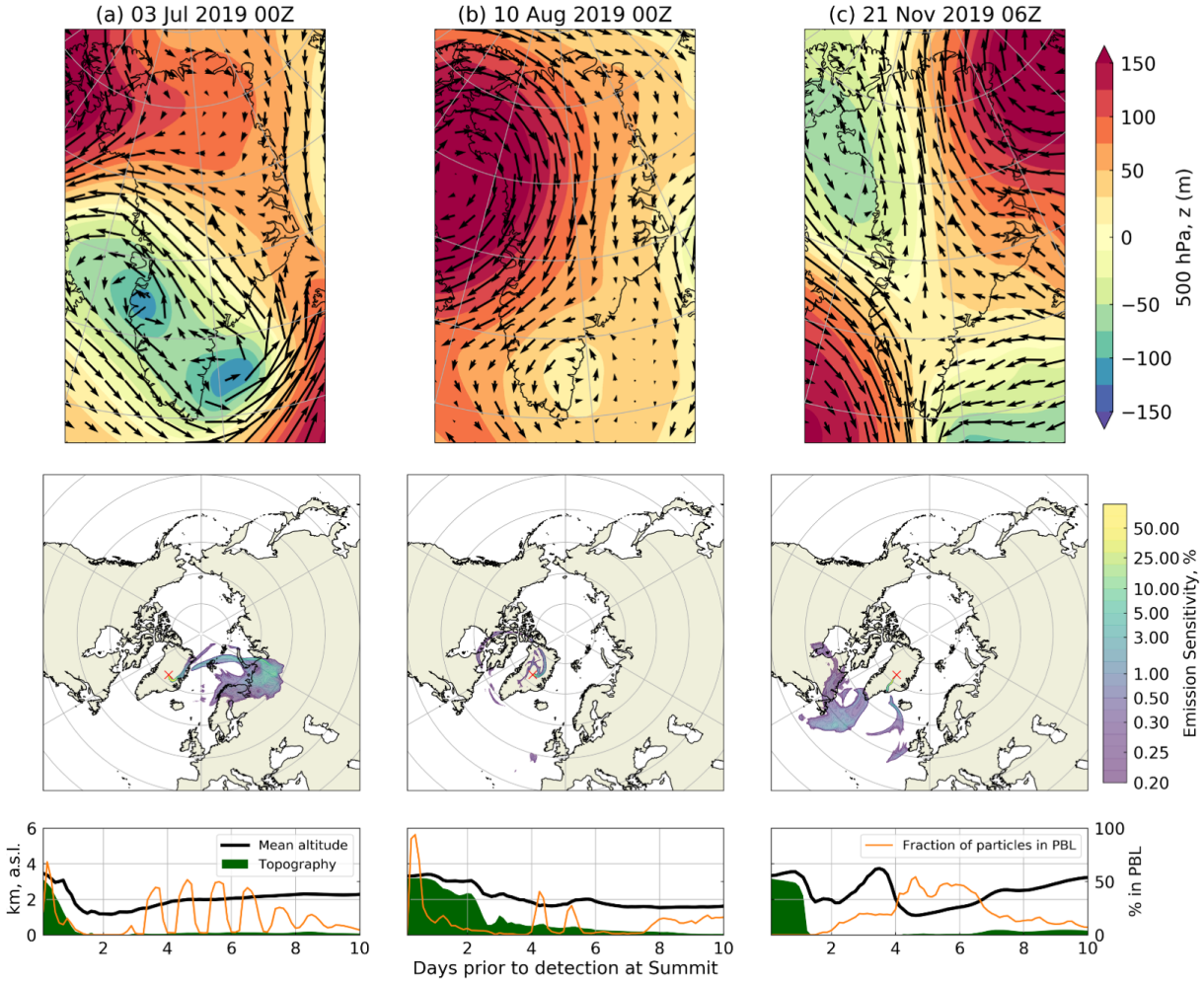

Figure 10. Synoptic anomaly plots and aerosol transport pathways during the three low-N_{20} cases studies. Upper row: 500 hPa geopotential height and horizontal wind anomalies from ERA5. Middle row: FLEXPART surface emission sensitivity (as a percentage of the maximum value) over the 10 d prior to aerosol detection at Summit. Lower row: FLEXPART mean aerosol transport height (back bold line) and percentage of particles within the planetary boundary layer (orange line) over the 10 d prior to detection at Summit. The shaded green area represents the mean height of topography beneath all particles.

particle concentrations ($N_{20} < 10\,\mathrm{cm}^{-3}$ for > 3 h) coincided with cloud dissipation in the absence of fog to look for further evidence of CCN-limited cloud regimes at Summit. All times throughout the discussion of these case studies are given in UTC.

For each of the three cases considered (3 July 2019, 10 August 2019, and 21 November 2019), air is advected to the top of the ice sheet from different directions: on 3 July 2019, the primary aerosol source region is northern Siberia (Fig. 10a); on 10 August 2019, air approaches Summit from the north via the Canadian Arctic Archipelago (Fig. 10b); and on 21 November 2019, air approaches Summit from the south-east and is sensitive to emissions from northern Quebec (Fig. 10c). Two of the three case studies (3 July 2019 and 21 November 2019) occur in the presence of anomalously low 500 hPa geopotential heights over south-east Greenland, with a stronger-than-usual south-easterly wind component drawing air up the ice sheet from the south-east coast (Fig. 10a and c). On both of these occasions > 50 % of particles are within the PBL 4–6 d prior to arrival at Summit. On the 10 August 2019 case, there is an anomalous region of high 500 hPa geopotential heights over north-west Greenland and a stronger-than-usual northerly wind component over Summit (Fig. 10b). Although the FLEXPART-simulated particles remain closer to the ground for a longer period of time, the percentage of particles within the PBL in the 10 d prior to detection at Summit is much lower on 10 August 2019 than in the other two cases (Fig. 10b). On all three occasions, air is advected up to the ice sheet to Summit from lower elevations and spends > 1 d prior to detection at Summit within the lowest 800 m a.g.l. over the GrIS. The local conditions associated with each case are outlined below.

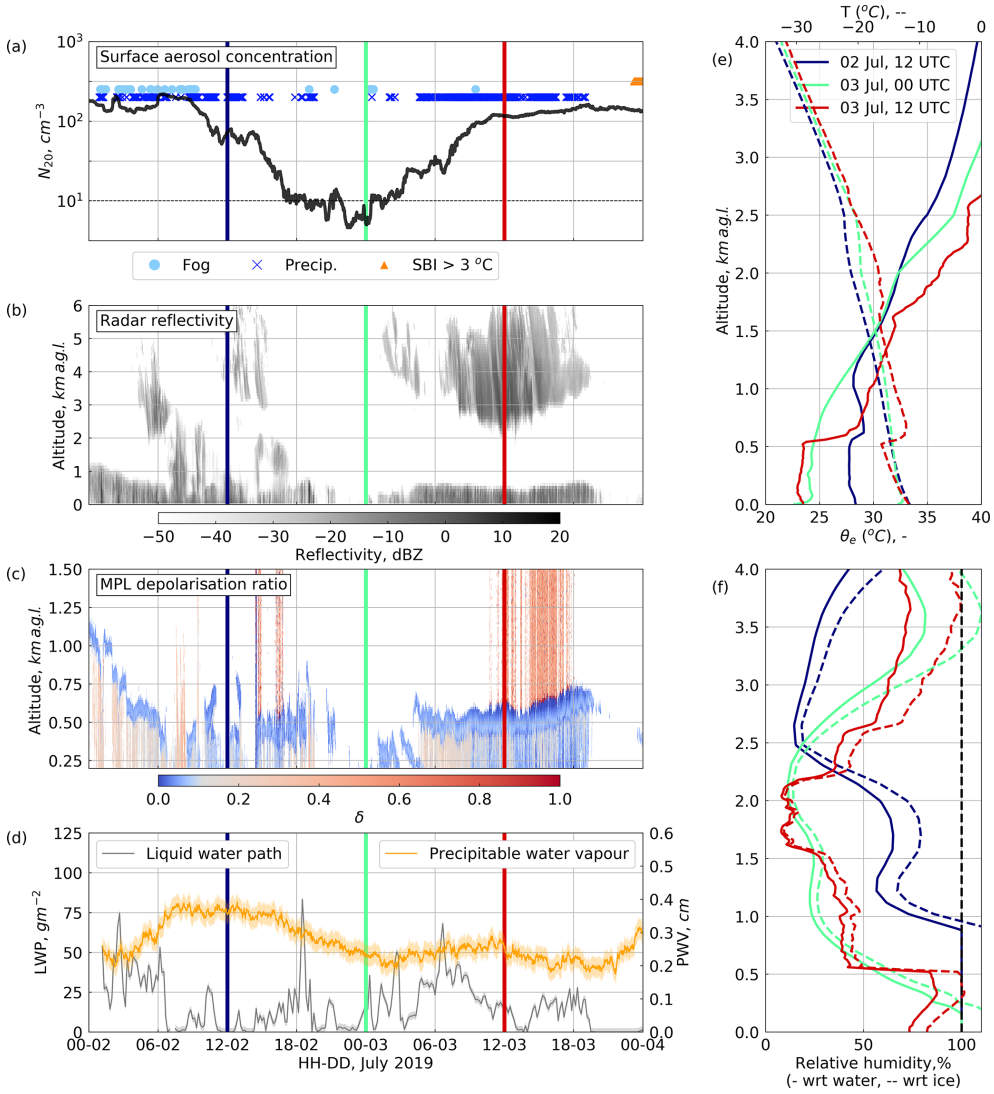

Figure 11. Conditions during the 3 July 2019 low-aerosol case study. **(a)** Surface N_{20} (CPC), with occurrences of fog (OPC-N3), precipitation (POSS), and SBI > 3 °C events indicated. **(b)** Radar reflectivity (MMCR). **(c)** Lidar depolarisation ratio (MPL); blue colours represent liquid droplets and reds are ice crystals. **(d)** Column integrated liquid water path and precipitable water vapour (MWR). **(e)** Temperature (dashed) and equivalent potential temperature (solid) radiosonde profiles. **(f)** Relative humidity with respect to water (solid) and ice (dashed) from radiosonde profiles. The coloured vertical lines on the left-hand plots correspond to the time of each vertical radiosonde profile in the right-hand plots.

3.4.1 3 July 2019

On 2 July 2019, N_{20} dropped rapidly from ∼200 to $< 10\,cm^{-3}$ over a period of ∼9 h (Fig. 11a). The 12:00 equivalent potential temperature profile on 2 July 2019 shows that the lowest layer of broken stratocumulus cloud existed within a well-mixed boundary layer (Fig. 11e). Shortly after 18:00, N_{20} dropped below $10\,cm^{-3}$, and there was a reduction in cloud cover (Fig. 11a–c). The on-site observer log recorded a transition from broken altocumulus at 18:00 to few clouds and unlimited visibility at 00:00 on 3 July 2019, despite the fact that the lowest 200 m a.s.l. remained saturated with respect to water (Fig. 11f). On this occasion, the 00:00 radiosonde was launched from the surface at 23:15, and typically the weather observation is recorded at the time of launch. Photographs from a webcam viewing the aerosol inlet (taken every 15 min and orientated towards the eastern horizon) confirm that skies were clear and visibility was good at 23:15, but by 23:30 there was a clearly visible fog bow, indicating liquid fog droplets (Fig. 12). Notably on this occasion, N_{20} fell to $< 10\,cm^{-3}$ in the absence of fog. At 00:15 visibility was obscured and the OPC-N3 detected fog at the surface (Fig. 12). The fact that the OPC-N3 did not detect fog droplets until 00:15, despite an increase in LWP at 23:30

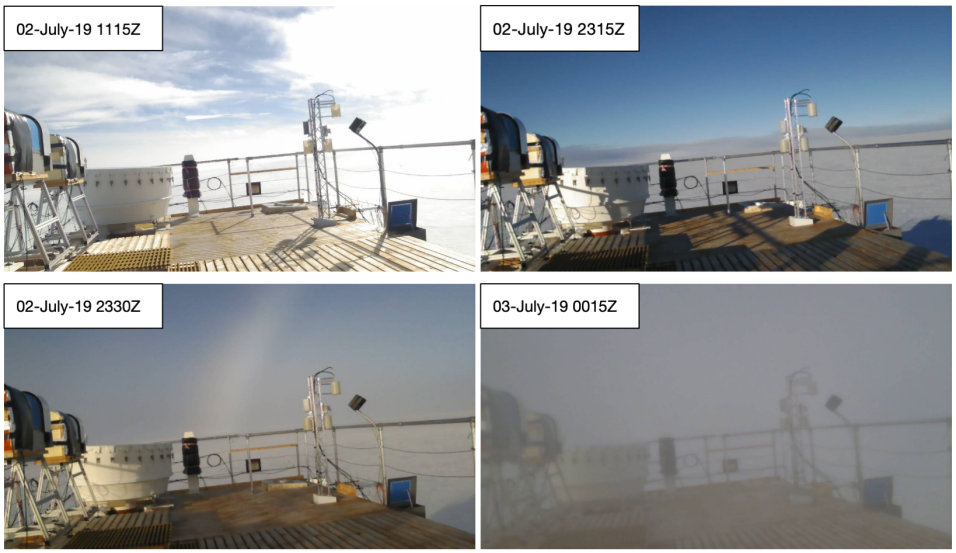

Figure 12. Photographs from a webcam oriented towards the eastern horizon on 2 and 3 July 2019. The aerosol inlet is visibly mounted on the mast in the SE corner.

(Fig. 11d), could be explained by the fact that either (a) the droplets forming the fog bow at 23:30 were too large to be detected by the OPC-N3 ($> 40\,\mu m$ diameter) or (b) the fog was in the process of descending to the surface. In either case, both (a) and (b) support the hypothesis of Mauritsen et al. (2011) – that in the absence of sufficient CCN, any existing CCN activate and grow to relatively large sizes, falling to the surface as drizzle.

The rapid transition from clear skies (despite a saturated surface layer) at 23:15 to fog at 00:15 coincided with N_{20} beginning to increase again (Fig. 11a). As N_{20} continued to increase, a thin low-level mixed-phase cloud returned and gradually lifted and thickened. By 12:00 on 3 July 2019, N_{20} had returned to $\sim 200\,cm^{-3}$, and the lowest cloud layer had developed into a typical Arctic mixed-phase cloud (Shupe et al., 2006; Morrison et al., 2012; Shupe et al., 2013b) with a cloud top close to 500 m (Fig. 11c), capping a well-mixed boundary layer (Fig. 11e).

3.4.2 10 August 2019

At 12:00 on 9 August 2019 there was a 2.5 km deep cloud over Summit (Fig. 13b) and surface N_{20} was $\sim 100\,cm^{-3}$ (Fig. 13a). Between 14:00 and 18:00, there was a sharp decrease in liquid water path (Fig. 13d) as the cloud thinned until there was nothing detected by the radar at 19:00 (Fig. 13b). At this time, the surface-based temperature inversion strengthened to $> 0.23\,°C\,m^{-1}$ (Fig. 13a), likely due to the increase in longwave cooling at the surface after the reduction in cloud cover. In this case, it was only after the strengthening of the surface temperature inversion that N_{20} began to decrease. At 21:40 the OPC-N3 detected fog, and N_{20} decreased more rapidly, falling below $10\,cm^{-3}$ at 23:35 and reaching a minimum of $0.5\,cm^{-3}$ at 01:00 on 10 August 2019, after which the fog thinned and cleared (Fig. 13a). N_{20} began to rise again from 02:15, and when the particle concentration increased above $10\,cm^{-3}$ at 04:00, there was a sudden sharp increase in liquid water path (Fig. 13d), and a thin low mixed-phase cloud developed (Fig. 13c). The cloud thickened as N_{20} continued to increase back to $\sim 100\,cm^{-3}$ at 07:00. Fig. 14 shows the transition from cloudy to clear skies, then to thin fog, and back to overcast again throughout this event.

3.4.3 21 November 2019

Surface N_{20} decreased from $50\,cm^{-3}$ at 06:00 on 20 November 2019 to a minimum of $0.5\,cm^{-3}$ at 06:30 on 21 November 2019 and remained below $10\,cm^{-3}$ for a total of 24 h (Fig. 15a). As N_{20} decreased, a low-level mixed-phase cloud thinned, and liquid water path fell to $0\,g\,m^{-2}$ by 09:00 (Fig. 15c and d). The 20 November 12:00 radiosonde shows that the boundary layer was neutrally stratified up to about 300 m, above a very shallow stable surface layer (where the air temperature increased 7 °C in the 4 m immediately above the surface) (Fig. 15e). At 00:00 on 21 November 2019 the temperature inversion in the lowest 4 m of the atmosphere strengthened to 12 °C, the sky above Summit was clear, and N_{20} continued to fall until 06:00. At 12:00 on 21 November 2019 a 3 km deep ice cloud moved across Summit (Fig. 15b and c), and N_{20} began to increase again (Fig. 15a). Liquid water path initially remained close to zero

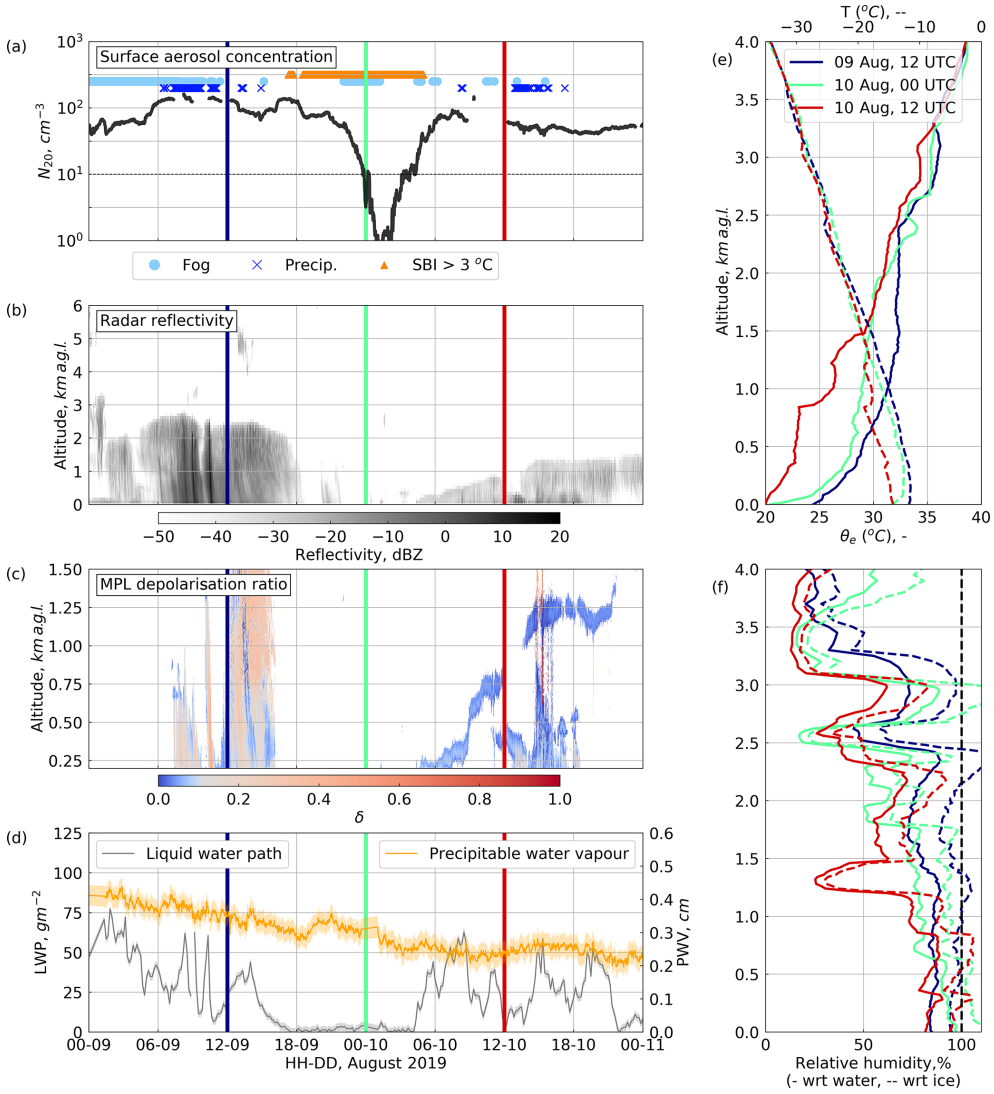

Figure 13. Same as Fig. 11 but during the 10 August 2019 low-aerosol case study.

but increased sharply when N_{20} rose above 10 cm^{-3} at 00:00 on 22 November 2019. Between the 20 November 2019 12:00 and the 22 November 2019 00:00 radiosonde profile, the 3 km a.g.l. potential temperature decreased by > 5 °C (Fig. 15e), possibly indicating an air mass transition during this period.

4 Discussion

4.1 The seasonal cycle of surface aerosol particle concentrations at Summit

Despite differences in the measured size ranges, the N_{20} values reported in the present study are of the same order of magnitude as previous summertime measurements of condensation nuclei at Summit (100–500 cm^{-3} in the first week of July 1992, Bergin et al., 1994) and from DYE III on the south-east GrIS (∼ 6–1000 cm^{-3} in July and August 1982, Hogan et al., 1984). These results are also comparable in magnitude to N_{10} concentrations measured at other Arctic stations (∼ 1–2000 cm^{-3} at Utqiaġvik, Alaska, and ∼ 5–3000 cm^{-3} at Pallas, Finland; Asmi et al., 2013); however, the seasonal cycle is notably different. The seasonal cycle in surface aerosol particle concentration at many sea level Arctic sites is dominated by the cycle of Arctic haze (e.g. Shaw, 1995); where anthropogenic pollutants build up in the winter, resulting in maximum aerosol particle concentrations in early spring, followed by a sharp reduction of particles in the summer. In contrast, at Summit we see minimum surface aerosol particle concentrations in the winter and higher concentrations in the late spring and summer. The seasonal cycle at Summit in 2019 is consistent with multi-year seasonal cycles of mineral particles in snow pit samples at Summit (Drab et al., 2002), as well as with measurements of bulk

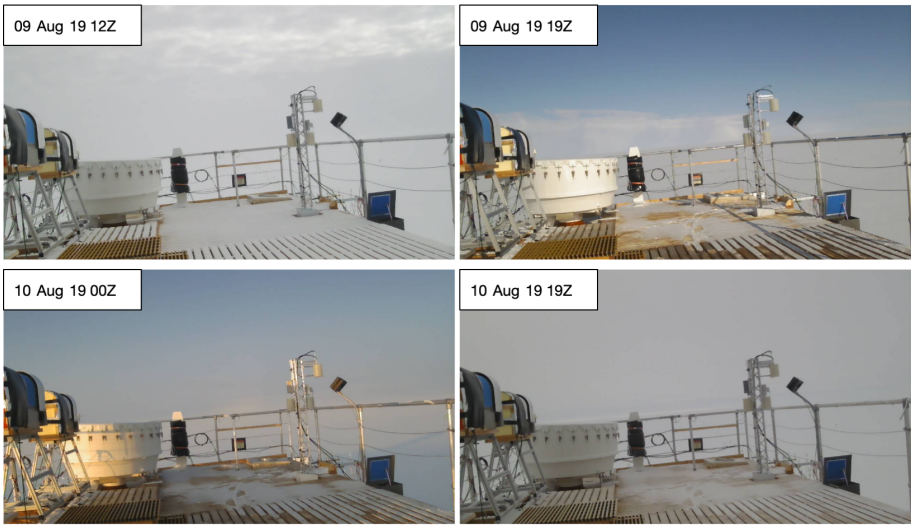

Figure 14. Photographs from a webcam oriented towards the eastern horizon on 9 and 10 August 2019. The aerosol inlet is visibly mounted on the mast in the SE corner.

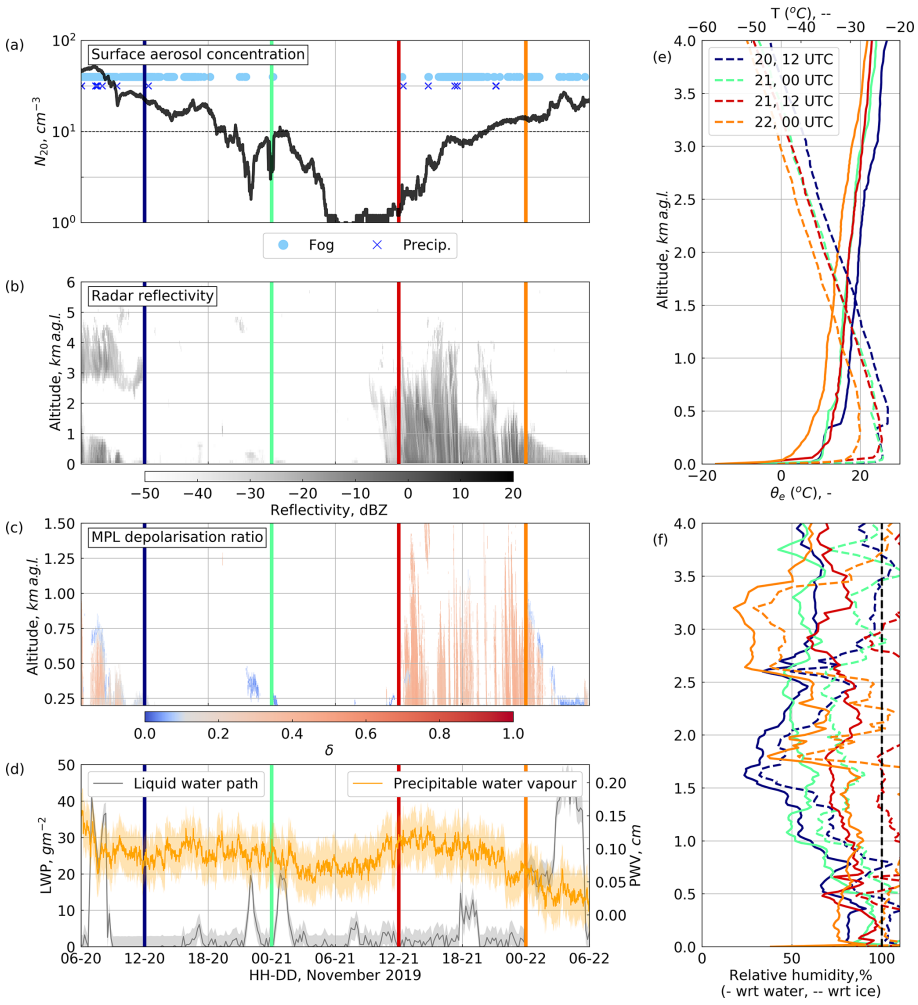

Figure 15. Same as Fig. 11 but during the 21 November 2019 low-aerosol case study. Note that there are no SBI events recorded during this period due to missing data but that the radiosonde profiles indicate a constant shallow surface-based temperature inversion throughout.

aerosol light scattering and absorption coefficients that are related to aerosol particle concentrations (Schmeisser et al., 2018), suggesting that it is a persistent annual feature.

Hirdman et al. (2009) used FLEXPART back trajectory simulations to show that surface aerosol particle concentrations at Summit are an order of magnitude less sensitive to surface emissions from within the Arctic compared to lower-altitude Arctic sites, which is a possible explanation for why Summit does not experience Arctic haze build-up during the winter. In contrast, the GrIS is more sensitive to aerosol sources above the boundary layer, often originating further south and descending to the GrIS via subsidence driven by radiative cooling (Stohl, 2006; Hirdman et al., 2009).

At sea level Arctic sites (both marine and coastal), the extremely low aerosol particle concentrations observed in the summer are largely attributed to increases in wet deposition (Garrett et al., 2010; Browse et al., 2012). An important distinction between Summit (where the 0 °C isotherm is always below the surface except in extreme situations; Shupe et al., 2013b; Bennartz et al., 2013) and sea level Arctic sites is that Summit does not currently experience rain during the summer. The fact that mean monthly N_{20} is relatively high in the summer at Summit could be related to the fact that wet deposition is much less efficient in ice-bearing clouds (Henning et al., 2004). In this case, future increases in the height of the 0 °C isotherm over the GrIS could result in lower summertime aerosol particle concentrations.

4.2 Controls on surface aerosol particle concentrations at Summit

The processes controlling surface aerosol particle concentrations over the central GrIS form a complex system, integrating local meteorological conditions, air mass history during aerosol transport, source regions, and transport pathways. Figure 16 illustrates some of the key components of this system, distinguishing between those processes that are supported by evidence in this study and those for which uncertainties still remain. We have made the assumption that there are no local sources of aerosol at the surface. There is a possibility that particle growth via condensation of precursor gases, possibly released from organic material in the snowpack, could occasionally contribute to near-surface CCN concentrations (Ziemba et al., 2010). We do not consider this process in the present study, but the contribution of ultra-fine particle growth to CCN concentrations over the GrIS remains unclear and warrants further investigation.

Out of the four surface processes considered in this study (fog, SBIs, precipitation and BLSN), only fog events have a strong and consistent effect on measured N_{20}. The effect of fog on surface aerosol particle concentrations is consistent with previous studies that were limited to the summer months (Bergin et al., 1994, 1995). Future studies should ensure that fog is accounted for before generalising sampled particle concentrations over wider regions or altitude ranges. Importantly, the observed decrease in aerosol particle number concentration during fog events reflects the number of particles that are incorporated into droplets too large to pass through the CPC inlet, either through CCN activation and growth or scavenging by fog droplets, and these particles are not necessarily deposited at the surface.

Despite the potential for SBIs to act as a barrier for turbulent mixing and hence reduce the rate that aerosol particles are transported down to the surface (Dibb et al., 1992; Li et al., 2019; Thomas et al., 2019), we found no consistent change in N_{20} during the first 3 h of SBI events and no relationship between the change in N_{20} and the mean intensity of the SBI, which ranges between 0.23 and 0.92 °C m^{-1} (not shown). SBIs may have a more important role on surface aerosol particle concentrations over longer timescales, especially because the loss of aerosol particles to the surface by dry deposition is slow (Garrett et al., 2010); however, because fog regularly forms during SBI events, it is difficult to isolate the influence of the SBI from the influence of fog scavenging on aerosol particle concentrations during longer events. SBIs may also contribute to observed reduction in N_{20} during fog events by restricting turbulent mixing. This study does not consider changes in mechanically induced turbulence over time or elevated temperature inversions; further studies are required to understand the role of changes in turbulent mixing on controlling surface aerosol particle concentrations.

N_{20} also does not respond consistently to the precipitation or BLSN events considered in this study (Fig. 6c and d). This is in agreement with Bergin et al. (1995), who did not observe a significant effect of precipitation on surface aerosol particle concentrations at Summit during the summer. Below-cloud scavenging rates are sensitive to a wide range of parameters that we do not consider here, including snow crystal size and habit, degree of riming, relative humidity, and Reynolds number (Feng, 2009; Browse et al., 2012). We also do not distinguish between below-cloud precipitation and clear-sky precipitation (diamond dust). However, although the rate of wet deposition might vary between events, below-cloud scavenging should reduce N_{20}, and the fact that we do not consistently observe this suggests that other processes are acting to maintain surface aerosol particle concentrations during precipitation. For example, in both the 3 July 2019 and 21 November 2019 case studies (Sect. 3.4), aerosol particle concentrations increase during precipitation. One explanation for this could be the release of particles near the surface via below-cloud evaporation of hydrometeors. Low-level mixed-phase clouds in particular can act to facilitate the transport of particles from the free troposphere into the boundary layer through entrainment and activation at cloud top and release through evaporation at cloud base (Igel et al., 2017). At Summit, the majority of precipitation occurs in the presence of these low-level mixed-phase clouds (Pettersen et al., 2018). Clouds can also act to increase the efficiency of turbulent mixing down to the surface because below-cloud

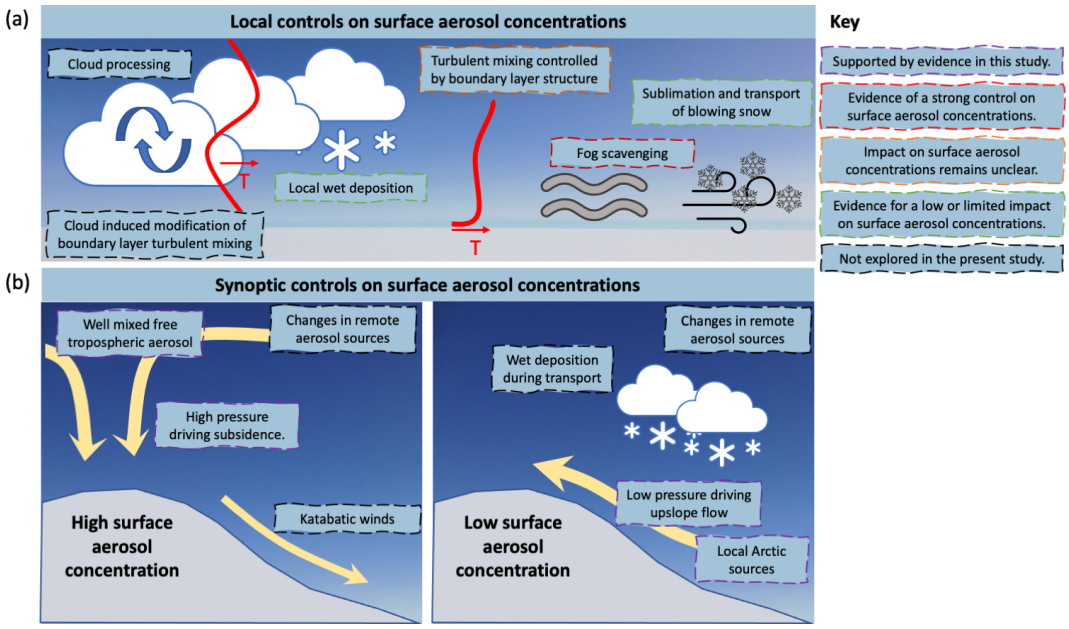

Figure 16. Conceptual model illustrating the key components controlling surface aerosol particle concentrations over the central GrIS, highlighting factors that are supported by evidence in this study and important areas for future research (see legend inset).

turbulent mixing driven by the sinking of radiatively cooled air near the cloud top can extend down into the mechanically driven surface mixed layer (Brooks et al., 2017; Shupe et al., 2013a). Precipitation itself might also contribute to this increase in turbulent mixing via drag. Given that most of the aerosol particles arriving at Summit descend from the free troposphere (Hirdman et al., 2009), the role of clouds in the transport of aerosol particles into the boundary layer of the GrIS is an important area for future research.

Synoptic conditions play an important role in controlling N_{20} at Summit, with most anomalously high-N_{20} events coinciding with anomalously high surface pressure during 2019 (Fig. 7). The difference in aerosol emission sensitivity and transport pathway simulations between anomalously high- and low-N_{20} events (Fig. 9), combined with the difference in mean synoptic anomalies (Fig. 8), implies that high surface aerosol particle concentrations occur at Summit when air is transported down to the surface from high in the free troposphere, associated with subsidence related to anomalously strong high-pressure systems over Greenland (Fig. 16b). This free-tropospheric air is sensitive to emissions from middle and low latitudes that can release particles high into the atmosphere where they remain suspended for long periods of time (i.e. >20 d) (Stohl, 2006; Hirdman et al., 2009; Roiger et al., 2011). This result is consistent with previous studies investigating the transport pathways of aerosol particles that arrive at Summit. Both Hirdman et al. (2009) and Schmeisser et al. (2018) conclude that because on average the majority of air arriving at Summit has only been in contact with the surface over the ice sheet itself, particles measured at Summit must have descended from the free troposphere after transportation at high altitudes over timescales >20 d. Persistent anomalously high geopotential heights over central Greenland are also associated with the occurrence of precipitating low-level mixed-phase stratocumulus clouds (McIlhattan et al., 2020) that can encourage the transport of aerosol particles from the free tropospheric into the boundary layer (Igel et al., 2017).

Anomalously low aerosol particle concentrations typically occur in the presence of anomalous cyclonic circulation and low geopotential heights off the south-east coast of Greenland (Fig. 8b) that drive air up to the top of the GrIS from the coast and surrounding ocean (Figs. 9b and 16b). During such events, adiabatic cooling due to orographic lifting as the air is advected up the GrIS results in increased condensation and precipitation (Schuenemann et al., 2009). These conditions are associated with deep glaciated clouds advecting over Summit from south-east Greenland (Pettersen et al., 2018). The associated increase in wet deposition en route to Summit could contribute to the relatively low N_{20}. These events are more common in the winter season, when the north Atlantic storm track is more active (Schuenemann et al., 2009). Hogan et al. (1984) also reached a similar conclusion based on surface aerosol particle measurements at DYE III during the summer; they observed that low particle concentrations followed moist upslope flow and precipitation driven by a low-pressure system to the south of Greenland and that concentrations increased after the establishment of a high-pressure system and downslope flow.

This study does not consider changes in emission or removal rates along the aerosol transport pathway. Emission rates vary seasonally within the Arctic due to changes in ice cover and biomass burning (Willis et al., 2018), and isolated events such as volcanic eruptions can have large impacts on background aerosol particle concentrations (e.g. Friberg et al., 2015). Removal rates vary along a particular transport pathway with changes in precipitation amount and phase (Garrett et al., 2010; Browse et al., 2012). Given this, it is quite remarkable that the relationship between anomalous aerosol particle concentrations at Summit and anomalous synoptic conditions is so evident. The strength of this relationship implies that future changes in Arctic large-scale circulation could affect aerosol particle concentrations and aerosol–cloud–radiation interactions over the GrIS. In particular, changes in the frequency of storms moving up the south-east coast of Greenland (Ulbrich et al., 2008) or the position of the Icelandic low (Berdahl et al., 2018) might affect the frequency of extremely-low-aerosol-particle-concentration events over the central GrIS.

4.3 Potential for cloud formation to be limited by low CCN concentrations and discussion of case studies

N_{20} fell below $10\,\mathrm{cm}^{-3}$ on multiple occasions year-round at Summit in 2019 (Fig. 4). Because CCN are a subset of total condensation nuclei concentration, it is likely that CCN concentrations fall low enough to limit cloud and fog formation, based on approximate threshold estimates determined from past observational and modelling studies over the Arctic Ocean (Mauritsen et al., 2011; Stevens et al., 2018). The ratio of CCN/N_{10} at a supersaturation of 0.55 % measured over Summit during a research flight in 2008 was 0.52 (Lathem et al., 2013), which is similar to the mean CCN/N_{10} ratio observed at the Zeppelin Observatory in Svalbard outside of the Arctic haze season (Jung et al., 2018). However this ratio is a function of supersaturation, and at very high supersaturations (that can occur under extremely low CCN concentrations) small particles that do not typically act as CCN can activate (Leaitch et al., 2016; Baccarini et al., 2020). If we make the assumption that all CCN are activated after the first 3 h of fog formation during the events in Fig. 6a, the fact that we see a median 20 % reduction in total N_{20} during these events implies a CCN/N_{20} ratio of 0.2, and for the individual event example in Fig. 3, the CCN/N_{20} would have been 0.46. Using the more conservative ratio estimation of 0.46, surface CCN concentrations will have fallen below $10\,\mathrm{cm}^{-3}$ for 46 d or 15 % of the measurement period during 2019. Because supercooled liquid fog can have a large effect on surface radiative fluxes at Summit (liquid fog at Summit has an average total (SW+LW) cloud radiative forcing of $26.1\,\mathrm{W\,m}^{-2}$ compared to clear skies, Cox et al., 2019), if fog formation is limited by low CCN concentrations, this could have an important effect on the ice sheet surface energy budget, especially over individual events which can play a role in pre-conditioning the snow surface in advance of melt (Miller et al., 2017). The same could be true for clouds where surface concentrations are representative of CCN concentrations at cloud level. For example, the exceptional July 2012 Greenland melt event was enhanced by the presence of low-level mixed-phase clouds with a LWP of $\sim 30\,\mathrm{g\,m}^{-2}$ (Bennartz et al., 2013); in this case, if small changes in CCN concentrations acted to either increase or decrease the cloud LWP, they could have controlled the presence versus absence of surface melt.

For all three of the case studies in Sect. 3.4, decreasing aerosol particle concentrations were associated with a reduction in cloud cover, and the reverse was also true. However, differences in timing and boundary layer structure imply that different processes were involved in each case. This demonstrates that it is not sufficient to use simple correlations between cloud properties and aerosol particle concentrations to investigate cloud–aerosol interactions, since there are many additional confounding variables. Although we cannot delineate the individual drivers of the changes in N_{20} during these case studies based purely on observations, the near-zero liquid water path is convincing evidence that low CCN concentrations are limiting the formation of liquid water droplets at the surface despite supersaturation when N_{20} is $< 10\,\mathrm{cm}^{-3}$ in all three case studies (i.e. fog formation). Note the only other events where we observed $N_{20} < 10\,\mathrm{cm}^{-3}$ and LWP $> 10\,\mathrm{g\,m}^{-2}$ occurred in February and March 2019 and were associated with clouds with base heights between 250 and 1000 m a.s.l. The static stability of the surface layer in these cases means it is not possible to know whether the surface N_{20} was representative of aerosol particle concentrations in the cloud layer.

Finally, for all three case studies, back trajectory simulations indicate that aerosol particles were transported upslope to Summit from lower elevations (Fig. 10), and two of the cases (July and November) occurred in the presence of cyclonic circulation off the south-east coast of Greenland – the typical synoptic condition associated with anomalously low aerosol particle concentrations at Summit (Fig. 8). Although the simulated aerosol source regions are all from high latitudes ($> 50°$N; Fig. 10), they originate from very different directions (Siberia on 3 July 2019, the Canadian Archipelago on 10 August 2019, and south-west of Greenland on 21 November 2019). This suggests that the upslope transport pathway to Summit, which is strongly linked to precipitation over the GrIS (Schuenemann et al., 2009) and notably from glaciated as opposed to mixed-phase clouds (Pettersen et al., 2018), has a stronger influence on N_{20} than the source region. These upslope flow enhanced precipitation events are also coupled to anomalously warm temperatures over the GrIS, which likely results in a higher percentage of rain (and hence increased wet deposition) en route to Summit (Pettersen et al., 2021). These results imply that increased wet deposition during transport may play a large role in driving CCN concentrations below the threshold where they can

sustain cloud formation. The role of wet deposition in controlling aerosol particle concentrations over the central GrIS is therefore an important area for future research.

5 Summary and conclusions

This study presents the first full year of surface aerosol particle number concentration measurements from the central Greenland Ice Sheet and assesses the local and synoptic controls on surface N_{20}. In 2019, the minimum aerosol particle concentrations occur in February (which has a monthly average concentration of just $18\,\mathrm{cm}^{-3}$ and a standard deviation of $\sigma_N = 16\,\mathrm{cm}^{-3}$), and the maximum concentrations occur in April (monthly mean: $247\,\mathrm{cm}^{-3}$, σ_N: $130\,\mathrm{cm}^{-3}$) and May (monthly mean: $206\,\mathrm{cm}^{-2}$, σ_N: $165\,\mathrm{cm}^{-3}$). Between May and October, concentrations remain on the order of $100\,\mathrm{cm}^{-3}$ before they decrease again between October and December. This seasonal cycle is distinct from that of many sea level Arctic sites which experience minimum surface aerosol concentrations in the summer (Freud et al., 2017; Schmeisser et al., 2018).

Changes in synoptic conditions strongly control N_{20}, with almost all anomalously high-N_{20} events associated with anomalously high surface pressure over Summit. High N_{20} occurs under anomalously high geopotential heights and strong anticyclonic circulation over Greenland, which act to enhance the descent of free-tropospheric air to the ice sheet surface. Low N_{20} occurs in the presence of anomalous cyclonic circulation over south-east Greenland, when low-pressure systems drive up slope flow that is associated with increased precipitation (Schuenemann et al., 2009; Pettersen et al., 2018). Below-average aerosol particle concentrations occur more often in the winter, when the frequency of low-pressure systems driven by the North Atlantic storm track increases (Schuenemann et al., 2009). The distinction between upslope flow and descent from higher altitudes appears to be a stronger control on N_{20} than aerosol source region, suggesting an important role for wet deposition along aerosol transport pathways.

We find that fog strongly effects surface aerosol particle concentration measurements, in agreement with previous studies that look at isolated events during the summer (Bergin et al., 1994, 1995). On average, there is a 20 % reduction in N_{20} after the first 3 h of a fog event. Because fog significantly modifies local surface aerosol particle concentrations, future studies should ensure that fog is accounted for before generalising sampled aerosol particle concentrations over wider regions or altitude ranges. In contrast, precipitation, blowing snow, and strong surface-based temperature inversions ($> 0.23\,^{\circ}\mathrm{C\,m}^{-1}$) do not have a consistent effect on N_{20} during the first 3 h of the event. Competing influences of advection, or either cloud or mechanically induced changes in the turbulent structure of the boundary layer, might play roles in modulating aerosol particle concentrations during these events and are not considered in this study.

This study uses a conservative estimate to determine that surface aerosol particle concentrations low enough to limit cloud and or fog formation (based on observations and model simulations over the Arctic ocean; Mauritsen et al., 2011; Stevens et al., 2018) do occur in both winter and summer over the central GrIS. However, long-term vertical profiles of CCN concentrations are necessary to determine how often this is relevant at cloud height. Although practically difficult, continuous vertical profiles of aerosol particle concentrations above the GrIS are essential for understanding the interaction between clouds, aerosols, and the ice sheet surface energy budget and should be a priority for future campaigns. Vertical aerosol profiles are particularly important over the central GrIS where most of the aerosol particles arriving at the surface descend from higher elevations in the free troposphere (Hirdman et al., 2009; Schmeisser et al., 2018; this study). The unique transport pathway and resulting seasonal cycle of aerosol particles over the central GrIS demonstrate that observations of aerosol properties at sea level Arctic sites cannot be generalised over the GrIS, in agreement with previous studies (e.g. Hirdman et al., 2009; Schmeisser et al., 2018; Schmale et al., 2021).

Data availability. All data are publicly available. ICECAPS-ACE aerosol measurements and multi-level temperature sensor data can be accessed through the CEDA archive at http://catalogue.ceda.ac.uk/uuid/f06c6aa727404ca788ee3dd0515ea61a (Guy et al., 2020). NOAA GML meteorological data are available at https://gml.noaa.gov/aftp/data/meteorology/in-situ/sum/2019 (GMLMET, 2021). All additional ICECAPS data are available from the Arctic Data Center: MMCR (https://doi.org/10.18739/A2Q52FD4V; Shupe, 2020a), MPL (https://doi.org/10.18739/A2862BC30; Shupe, 2020b), POSS (https://doi.org/10.18739/A2GQ6R30G; Shupe, 2020c), HATPRO and MWRHF (https://doi.org/10.18739/A2542J92G; Turner and Bennartz, 2020), and radiosonde profiles (https://doi.org/10.18739/A20P0WR53; Walden and Shupe, 2020). ERA5 reanalysis data are made available by the European Centre for Medium-Range Weather Forecasts (ECMWF) and can be accessed at the Copernicus Climate Data Store (https://doi.org/10.24381/cds.bd0915c6; Hersbach et al., 2018).

Author contributions. The original ICECAPS project proposal was conceived by MDS, VPW, DDT, and RB. HG led data collection and curation of ICECAPS-ACE aerosol data supervised by RRN and IMB. HG led the analysis with contributions from RRN, IMB, BJM, CP, MDS, and CJC. HG prepared the manuscript with contributions from all co-authors.

Competing interests. The contact author has declared that neither they nor their co-authors have any competing interests.

Acknowledgements. The efforts of technicians at Summit Station and science support provided by Polar Field Services were crucial to maintaining data quality and continuity at Summit. We acknowledge Bethany Wyld for assistance during the ICECAPS-ACE field installation and Richard Rigby for his support setting up and running the FLEXPART model. We also gratefully acknowledge support from the National Centre for Atmospheric Science (NCAS), the NCAS Atmospheric Measurement and Observation Facility, and notably Barbara Brooks for support in instrument troubleshooting and data quality control. ICECAPS is a long-term research programme with a large number of collaborators, and we are grateful for all their efforts in developing and maintaining the various instruments and data products used in this study. Matthew D. Shupe and William D. Neff were supported by National Science Foundation grant no. OPP1801477. We are grateful for the thoughtful suggestions of two anonymous reviewers that have improved the quality of this paper.

Financial support. This research has been supported by the Natural Environment Research Council (grant no. NE/L002574/1 and NSFGEO-NERC grant no. 1801477).

Review statement. This paper was edited by Armin Sorooshian and reviewed by two anonymous referees.

References

Asmi, A., Collaud Coen, M., Ogren, J. A., Andrews, E., Sheridan, P., Jefferson, A., Weingartner, E., Baltensperger, U., Bukowiecki, N., Lihavainen, H., Kivekäs, N., Asmi, E., Aalto, P. P., Kulmala, M., Wiedensohler, A., Birmili, W., Hamed, A., O'Dowd, C., G Jennings, S., Weller, R., Flentje, H., Fjaeraa, A. M., Fiebig, M., Myhre, C. L., Hallar, A. G., Swietlicki, E., Kristensson, A., and Laj, P.: Aerosol decadal trends – Part 2: In-situ aerosol particle number concentrations at GAW and ACTRIS stations, Atmos. Chem. Phys., 13, 895–916, https://doi.org/10.5194/acp-13-895-2013, 2013.

Baccarini, A., Karlsson, L., Dommen, J., Duplessis, P., Vüllers, J., Brooks, I. M., Saiz-Lopez, A., Salter, M., Tjernström, M., Baltensperger, U., Zieger, P., and Schmale, J.: Frequent new particle formation over the high Arctic pack ice by enhanced iodine emissions, Nat. Commun., 11, 1–11, 2020.

Backman, J., Schmeisser, L., and Asmi, E.: Asian emissions explain much of the Arctic Black Carbon events, Geophys. Res. Lett., 48, e2020GL091913, https://doi.org/10.1029/2020GL091913, 2021.

Bamber, J. L., Westaway, R. M., Marzeion, B., and Wouters, B.: The land ice contribution to sea level during the satellite era, Environ. Res. Lett., 13, 063008, https://doi.org/10.1088/1748-9326/aac2f0, 2018.

Bennartz, R., Shupe, M. D., Turner, D. D., Walden, V. P., Steffen, K., Cox, C. J., Kulie, M. S., Miller, N. B., and Pettersen, C.: July 2012 Greenland melt extent enhanced by low-level liquid clouds, Nature, 496, 83–86, https://doi.org/10.1038/nature12002, 2013.

Bennartz, R., Fell, F., Pettersen, C., Shupe, M. D., and Schuettemeyer, D.: Spatial and temporal variability of snowfall over Greenland from CloudSat observations, Atmos. Chem. Phys., 19, 8101–8121, https://doi.org/10.5194/acp-19-8101-2019, 2019.

Berdahl, M., Rennermalm, A., Hammann, A., Mioduszweski, J., Hameed, S., Tedesco, M., Stroeve, J., Mote, T., Koyama, T., and McConnell, J. R.: Southeast greenland winter precipitation strongly linked to the Icelandic Low position, J. Climate, 31, 4483–4500, 2018.

Bergin, M. H., Jaffrezo, J. L., Davidson, C. I., Caldow, R., and Dibb, J.: Fluxes of chemical species to the Greenland ice sheet at Summit by fog and dry deposition, Geochim. Cosmochim. Ac., 58, 3207–3215, 1994.

Bergin, M. H., Jaffrezo, J.-L., Davidson, C. I., Dibb, J. E., Pandis, S. N., Hillamo, R., Maenhaut, W., Kuhns, H. D., and Makela, T.: The contributions of snow, fog, and dry deposition to the summer flux of anions and cations at Summit, Greenland, J. Geophys. Res., 100, 16275–16288, https://doi.org/10.1029/95JD01267, 1995.

Box, J. E., Fettweis, X., Stroeve, J. C., Tedesco, M., Hall, D. K., and Steffen, K.: Greenland ice sheet albedo feedback: thermodynamics and atmospheric drivers, The Cryosphere, 6, 821–839, https://doi.org/10.5194/tc-6-821-2012, 2012.

Brooks, I. M., Tjernström, M., Persson, P. O. G., Shupe, M. D., Atkinson, R. A., Canut, G., Birch, C. E., Mauritsen, T., Sedlar, J., and Brooks, B. J.: The Turbulent Structure of the Arctic Summer Boundary Layer During The Arctic Summer Cloud-Ocean Study, J. Geophys. Res.-Atmos., 122, 9685–9704, 2017.

Browse, J., Carslaw, K. S., Arnold, S. R., Pringle, K., and Boucher, O.: The scavenging processes controlling the seasonal cycle in Arctic sulphate and black carbon aerosol, Atmos. Chem. Phys., 12, 6775–6798, https://doi.org/10.5194/acp-12-6775-2012, 2012.

Castellani, B. B., Shupe, M. D., Hudak, D. R., and Sheppard, B. E.: The annual cycle of snowfall at Summit, Greenland, J. Geophys. Res.-Atmos., 120, 6654–6668, 2015.

Cheng, C.-T., Wang, W.-C., and Chen, J.-P.: Simulation of the effects of increasing cloud condensation nuclei on mixed-phase clouds and precipitation of a front system, Atmos. Res., 96, 461–476, 2010.

Cox, C. J., Noone, D. C., Berkelhammer, M., Shupe, M. D., Neff, W. D., Miller, N. B., Walden, V. P., and Steffen, K.: Supercooled liquid fogs over the central Greenland Ice Sheet, Atmos. Chem. Phys., 19, 7467–7485, https://doi.org/10.5194/acp-19-7467-2019, 2019.

Crilley, L. R., Shaw, M., Pound, R., Kramer, L. J., Price, R., Young, S., Lewis, A. C., and Pope, F. D.: Evaluation of a low-cost optical particle counter (Alphasense OPC-N2) for ambient air monitoring, Atmos. Meas. Tech., 11, 709–720, https://doi.org/10.5194/amt-11-709-2018, 2018.

Curry, J. A., Rossow, W. B., Randall, D., Schramm, J. L., Rossow, W. B., Randall, D., and Schramm, J. L.: Overview of Arctic cloud and radiation characteristics, J. Climate, 9, 1731–1764, 1996.

Davidson, C., Jaffrezo, J.-L., Mosher, B., Dibb, J. E., Borys, R., Bodhaine, B., Rasmussen, R., Boutron, C., Gorlach, U., Cachier, H., Ducret, J., Colin, J.-L., Heidam, N. Z., Kemp, K., and

Hillamo, R.: Chemical constituents in the air and snow at Dye 3, Greenland–I. Seasonal variations, Atmos. Environ. A-Gen., 27, 2709–2722, https://doi.org/10.1016/0960-1686(93)90304-H, 1993.

Dibb, J. E., Jaffrezo, J. L., and Legrand, M.: Initial findings of recent investigations of air-snow relationships in the summit region of the Greenland ice sheet, J. Atmos. Chem., 14, 167–180, 1992.

Drab, E., Gaudichet, A., Jaffrezo, J. L., and Colin, J. L.: Mineral particles content in recent snow at Summit (Greenland), Atmos. Environ., 36, 5365–5376, 2002.

Enderlin, E. M., Howat, I. M., Jeong, S., Noh, M.-J., VanAngelen, J. H., and Van den Broeke, M. R.: An improved mass budget for the Greenland ice sheet, Geophys. Res. Lett., 41, 866–872, https://doi.org/10.1002/2013GL059010, 2014.

Feng, J.: A size-resolved model for below-cloud scavenging of aerosols by snowfall, J. Geophys. Res.-Atmos., 114, 1–8, 2009.

Fettweis, X., Box, J. E., Agosta, C., Amory, C., Kittel, C., Lang, C., van As, D., Machguth, H., and Gallée, H.: Reconstructions of the 1900–2015 Greenland ice sheet surface mass balance using the regional climate MAR model, The Cryosphere, 11, 1015–1033, https://doi.org/10.5194/tc-11-1015-2017, 2017.

Flyger, H., Heidam, N., Hansen, K., Megaw, W., Walther, E., and Hogan, A.: The background level of the summer tropospheric aerosol, sulphur dioxide and ozone over Greenland and the North Atlantic Ocean, J. Aerosol Sci., 7, 103–140, 1976.

Flynna, C. J., Mendozaa, A., Zhengb, Y., and Mathurb, S.: Novel polarization-sensitive micropulse lidar measurement technique, Opt. Express, 15, 2785–2790, 2007.

Forster, C., Stohl, A., and Seibert, P.: Parameterization of Convective Transport in a Lagrangian Particle Dispersion Model and Its Evaluation, J. Appl. Meteorol. Clim., 46, 403–422, 2007.

Freud, E., Krejci, R., Tunved, P., Leaitch, R., Nguyen, Q. T., Massling, A., Skov, H., and Barrie, L.: Pan-Arctic aerosol number size distributions: seasonality and transport patterns, Atmos. Chem. Phys., 17, 8101–8128, https://doi.org/10.5194/acp-17-8101-2017, 2017.

Friberg, J., Martinsson, B. G., Sporre, M. K., Andersson, S. M., Brenninkmeijer, C. A. M., Hermann, M., Velthoven, P. F. J., and Zahn, A.: Influence of volcanic eruptions on midlatitude upper tropospheric aerosol and consequences for cirrus clouds, Earth and Space Science, 2, 285–300, 2015.

Garrett, T. J. and Zhao, C.: Increased Arctic cloud longwave emissivity associated with pollution from mid-latitudes, Nature, 440, 787–789, 2006.

Garrett, T. J., Zhao, C., and Novelli, P. C.: Assessing the relative contributions of transport efficiency and scavenging to seasonal variability in Arctic aerosol, Tellus B, 62, 190–196, 2010.

Giorgi, F.: A particle dry-deposition parameterization scheme for use in tracer transport models, J. Geophys. Res., 91, 9794–9806, https://doi.org/10.1029/JD091iD09p09794, 1986.

GMLMET: Meteorology Measurements from the NOAA/ESRL/GMD Baseline Observatory Summit Station, GMLMET [data set], available at: https://gml.noaa.gov/aftp/data/meteorology/in-situ/sum/2019, last access: 1 April 2021.

Guy, H., Neely III, R. R., and Brooks, I.: ICECAPS-ACE: Integrated Characterization of Energy, Clouds, Atmospheric state, and Precipitation at Summit, Greenland – Aerosol Cloud Experiment measurements, Centre for Environmental Data Analysis [data set], available at: http://catalogue.ceda.ac.uk/uuid/f06c6aa727404ca788ee3dd0515ea61a (last access: 1 April 2021), 2020.

Hanna, E., Cropper, T. E., Hall, R. J., and Cappelen, J.: Greenland Blocking Index 1851-2015: a regional climate change signal, Int. J. Climatol., 36, 4847–4861, 2016.

Heinemann, G. and Klein, T.: Modelling and observations of the katabatic flow dynamics over Greenland, Tellus A, 54, 542–554, 2002.

Henning, S., Bojinski, S., Diehl, K., Ghan, S., Nyeki, S., Weingartner, E., Wurzler, S., and Baltensperger, U.: Aerosol partitioning in natural mixed-phase clouds, Geophys. Res. Lett., 31, L06101, https://doi.org/10.1029/2003GL019025, 2004.

Hersbach, H., Bell, B., Berrisford, P., Biavati, G., Horányi, A., Muñoz Sabater, J., Nicolas, J., Peubey, C., Radu, R., Rozum, I., Schepers, D., Simmons, A., Soci, C., Dee, D., and Thépaut, J.-N.: ERA5 hourly data on pressure levels from 1979 to present, Copernicus Climate Change Service (C3S) Climate Data Store (CDS) [data set], https://doi.org/10.24381/cds.bd0915c6, 2018.

Hersbach, H., Bell, B., Berrisford, P., Hirahara, S., Horányi, A., Muñoz-Sabater, J., Nicolas, J., Peubey, C., Radu, R., Schepers, D., Simmons, A., Soci, C., Abdalla, S., Abellan, X., Balsamo, G., Bechtold, P., Biavati, G., Bidlot, J., Bonavita, M., De Chiara, G., Dahlgren, P., Dee, D., Diamantakis, M., Dragani, R., Flemming, J., Forbes, R., Fuentes, M., Geer, A., Haimberger, L., Healy, S., Hogan, R. J., Hólm, E., Janisková, M., Keeley, S., Laloyaux, P., Lopez, P., Lupu, C., Radnoti, G., de Rosnay, P., Rozum, I., Vamborg, F., Villaume, S., and Thépaut, J. N.: The ERA5 global reanalysis, Q. J. Roy. Meteor. Soc., 146, 1999–2049, 2020.

Hirdman, D., Sodemann, H., Eckhardt, S., Burkhart, J. F., Jefferson, A., Mefford, T., Quinn, P. K., Sharma, S., Ström, J., and Stohl, A.: Source identification of short-lived air pollutants in the Arctic using statistical analysis of measurement data and particle dispersion model output, Atmos. Chem. Phys., 10, 669–693, https://doi.org/10.5194/acp-10-669-2010, 2010.

Hobbs, W. H.: The Greenland Glacial Anticyclone, J. Meteorol., 2, 143–153, 1945.

Hofer, S., Tedstone, A. J., Fettweis, X., and Bamber, J. L.: Decreasing cloud cover drives the recent mass loss on the Greenland Ice Sheet, Science Advances, 3, e1700584, https://doi.org/10.1126/sciadv.1700584, 2017.

Hofer, S., Tedstone, A. J., Fettweis, X., and Bamber, J. L.: Cloud microphysics and circulation anomalies control differences in future Greenland melt, Nat. Clim. Change, 9, 523–528, 2019.

Hogan, A. W., Barnard, S. C., Kebschull, K., Townsend, R., and Samson, J. A.: Aerosol variation in the western hemisphere Arctic, J. Aerosol Sci., 15, 13–33, 1984.

Howat, I., Negrete, A., and Smith, B.: The Greenland Ice Mapping Project (GIMP) Land Ice and Ocean Classification Mask, Version 1, NASA National Snow and Ice Data Center Distributed Active Archive Center, https://doi.org/10.5067/B8X58MQBFUPA, 2017.

Hudson, J. G. and Da, X.: Volatility and size of cloud condensation nuclei, J. Geophys. Res.-Atmos., 101, 4435–4442, 1996.

Igel, A. L., Ekman, A. M. L., Leck, C., Tjernström, M., Savre, J., and Sedlar, J.: The free troposphere as a potential source of arctic boundary layer aerosol particles, Geophys. Res. Lett., 44, 7053–7060, 2017.

Intrieri, J. M., Fairall, C. W., Shupe, M. D., Persson, P. O. G., Andreas, E. L., Guest, P. S., and Moritz, R. E.: An annual cycle of Arctic surface cloud forcing at SHEBA, J. Geophys. Res.-Oceans, 107, 8039, https://doi.org/10.1029/2000JC000439, 2002.

Jaenicke, R.: Problems of the Distribution of the Global Aerosol, Russ. Chem. Rev., 59, 959–972, https://doi.org/10.1070/rc1990v059n10abeh00356, 1990.

Jung, C. H., Yoon, Y. J., Kang, H. J., Gim, Y., Lee, B. Y., Ström, J., Krejci, R., and Tunved, P.: The seasonal characteristics of cloud condensation nuclei (CCN) in the arctic lower troposphere, Tellus B, 70, 1–13, 2018.

Kanji, Z. A., Ladino, L. A., Wex, H., Boose, Y., Burkert-Kohn, M., Cziczo, D. J., and Krämer, M.: Overview of ice nucleating particles, Meteoro. Mon., 58, 1–1, 2017.

Kay, J. E., L'Ecuyer, T., Pendergrass, A., Chepfer, H., Guzman, R., and Yettella, V.: Scale-aware and definition-aware evaluation of modeled near-surface precipitation frequency using CloudSat observations, J. Geophys. Res.-Atmos., 123, 4294–4309, 2018.

Lance, S., Shupe, M. D., Feingold, G., Brock, C. A., Cozic, J., Holloway, J. S., Moore, R. H., Nenes, A., Schwarz, J. P., Spackman, J. R., Froyd, K. D., Murphy, D. M., Brioude, J., Cooper, O. R., Stohl, A., and Burkhart, J. F.: Cloud condensation nuclei as a modulator of ice processes in Arctic mixed-phase clouds, Atmos. Chem. Phys., 11, 8003–8015, https://doi.org/10.5194/acp-11-8003-2011, 2011.

Lathem, T. L., Beyersdorf, A. J., Thornhill, K. L., Winstead, E. L., Cubison, M. J., Hecobian, A., Jimenez, J. L., Weber, R. J., Anderson, B. E., and Nenes, A.: Analysis of CCN activity of Arctic aerosol and Canadian biomass burning during summer 2008, Atmos. Chem. Phys., 13, 2735–2756, https://doi.org/10.5194/acp-13-2735-2013, 2013.

Leaitch, W. R., Korolev, A., Aliabadi, A. A., Burkart, J., Willis, M. D., Abbatt, J. P. D., Bozem, H., Hoor, P., Köllner, F., Schneider, J., Herber, A., Konrad, C., and Brauner, R.: Effects of 20–100 nm particles on liquid clouds in the clean summertime Arctic, Atmos. Chem. Phys., 16, 11107–11124, https://doi.org/10.5194/acp-16-11107-2016, 2016.

Leck, C. and Svensson, E.: Importance of aerosol composition and mixing state for cloud droplet activation over the Arctic pack ice in summer, Atmos. Chem. Phys., 15, 2545–2568, https://doi.org/10.5194/acp-15-2545-2015, 2015.

Lenaerts, J. T. M., Camron, M. D., Wyburn-Powell, C. R., and Kay, J. E.: Present-day and future Greenland Ice Sheet precipitation frequency from CloudSat observations and the Community Earth System Model, The Cryosphere, 14, 2253–2265, https://doi.org/10.5194/tc-14-2253-2020, 2020.

Li, J., Chen, H., Li, Z., Wang, P., Fan, X., He, W., and Zhang, J.: Analysis of Low-level Temperature Inversions and Their Effects on Aerosols in the Lower Atmosphere, Adv. Atmos. Sci., 36, 1235–1250, 2019.

Lohmann, U. and Feichter, J.: Global indirect aerosol effects: a review, Atmos. Chem. Phys., 5, 715–737, https://doi.org/10.5194/acp-5-715-2005, 2005.

Lubin, D. and Vogelmann, A. M.: A climatologically significant aerosol longwave indirect effect in the Arctic, Nature, 439, 453–456, 2006.

Mann, G. W., Anderson, P. S., and Mobbs, S. D.: Profile measurements of blowing snow at Halley, Antarctica, J. Geophys. Res., 105, 491–508, 2000.

Martin, S. J., Wang, P. K., and Pruppacher, H. R.: A Theoretical Determination of the Efficiency with which Aerosol Particles are Collected by Simple Ice Crystal Plates, J. Atmos. Sci., 37, 1628–1638, 1980.

Mauritsen, T., Sedlar, J., Tjernström, M., Leck, C., Martin, M., Shupe, M., Sjogren, S., Sierau, B., Persson, P. O. G., Brooks, I. M., and Swietlicki, E.: An Arctic CCN-limited cloud-aerosol regime, Atmos. Chem. Phys., 11, 165–173, https://doi.org/10.5194/acp-11-165-2011, 2011.

McIlhattan, E. A., L'Ecuyer, T. S., and Miller, N. B.: Observational evidence linking Arctic supercooled liquid cloud biases in CESM to snowfall processes, J. Climate, 30, 4477–4495, 2017.

McIlhattan, E. A., Pettersen, C., Wood, N. B., and L'Ecuyer, T. S.: Satellite observations of snowfall regimes over the Greenland Ice Sheet, The Cryosphere, 14, 4379–4404, https://doi.org/10.5194/tc-14-4379-2020, 2020.

Miller, N. B., Turner, D. D., Bennartz, R., Shupe, M. D., Kulie, M. S., Cadeddu, M. P., and Walden, V. P.: Surface-based inversions above central Greenland, J. Geophys. Res.-Atmos., 118, 495–506, 2013.

Miller, N. B., Shupe, M. D., Cox, C. J., Walden, V. P., Turner, D. D., and Steffen, K.: Cloud radiative forcing at Summit, Greenland, J. Climate, 28, 6267–6280, 2015.

Miller, N. B., Shupe, M. D., Cox, C. J., Noone, D., Persson, P. O. G., and Steffen, K.: Surface energy budget responses to radiative forcing at Summit, Greenland, The Cryosphere, 11, 497–516, https://doi.org/10.5194/tc-11-497-2017, 2017.

Moran, K. P., Mariner, B. E., Post, M. J., Kropfli, R. A., Welsh, D. C., and Widener, K. B.: An Unattended Cloud-Profiling Radar for Use in Climate Research, B. Am. Meteorol. Soc., 79, 443–455, 1998.

Morrison, H., De Boer, G., Feingold, G., Harrington, J., Shupe, M. D., and Sulia, K.: Resilience of persistent Arctic mixed-phase clouds, Nat. Geosci., 5, 11–17, 2012.

Norgren, M. S., de Boer, G., and Shupe, M. D.: Observed aerosol suppression of cloud ice in low-level Arctic mixed-phase clouds, Atmos. Chem. Phys., 18, 13345–13361, https://doi.org/10.5194/acp-18-13345-2018, 2018.

Paramonov, M., Grönholm, T., and Virkkula, A.: Below-cloud scavenging of aerosol particles by snow at an urban site in Finland, Boreal Environ. Res., 16, 304–320, 2011.

Pettersen, C., Bennartz, R., Merrelli, A. J., Shupe, M. D., Turner, D. D., and Walden, V. P.: Precipitation regimes over central Greenland inferred from 5 years of ICECAPS observations, Atmos. Chem. Phys., 18, 4715–4735, https://doi.org/10.5194/acp-18-4715-2018, 2018.

Pettersen, C., Henderson, S., Mattingly, K., Bennartz, R., and Breeden, M.: The Critical Role of Euro-Atlantic Blocking in Promoting Snowfall in Central Greenland, J. Geophys. Res.-Atmos., in review, 2021.

Pisso, I., Sollum, E., Grythe, H., Kristiansen, N. I., Cassiani, M., Eckhardt, S., Arnold, D., Morton, D., Thompson, R. L., Groot Zwaaftink, C. D., Evangeliou, N., Sodemann, H., Haimberger, L., Henne, S., Brunner, D., Burkhart, J. F., Fouilloux, A., Brioude, J., Philipp, A., Seibert, P., and Stohl, A.: The Lagrangian particle dispersion model FLEX-

PART version 10.4, Geosci. Model Dev., 12, 4955–4997, https://doi.org/10.5194/gmd-12-4955-2019, 2019.

Possner, A., Ekman, A. M., and Lohmann, U.: Cloud response and feedback processes in stratiform mixed-phase clouds perturbed by ship exhaust, Geophys. Res. Lett., 44, 1964–1972, 2017.

Prenni, A. J., Harrington, J. Y., Tjernström, M., DeMott, P. J., Avramov, A., Long, C. N., Kreidenweis, S. M., Olsson, P. Q., and Verlinde, J.: Can ice-nucleating aerosols affect Arctic seasonal climate?, B. Am. Meteorol. Soc., 88, 541–550, 2007.

Rignot, E., Box, J. E., Burgess, E., and Hanna, E.: Mass balance of the Greenland ice sheet from 1958 to 2007, Geophys. Res. Lett., 35, 1–5, 2008.

Rignot, E., Velicogna, I., van den Broeke, M. R., Monaghan, A., and Lenaerts, J. T.: Acceleration of the contribution of the Greenland and Antarctic ice sheets to sea level rise, Geophys. Res. Lett., 38, L05503, https://doi.org/10.1029/2011GL046583, 2011.

Roiger, A., Schlager, H., Schäfler, A., Huntrieser, H., Scheibe, M., Aufmhoff, H., Cooper, O. R., Sodemann, H., Stohl, A., Burkhart, J., Lazzara, M., Schiller, C., Law, K. S., and Arnold, F.: In-situ observation of Asian pollution transported into the Arctic lowermost stratosphere, Atmos. Chem. Phys., 11, 10975–10994, https://doi.org/10.5194/acp-11-10975-2011, 2011.

Schmale, J., Henning, S., Decesari, S., Henzing, B., Keskinen, H., Sellegri, K., Ovadnevaite, J., Pöhlker, M. L., Brito, J., Bougiatioti, A., Kristensson, A., Kalivitis, N., Stavroulas, I., Carbone, S., Jefferson, A., Park, M., Schlag, P., Iwamoto, Y., Aalto, P., Äijälä, M., Bukowiecki, N., Ehn, M., Frank, G., Fröhlich, R., Frumau, A., Herrmann, E., Herrmann, H., Holzinger, R., Kos, G., Kulmala, M., Mihalopoulos, N., Nenes, A., O'Dowd, C., Petäjä, T., Picard, D., Pöhlker, C., Pöschl, U., Poulain, L., Prévôt, A. S. H., Swietlicki, E., Andreae, M. O., Artaxo, P., Wiedensohler, A., Ogren, J., Matsuki, A., Yum, S. S., Stratmann, F., Baltensperger, U., and Gysel, M.: Long-term cloud condensation nuclei number concentration, particle number size distribution and chemical composition measurements at regionally representative observatories, Atmos. Chem. Phys., 18, 2853–2881, https://doi.org/10.5194/acp-18-2853-2018, 2018.

Schmale, J., Zieger, P., and Ekman, A. M. L.: Aerosols in current and future Arctic climate, Nat. Clim. Change, 11, 95–105, https://doi.org/10.1038/s41558-020-00969-5, 2021.

Schmeisser, L., Backman, J., Ogren, J. A., Andrews, E., Asmi, E., Starkweather, S., Uttal, T., Fiebig, M., Sharma, S., Eleftheriadis, K., Vratolis, S., Bergin, M., Tunved, P., and Jefferson, A.: Seasonality of aerosol optical properties in the Arctic, Atmos. Chem. Phys., 18, 11599–11622, https://doi.org/10.5194/acp-18-11599-2018, 2018.

Schmidt, R. A.: Properties of blowing snow, Rev. Geophys., 20, 39–44, 1982.

Schuenemann, K. C., Cassano, J. J., and Finnis, J.: Synoptic forcing of precipitation over greenland: Climatology for 1961–99, J. Hydrometeorol., 10, 60–78, 2009.

Seinfeld, J. H., Bretherton, C., Carslaw, K. S., Coe, H., DeMott, P. J., Dunlea, E. J., Feingold, G., Ghan, S., Guenther, A. B., Kahn, R., Kraucunas, I., Kreidenweis, S. M., Molina, M. J., Nenes, A., Penner, J. E., Prather, K. A., Ramanathan, V., Ramaswamy, V., Rasch, P. J., Ravishankara, A. R., Rosenfeld, D., Stephens, G., and Wood, R.: Improving our fundamental understanding of the role of aerosol–cloud interactions in the climate system, P. Natil. Acad. Sci. USA, 113, 5781–5790, 2016.

Shaw, G. E.: The Arctic haze phenomenon, B. Am. Meteorol. Soc., 76, 2403–2414, 1995.

Sheppard, B. E. and Joe, P. I.: Performance of the precipitation occurrence sensor system as a precipitation gauge, J. Atmos. Ocean. Tech., 25, 196–212, 2008.

Shupe, M.: Millimeter Cloud Radar measurements taken at Summit Station, Greenland, 2019, Arctic Data Center [data set], https://doi.org/10.18739/A2Q52FD4V, 2020a.

Shupe, M.: Micropulse lidar (MPL) measurements taken at Summit Station, Greenland, 2019, Arctic Data Center [data set], https://doi.org/10.18739/A2862BC30, 2020b.

Shupe, M.: Precipitation Occurrence Sensor System measurements taken at Summit Station, Greenland, 2019, Arctic Data Center [data set], https://doi.org/10.18739/A2GQ6R30G, 2020c.

Shupe, M. D. and Intrieri, J. M.: Cloud radiative forcing of the Arctic surface: The influence of cloud properties, surface albedo, and solar zenith angle, J. Climate, 17, 616–628, 2004.

Shupe, M. D., Matrosov, S. Y., and Uttal, T.: Arctic mixed-phase cloud properties derived from surface-based sensors at SHEBA, J. Atmos. Sci., 63, 697–711, 2006.

Shupe, M. D., Persson, P. O. G., Brooks, I. M., Tjernström, M., Sedlar, J., Mauritsen, T., Sjogren, S., and Leck, C.: Cloud and boundary layer interactions over the Arctic sea ice in late summer, Atmos. Chem. Phys., 13, 9379–9399, https://doi.org/10.5194/acp-13-9379-2013, 2013a.

Shupe, M. D., Turner, D. D., Walden, V. P., Bennartz, R., Cadeddu, M. P., Castellani, B. B., Cox, C. J., Hudak, D. R., Kulie, M. S., Miller, N. B., Others, Neely, R. R., Neff, W. D., and Rowe, P. M.: High and dry: New observations of tropospheric and cloud properties above the Greenland Ice Sheet, B. Am. Meteorol. Soc., 94, 169–186, 2013b.

Slater, T., Hogg, A. E., and Mottram, R.: Ice-sheet losses track high-end sea-level rise projections, Nat. Clim. Change, 10, 879–881, https://doi.org/10.1038/s41558-020-0893-y, 2020.

Solomon, A., de Boer, G., Creamean, J. M., McComiskey, A., Shupe, M. D., Maahn, M., and Cox, C.: The relative impact of cloud condensation nuclei and ice nucleating particle concentrations on phase partitioning in Arctic mixed-phase stratocumulus clouds, Atmos. Chem. Phys., 18, 17047–17059, https://doi.org/10.5194/acp-18-17047-2018, 2018.

Stevens, R. G., Loewe, K., Dearden, C., Dimitrelos, A., Possner, A., Eirund, G. K., Raatikainen, T., Hill, A. A., Shipway, B. J., Wilkinson, J., Romakkaniemi, S., Tonttila, J., Laaksonen, A., Korhonen, H., Connolly, P., Lohmann, U., Hoose, C., Ekman, A. M. L., Carslaw, K. S., and Field, P. R.: A model intercomparison of CCN-limited tenuous clouds in the high Arctic, Atmos. Chem. Phys., 18, 11041–11071, https://doi.org/10.5194/acp-18-11041-2018, 2018.

Stohl, A.: Characteristics of atmospheric transport into the Arctic troposphere, J. Geophys. Res.-Atmos., 111, 1–17, 2006.

Storelvmo, T.: Aerosol effects on climate via mixed-phase and ice clouds, Annu. Rev. Earth Pl. Sc., 45, 199–222, 2017.

The IMBIE Team: Mass balance of the Greenland Ice Sheet from 1992 to 2018, Nature, 579, 233–239, https://doi.org/10.1038/s41586-019-1855-2, 2020.

Thomas, M. A., Devasthale, A., Tjernström, M., and Ekman, A. M. L.: The Relation Between Aerosol Vertical Distribution and Temperature Inversions in the Arctic in Winter and Spring, Geophys. Res. Lett., 46, 2836–2845, 2019.

Trusel, L. D., Das, S. B., Osman, M. B., Evans, M. J., Smith, B. E., Fettweis, X., Mcconnell, J. R., Noël, B. P. Y., and van den Broeke, M. R.: Nonlinear rise in Greenland runoff in response to post-industrial Arctic warming, Nature, 564, 104–108, 2018.

Turner, D. and Bennartz, R.: Microwave Radiometer measurements of sky brightness temperature taken at Summit Station, Greenland, 2019, Arctic Data Center [data set], https://doi.org/10.18739/A2542J92G, 2020.

Turner, D. D., Clough, S. A., Liljegren, J. C., Clothiaux, E. E., Cady-Pereira, K. E., and Gaustad, K. L.: Retrieving Liquid Water Path and Precipitable Water Vapor From the Atmospheric Radiation Measurement (ARM) Microwave Radiometers, IEEE T. Geosci. Remote, 45, 3680–3690, 2007.

Twomey, S.: The influence of pollution on the shortwave albedo of clouds, J. Atmos. Sci., 34, 1149–1152, 1977.

Ulbrich, U., Pinto, J. G., Kupfer, H., Leckebusch, G. C., Spangehl, T., and Reyers, M.: Changing Northern Hemisphere storm tracks in an ensemble of IPCC climate change simulations, J. Climate, 21, 1669–1679, 2008.

van den Broeke, M. R., Enderlin, E. M., Howat, I. M., Kuipers Munneke, P., Noël, B. P. Y., van de Berg, W. J., van Meijgaard, E., and Wouters, B.: On the recent contribution of the Greenland ice sheet to sea level change, The Cryosphere, 10, 1933–1946, https://doi.org/10.5194/tc-10-1933-2016, 2016.

Van Tricht, K., Lhermitte, S., Lenaerts, J., Gorodetskaya, I., L'Ecuyer, S., Noël, B., Van Den Broeke, M., Turner, D., and Van Lipzig, N.: Clouds enhance Greenland ice sheet meltwater runoff, Nat. Commun., 7, 10266, https://doi.org/10.1038/ncomms10266, 2016.

von der Weiden, S.-L., Drewnick, F., and Borrmann, S.: Particle Loss Calculator – a new software tool for the assessment of the performance of aerosol inlet systems, Atmos. Meas. Tech., 2, 479–494, https://doi.org/10.5194/amt-2-479-2009, 2009.

Walden, V. P. and Shupe, M.: Radiosonde temperature and humidity profiles taken at Summit Station, Greenland, 2019, Arctic Data Center [data set], https://doi.org/10.18739/A20P0WR53, 2020.

Wex, H., Huang, L., Zhang, W., Hung, H., Traversi, R., Becagli, S., Sheesley, R. J., Moffett, C. E., Barrett, T. E., Bossi, R., Skov, H., Hünerbein, A., Lubitz, J., Löffler, M., Linke, O., Hartmann, M., Herenz, P., and Stratmann, F.: Annual variability of ice-nucleating particle concentrations at different Arctic locations, Atmos. Chem. Phys., 19, 5293–5311, https://doi.org/10.5194/acp-19-5293-2019, 2019.

Willis, M. D., Leaitch, W. R., and Abbatt, J. P.: Processes Controlling the Composition and Abundance of Arctic Aerosol, Rev. Geophys., 56, 621–671, https://doi.org/10.1029/2018RG000602, 2018.

Ziemba, L. D., Dibb, J. E., Griffin, R. J., Huey, L. G., and Beckman, P.: Observations of particle growth at a remote, Arctic site, Atmos. Environ., 44, 1649–1657, 2010.

6. Errata for Guy et al., 2021

Page 38, paragraph 3 '...where CCN are extremely low...' should be '...when CCN are extremely low...'

Page 39, paragraph 2 Ship based INP measurements collected by Welti et al., (2020) should also be referenced here. *Welti, A., Bigg, E. K., DeMott, P. J., Gong, X., Hartmann, M., Harvey, M., Henning, S., Herenz, P., Hill, T. C., Hornblow, B., et al.: Ship-based mea- surements of ice nuclei concentrations over the Arctic, Atlantic, Pacific and Southern oceans, Atmospheric Chemistry and Physics, 20, 15 191–15 206, 2020.*
'...due their relative...' should be 'due to their relative...'

Page 39, paragraph 6 '...three case studies where..' should be '...three case studies when..'

Page 41, paragraph 3 '...when wind speeds are < 1 m s^{-1} and when the wind direction...' should be '...when wind speeds are < 1 m s^{-1} or when the wind direction...'
'...confirmed that these criteria are sufficient to account for...' should be '...confirmed that these criteria are sufficiently accurate to account for...'

Page 42, paragraph 2 '...to positively identify BLSN events we use a 10 m wind speed threshold of 9 m s^{-1}.' should be '...to positively identify BLSN events we use a 10 m (1 minutely mean) wind speed threshold of 9 m s^{-1}.'

Page 42, paragraph 4 '..linear decay constants based on a user input particle mean diameter, density, water, and ice nucleation efficiency.' should be '..linear decay constants based on a user specified particle characteristics (mean particle diameter and density, and nucleation efficiency). '100 m a.s.l.' should be '100 m a.g.l.'

Page 43, paragraph 1 'In both cases deposition acts to...' should be 'Deposition (both wet and dry) acts to...'

Page 46, paragraph 1 '...occasions where...' and 'events where...' should be '...occasions when...' and 'events when...'

Page 47, paragraph 2 'Siberia' should be 'Russia'

Page 54, paragraph 4 'Siberia' should be 'Russia'

Chapter 3.

Passive ground-based remote sensing of radiation fog

Published in *Atmospheric Measurement Techniques* (2022)

Atmos. Meas. Tech., 15, 5095–5115, 2022
https://doi.org/10.5194/amt-15-5095-2022

Atmospheric Measurement Techniques
Open Access
EGU

Passive ground-based remote sensing of radiation fog

Heather Guy[1,2], **David D. Turner**[3], **Von P. Walden**[4], **Ian M. Brooks**[2], **and Ryan R. Neely**[1,2]

[1]National Centre for Atmospheric Science, Leeds, UK
[2]School of Earth and Environment, University of Leeds, Leeds, UK
[3]Global Systems Laboratory, National Oceanic and Atmospheric Administration, Boulder, CO, USA
[4]Department of Civil and Environmental Engineering, Laboratory for Atmospheric Research, Washington State University, Pullman, WA, USA

Correspondence: Heather Guy (heather.guy@ncas.ac.uk)

Received: 10 January 2022 – Discussion started: 24 March 2022
Revised: 3 August 2022 – Accepted: 8 August 2022 – Published: 7 September 2022

Abstract. Accurate boundary layer temperature and humidity profiles are crucial for successful forecasting of fog, and accurate retrievals of liquid water path are important for understanding the climatological significance of fog. Passive ground-based remote sensing systems such as microwave radiometers (MWRs) and infrared spectrometers like the Atmospheric Emitted Radiance Interferometer (AERI), which measures spectrally resolved infrared radiation (3.3 to 19.2 µm), can retrieve both thermodynamic profiles and liquid water path. Both instruments are capable of long-term unattended operation and have the potential to support operational forecasting. Here we compare physical retrievals of boundary layer thermodynamic profiles and liquid water path during 12 cases of thin (LWP $< 40\,\mathrm{g\,m^{-2}}$) supercooled radiation fog from an MWR and an AERI collocated in central Greenland. We compare both sets of retrievals to in-situ measurements from radiosondes and surface-based temperature and humidity sensors. The retrievals based on AERI observations accurately capture shallow surface-based temperature inversions (0–10 m a.g.l.) with lapse rates of up to $-1.2\,^{\circ}\mathrm{C\,m^{-1}}$, whereas the strength of the surface-based temperature inversions retrieved from MWR observations alone are uncorrelated with in-situ measurements, highlighting the importance of constraining MWR thermodynamic profile retrievals with accurate surface meteorological data. The retrievals based on AERI observations detect fog onset (defined by a threshold in liquid water path) earlier than those based on MWR observations by 25 to 185 min. We propose that, due to the high sensitivity of the AERI instrument to near-surface temperature and small changes in liquid water path, the AERI (or an equivalent infrared spectrometer) could be a useful instrument for improving fog monitoring and nowcasting, particularly for cases of thin radiation fog under otherwise clear skies, which can have important radiative impacts at the surface.

1 Introduction

The socioeconomic and climatological impacts of fog are far reaching. The reduction in visibility associated with fog disrupts transportation, resulting in economic losses equivalent to those associated with tornadoes and severe storms (Gultepe et al., 2007). Poor visibility due to fog is the most impactful extreme weather event in Arctic maritime operations (Panahi et al., 2020) and the second largest contributor after adverse winds to weather-related accidents in aviation (Gultepe et al., 2019). Supercooled fog is particularly impactful, since the collision of supercooled liquid droplets with a cold surface can result in the formation of rime or glaze ice. The build-up of ice can damage structures and power transmission lines (Ducloux and Nygaard, 2018) and presents an additional safety hazard in both shipping and aviation (Cao et al., 2018; Panahi et al., 2020), making accurate forecasts of supercooled fog critical for risk mitigation. From a climatological perspective, fog is an important moisture source, particularly in arid regions, (e.g. Hachfeld and Jürgens, 2000), and impacts the surface energy budget by modifying radiant and turbulent energy transfers (Shupe and Intrieri, 2004; Beiderwieden et al., 2007; Anber et al., 2015). The hydrological and radiative impacts of fog are both directly related to fog duration and liquid water content, and so accurate monitoring

of the liquid water content of fog is vital for understanding the role of fog in local climate and hydrological cycles.

Fog forms when the near-surface air reaches saturation, resulting in the formation of liquid water droplets on condensation nuclei (e.g. Oke, 2002). The air can reach saturation either through cooling until it reaches the dew point or through a moistening process such as the evaporation of surface water/drizzle or moist air advection (Gultepe et al., 2007). The cooling of air near the surface can result from advection (either cold air advection or the advection of a warm air mass over a cooler surface), through orographic effects (i.e. the adiabatic cooling of air rising over topography or cold air pooling in valleys), or through direct radiative cooling of the surface. Fogs that primarily form through radiative cooling of the surface are known as radiation fogs and commonly form on clear evenings with light winds, where the net surface cooling is maximised through the reduction of direct solar heating and limited turbulent mixing of heat downward to the surface (e.g. Savijärvi, 2006). Due to the rapid cooling of the surface, the formation of radiation fog is associated with a surface temperature inversion, which can be extremely shallow, with most of the inversion often developing in the lowest 10 m above the surface (Hudson and Brandt, 2005; Price, 2011; Izett et al., 2019).

The onset of radiation fog in numerical weather prediction (NWP) models is particularly sensitive to the initial thermodynamic structure of the boundary layer (Steeneveld et al., 2014). Accurate representation of the boundary layer structure, particularly temperature and humidity profiles in the lowest 1 km a.g.l. and the development of the surface-based temperature inversion, is thus crucial for forecasting radiation fog (Steeneveld et al., 2014; Gultepe et al., 2007; Bergot et al., 2007; Tardif, 2007); however, NWP models often fail to reproduce the strong but shallow gradients associated with it (Martinet et al., 2020; Westerhuis and Fuhrer, 2021).

The assimilation of boundary layer thermodynamic profile measurements is one possibility for improving NWP forecasts of radiation fog. However, making continuous high-resolution observations of temperature and humidity profiles is challenging. Despite improvements in recent years, satellite retrievals of boundary layer profiles and fog characteristics remain insufficient due to their coarse vertical resolution (> 1 km) and poor spatial coverage (Wulfmeyer et al., 2015; Wu et al., 2015; Wilcox, 2017; Yi et al., 2019). Surface-based in-situ measurements are limited by a maximum height (usually less than 50 m), while radiosonde profiles are spatially and temporally sparse and resource intensive, and the development of a coordinated, unmanned aerial system profiling platform is still in its infancy (Jacob et al., 2018; McFarquhar et al., 2020). Active ground-based remote sensors, such as differential absorption lidars (DIALs), can produce accurate thermodynamic profiles with a high temporal resolution but have a typical lowest range gate of greater than 50 m, making them unsuitable for fog monitoring (Newsom et al., 2020; Stillwell et al., 2020; Turner and Lohnert, 2021).

In addition to thermodynamic profiles, accurate monitoring of liquid water content is important to understand the climatological and hydrological impacts of fog. One metric to describe the liquid water content is fog liquid water path (LWP), defined as the integral of liquid water content over the depth of the fog layer. LWP is directly related to visibility; for example, given a homogeneous, monodisperse fog with a depth of 100 m and a uniform droplet effective radius of 10 µm, increasing the LWP from 10 to 20 g m^{-2} corresponds to a reduction in horizontal visibility from 200 to 100 m (assuming a visible contrast threshold of 0.05; Bendix, 1995), highlighting the importance of accurate LWP retrievals for visibility nowcasting. The LWP of thin fogs (LWP < 40 g m^{-2}) is important from a climatological perspective, because both longwave and shortwave surface radiative fluxes become extremely sensitive to small changes in LWP (Turner et al., 2007). Although thin liquid clouds and fogs are common globally (Turner et al., 2007), they are especially important in the Arctic, where they dominate cloud radiative forcing of the surface (Shupe and Intrieri, 2004; Miller et al., 2015). Cloud LWP was a critical control on the exceptional Greenland Ice Sheet melt event of 2012 (Bennartz et al., 2013). At the highest point on the ice sheet, had the cloud LWP been 20 g m^{-2} higher than observed, the reduction in downwelling shortwave radiation would have prevented surface melt. Equally, had the LWP been 20 g m^{-2} lower, the reduction in downwelling longwave radiation would have prevented surface melt (Bennartz et al., 2013).

Ground-based microwave radiometers (MWRs) are passive sensors that measure downwelling radiation. Commercial MWRs for temperature and water vapour profiling typically operate 14–35 spectral channels at 22–31 GHz and 51–58 GHz and are sensitive to the lowest 6 km of the atmosphere (Löhnert and Maier, 2012; Blumberg et al., 2015). Because MWRs can retrieve continuous (< 10 s) boundary layer temperature and humidity profiles as well as LWP under both clear skies and non-precipitating clouds, they are frequently used for fog monitoring (e.g. Gultepe et al., 2009; Wærsted et al., 2017; Temimi et al., 2020; Martinet et al., 2020). Recent studies have demonstrated that the assimilation of MWR brightness temperatures into NWP models has the potential to improve forecasts of stable boundary layers and fog by correcting errors in the temperature profile in the lowest 500 m above the surface (Martinet et al., 2017, 2020). The success of these trials contributed to EUMETNET's recent decision to establish a homogeneous European network of MWRs by 2023 (Illingworth et al., 2019; Rüfenacht et al., 2021).

However, the maximum vertical resolution of boundary layer temperature profile retrievals from the MWR is 50 m at the surface, decreasing to 1.7 km at 1 km a.g.l. (Rose et al., 2005; Cadeddu et al., 2013), which is insufficient to resolve the shallow surface-based temperature inversions that often portend the onset of radiation fog (Price, 2011; Izett

et al., 2019). Although combining the MWR with active remote sensing instruments such as DIALs or radio acoustic sounding systems (RASS) can improve the vertical resolution of the temperature profile retrievals in the lowest 2 km of the atmosphere, these improvements do not extend down to the lowest 100 m a.g.l. due to the height of the lowest range gate of the active remote sensing instruments (Turner and Lohnert, 2021; Djalalova et al., 2022). In addition, large absolute uncertainties in LWP retrievals from the MWR ($\pm$12–25 g m^{-2}) result in large relative errors during thin fog (LWP $<$ 40 g m^{-2}; Turner, 2007; Marke et al., 2016). These errors can be reduced by combining the MWR data with measurements from infrared spectrometers (either with single or multiple channels) that are more sensitive to small amounts of liquid water (Marke et al., 2016).

One such infrared spectrometer is the Atmospheric Emitted Radiance Interferometer (AERI, Knuteson et al., 2004a), a passive remote sensing instrument that has greater sensitivity than MWRs to both changes in near-surface ($<$ 1 km) thermodynamic profiles (Blumberg et al., 2015; Turner and Lohnert, 2021) and small changes in LWP (for LWP $<$ 40 g m^{-2}, Turner, 2007; Marke et al., 2016). The AERI measures spectrally resolved downwelling infrared radiation between 3.3 and 19.2 µm. Because of the higher opacity at infrared wavelengths relative to the optical depths spanned by the MWR, the AERI can detect changes in the boundary layer thermodynamic profile at a finer vertical resolution and with greater accuracy than the MWR (Blumberg et al., 2015; Turner and Lohnert, 2021). The primary disadvantage is that the AERI is not sensitive to atmospheric properties above a cloud with a LWP $>\sim$ 40 g m^{-2}, for which the cloud is nearly opaque in the infrared. This means that retrievals of thermodynamic profiles above optically thick clouds are not possible, and retrievals below them are only possible if the cloud temperature and height are well characterised.

Although several studies have compared the performance of AERI and MWR retrievals of thermodynamic profiles and LWP under different conditions (Blumberg et al., 2015; Turner, 2007; Löhnert et al., 2009; Turner and Lohnert, 2021), none of these studies have included cases of fog. Fog is distinct from "cloudy scenes" in general because the LWP and changes in the thermodynamic profile that are relevant for fog development and lifetime are concentrated in the lowest layers ($<$ 100 m) above the surface. The goal of this study is to compare the performance of thermodynamic and LWP retrievals based on MWR and AERI observations during radiatively thin (LWP $<$ 40 g m^{-}2) fog events, with an emphasis on those aspects that are crucial for making accurate forecasts and understanding the climatic impact of fog: the representation of the thermodynamic profile in the lowest 1 km a.g.l., the detection of shallow surface-based temperature inversions, and accurate measurements of small changes in fog LWP.

We take advantage of the collocation of an MWR and an AERI alongside a large suite of supplementary instruments for monitoring atmospheric properties at Summit Station (Summit) in the centre of the Greenland Ice Sheet (Shupe et al., 2013). The surface air temperature at Summit approaches 0 °C only in exceptional circumstances (NSIDC, 2021), and supercooled radiation fog is common, occurring over 10 % of the time in the summer (Cox et al., 2019). Although usually shallow, summer-time radiation fog in central Greenland is particularly impactful, because it forms during the coldest part of the day and has a net warming effect at the surface, effectively dampening the diurnal temperature cycle with the potential to precondition the ice sheet surface for melt (Solomon et al., 2017; Cox et al., 2019). Aviation operations at Summit are also frequently disrupted by the low visibility.

Using a consistent physical retrieval algorithm for both instruments, we compare the suitability of the MWR and the AERI for retrieving near-surface thermodynamic profiles and LWP during supercooled radiation fog events at Summit in the summer of 2019. We evaluate the retrieved thermodynamic profiles against radiosonde profiles and in-situ temperature and humidity measurements and assess the ability of each set of retrievals to detect the increase in LWP associated with the onset of fog. Henceforth in this study, 'fog' will specifically pertain to supercooled radiation fog unless otherwise specified. The applicability of the results of this study to other (less extreme) environments and to different types of fog is discussed in Sect. 4.

2 Methods

2.1 Measurement site and instrumentation

The Integrated Characterization of Energy, Clouds, Atmospheric state and Precipitation at Summit (ICECAPS) project collected continuous observations of the atmosphere above Summit from 2010 to 2021 (Shupe et al., 2013). At the highest point of the Greenland Ice Sheet (−38.45° E, 72.58° N, 3250 m a.s.l.), the atmosphere above Summit is extremely dry, and temperatures are rarely above freezing (Shupe et al., 2013). The ice sheet surface is homogeneous in all directions so that the atmospheric conditions at Summit are minimally influenced by local topography. During the summer (JJAS), freezing fog (defined as fog that reduces visibility to less than 1000 m) was reported by on-site observers 10 % of the time (2010–2020). These fogs can occur when surface temperatures are as low as −35 °C and almost always contain supercooled liquid droplets (Cox et al., 2019), presumably due to a lack of ice-nucleating particles (near-surface aerosol concentrations at Summit are exceptionally low, Guy et al., 2021).

The Aerosol Cloud Experiment (ACE) was added to the ICECAPS project in 2019 and included the addition of temperature and humidity sensors and sonic anemometers at four levels on a 15 m tower for high resolution monitoring of the near-surface turbulent and thermodynamic structure (Guy

et al., 2021). For this study, we focus on fog events during the summer of 2019 for which time the multi-level temperature data from the tower are available. Figure 1 shows the experimental setup of the MWR and AERI at Summit, and Table 1 provides details of all the ICECAPS-ACE instrumentation used in this study.

We use the tower-mounted temperature probes (Vaisala HMP155, installed in aspirated shields) as "true" reference points to assess the performance of the surface temperature retrievals from the MWR and AERI. The instrument uncertainty for the HMP155 is $< \pm 0.3\,^{\circ}\mathrm{C}$. For this study, we define the "surface" as the height of the raised platform photographed in Fig. 1, where both the AERI and MWR windows are situated. This surface is aligned with the HMP155 sensor mounted on the tower at 4 m above the snow surface; measurements from this sensor are henceforth referred to as surface temperature. Measurements from the HMP155 sensor located 10 m higher on the tower are compared to the 10 m thermodynamic retrievals. The same height adjustment is applied to the radiosonde profiles prior to comparison (which are launched approximately 3 m below the platform "surface" or 1 m above the snow surface). The uncertainty in the radiosonde measurements is $\pm 4\,\%$ relative humidity and $\pm 0.3\,^{\circ}\mathrm{C}$ (Jensen et al., 2016).

2.1.1 The AERI

The polar AERI (PAERI) at Summit was designed and manufactured by personnel at the Space Science and Engineering Center (SSEC) at the University of Wisconsin-Madison and is one of the original AERIs developed for the US Department of Energy's Atmospheric Radiation Measurement (ARM) program (Turner et al., 2016). It was built and calibrated according to specifications in Knuteson et al. (2004a) and adheres to the performance requirements of radiometric calibration ($< 1\,\%$, 3σ, of ambient radiance) and spectral calibration (1.5 ppm, 1σ), as explained by Knuteson et al. (2004b). The PAERI measures downwelling spectral infrared radiance between 3 and 19 µm at an unapodized spectral resolution of about $0.48\,\mathrm{cm}^{-1}$ (see Table 3 from Knuteson et al., 2004a). The PAERI operates on a continuous measurement schedule where it obtains views of the hot and ambient calibration sources followed by eight consecutive views of the sky at zenith. The sequence is repeated so that each set of eight sky views is bracketed in time by views of both calibration sources; these sources are then used to calibrate the eight sky views. Each of the spectral measurements is a "co-addition" of six interferometric scans. Each complete, calibrated measurement sequence takes approximately 3 min with the sky views separated by approximately 15–20 s. This yields more than 3300 infrared spectra each day. Quality control is then applied to each of the spectra by eliminating those that have instrument parameters outside of acceptable limits; the acceptable limits were set by SSEC personnel. The important instrument parameters are the responsivities and noise-equivalent radiances of the hot blackbody calibration source measured by both of the PAERI detectors (InSb and MCT) plus the electric current and temperature of the Stirling cooler that maintains the detectors at 77 K. In actuality, the instrument responsivities are a very sensitive indicator of the PAERI's health, and most unusable spectra are eliminated by low responsivity associated with small amounts of snow on the PAERI scene mirror. Finally, the remaining calibrated sky views are subjected to noise filtering using the technique described by Antonelli et al. (2004) and Turner et al. (2006).

2.1.2 The MWR

The MWR at Summit, a Humidity and Temperature Profiler (HATPRO) from Radiometer Physics GmbH, observed downwelling radiation in all 14 channels simultaneously every 4 s (see Table 2 for channel details). After collecting 600 zenith views, the HATPRO collected elevation scans at 5.4, 10.2, 16.2, 19.2, 23.4, 30.0, and 42.0 on either side of zenith. These elevation scans were used to both evaluate and update the calibration accuracy of the K-band channels (i.e. the low opacity channels between 22 and 32 GHz) using the tip-curve technique (Han, 2000). The more opaque V-band channels (i.e. in the 51–58 GHz band) were calibrated twice yearly using an external liquid nitrogen target; the most recent calibration used for this analysis was performed on 1 May 2019. Both the tip curves and the liquid nitrogen views are used to determine the effective temperature of the internal noise diode, which is used regularly when viewing the internal blackbody to establish two different reference values (i.e. one ambient blackbody view with the noise diode off and one "hot" blackbody view with the noise diode on). These internal blackbody views, which are done every minute, are used to continually update the gain of the radiometer and convert the observed signal to brightness temperature (T_b) following the calibration principles outlined in Liljegren (2000).

However, since the liquid nitrogen calibrations are performed infrequently, any drift in the effective temperature of the noise diode in the V-band channels will result in a calibration bias. Using a radiative transfer model (the monochromatic MonoRTM, Clough et al., 2005) with radiosonde profiles as input, we have determined a T_b offset that is subtracted from the observed brightness temperatures. The bias correction and the impact of not applying this correction prior to performing the thermodynamic retrievals are discussed in Appendix A.

2.2 Case study identification

For forecasting and nowcasting purposes, fog is usually defined by a threshold in horizontal visibility (typically $<$ 1000 m), which has important implications from a safety perspective (Gultepe et al., 2007). However, limiting the definition of fogs to those that reduce visibility to < 1000 m encourages thinner fogs (or mists) to be ignored or incor-

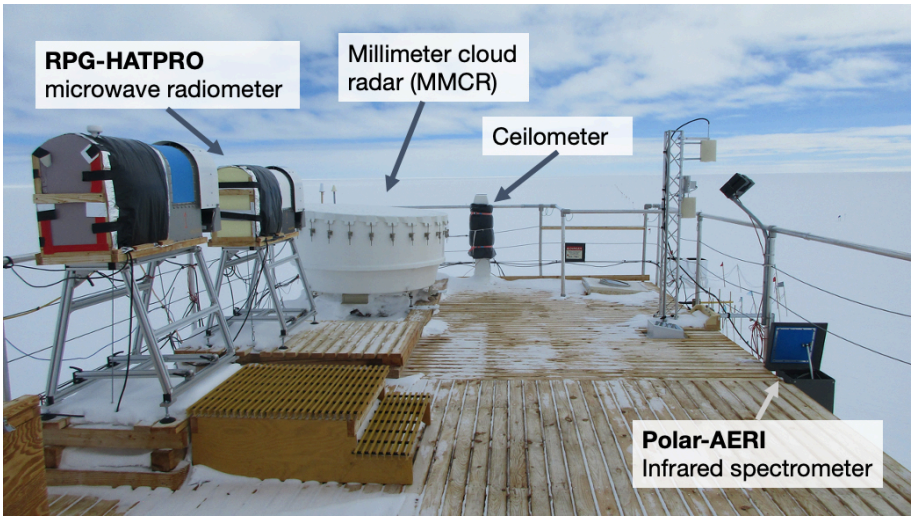

Figure 1. Key ICECAPS-ACE instrumentation at Summit Station (photographed by the author, 16 May 2019).

Table 1. Overview of instrumentation used in this study. All instruments were installed at Summit as part of the ICECAPS project (Shupe et al., 2013) or ICECAPS-ACE project (Guy et al., 2021).

Title	Instrument	Key specifications	References
PAERI	Polar Atmospheric Emitted Radiance Interferometer	530–3000 cm^{-1} (3–19 µm), 1 cm^{-1} res. < 1 min time res.	Knuteson et al. (2004a) Walden et al. (2005)
HATPRO MWR	RGP Humidity and Temperature Profiler, microwave radiometer	Frequencies: 7 channels 22-32 GHz, 7 channels 51–58 GHz, 2–4 s time resolution.	Rose et al. (2005)
MMCR	Millimetre cloud radar	Ka band (35 GHz), 8 mm wavelength, 45 m vertical res. 2 s time res.	Moran et al. (1998)
Ceilometer	Vaisala laser ceilometer CT25K	905 nm wavelength. 15 m vertical res., 15 s time res.	Münkel et al. (2006)
POSS	Precipitation Occurrence Sensor System	X-band radar (10.5 GHz) 1 min time res. Single volume near surface.	Sheppard and Joe (2008)
Temperature and humidity probes	Vaisala HMP155, aspirated	1 min averages at 0 and 10 m.	Guy et al. (2020)
Radiosondes	Vaisala RS41-SG	Launched at 12:00 and 00:00 UTC daily.	Jensen et al. (2016)

rectly classified as clear-sky events. Being able to accurately measure thinner fogs is extremely important because (a) they form the precursor to thick fog, (b) they modify the surface moisture, aerosol, temperature, and radiative structure that might impact fog development further down the line (Haeffelin et al., 2013), and (c) they can have important radiative and climatological impacts even without developing into a thick fog (Cox et al., 2019; Hachfeld and Jürgens, 2000). Because both the MWR and AERI are directly sensitive to the radiative impact of fog (as opposed to visibility), for the purpose of this study, we define fog as the presence of near-surface liquid water that has a detectable radiative impact. Radiation fogs typically form under clear skies; as such, we only consider cases of fog under otherwise clear skies, which allows us to be certain that the LWP retrievals are a measure of fog LWP alone. The applicability of the results of this study to other types of fog is discussed in Sect. 4.

To identify case studies of radiation fog under otherwise clear skies, we only considered times when there were no clouds detected by the MMCR, which has a lowest range

Table 2. Centre frequencies, assumed noise level, whether the elevation scans for the frequency are included in the observation vector, and the bias offset applied to the observations for the HATPRO MWR at Summit.

Frequency GHz	Noise level K	Used in elev. scan	Bias offset K
22.24	0.30	No	0.23
23.04	0.30	No	0.08
23.84	0.30	No	0.09
25.44	0.30	No	0.00
26.24	0.30	No	0.12
27.84	0.30	No	0.17
31.40	0.30	No	0.15
51.26	0.80	No	2.02
52.28	0.80	No	2.15
53.86	0.50	No	2.03
54.94	0.30	Yes	−0.45
56.66	0.30	Yes	−0.32
57.30	0.25	Yes	−0.12
58.00	0.25	Yes	−0.11

gate close to 200 m a.g.l. and is therefore insensitive to fog, and when there was no precipitation detected by the POSS, which is particularly sensitive to ice crystals. Of the times that these criteria were met, fog was provisionally identified when the 962 cm^{-1} downwelling radiance measured by the AERI was greater than a threshold of 1.7 RU (radiance units, 1 RU = 1 mW m^{-2} sr^{-1} cm^{-1}). In the extremely dry atmosphere over Summit, the 962 cm^{-1} microwindow is almost completely transparent under clear skies and is therefore particularly sensitive to the presence of clouds (e.g. Cox et al., 2012). The threshold value of 1.7 RU was 3 standard deviations above the mean 962 cm^{-1} radiance during 179 verified clear-sky hours between June and September 2019 and therefore identified when the AERI window was obscured by cloud/fog with a detectable radiative impact. Ambiguous cases when there was evidence that something other than fog may have caused the 962 cm^{-1} radiance increase, such as clear-sky ice crystal precipitation, high cirrus clouds, or the plume from the station generator, were removed based on the observer log and photographs. Table 3 details the 12 cases that met the criteria above and were selected for the intercomparison. In each case, the fog formed in late evening or early morning and usually dissipated by midday, as is characteristic of radiation fog (Fig. 2). Note that for 11 of these cases, there was no cloud base height detected by the ceilometer during the event, indicating that the events were indeed fog as opposed to low cloud. The only exception is for case ID 11, during which the ceilometer detected a cloud base between 52 and 105 m intermittently between periods of obscured vertical visibility.

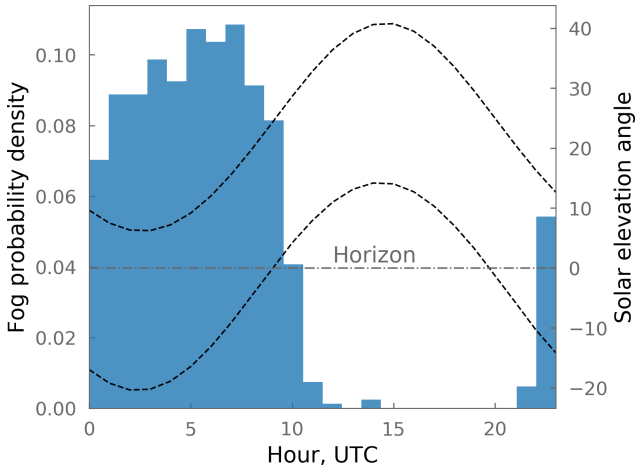

Figure 2. Diurnal distribution of fog during the summer 2019 case studies listed in Table 3 (blue bars). Black dashed lines show the maximum and minimum solar elevation angles (June–September 2019). Local time at Summit is UTC−3 h.

2.3 Retrieval methodology

We retrieve boundary layer thermodynamic profiles (temperature, T, and water vapour mixing ratio, wv) and LWP at a 5 min temporal resolution using the TROPoe iterative optimal estimation physical retrieval algorithm that is detailed in Turner and Lohnert (2021) and Turner and Blumberg (2019). TROPoe uses a forward model to calculate the observation vector from the current state vector, where the state vector is the retrieved thermodynamic profile and LWP, and the observation vector is the downwelling radiance observed by either the polar AERI or HATPRO MWR. Note that the observation vector from the MWR includes data from the elevation scans at 10.2, 16.2, and 19.2 degrees for the four most opaque V-band channels; including elevation scans in the retrieval has been shown to increase the accuracy of the retrieved temperature profile (Crewell and Lohnert, 2007). The forward models are line-by-line radiative transfer models; the LBLRTM version 12.1 (Clough and Iacono, 1995) simulates the AERI spectral radiances, and the monochromatic MonoRTM (Clough et al., 2005) simulates the MWR radiances. Note that the latter uses the improved temperature-dependent liquid water absorption coefficients (Turner et al., 2016). The state vector is incrementally adjusted to minimise the difference between the forward model calculation and the observation vector until the change between successive iterations is less than the uncertainty in the current state vector (Rodgers, 2000).

Due to the limited vertical resolution of the MWR, operational retrievals of thermodynamic profiles from MWRs are typically also constrained by an in-situ measurement of surface temperature, usually from a sensor that is integrated with the MWR (e.g. Cimini et al., 2015). For this study, we run TROPoe in three physically consistent configurations: once

Table 3. Details of the 12 radiation fog cases used in this study, including mean temperatures (T) and water vapour mixing ratios (wv). Note that the minimum visibility comes from observer reports at 00:00, 12:00, and 18:00 UTC and may not represent the minimum visibility outside of these times. Values where data were not available are indicated by NA – for example, when the observer did not log a visibility within the fog time frame or when the ceilometer did not report an obscured vertical visibility. Local time is UTC−3 h.

ID	Case start Date, time UTC, 2019	Case end Date, time UTC, 2019	Duration (h)	Mean surface T (°C)	Mean surface wv ($g\,kg^{-1}$)	Min visibility observer log. (m)	Min ceilometer vertical visibility (m)
1	8 Jun, 03:30	8 Jun, 05:50	2.3	−17	1.3	NA	30
2	12 Jun, 02:55	12 Jun, 10:30	7.6	−8.9	2.7	NA	30
3	13 Jul, 23:25	14 Jul, 04:30	5.1	−21	0.93	1600	30
4	15 Jul, 23:10	16 Jul, 10:30	11	−19	1.0	400	30
5	31 Jul, 23:25	1 Aug, 04:35	5.2	−8.6	2.7	400	25
6	1 Aug, 22:00	2 Aug, 14:40	17	−12	2.0	800	20
7	4 Aug, 06:35	4 Aug, 08:15	1.7	−17	1.2	NA	NA
8	4 Aug, 22:40	5 Aug, 11:50	13	−18	1.2	400	15
9	6 Aug, 01:05	6 Aug, 10:00	8.9	−21	0.82	NA	30
10	14 Aug, 23:05	15 Aug, 08:00	8.9	−27	0.49	3200	43
11	5 Sep, 04:30	5 Sep, 08:35	4.1	−25	0.61	NA	30
12	30 Sep, 03:30	30 Sep, 11:05	7.6	−28	0.46	NA	NA

using only the PAERI radiances as the observation vector (as in Turner and Löhnert, 2014, henceforth named AERIoe), once using only the microwave brightness temperature observations from the HATPRO MWR (as in Löhnert et al., 2009) to provide a direct comparison of the relative sensitivity of the two instruments (henceforth named MWRoe), and lastly using the same configuration as the MWRoe but this time being additionally constrained by the in-situ surface temperature and water vapour observations from the HMP155, as it would be in an operational setting (henceforth named MWRoe-sfc).

Thermodynamic retrieval from passive spectral radiance observations is an ill-posed problem; hence the optimal-estimation retrieval is necessarily constrained by an a priori probability density function (the prior) that provides the first guess state vector that stabilises the retrieval (Turner and Löhnert, 2014). Typically, a location-specific prior can be derived from a database of historical observations (i.e. from radiosonde profiles) at or near the location of interest. The prior for Summit is computed from 1756 summer radiosonde launches (2010–2018). However, due to the rapid warming in the Arctic (e.g. Koenigk et al., 2020), this does not encapsulate the exceptionally warm and moist conditions at Summit during the summer of 2019 (NSIDC, 2019). To allow the retrievals more flexibility to account for the exceptional conditions, we have re-centred the prior using the mean of the three radiosondes closest to the retrieval date (whilst conserving relative humidity) and increased the wv variance in the prior by a factor of 4 at the surface (decreasing to 0 by 1 km a.g.l.).

Previous studies have used cloud base height (CBH) derived from a collocated ceilometer as an additional constraint on the retrieval, which allows the retrieval of below-cloud thermodynamic profiles from the AERI in the presence of thick clouds (Turner et al., 2007; Turner and Löhnert, 2014; Blumberg et al., 2015). Because we focus on radiation fogs under otherwise clear skies – which are, by definition, based at the surface – we initially assumed that the CBH is 5 m a.g.l. in all cases. However, large temperature biases (> 5 K) in the AERIoe retrievals during fog illustrated that the TROPoe is highly sensitive to the CBH assumption when using AERI data as an input (see Sect. 3.1). For the final retrievals, we used CBH from the ceilometer to constrain the retrieval if the ceilometer detected a cloud base within 10 min of the retrieval time; if the ceilometer reported obscured vertical visibility, then the detected vertical visibility height (Morris, 2016) was input as the CBH. If neither of these situations occurred, the CBH assumption defaulted to 5 m a.g.l. The sensitivity of the retrievals to this choice is discussed further in Sect. 3.1. We ran all retrievals for up to 3 h before and after each fog event to encapsulate the atmospheric conditions on either side of radiation fog formation. The retrieval algorithm outputs 1σ uncertainties for all variables that incorporate the random error from the observations, the correlated error propagated from the prior, and the sensitivity of the forward model. Errors related to the CBH assumption or phase assumption (when only liquid water is considered) are not included, and we discuss these below in Sects. 3.1 and 4.

2.4 Evaluation metrics

To evaluate the three TROPoe retrieval configurations (AERIoe, MWRoe, and MWRoe-sfc), we focus on three aspects that are crucial for making accurate fog forecasts with NWP models, for visibility nowcasting, and for understanding the climatic impact of fog:

1. accurate representation of the structure of the temperature and humidity profile in the lowest 1 km a.g.l.

2. detection of the presence and strength of shallow surface-based temperature inversions that typically portend the formation of radiation fog

3. detection of the initial increase in LWP that signifies the onset of fog and a reduction in horizontal visibility.

To evaluate the accuracy of the temperature and humidity profile retrievals in the lowest 1 km a.g.l., we assess the performance of the MWRoe-sfc and AERIoe against 14 coincident radiosonde profiles by evaluating the mean bias and spread between the radiosonde profiles (truth) and the retrievals. We use modified Taylor diagrams (Taylor, 2001; Turner and Löhnert, 2014) to assess how well the retrieved profiles capture the shape of the true profiles by considering the Pearson's correlation coefficient and the ratio of the standard deviation of the retrieval to that of the truth profile. These results allow for a direct comparison with Blumberg et al. (2015), who compare TROPoe retrievals based on MWR and AERI observations to a larger number of radiosonde profiles (127) in southwestern Germany (but only consider clear-sky days or clouds with bases > 500 m a.g.l.).

To evaluate the ability of each retrieval to detect the occurrence and strength of surface-based temperature inversions, we compare the retrieved surface (0 m) and 10 m temperatures with measurements from in-situ temperature sensors (see Sect. 2.1). We define the inversion "strength" as the 10–0 m temperature and evaluate the Pearson's correlation coefficients and root-mean-squared error (RMSE) between the retrieved values and the "truth" (the in-situ temperature sensors). Although we are limited by a maximum sensor height on the tower, we expect the 10–0 m temperature difference to be a good indicator of whether or not the retrieval captures the surface-based temperature inversion, since most of the inversion during radiation fog often occurs in the lowest 10 m a.g.l. (Price, 2011; Izett et al., 2019). We also compare the retrieved inversion strength over a deeper layer (100–10 m) with the 14 coincident radiosonde profiles.

Finally, in the absence of an independent method of determining LWP, we evaluate the ability of each retrieval to detect the initial increase in LWP, which is defined in this study as an indicator of fog formation that might lead to visibility reduction, with "fog onset" being defined as the point at which the retrieved LWP minus 2σ uncertainty (which is directly computed by TROPoe) increases above $0.1\,\mathrm{g\,m^{-2}}$ for at least 10 min. We then compare the difference in fog onset detection time between the MWRoe and the AERIoe for each case study. We use the ceilometer range-corrected attenuated backscatter as an independent indicator of fog onset time. This methodology allows us to compare the sensitivity of the two sets of retrievals to small increases in liquid water that can begin to reduce visibility and impact radiative energy fluxes at the surface.

3 Results

3.1 Retrieval performance and sensitivity to cloud base height assumption

All 2045 retrievals from each configuration of TROPoe converged, meaning that the retrieval algorithm was able to find a solution within the maximum number of iterations. The mean RMSE between the final forward model calculation and the observed PAERI radiance across all AERIoe retrievals was 0.54 ± 0.09 RU, which is of the order of the instrument noise level (Blumberg et al., 2015). For the MWRoe retrievals the mean RMSE between the final forward model calculation and the MWR brightness temperatures was 0.38 ± 0.12 K, again within the instrument noise level (Rose et al., 2005). The MWRoe and MWRoe-sfc are comparable in terms of RMSE, liquid water path retrieval and thermodynamic profile retrievals above 100 m a.g.l., so we only discuss the difference between the MWRoe and MWRoe-sfc when we consider the ability of each retrieval configuration to capture the strong surface-based temperature inversions associated with radiation fog in Sect. 3.3.

The AERIoe retrievals were very sensitive to the cloud base height (CBH) assumption. Because we are only considering cases of radiation fog under otherwise clear skies, the first iteration of retrievals assumed that, if liquid water was detected, the cloud base height was 5 m a.g.l., removing the requirement for additional instrumentation to detect CBH. Figure 3a demonstrates that, under this assumption, the AERIoe retrieved unrealistic temperature profiles in some cases when the fog was optically thick (i.e. ceilometer is obscured) or when the ceilometer detected a cloud with a base close to 1300 m a.g.l. prior to the start of the fog event. The unrealistic temperature profiles manifest as exceptionally warm temperatures just above the surface, indicated by red colours in Fig. 3.

Previous AERIoe algorithms have used the ceilometer "first cloud base height field" (an output of the Vaisala proprietary software) to estimate CBH (Turner and Löhnert, 2014; Blumberg et al., 2015). Using this assumption rather than simply assuming the CBH to be 5 m a.g.l. reduced the temperature profile artefacts in some but not all cases (Fig. 3b). The ceilometer software also outputs a vertical visibility field (described in Morris, 2016) when the extinction profile is such that the atmosphere is obscured but no distinct cloud base can be determined, as often happens in the case of thick fog. The remaining artefacts in the example case study occur when the ceilometer reports a vertical visibility value (Fig. 3b). When we used the vertical visibility field in addition to the first cloud base height field to provide the CBH assumption in the AERIoe retrieval, the remaining artefacts were removed (Fig. 3c).

Even if the fog is reducing visibility at the surface, the cloud base height is the height at which the fog becomes optically thick to the PAERI, which is similar to when it

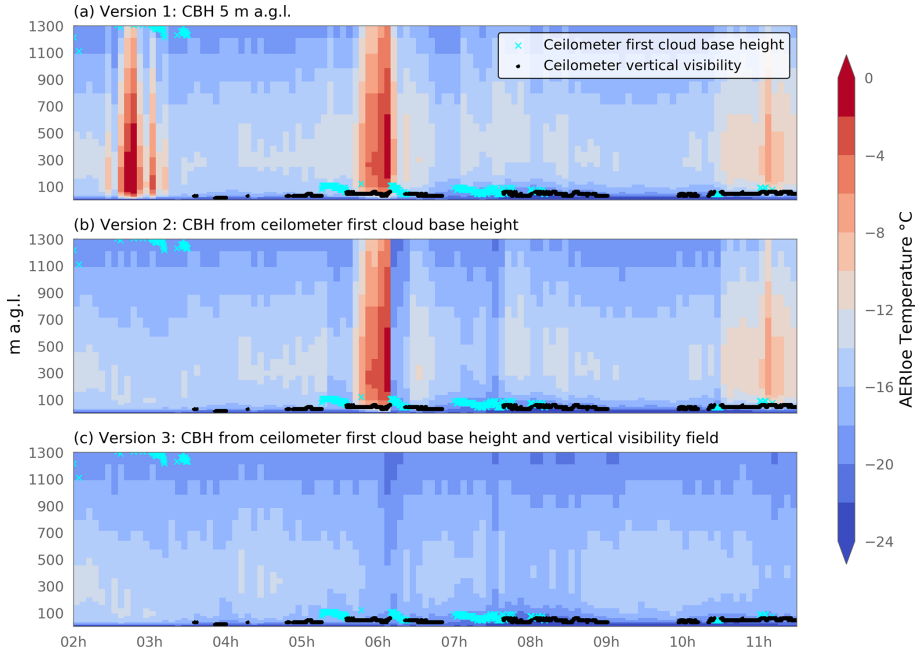

Figure 3. Temperature profiles during the 5 September case study from three iterations of the AERIoe retrieval using different CBH assumptions. The ceilometer first cloud base height field is overlaid as cyan crosses, and the vertical visibility field is overlaid as black circles. **(a)** Assumed CBH was 5 m a.g.l. any time LWP > 0; **(b)** assumed CBH was set to the ceilometer first cloud base height if the ceilometer detected a cloud within the 10 min centred on the retrieval time, otherwise 5 m a.g.l.; **(c)** as in **(b)** except if the ceilometer reported "obscured" the CBH was set equal to the ceilometer maximum vertical visibility field.

becomes optically thick for the ceilometer (which uses radiation in the near-infrared, 905 nm). Figure 3 shows that a difference in CBH of just 30 m can make a significant difference to the retrieval when the cloud is close to the surface, demonstrating that accurate CBH measurements are a necessary input to the AERIoe for retrieving thermodynamic profiles in the presence of fog or near-surface clouds. In contrast, the MWRoe was not sensitive to the CBH assumption, because clouds are markedly more transparent at microwave frequencies. For the remainder of this study, all retrieval configurations derive CBH from both the first cloud base height and the vertical visibility field of the ceilometer.

3.2 Performance of retrieved thermodynamic profiles in the lowest 1 km a.g.l.

The AERIoe temperature profiles (0–1 km a.g.l.) compared extremely well to the 14 radiosonde profiles considered, with a mean bias of $-0.43\,^{\circ}\mathrm{C}$ and a mean RMSE of $1.0\,^{\circ}\mathrm{C}$ (Fig. 4a). The MWRoe temperature profiles exhibited a vertically consistent negative bias compared to the radiosonde profiles, with an average value of $-1.5\,^{\circ}\mathrm{C}$ and an average RMSE of $1.7\,^{\circ}\mathrm{C}$ (Fig. 4a). Although investigating the source of the negative bias in the MWRoe temperature profile is outside the scope of this study, such systematic biases can often be corrected for, and the similar spread in bias magnitude between the AERIoe and the MWRoe temperature retrievals imply that the performance of the two sets of retrievals would be similar after an additional bias correction (Fig. 4a). For both sets of retrievals, the temperature RMSE is largest in the lowest 50 m a.g.l., where it approaches $2.0\,^{\circ}\mathrm{C}$ (Fig. 4a); this is also the case for the MWRoe-sfc, which looks qualitatively similar (not shown).

For water vapour, the performance of the AERIoe and MWRoe retrievals compared to the radiosonde profiles was very similar (Fig. 4b). Neither set of retrievals exhibited a mean bias, and the RMSE of the AERIoe retrievals was slightly smaller than the MWRoe up to 800 m a.g.l., with a mean value of $0.39\,\mathrm{g\,kg^{-1}}$ (compared to $0.44\,\mathrm{g\,kg^{-1}}$ for the MWRoe).

Figure 4c and d show that both sets of temperature profile retrievals are better correlated with the radiosonde profiles ($r > 0.98$, Fig. 4c,) than the water vapour profile retrievals, which in some cases have correlation coefficients < 0.7 (Fig. 4d), and the spread in the standard deviation ratio is much smaller for the temperature retrievals (0.9–1.2) than for the water vapour profile retrievals (0.6–1.3). The AERIoe retrievals (for both temperature and water vapour) have a similar spread in correlation coefficients and standard deviation ratios than the MWRoe retrievals, indicating that the performance of the two retrievals was comparable across this subset of profiles.

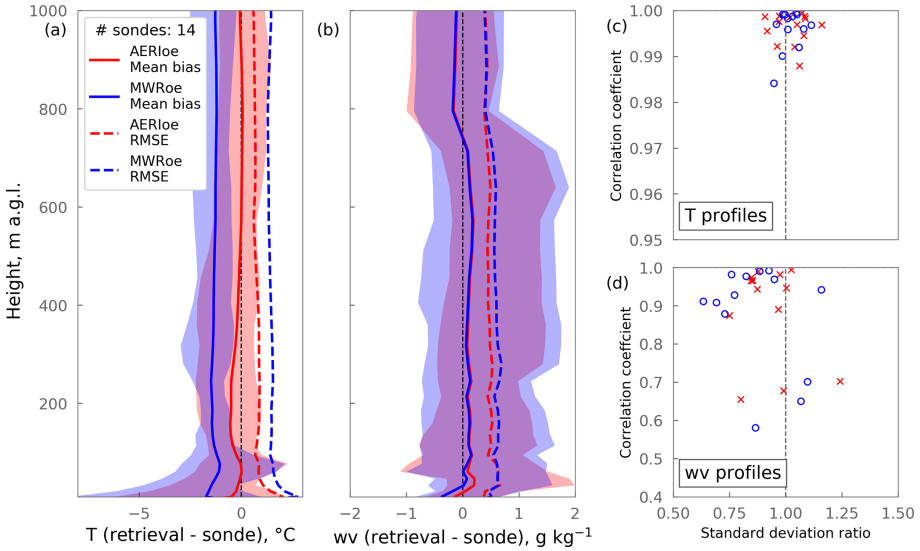

Figure 4. Comparison between retrieved thermodynamic profiles and the 14 coincident radiosonde profiles in the lowest 1 km a.g.l. **(a)** The temperature and **(b)** and water vapour bias (retrieval – radiosonde) for AERIoe retrievals (red) and MWRoe retrievals (blue); the solid line shows the mean bias and the shaded represents the range. Dashed lines show the root-mean-squared error (RMSE). **(c)** The temperature and **(d)** water-vapour-modified Taylor plots showing the relationship between the correlation coefficient and standard deviation ratio for each retrieval/radiosonde pair ([1,1] represents a perfect score) for the AERIoe retrievals (red) and the MWRoe retrievals (blue).

3.3 Characterisation of shallow surface-based inversions

The AERIoe temperature retrievals at 0 and 10 m a.g.l. are equally well correlated with observations ($r = 0.99$, RMSE $= 1.1\,°C$), indicating that the AERIoe captures vertical temperature gradients in the lowest 10 m of the atmosphere well and retrieves surface temperatures with consistently high accuracy (Fig. 5). In comparison, the MWRoe retrievals perform worse than the AERIoe at both heights, with $r = 0.86$, RMSE $= 4.2\,°C$ at 0 m, and $r = 0.95$, RMSE $= 2.1\,°C$ at 10 m (Fig. 5). Notably, the performance of the MWRoe is worst at 0 m, where the MWRoe typically has a warm bias at colder temperatures (72 % of the time when $T < -7\,°C$) and a cold bias at warmer temperatures (93 % of the time when $T > -7\,°C$). This bias reduced at 10 m, implying that the temperature lapse rate between 0 and 10 m a.g.l. is often incorrect in the MWRoe retrieval (Fig. 5).

For the MWRoe-sfc, which includes the surface temperature as an additional constraint in the retrieval, the correlation with in-situ surface temperature measurement is perfect, suggesting that very little additional variability is introduced by the microwave radiance measurements. Despite this, the 10 m temperature retrievals from the MWRoe-sfc perform only marginally better than those of the MWRoe compared to the in-situ measurements and not as well as the AERIoe, which did not have the advantage of the extra information from the in-situ surface temperature probe (Fig. 5). This suggests that constraining the retrieval by the in-situ surface temperature does not translate to improvements in the temperature profile retrieval above that level.

Figure 6a confirms that the MWRoe is not able to capture the 0–10 m temperature lapse rate by demonstrating that there is no correlation between the measured surface-inversion strength (10–0 m T) and that retrieved by the MWRoe. In fact, the 10–0 m lapse rate is essentially constant in the MWRoe, implying that retrieved temperatures at 0 and 10 m are highly correlated. In contrast, the AERIoe surface-inversion strength is well correlated with in-situ measurements ($r = 0.80$) with an RMSE of 1.9 °C (Fig. 6a), demonstrating that the AERIoe can accurately retrieve shallow surface temperature inversions with lapse rates of up to $-1.2\,°C\,m^{-1}$. When the in-situ surface temperatures are used to constrain the MWR retrieval (in the MWRoe-sfc), the ability of the retrieval to capture the shallow temperature inversions is considerably improved (Fig. 6a). Note that the correlation between the MWRoe-sfc near-surface temperature inversion and the in-situ measurements in Fig. 6a is not a fair assessment of performance, since the retrieval results are not independent from the in-situ measurements. Nonetheless, it highlights the importance of using accurate surface temperature measurements to constrain MWR temperature retrievals.

The radiosonde profiles provide an alternative independent measure of surface-inversion strength, allowing the comparison of the ability of each retrieval configuration to capture surface temperature inversions over a deeper layer. Figure 6b compares the 100–10 m retrieved inversion strength with that measured by the 14 coincident radiosonde profiles. Over this depth, the RMSE of the AERIoe and the MWRoe-

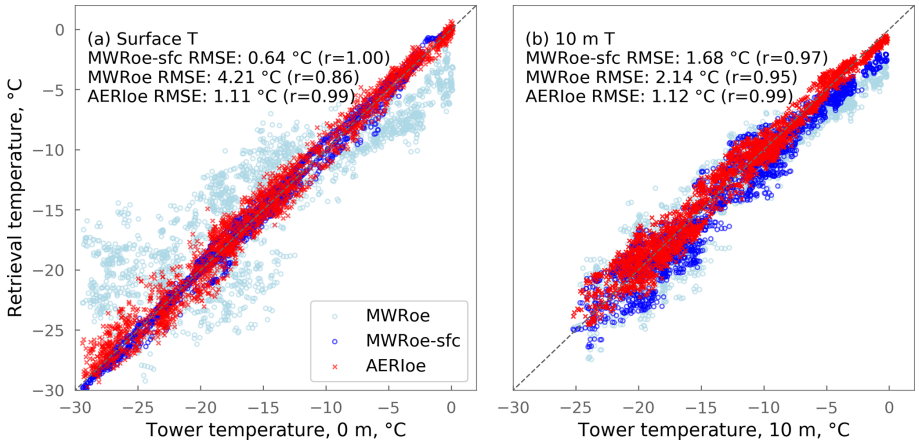

Figure 5. Retrieved temperature versus in-situ measurements from the tower at the surface **(a)** and 10 m **(b)**. The MWRoe retrievals are plotted as pale blue circles, the AERIoe retrievals as red crosses, and the MWRoe retrievals that are constrained by the surface temperature (MWRoe-sfc) are dark blue circles. The Pearson's correlation coefficient (r) and root-mean-squared error (RMSE) between each set of retrievals and the tower measurements are included on the figure. All correlations are significant at the 99 % confidence level. The dashed grey line represents perfect agreement.

sfc are comparable to the values for the 10–0 m comparison (1.65 and 1.83 °C m^{-1} respectively), but the MWRoe RMSE remains much larger (2.22 °C m^{-1}), demonstrating that the MWRoe alone is not capable of accurate retrievals of surface temperature inversions even in this deeper layer. Only the AERIoe retrievals in this case are significantly correlated ($r = 0.46$) with the radiosonde measurements, although the small number of radiosondes available for comparison makes it difficult to draw robust conclusions from this result. Klein et al. (2015) compared AERI-derived lapse rate 100–10 m against more than 200 radiosondes in Oklahoma (southern US) and found very good agreement with r^2 values > 0.93.

The reason that the AERIoe can accurately retrieve shallow surface-based temperature inversions but the MWRoe cannot is because the AERI infrared radiance measurements theoretically contain much more information about the near-surface temperature profile than the MWR brightness temperatures (Blumberg et al., 2015). Figure 7 supports this by illustrating that the degrees of freedom for signal for temperature from the AERIoe retrievals is greater than that from the MWRoe retrievals, especially at the surface. The degrees of freedom for signal is a measure of the number of independent pieces of information from the observation vector that the retrieval used to generate the solution (Rodgers, 2000). Figure 7 shows that the AERIoe has around 6 times as much information about the surface temperature than the MWRoe and twice as much at 10 m. The mean degrees of freedom for signal for the surface temperature retrieval is over 4 times higher for the MWRoe-sfc compared to the MWRoe due to the additional information about the surface temperature in the observation vector. However, above the surface, the AERIoe still contains more information about the temperature profile than the MWRoe-sfc in the lowest 500 m of the boundary layer, the region in which accurate temperature profiles in NWP models are critical for successful fog forecasts (Martinet et al., 2020).

3.4 LWP retrievals and the detection of fog onset

The LWP retrievals from the AERIoe and MWRoe were well correlated ($r = 0.88$) and fell within ± 5 g m^{-2} of each other in ~ 90 % of all retrievals; however, on occasion, there were discrepancies of up to 10 g m^{-2} (Fig. 8), which can be equivalent to significant differences in horizontal visibility and net surface radiative forcing (see example in Sect. 1).

Although we do not have an independent measure of the "true" LWP, Fig. 9 illustrates the difference in the sensitivity of the MWRoe and the AERIoe to LWP as a function of LWP magnitude. The PAERI radiance observations are very sensitive to changes in LWP when the LWP is small, and so the 1σ uncertainty in the retrieved LWP from the AERIoe is less than 1 g m^{-2} for LWP < 20 g m^{-2} (or less than 10 %, Fig. 9). In contrast, the uncertainties in LWP derived from MWR brightness temperatures are related to absolute radiometric uncertainties that are approximately constant with respect to LWP, equating to at least 50 % uncertainty for LWP < 10 g m^{-2} (Fig. 9). However, as the LWP approaches opacity in the infrared (> 40 g m^{-2}), the sensitivity of the PAERI radiance observations to changes in LWP decreases until the uncertainties in the LWP retrievals from the AERIoe become equivalent to those from the MWRoe (~ 3 g m^{-2} or ~ 6 % uncertainty at 50 g m^{-2}).

The high sensitivity of the AERIoe to changes in LWP when LWP is small means that the increase in LWP associated with the development of radiation fog under clear skies is detected earlier in the AERIoe retrievals compared to the MWRoe retrievals (following our fog definition as the

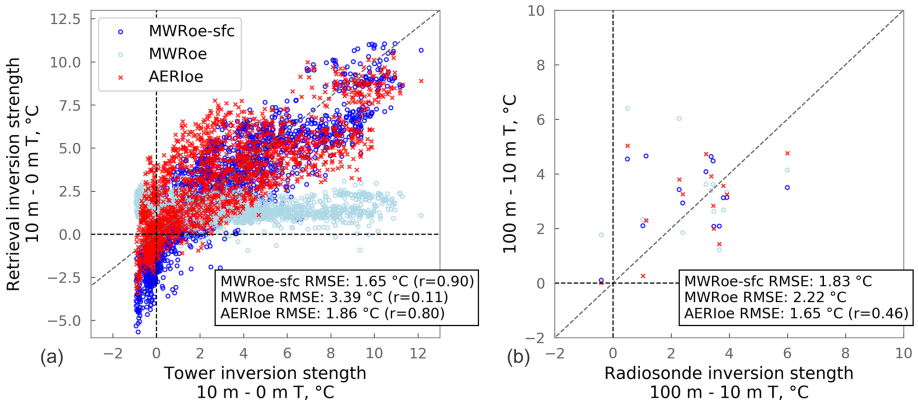

Figure 6. (a) Inversion strength (10–0 m temperature, T) retrieved from the AERIoe (red), the MWRoe (light blue), and the MWRoe-sfc (dark blue) versus observations from the tower-mounted HMP155 probes. **(b)** The same as **(a)** except for the 100–10 m inversion strength compared to observations from 14 coincident radiosonde profiles. On both subplots, the diagonal grey dashed line represents perfect agreement, and the horizontal and vertical dashed black lines at 0 °C delineate when a surface-based temperature inversion is present (right quadrants) versus absent (left quadrants). The root-mean-squared error (RMSE) values are included on the plots, and the Pearson's correlation coefficients (r) are only included when they are significant at the 90 % confidence level.

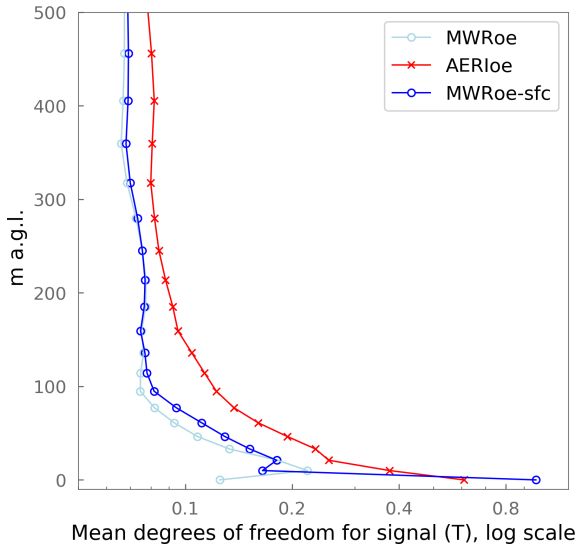

Figure 7. Mean degrees of freedom for signal across all temperature retrievals from the MWRoe (pale blue), the AERIoe (red), and the MWRoe constrained by the in-situ surface temperature measurement, MWRoe-sfc (dark blue).

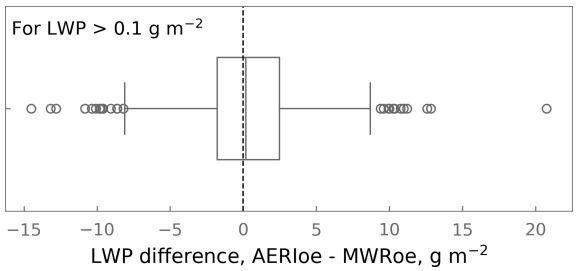

Figure 8. The differences in retrieved liquid water path (LWP) between all AERIoe and the MWRoe retrievals (LWP > 0.1 g m^{-2}). A total of 50 % of all retrievals fall within the central box, 90% of all retrievals fall within the box plot "whiskers", and the remaining data are plotted as outliers (circles).

presence of near-surface liquid water that has a detectable radiative impact). The increased sensitivity of the infrared over the microwave to small LWP values was described in (Turner, 2007). This is illustrated in Fig. 10, which shows the development of LWP during the 15 July 2019 case study. Shortly after 23 h on 15 July, the AERIoe detected a significant LWP that continued to increase gradually at a rate of $\sim 1.4\,\mathrm{g\,m^{-2}\,h^{-1}}$, until 02:00 h on 16 July, after which it increased rapidly to $\sim 30\,\mathrm{g\,m^{-2}}$ at 03:00 h (Fig. 10). In contrast, due to the larger uncertainties in the MWRoe LWP retrieval, the MWRoe LWP did not increase to a value that was significantly different from the noise until the onset of the rapid LWP increase just after 02:00 h.

For independent verification, we also determine fog onset from the ceilometer range-corrected attenuated backscatter. We define the ceilometer fog onset as being where the 5 min mean total backscatter increases by more than 3 standard deviations from the mean clear-sky backscatter at Summit between 1 June and 30 September 2019 (the mean clear-sky backscatter is determined using the same subset of verified clear-sky hours used to identify fog events from the AERI radiance, Sect. 2.2). Ceilometer attenuated backscatter is sensitive to the scattering cross section of molecules and particles in the atmosphere and can be sensitive to the presence of atmospheric aerosols (e.g. Markowicz et al., 2008) and to the hygroscopic growth of aerosols prior to their activation into fog droplets (Haeffelin et al., 2016), the latter of which can be a precursor to radiation fog formation (Haeffe-

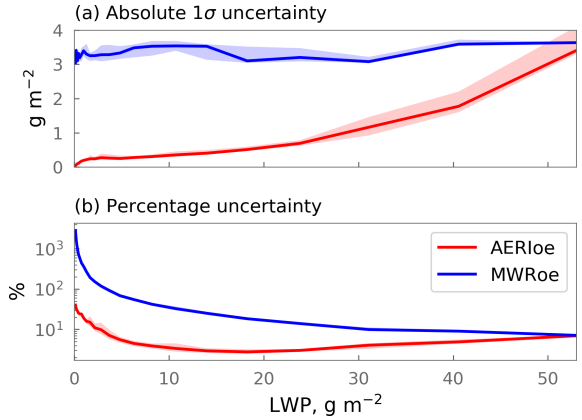

Figure 9. 1σ uncertainty in the AERIoe (red) and MWRoe (blue) liquid water path (LWP) retrievals as a function of LWP. **(a)** Shows the absolute uncertainties, and **(b)** shows the percentage uncertainties. The solid line is the median of all retrievals and shading is the interquartile range.

lin et al., 2016). At Summit, the aerosol scattering cross section is usually extremely small ($< 2 \times 10^{-6}$ m^{-1} at 550 nm, Schmeisser et al., 2018), and any signal due to the presence of aerosols is incorporated into the calculation into the mean clear-sky backscatter. We do not distinguish between the detection of aerosol hygroscopic growth and droplet formation in the ceilometer backscatter.

For the 15 July 2019 case, the ceilometer detected fog onset shortly before 00:00 on 16 July, 40 min after the AERIoe (Fig. 10b). Despite the relatively low LWP, the visibility at 00:00 h was only 400 m, and the observer reported freezing fog, indicating that this signal was indeed due to the presence of liquid droplets. In this case, if the MWRoe LWP retrieval was used to detect fog or for visibility nowcasting, the fog at 00:00 h on 16 July would not have been detected, whereas if the AERIoe LWP retrieval was used instead, it would have been.

The ceilometer detects fog (or aerosol hygroscopic growth) for all cases, with the exception of case 7 (4 August). During this case, the fog was extremely thin (maximum LWP from the AERI only 2 g m^{-2}), but the onsite observer logged the presence of a fog bow between 07:15 and 08:30, demonstrating that liquid water droplets were indeed present. This was a very marginal case that demonstrates the ability of the AERI to detect very small amounts of liquid water when even the ceilometer cannot. The MWRoe retrieval only detects fog for 6/12 cases (Fig. 11), and for those 6 cases, the AERIoe retrieval consistently detects the onset of fog (via the increase in LWP) before the MWRoe retrieval by 25 to 185 min (Fig. 11). For the 6 cases where the MWRoe does not detect the fog, the mean LWP detected by the AERIoe is very low (1.4 to 3.1 g m^{-2}).

4 Discussion

Central Greenland provides an excellent opportunity to study climatologically relevant radiation fog due to the pristine environment, commonality of events, and presence of the ICECAPS's long-term, multi-instrument platform. Nonetheless, it is a unique environment, and therefore the applicability of the results of this study in other environments is not guaranteed. Comparing retrievals between locations is complicated by the dependence on the quality of different prior datasets and instrument calibrations. However, in general, the performance of the MWRoe and AERIoe thermodynamic profile retrievals in the lowest 1 km a.g.l. are comparable to the performance assessed in a similar way against 127 radiosonde profiles in southwestern Germany (Blumberg et al., 2015). Blumberg et al. (2015) found the mean RMSE in the temperature profiles (lowest 1 km a.g.l.) to be ~ 0.9 °C for the AERIoe and ~ 1.1 °C for the MWRoe (compared to 1.0 and 1.6 °C in this study); for water vapour profiles, an RMSE of 0.7 g kg^{-1} for the AERIoe and 1.0 g kg^{-1} for the MWRoe was found (compared to 0.38 and 0.43 g kg^{-1} in this study). Nevertheless, under certain conditions, we might expect the performance of the AERIoe to deteriorate. For example, in environments where the total column water vapour is very high (e.g. tropical regions), the atmosphere will have a higher opacity in the infrared and the AERI sensitivity will be reduced (Löhnert et al., 2009). Additionally, the high sensitivity of the AERI, which makes it so suited to the study of fog, also makes it sensitive to localised plumes of pollution or smoke and, in some cases, to atmospheric aerosols (e.g. Turner and Eloranta, 2008). Both sets of retrievals are also sensitive to the quality of the prior that is used to constrain the retrieval and provide a first guess (Turner and Löhnert, 2014) and to the calibration and characterisation of the particular instrument, which is typically more challenging for the MWR (see Appendix A, Blumberg et al., 2015, and Löhnert and Maier, 2012). All of these factors may impact performance at different locations and should be considered during experimental design. Note that neither instrument operates effectively in rain.

The radiation fog case studies presented in this study are all composed of supercooled water droplets, with some occurring at surface temperatures as low as -28 °C (Table 3). Supercooled fogs at such cold temperatures are common at Summit, whereas ice fogs during the summer are rare (Cox et al., 2019). Observations of "fog bows" – atmospheric optics associated with the scattering of light by liquid water droplets – during most case studies confirm the presence of liquid water, as does the fact that the fogs are also detected by the ceilometer, which is not very sensitive to ice crystals (Van Tricht et al., 2014). However, the possibility exists that some (or even all) of these case studies contain ice crystals in addition to liquid water droplets. The scattering and absorption properties of ice crystals can be quite different to those of water droplets at wavelengths that are relevant for the

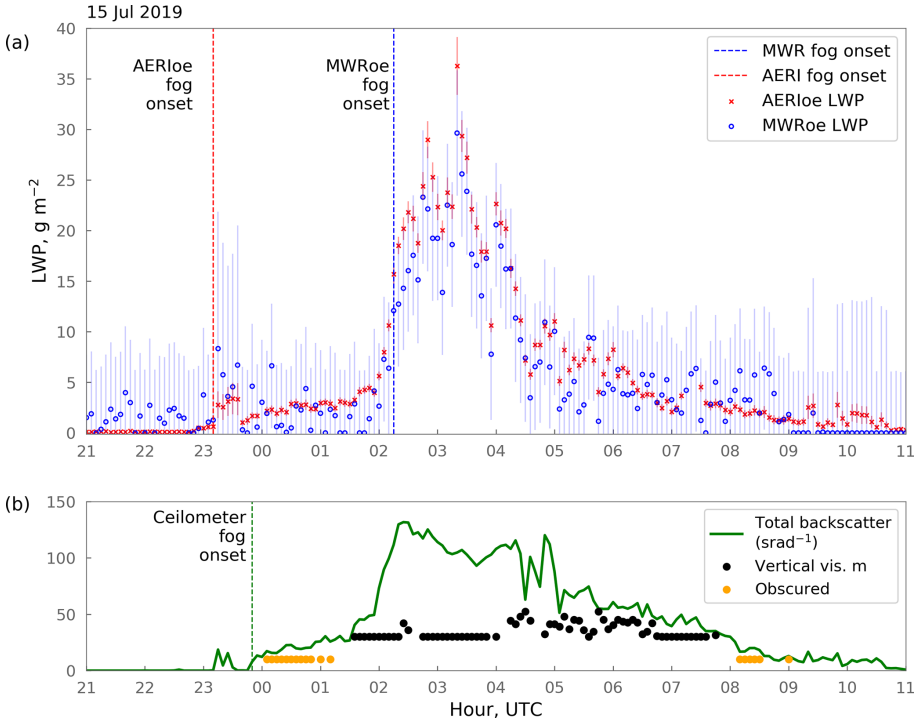

Figure 10. (a) The evolution of fog liquid water path (LWP) during the 15 July 2019 case study retrieved from the AERIoe (red) and the MWRoe (blue). Error bars show the 2σ uncertainty of the retrievals. The vertical red line shows the fog onset determined from the AERIoe retrievals, and the vertical blue line shows the fog onset determined by the MWRoe retrievals 3 h later. **(b)** Total range-corrected attenuated backscatter (5 min mean, green line) and vertical visibility (black points) from the ceilometer. Orange points indicate when the ceilometer reports obscured.

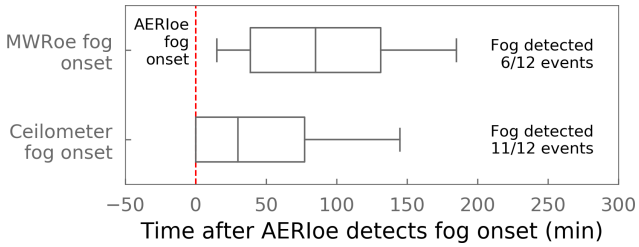

Figure 11. Time between fog onset detection from the AERIoe (vertical red line, $t = 0$) and fog onset detection from the MWRoe (upper) and ceilometer (lower). Only cases where both methods detected fog are included (6/12 for the MWRoe and 11/12 for the ceilometer). The whiskers capture all data points; the box shows the interquartile range.

AERIoe (e.g. Turner, 2005, Rowe et al., 2013), potentially resulting in biases in the AERIoe LWP retrievals that assume a liquid-only cloud. The lack of an independent "truth" value for LWP means that we cannot quantify any such biases. Nevertheless, the smaller uncertainties in the AERIoe LWP retrieval relative to the MWRoe LWP retrieval are related to the physical sensitivity of the measurement, and so we can expect this result to be consistent across other cases of warm fog.

This study focuses on cases of thin radiative fog (LWP $<$ 40 g m^{-2}), which is the most common type of fog at Summit, and draws attention to the benefits of the AERI, which is particularly sensitive to the small changes in LWP and strong shallow temperature inversions that are characteristic of these events. For other types of fog, onset might not be initiated by a small increase in LWP; for example, in stratus-lowering events, the reduction in cloud base height from the ceilometer might be a better indicator of fog onset. At other locations (in the mid-latitudes, for example), thicker fogs with LWP $>$ 50 g m^{-2} are more common and can be 100's of metres deep (Toledo et al., 2021). Although the AERI might still be a useful instrument for the early detection of such events, once the fog becomes optically thick in the infrared, the AERI can no longer provide information about the thermodynamic profile above the fog or the trend in LWP, both of which are useful parameters for understanding the development of deep well-mixed fog (Toledo et al., 2021). In such cases, thermodynamic profile and LWP retrievals from the MWR are valuable. The TROPoe algorithm can combine both AERI and MWR measurements in the same retrieval. Below-cloud thermodynamic profiles from the combined MWR+AERI are essentially the same as retrievals based on AERI measurements alone (Turner and Lohnert, 2021), but the uncertainty in the LWP retrieval when both

instruments are combined is $< 20\,\%$ across the entire range in LWP from 1 to $< 500\,\mathrm{g\,m^{-2}}$ (Turner, 2007).

Although this study focuses on the passive remote sensing instruments that are essential for fog detection (since the active remote sensing instruments have a blind spot immediately above the surface), complementary information from active remote sensing instruments are also necessary for accurate results. We demonstrate in Sect. 3.1 that accurate cloud base height detection (from the ceilometer) is an important input for the AERIoe retrievals, and the radar is also required to filter out precipitation events than can invalidate retrievals from both the MWR and the AERI. Overall, this study highlights the importance of instrument synergy to provide optimal thermodynamic profiles and LWP retrievals, supporting the findings of previous studies (Turner et al., 2007; Löhnert et al., 2009; Turner and Lohnert, 2021; Smith et al., 2021; Djalalova et al., 2022) and expanding on this conclusion to include the specific conditions pertaining to the development of radiation fog.

5 Summary and conclusions

Previous studies have demonstrated that AERI measurements of spectral infrared radiance are more sensitive to the structure of the near-surface temperature profile and to small changes in liquid water path (LWP) than MWR measurements of microwave brightness temperatures (Turner, 2007; Löhnert et al., 2009; Blumberg et al., 2015). The purpose of this study was to compare retrievals of boundary layer thermodynamic profiles and LWP from these two instrument types during cases of thin supercooled radiation fog in central Greenland using a consistent physical retrieval algorithm (the AERIoe retrieval based on observations of infrared radiance and the MWRoe based on microwave brightness temperatures). We assess the performance of the two retrievals against three criteria that are critically important for the forecast and detection of radiation fog:

1. ability to retrieve accurate thermodynamic profiles in the lowest 1 km a.g.l. of the atmosphere
2. ability to capture the strength and development of shallow surface-based temperature inversions that typically portend the formation of radiation fog
3. ability to detect the initial increase in LWP that signifies the onset of fog and a reduction in horizontal visibility.

Although there are only 14 coincident radiosonde profiles available for comparison, the bias and RMSE statistics of the temperature and water vapour profiles in the lowest 1 km a.g.l. are consistent with the findings of Löhnert et al. (2009) and Blumberg et al. (2015), suggesting that the performance of both sets of retrievals in the Arctic and under conditions for the formation of supercooled fog are similar to the performance in the mid-latitudes and under other sky conditions (clear skies or below clouds with bases above 500 m a.g.l.). We find that the water vapour profile retrievals in the lowest 1 km a.g.l. are comparable for both the MWRoe and the AERIoe, with RMSE of $0.44\,\mathrm{g\,kg^{-1}}$ for the MWRoe and $0.39\,\mathrm{g\,kg^{-1}}$ for the AERIoe. The AERIoe temperature profile retrievals perform better in terms of bias and RMSE than the MWRoe for the 14 cases considered (MWRoe bias: $-1.5\,^{\circ}\mathrm{C}$, RMSE: $1.7\,^{\circ}\mathrm{C}$; AERIoe bias: $-0.43\,^{\circ}\mathrm{C}$, RMSE: $1.0\,^{\circ}\mathrm{C}$); however, the consistency of the negative temperature bias in the MWRoe suggests that an additional bias correction may be possible, which would result in comparable performance between the two sets of retrievals.

A unique aspect of this study was the assessment of the ability of the two retrieval types to characterise shallow (0–10 m a.g.l.) surface-based temperature inversions. Despite the similar performance of the temperature profile retrievals up to 1 km a.g.l. in general, the ability of the two retrieval types to characterise the 0–10 m temperature lapse rate was markedly different. The AERIoe 0–10 m temperature differences were well correlated with in-situ observations, capturing surface temperature inversions well up to a lapse rate of $-1.2\,^{\circ}\mathrm{C\,m^{-1}}$ (previous studies have demonstrated the ability of the AERIoe to characterise near-surface lapse rates well for values of -0.01 to $0.01\,^{\circ}\mathrm{C\,m^{-1}}$, Klein et al., 2015). However, the MWRoe 0–10 m temperature differences were not correlated with observations and did not deviate more than $1\,^{\circ}\mathrm{C}$ from the prior. The reason for this difference is that the infrared radiance measurements from the AERI contain more information about the temperature near the surface than the MWR measurements. This highlights the importance of using accurate surface temperature measurements to constrain MWR thermodynamic profile retrievals.

In addition to increased sensitivity to shallow surface temperature inversions, the AERI is much more sensitive to small changes in LWP, with the result that the uncertainties in retrieved LWP from the AERIoe are much smaller than those retrieved from the MWRoe for LWP $< 50\,\mathrm{g\,m^{-2}}$. This means that the AERIoe is consistently able to detect small changes in LWP, which might initiate radiation fog and reduce horizontal visibility, by up to 185 min before the MWRoe. This has important implications for fog detection and visibility nowcasting, because even a very small LWP ($< 5\,\mathrm{g\,m^{-2}}$) can reduce horizontal visibility, and the MWRoe alone would not have detected fog on some occasions when reported visibility was as low as 400 m.

Based on these results, we hypothesise that the assimilation of near-surface temperature profile retrievals from an AERI into NWP models could improve fog forecasts beyond the improvements already seen through the assimilation of MWR measurements (Martinet et al., 2020). In addition, the increased sensitivity of the AERI to small changes in LWP (compared to the MWR) will allow the AERI to detect the onset of radiation fog events earlier, with the potential to increase the skill of fog nowcasting products and improve climatological analyses of fog radiative effects.

Although this study demonstrates that the AERI is particularly well suited to retrieving boundary layer properties that are key for radiation fog formation, there are trade-offs that must be considered when selecting instruments for operational use, notably that the AERI is unable to retrieve thermodynamic profiles above optically thick clouds/fog (LWP > 40 g m^{-2}), and that the AERIoe retrieval is particularly sensitive to the CBH assumption during fog/low cloud. This highlights the importance of a multi-instrument approach to improve fog forecasting under all sky conditions: ceilometer cloud base heights are necessary to generate accurate thermodynamic profile retrievals from the AERI; MWRs are needed to retrieve LWP and thermodynamic profiles above optically thick fog/clouds, and radar data is required to determine the presence of precipitation, which can invalidate retrievals from both passive instruments.

The results of this study present a case for future observing-system experiments (or observing-system simulation experiments, as in Otkin et al., 2011; Hartung et al., 2011) to quantify the impact of the operational use of AERI observations in terms of improvements to NWP skill, particularly in the case of radiation fog.

Data availability. ICECAPS data are available from the Arctic Data Center: HATPRO MWR (https://doi.org/10.18739/A2TX3568P, Turner and Bennartz, 2020), MMCR (https://doi.org/10.18739/A2Q52FD4V, Shupe, 2020a), POSS (https://doi.org/10.18739/A2GQ6R30G, Shupe, 2020b), and radiosonde profiles (https://doi.org/10.18739/A20P0WR53, Von P. Walden and Shupe, 2020). PAERI data and retrieval output from the TROPoe are in the process of being submitted to the Arctic Data Center (https://doi.org/10.5439/1880028). ICECAPS-ACE HMP155 temperature/humidity sensor data can be accessed through the CEDA archive at http://catalogue.ceda.ac.uk/uuid/f06c6aa727404ca788ee3dd0515ea61a (last access: 5 July 2021).

Appendix A: MWR T_b bias correction

An external liquid nitrogen target is used to determine the effective temperature of the MWR internal noise diode, which is required to convert the observed signal into brightness temperature (T_b) values, as described in Sect. 2.1.2. Due to the personnel and resource requirements, this calibration is only performed twice a year at Summit. Imperfect calibrations can result in a radiometric bias in the T_b measurements, and drift in the effective temperature of the internal noise diode can occur in between calibrations (Löhnert and Maier, 2012; Blumberg et al., 2015).

To determine this radiometric bias in the observed T_b values, the twice-daily radiosondes launched at Summit between 1 June and 31 August 2019 were used as input in the MonoRTM, and the bias between the observed and computed T_b values was determined. The evolution of the bias over time is well illustrated by showing the bias values for the cases used in this analysis (Fig. A1). The bias in the K-band channels remained very small (absolute value less than 0.5 K), confirming that the automated tip-curve calibration method applied to those transparent channels was working well. However, there is a significant negative bias (calculation larger than the observed radiance) in the 51 to 54 GHz channels, and this bias changes with time. However, the bias in the 51.26 and 52.28 GHz channels is variable with time with no apparent pattern (inset in Fig. A1). Fortunately, the T_b bias in the 55 to 58 GHz channels is stable with time, and the magnitude is relatively small (less than 0.7 K for those channels).

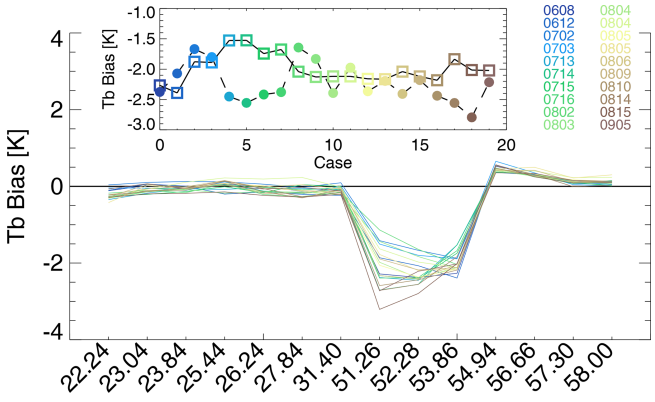

Figure A1. The T_b bias offset for the cases used in this analysis. The inset plot shows the temporal variability of the 51.26 (filled circles) and 52.28 (open squares) GHz channels for these cases, where the colours indicate the date (MMDD) of the case.

Note that we do not consider or correct for possible spectral biases in the MWR frequencies channels (Löhnert and Maier, 2012). It is possible that the large T_b biases in the 51.26, 52.28, and 53.86 GHz channels are a combination of both spectral and radiometric biases. It is important to note that the biases in those channels might not be entirely due to the calibration accuracy of the microwave radiometer; the bias could also be explained by systematic errors in the radiative transfer model used, as the various uncertainties of the absorption line properties at those frequencies results in large model uncertainty (Cimini et al., 2018).

Figure A2 illustrates the difference between the MWRoe-retrieved thermodynamic profile compared to the radiosondes during the radiation fog case studies with and without the mean radiosonde-derived bias correction applied. The application of the bias correction reduces the mean bias in the water vapour profile from 0.14 to 0.01 g kg^{-1} and the mean RMSE from 0.47 to 0.43 g kg^{-1}. However, the bias correction has little effect on the temperature profiles. The reason for the consistent small negative temperature bias in the MWRoe both with (mean −1.45 °C) and without (mean −1.26 °C) the bias correction is currently unknown, espe-

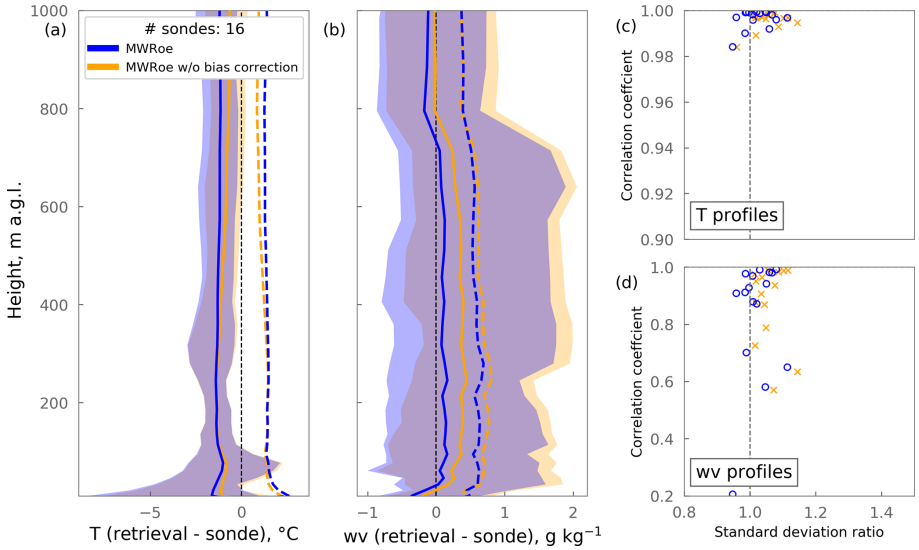

Figure A2. As Fig. 4 but comparing the performance of the final MWRoe retrieval (blue) with that of the MWRoe retrieval without the additional T_b bias correction applied (orange). The solid line shows the mean bias and the shaded represents the range. Dashed lines show the root-mean-squared error (RMSE).

cially since the mean T_b bias in the high-frequency end of the V-band is very close to zero.

The reduction in the bias and RMSE of the MWRoe-retrieved water vapour profile compared to the radiosondes demonstrates that the application of the additional T_b bias correction is essential for making accurate MWR thermodynamic profile retrievals. Currently, the only way of performing this bias correction is by using an alternative "truth" profile (in this case, radiosonde profiles); this is a significant disadvantage of the MWR, since radiosondes are spatially sparse, resource intensive, and expensive. However, a method using only the climatology data, as encapsulated in the a priori data, has been proposed by Djalalova et al. (2022); this new method helps to account for some of the spectral artefacts in the bias but needs additional research to help characterise any systematic error that might be introduced by the method.

Author contributions. DT conceived the study, developed and ran the TROPoe retrieval algorithm, processed the MWR data, calculated the T_b bias correction, and contributed to the text. VW prepared the PAERI data and contributed to the text. HG led the analysis with contributions from DT and RN. HG prepared the manuscript with contributions from all co-authors.

Competing interests. The contact author has declared that none of the authors has any competing interests.

Disclaimer. Publisher's note: Copernicus Publications remains neutral with regard to jurisdictional claims in published maps and institutional affiliations.

Acknowledgements. The efforts of technicians at Summit Station and science support provided by Polar Field Services were crucial to maintaining data quality and continuity at Summit. ICECAPS is a long-term research program with many collaborators, and we are grateful for all their efforts in developing and maintaining the various instruments and data products used in this study. We would like to thank Maria Cadeddu, Argonne National Laboratory, for her work in updating the HATPRO's calibration using automated tip curves. Finally we are grateful for feedback from the PROBE-COST fog alerts meeting (23 November 2021) and three anonymous reviewers that improved this manuscript.

Financial support. This research has been supported by the Natural Environment Research Council, National Centre for Earth Observation (grant nos. NE/L002574/1 and NE/S00906X/1) and the National Science Foundation, Directorate for Geosciences (grant no. 1801477).

Review statement. This paper was edited by Domenico Cimini and reviewed by three anonymous referees.

References

Anber, U., Gentine, P., Wang, S., and Sobel, A. H.: Fog and rain in the Amazon, P. Natl. Acad. Sci. USA, 112, 11473–11477, 2015.

Antonelli, P., Revercomb, H., Sromovsky, L., Smith, W., Knuteson, R., Tobin, D., Garcia, R., Howell, H., Huang, H.-L., and Best, F.: A principal component noise filter for high spectral resolution infrared measurements, J. Geophys. Res.-Atmos., 109, D23, https://doi.org/10.1029/2004JD004862, 2004.

Beiderwieden, E., Klemm, O., and Hsia, Y. J.: The impact of fog on the energy budget of a subtropical cypress forest in Taiwan, Taiwan J. Forest Sci., 22, 227–239, https://doi.org/10.7075/TJFS.200709.0227, 2007.

Bendix, J.: A case study on the determination of fog optical depth and liquid water path using AVHRR data and relations to fog liquid water content and horizontal visibility A case study on the determination of fog optical depth and liquid water path using AVHRR data and relations to fog liquid water content and horizontal visibility, Int. J. Remote Sens., 16, 515–530, https://doi.org/10.1080/01431169508954416, 1995.

Bennartz, R., Shupe, M. D., Turner, D. D., Walden, V. P., Steffen, K., Cox, C. J., Kulie, M. S., Miller, N. B., and Pettersen, C.: July 2012 Greenland melt extent enhanced by low-level liquid clouds, Nature, 496, 83, https://doi.org/10.1038/nature12002, 2013.

Bergot, T., Terradellas, E., Cuxart, J., Mira, A., Liechti, O., Mueller, M., and Nielsen, N. W.: Intercomparison of Single-Column Numerical Models for the Prediction of Radiation Fog, J. Appl. Meteorol. Climatol., 46, 504–521, https://doi.org/10.1175/JAM2475.1, 2007.

Blumberg, W. G., Turner, D. D., Löhnert, U., and Castleberry, S.: Ground-Based Temperature and Humidity Profiling Using Spectral Infrared and Microwave Observations. Part II: Actual Retrieval Performance in Clear-Sky and Cloudy Conditions, J. Appl. Meteorol. Climatol., 54, 2305–2319, https://doi.org/10.1175/JAMC-D-15-0005.1, 2015.

Cadeddu, M. P., Liljegren, J. C., and Turner, D. D.: The Atmospheric radiation measurement (ARM) program network of microwave radiometers: instrumentation, data, and retrievals, Atmos. Meas. Tech., 6, 2359–2372, https://doi.org/10.5194/amt-6-2359-2013, 2013.

Cao, Y., Tan, W., and Wu, Z.: Aircraft icing: An ongoing threat to aviation safety, Aero. Sci. Technol., 75, 353–385, 2018.

Cimini, D., Nelson, M., Güldner, J., and Ware, R.: Forecast indices from a ground-based microwave radiometer for operational meteorology, Atmos. Meas. Tech., 8, 315–333, https://doi.org/10.5194/amt-8-315-2015, 2015.

Cimini, D., Rosenkranz, P. W., Tretyakov, M. Y., Koshelev, M. A., and Romano, F.: Uncertainty of atmospheric microwave absorption model: impact on ground-based radiometer simulations and retrievals, Atmos. Chem. Phys., 18, 15231–15259, https://doi.org/10.5194/acp-18-15231-2018, 2018.

Clough, S. A. and Iacono, M. J.: Line-by-line calculation of atmospheric fluxes and cooling rates: 2. Application to carbon dioxide, ozone, methane, nitrous oxide and the halocarbons, J. Geophys. Res.-Atmos., 100, 16519–16535, https://doi.org/10.1029/95JD01386, 1995.

Clough, S., Shephard, M., Mlawer, E., Delamere, J., Iacono, M., Cady-Pereira, K., Boukabara, S., and Brown, P.: Atmospheric radiative transfer modeling: A summary of the AER codes, J. Quant. Spectrosc. Ra. Transf., 91, 233–244, 2005.

Cox, C. J., Walden, V. P., and Rowe, P. M.: A comparison of the atmospheric conditions at Eureka, Canada, and Barrow, Alaska (2006–2008), J. Geophys. Res.-Atmos., 117, D12, https://doi.org/10.1029/2011JD017164, 2012.

Cox, C. J., Noone, D. C., Berkelhammer, M., Shupe, M. D., Neff, W. D., Miller, N. B., Walden, V. P., and Steffen, K.: Supercooled liquid fogs over the central Greenland Ice Sheet, Atmos. Chem. Phys., 19, 7467–7485, https://doi.org/10.5194/acp-19-7467-2019, 2019.

Crewell, S. and Lohnert, U.: Accuracy of Boundary Layer Temperature Profiles Retrieved with Multi-frequency, Multiangle Microwave Radiometry, SPECIAL ISSUE ON MICROWAVE RADIOMETRY AND REMOTE SENSING APPLICATIONS, 2195–2201, https://doi.org/10.1109/TGRS.2006.888434, 2007.

Djalalova, I. V., Turner, D. D., Bianco, L., Wilczak, J. M., Duncan, J., Adler, B., and Gottas, D.: Improving thermodynamic profile retrievals from microwave radiometers by including radio acoustic sounding system (RASS) observations, Atmos. Meas. Tech., 15, 521–537, https://doi.org/10.5194/amt-15-521-2022, 2022.

Ducloux, H. and Nygaard, B. E.: Ice loads on overhead lines due to freezing radiation fog events in plains, Cold Reg. Sci. Technol., 153, 120–129, https://doi.org/10.1016/J.COLDREGIONS.2018.04.018, 2018.

Gultepe, I., Tardif, R., Michaelides, S. C., Cermak, J., Bott, A., Bendix, J., Müller, M. D., Pagowski, M., Hansen, B., Ellrod, G., Jacobs, W., Toth, G., and Cober, S. G.: Fog research: A review of past achievements and future perspectives, Pure Appl. Geophys., 164, 1121–1159, https://doi.org/10.1007/s00024-007-0211-x, 2007.

Gultepe, I., Pearson, G., Milbrandt, J. A., Hansen, B., Platnick, S., Taylor, P., Gordon, M., Oakley, J. P., and Cober, S. G.: The Fog Remote Sensing and Modeling Field Project, B. Am. Meteorol. Soc., 90, 341–360, https://doi.org/10.1175/2008BAMS2354.1, 2009.

Gultepe, I., Sharman, R., Williams, P. D., Zhou, B., Ellrod, G., Minnis, P., Trier, S., Griffin, S., Yum, S. S., and Gharabaghi, B.: A Review of High Impact Weather for Aviation Meteorology, Pure Appl. Geophys., 176, 18, https://doi.org/10.1007/s00024-019-02168-6, 2019.

Guy, H., Neely III, R. R., and Brooks, I.: ICECAPS-ACE: Integrated Characterization of Energy, Clouds, Atmospheric state, and Precipitation at Summit, Greenland – Aerosol Cloud Experiment measurements, Centre for Environmental Data Analysis [data set], http://catalogue.ceda.ac.uk/uuid/f06c6aa727404ca788ee3dd0515ea61a (last access: 5 July 2021), 2020.

Guy, H., Brooks, I. M., Carslaw, K. S., Murray, B. J., Walden, V. P., Shupe, M. D., Pettersen, C., Turner, D. D., Cox, C. J., Neff, W. D., Bennartz, R., and Neely III, R. R.: Controls on surface aerosol particle number concentrations and aerosol-limited cloud regimes over the central Greenland Ice Sheet, Atmos. Chem. Phys., 21, 15351–15374, https://doi.org/10.5194/acp-21-15351-2021, 2021.

Hachfeld, B. and Jürgens, N.: Climate patterns and their impact on the vegetation in a fog driven desert: the Central Namib Desert in Namibia, Phytocoenologia, 30, 567–589, 2000.

Haeffelin, M., Dupont, J. C., Boyouk, N., Baumgardner, D., Gomes, L., Roberts, G., and Elias, T.: A Comparative Study of Radiation Fog and Quasi-Fog Formation Processes During the ParisFog Field Experiment 2007, Pure Appl. Geophys., 170, 2283–2303, https://doi.org/10.1007/s00024-013-0672-z, 2013.

Haeffelin, M., Laffineur, Q., Bravo-Aranda, J.-A., Drouin, M.-A., Casquero-Vera, J.-A., Dupont, J.-C., and De Backer, H.: Radiation fog formation alerts using attenuated backscatter power from automatic lidars and ceilometers, Atmos. Meas. Tech., 9, 5347–5365, https://doi.org/10.5194/amt-9-5347-2016, 2016.

Han, Y.: Analysis and improvement of tipping calibration for ground-based microwave radiometers, IEEE Trans. Geosci. Remote Sens., 38, 1260–1276, https://doi.org/10.1109/36.843018, 2000.

Hartung, D. C., Otkin, J. A., Petersen, R. A., Turner, D. D., and Feltz, W. F.: Assimilation of Surface-Based Boundary Layer Profiler Observations during a Cool-Season Weather Event Using an Observing System Simulation Experiment. Part II: Forecast Assessment, Mon. Weather Rev., 139, 2327–2346, https://doi.org/10.1175/2011MWR3623.1, 2011.

Hudson, S. R. and Brandt, R. E.: A look at the surface-based temperature inversion on the Antarctic Plateau, J. Climate, 18, 1673–1696, 2005.

Illingworth, A. J., Cimini, D., Haefele, A., Haeffelin, M., Hervo, M., Kotthaus, S., Löhnert, U., Martinet, P., Mattis, I., O'Connor, E. J., and Potthast, R.: How Can Existing Ground-Based Profiling Instruments Improve European Weather Forecasts?, B. Am. Meteorol. Soc., 100, 605–619, https://doi.org/10.1175/BAMS-D-17-0231.1, 2019.

Izett, J. G., Schilperoort, B., Coenders-Gerrits, M., Baas, P., Bosveld, F. C., and van de Wiel, B. J. H.: Missed Fog?, Bound.-Lay. Meteorol. 2019, 173, 289–309, https://doi.org/10.1007/S10546-019-00462-3, 2019.

Jacob, J. D., Chilson, P. B., Houston, A. L., and Smith, S. W.: Considerations for atmospheric measurements with small unmanned aircraft systems, Atmosphere, 9, 252, https://doi.org/10.3390/atmos9070252, 2018.

Jensen, M. P., Holdridge, D. J., Survo, P., Lehtinen, R., Baxter, S., Toto, T., and Johnson, K. L.: Comparison of Vaisala radiosondes RS41 and RS92 at the ARM Southern Great Plains site, Atmos. Meas. Tech., 9, 3115–3129, https://doi.org/10.5194/amt-9-3115-2016, 2016.

Klein, P., Bonin, T. A., Newman, J. F., Turner, D. D., Chilson, P. B., Wainwright, C. E., Blumberg, W. G., Mishra, S., Carney, M., Jacacobsen, E. P., Wharton, S., and Newsom, R. K.: LABLE: A Multi-Institutional, Student-Led, Atmospheric Boundary Layer Experiment, B. Am. Meteorol. Soc., 96, 1743–1764, https://doi.org/10.1175/BAMS-D-13-00267.1, 2015.

Knuteson, R., Revercomb, H., Best, F., Ciganovich, N., Dedecker, R., Dirkx, T., Ellington, S., Feltz, W., Garcia, R., Howell, H., Smith, W. L., Short, J. F., and Tobin, D. C.: Atmospheric emitted radiance interferometer. Part I: Instrument design, J. Atmos. Ocean. Technol., 21, 1763–1776, 2004a.

Knuteson, R., Revercomb, H., Best, F., Ciganovich, N., Dedecker, R., Dirkx, T., Ellington, S., Feltz, W., Garcia, R., Howell, H., and Smith, W. L.: Atmospheric emitted radiance interferometer. Part II: Instrument design, J. Atmos. Ocean. Technol., 21, 1763–1776, 2004b.

Koenigk, T., Key, J., and Vihma, T.: Climate change in the Arctic, in: Physics and chemistry of the Arctic atmosphere, 673–705, https://doi.org/10.1007/978-3-030-33566-3_11, Springer, 2020.

Liljegren, J. C.: Automatic self-calibration of ARM microwave radiometers, Microw. Rad. Remote Sens. Earth's Surf. Atmos., 433, 433–443, 2000.

Löhnert, U. and Maier, O.: Operational profiling of temperature using ground-based microwave radiometry at Payerne: prospects and challenges, Atmos. Meas. Tech., 5, 1121–1134, https://doi.org/10.5194/amt-5-1121-2012, 2012.

Löhnert, U., Turner, D. D., and Crewell, S.: Ground-Based Temperature and Humidity Profiling Using Spectral Infrared and Microwave Observations. Part I: Simulated Retrieval Performance in Clear-Sky Conditions, J. Appl. Meteorol. Climatol., 48, 1017–1032, https://doi.org/10.1175/2008JAMC2060.1, 2009.

Marke, T., Ebell, K., Löhnert, U., and Turner, D. D.: Statistical retrieval of thin liquid cloud microphysical properties using ground-based infrared and microwave observations, J. Geophys. Res.-Atmos., 121, 14558–14573, https://doi.org/10.1002/2016JD025667, 2016.

Markowicz, K., Flatau, P., Kardas, A., Remiszewska, J., Stelmaszczyk, K., and Woeste, L.: Ceilometer retrieval of the boundary layer vertical aerosol extinction structure, J. Atmos. Ocean. Technol., 25, 928–944, 2008.

Martinet, P., Cimini, D., De Angelis, F., Canut, G., Unger, V., Guillot, R., Tzanos, D., and Paci, A.: Combining ground-based microwave radiometer and the AROME convective scale model through 1DVAR retrievals in complex terrain: an Alpine valley case study, Atmos. Meas. Tech., 10, 3385–3402, https://doi.org/10.5194/amt-10-3385-2017, 2017.

Martinet, P., Cimini, D., Burnet, F., Ménétrier, B., Michel, Y., and Unger, V.: Improvement of numerical weather prediction model analysis during fog conditions through the assimilation of ground-based microwave radiometer observations: a 1D-Var study, Atmos. Meas. Tech., 13, 6593–6611, https://doi.org/10.5194/amt-13-6593-2020, 2020.

McFarquhar, G. M., Smith, E., Pillar-Little, E. A., Brewster, K., Chilson, P. B., Lee, T. R., Waugh, S., Yussouf, N., Wang, X., Xue, M., Gijs de Boer, Gibbs, J. A., Fiebrich, C., Baker, B., Brotzge, J., Carr, F., Christophersen, H., Fengler, M., Hall, P., Hock, T., Houston, A., Huck, R., Jacob, J., Palmer, R., Quinn, P. K., Wagner, M., Zhang, Y. (Rockee), and Hawk, D.: Current and future uses of UAS for improved forecasts/warnings and scientific studies, B. Am. Meteorol. Soc., 101, E1322–E1328, 2020.

Miller, N. B., Shupe, M. D., Cox, C. J., Walden, V. P., Turner, D. D., and Steffen, K.: Cloud radiative forcing at Summit, Greenland, J. Climate, 28, 6267–6280, 2015.

Moran, K. P., Martner, B. E., Post, M., Kropfli, R. A., Welsh, D. C., and Widener, K. B.: An unattended cloud-profiling radar for use in climate research, B. Am. Meteorol. Soc., 79, 443–456, 1998.

Morris, V. R.: Ceilometer instrument handbook, DOE Office of Science Atmospheric Radiation Measurement (ARM) User Facility, OSTI Identifier 1036530, DOE/SC-ARM-TR-020, 2016.

Münkel, C., Eresmaa, N., Räsänen, J., and Karppinen, A.: Retrieval of mixing height and dust concentration with lidar ceilometer, Bound.-Lay. Meteorol., 124, 117–128, https://doi.org/10.1007/S10546-006-9103-3, 2006.

Newsom, R. K., Turner, D. D., Lehtinen, R., Münkel, C., Kallio, J., and Roininen, R.: Evaluation of a Compact Broadband Differential Absorption Lidar for Routine Water Vapor Profiling in the Atmospheric Boundary Layer, J. Atmos. Ocean. Technol., 37, 47–65, https://doi.org/10.1175/JTECH-D-18-0102.1, 2020.

NSIDC: Europe's warm air spikes Greenland melting to record levels., National Snow and Ice Data Center, http://nsidc.org/

greenland-today/2021/08/rain-at-the-summit-of-greenland/ (last access: October 2021), 2019.

NSIDC: Rain at the summit of Greenland., National Snow and Ice Data Center, http://nsidc.org/greenland-today/2021/08/rain-at-the-summit-of-greenland/, last access: October 2021.

Oke, T. R.: Boundary layer climates, Routledge, Google Scholar, eISBN 1134951345, ISBN-13 9781134951345, 2002.

Otkin, J. A., Hartung, D. C., Turner, D. D., Petersen, R. A., Feltz, W. F., and Janzon, E.: Assimilation of Surface-Based Boundary Layer Profiler Observations during a Cool-Season Weather Event Using an Observing System Simulation Experiment. Part I: Analysis Impact, Mon. Weather Rev., 139, 2309–2326, https://doi.org/10.1175/2011MWR3622.1, 2011.

Panahi, R., Ng, A. K., Afenyo, M. K., and Haeri, F.: A novel approach in probabilistic quantification of risks within the context of maritime supply chain: The case of extreme weather events in the Arctic, Acc. Anal. Prev., 144, 105673, https://doi.org/10.1016/j.aap.2020.105673, 2020.

Price, J.: Radiation Fog. Part I: Observations of Stability and Drop Size Distributions, Bound.-Lay. Meteorol., 139, 167–191, https://doi.org/10.1007/S10546-010-9580-2, 2011.

Rodgers, C. D.: Inverse methods for atmospheric sounding: theory and practice, vol. 2, World scientific, ISBN 981-02-2740-X, 2000.

Rose, T., Crewell, S., Löhnert, U., and Simmer, C.: A network suitable microwave radiometer for operational monitoring of the cloudy atmosphere, Atmos. Res., 75, 183–200, https://doi.org/10.1016/j.atmosres.2004.12.005, 2005.

Rowe, P. M., Neshyba, S., and Walden, V. P.: Radiative consequences of low-temperature infrared refractive indices for supercooled water clouds, Atmos. Chem. Phys., 13, 11925–11933, https://doi.org/10.5194/acp-13-11925-2013, 2013.

Rüfenacht, R., Haefele, A., Pospichal, B., Cimini, D., Bircher-Adrot, S., Turp, M., and Sugier, J.: EUMETNET opens to microwave radiometers for operational thermodynamical profiling in Europe, B. Atmos. Sci. Technol., 2, 1–5, https://doi.org/10.1007/S42865-021-00033-W, 2021.

Savijärvi, H.: Radiative and turbulent heating rates in the clear-air boundary layer, Q. J. Roy. Meteorol. Soc., 132, 147–161, https://doi.org/10.1256/QJ.05.61, 2006.

Schmeisser, L., Backman, J., Ogren, J. A., Andrews, E., Asmi, E., Starkweather, S., Uttal, T., Fiebig, M., Sharma, S., Eleftheriadis, K., Vratolis, S., Bergin, M., Tunved, P., and Jefferson, A.: Seasonality of aerosol optical properties in the Arctic, Atmos. Chem. Phys., 18, 11599–11622, https://doi.org/10.5194/acp-18-11599-2018, 2018.

Sheppard, B. and Joe, P.: Performance of the precipitation occurrence sensor system as a precipitation gauge, J. Atmos. Ocean. Technol., 25, 196–212, 2008.

Shupe, M.: Millimeter Cloud Radar measurements taken at Summit Station, Greenland, 2019, Artic Data Center [data set], https://doi.org/10.18739/A2Q52FD4V, 2020a.

Shupe, M.: Precipitation Occurrence Sensor System measurements taken at Summit Station, Greenland, 2019, Artic Data Center [data set], https://doi.org/10.18739/A2GQ6R30G, 2020b.

Shupe, M. D. and Intrieri, J. M.: Cloud radiative forcing of the Arctic surface: The influence of cloud properties, surface albedo, and solar zenith angle, J.f Climate, 17, 616–628, 2004.

Shupe, M. D., Turner, D. D., Walden, V. P., Bennartz, R., Cadeddu, M. P., Castellani, B. B., Cox, C. J., Hudak, D. R., Kulie, M. S., Miller, N. B., Neely, R. R., Neff, W. D., Rowe, P. M., Others, Neely, R. R., Neff, W. D., and Rowe, P. M.: High and dry: New observations of tropospheric and cloud properties above the Greenland Ice Sheet, B. Am. Meteorol. Soc., 94, 169–186, https://doi.org/10.1175/BAMS-D-11-00249.1, 2013.

Smith, E. N., Greene, B. R., Bell, T. M., Blumberg, W. G., Wakefield, R., Reif, D., Niu, Q., Wang, Q., and Turner, D. D.: Evaluation and Applications of Multi-Instrument Boundary-Layer Thermodynamic Retrievals, Bound.-Lay. Meteorol., 181, 95–123, https://doi.org/10.1007/S10546-021-00640-2, 2021.

Solomon, A., Shupe, M. D., and Miller, N. B.: Cloud–atmospheric boundary layer–surface interactions on the Greenland Ice Sheet during the July 2012 extreme melt event, J. Climate, 30, 3237–3252, 2017.

Steeneveld, G. J., Ronda, R. J., and Holtslag, A. A. M.: The Challenge of Forecasting the Onset and Development of Radiation Fog Using Mesoscale Atmospheric Models, Bound.-Lay. Meteorol., 154, 265–289, https://doi.org/10.1007/S10546-014-9973-8, 2014.

Stillwell, R. A., Spuler, S. M., Hayman, M., Repasky, K. S., and Bunn, C. E.: Demonstration of a combined differential absorption and high spectral resolution lidar for profiling atmospheric temperature, Opt. Express, 28, 71–93, 2020.

Tardif, R.: The impact of vertical resolution in the explicit numerical forecasting of radiation fog: A case study, in: Fog and boundary layer clouds: Fog visibility and forecasting, 1221–1240, Springer, https://doi.org/10.1007/978-3-7643-8419-7_8, 2007.

Taylor, K. E.: Summarizing multiple aspects of model performance in a single diagram, J. Geophys. Res.-Atmos., 106, 7183–7192, https://doi.org/10.1029/2000JD900719, 2001.

Temimi, M., Fonseca, R. M., Nelli, N. R., Valappil, V. K., Weston, M. J., Thota, M. S., Wehbe, Y., and Yousef, L.: On the analysis of ground-based microwave radiometer data during fog conditions, Atmos. Res., 231, 104652, https://doi.org/10.1016/J.ATMOSRES.2019.104652, 2020.

Toledo, F., Haeffelin, M., Wærsted, E., and Dupont, J.-C.: A new conceptual model for adiabatic fog, Atmos. Chem. Phys., 21, 13099–13117, https://doi.org/10.5194/acp-21-13099-2021, 2021.

Turner, D. and Bennartz, R.: Microwave Radiometer measurements of sky brightness temperature taken at Summit Station, Greenland, 2019, Artic Data Center [data set], https://doi.org/10.18739/A2TX3568P, 2020.

Turner, D., Knuteson, R., Revercomb, H., Lo, C., and Dedecker, R.: Noise reduction of Atmospheric Emitted Radiance Interferometer (AERI) observations using principal component analysis, J. Atmos. Ocean. Technol., 23, 1223–1238, 2006.

Turner, D. D.: Arctic mixed-phase cloud properties from AERI lidar observations: Algorithm and results from SHEBA, J. Appl. Meteorol., 44, 427–444, https://doi.org/10.1175/JAM2208.1, 2005.

Turner, D. D.: Improved ground-based liquid water path retrievals using a combined infrared and microwave approach, J. Geophys. Res.-Atmos., 112, 15204, https://doi.org/10.1029/2007JD008530, 2007.

Turner, D. D. and Blumberg, W. G.: Improvements to the AERIoe thermodynamic profile retrieval algorithm, IEEE J. Se-

lect. Top. Appl. Earth Observ. Remote Sens., 12, 1339–1354, https://doi.org/10.1109/JSTARS.2018.2874968, 2019.

Turner, D. D. and Eloranta, E. W.: Validating mixed-phase cloud optical depth retrieved from infrared observations with high spectral resolution lidar, IEEE Geosci. Remote Sens. Lett., 5, 285–288, https://doi.org/10.1109/LGRS.2008.915940, 2008.

Turner, D. D. and Löhnert, U.: Information Content and Uncertainties in Thermodynamic Profiles and Liquid Cloud Properties Retrieved from the Ground-Based Atmospheric Emitted Radiance Interferometer (AERI), J. Appl. Meteorol. Climatol., 53, 752–771, https://doi.org/10.1175/JAMC-D-13-0126.1, 2014.

Turner, D. D. and Löhnert, U.: Ground-based temperature and humidity profiling: combining active and passive remote sensors, Atmos. Meas. Tech., 14, 3033–3048, https://doi.org/10.5194/amt-14-3033-2021, 2021.

Turner, D. D., Vogelmann, A., Austin, R. T., Barnard, J. C., Cady-Pereira, K., Chiu, J. C., Clough, S. A., Flynn, C., Khaiyer, M. M., Liljegren, J., Johnson, K. Lin, B., Long, C., Marshak, A., Matrosov, S. Y., Mcfarlane, S. A., Miller, M., Min, Q., Minimis, P., O'Hirok, W., Wang, Z., and Wiscombe, D. W.: Thin liquid water clouds: Their importance and our challenge, B. Am. Meteorol. Soc., 88, 177–190, 2007.

Turner, D. D., Kneifel, S., and Cadeddu, M. P.: An Improved Liquid Water Absorption Model at Microwave Frequencies for Supercooled Liquid Water Clouds, J. Atmos. Ocean. Technol., 33, 33–44, https://doi.org/10.1175/JTECH-D-15-0074.1, 2016.

Van Tricht, K., Gorodetskaya, I. V., Lhermitte, S., Turner, D. D., Schween, J. H., and Van Lipzig, N. P. M.: An improved algorithm for polar cloud-base detection by ceilometer over the ice sheets, Atmos. Meas. Tech., 7, 1153–1167, https://doi.org/10.5194/amt-7-1153-2014, 2014.

Von P. Walden and Shupe, M.: Radiosonde temperature and humidity profiles taken at Summit Station, Greenland, 2019, Artic Data Center [data set], https://doi.org/10.18739/A20P0WR53, 2020.

Wærsted, E. G., Haeffelin, M., Dupont, J.-C., Delanoë, J., and Dubuisson, P.: Radiation in fog: quantification of the impact on fog liquid water based on ground-based remote sensing, Atmos. Chem. Phys., 17, 10811–10835, https://doi.org/10.5194/acp-17-10811-2017, 2017.

Walden, V., Town, M., Halter, B., and Storey, J.: First measurements of the infrared sky brightness at Dome C, Antarctica, Publications of the Astronomical Society of the Pacific, 117, 300, 2005.

Westerhuis, S. and Fuhrer, O.: A Locally Smoothed Terrain-Following Vertical Coordinate to Improve the Simulation of Fog and Low Stratus in Numerical Weather Prediction Models, J. Adv. Model. Earth Syst., 13, e2020MS002437, https://doi.org/10.1029/2020MS002437, 2021.

Wilcox, E. M.: Multi-spectral Remote Sensing of Sea Fog with Simultaneous Passive Infrared and Microwave Sensors, Marine Fog: Challenges and Advancements in Observations, Modeling, and Forecasting, Springer Atmospheric Sciences, Springer, Cham, 511–526, https://doi.org/10.1007/978-3-319-45229-6_11, 2017.

Wu, D., Lu, B., Zhang, T., and Yan, F.: A method of detecting sea fogs using CALIOP data and its application to improve MODIS-based sea fog detection, J. Quant. Spectrosc. Rad. Transf., 153, 88–94, https://doi.org/10.1016/J.JQSRT.2014.09.021, 2015.

Wulfmeyer, V., Hardesty, R. M., Turner, D. D., Behrendt, A., Cadeddu, M. P., Girolamo, P. D., Schlüssel, P., Baelen, J. V., and Zus, F.: A review of the remote sensing of lower tropospheric thermodynamic profiles and its indispensable role for the understanding and the simulation of water and energy cycles, Rev. Geophys., 53, 819–895, https://doi.org/10.1002/2014RG000476, 2015.

Yi, L., Li, K.-F., Chen, X., and Tung, K.-K.: Arctic Fog Detection Using Infrared Spectral Measurements, J. Atmos. Ocean. Technol., 36, 1643–1656, https://doi.org/10.1175/JTECH-D-18-0100.1, 2019.

Chapter 4.

Observations of fog-aerosol interactions over central Greenland

Prepared for submission to *Journal of Geophysical Research: Atmospheres*.

Observations of fog-aerosol interactions over central Greenland

Heather Guy[1,2], Ian M. Brooks[2], David D. Turner[3], Christopher J. Cox[4], Penny M. Rowe[5], Matthew D. Shupe[6,4], Von P. Walden[7], Ryan R. Neely III[1,2]

[1]National Centre for Atmospheric Science, Leeds, U.K.
[2]School of Earth and Environment, University of Leeds, U.K.
[3]3Global Systems Laboratory, National Oceanic and Atmospheric Administration, Boulder, CO, USA
[4]Physical Sciences Laboratory, National Oceanic and Atmospheric Administration, Boulder, USA
[5]NorthWest Research Associates, Redmond, WA, USA
[6]University of Colorado, Cooperative Institute for Research in Environmental Sciences, Boulder, USA
[7]Department of Civil and Environmental Engineering, Laboratory for Atmospheric Research, Washington State University, Pullman, WA, USA

Key Points:

- Ground-based measurements of downwelling longwave radiation can be used to determine the microphysical properties of optically thin fogs.
- Almost all aerosol particles larger than 250 nm diameter are scavenged during twelve summer fog events in central Greenland.
- Multiple pathways exist through which the aerosol population can impact fog development, and fog can modify the surface aerosol population.

Corresponding author: Heather Guy, heather.guy@ncas.ac.uk

Abstract

Supercooled fogs can have an important radiative impact at the surface of the Greenland Ice Sheet, but they are difficult to detect and our understanding of the factors that control their lifetime and radiative properties is limited by a lack of observations. This study demonstrates that spectrally resolved measurements of downwelling longwave radiation can be used to generate retrievals of fog microphysical properties (phase and particle effective radius) when the fog visible optical depth is greater than ∼0.25. For twelve cases of fog under otherwise clear skies between June and September 2019 at Summit Station in central Greenland, nine cases were mixed-phase. The mean ice particle (optically-equivalent sphere) effective radius was 24.0 ± 7.8 μm, and the mean liquid droplet effective radius was 14.0 ± 2.7 μm. These results, combined with measurements of aerosol particle number concentrations, provide observational evidence supporting the hypotheses that (a) low surface aerosol particle number concentrations can limit fog liquid water path, (b) fog can act to increase near-surface aerosol particle number concentrations through enhanced mixing, and (c) multiple fog events in quiescent periods gradually deplete near-surface aerosol particle number concentrations.

Plain Language Summary

Fogs over the central Greenland Ice Sheet can modify the net radiation that reaches the ice surface. How much a fog influences the net surface radiation is related to the fog lifetime and optical depth. These properties are related to the phase and size distribution of the particles that make up the fog, that in turn depend on the characteristics of the atmospheric aerosol particles on which the fog forms. This study shows that the phase and size distribution of fog particles can be determined from ground-based measurements of downwelling longwave radiation, and explores how fogs interact with the number concentration of atmospheric aerosols measured near the surface during twelve cases of summertime fog in central Greenland.

1 Introduction

Central Greenland is a unique environment in the Northern Hemisphere: A uniform surface of snow-covered ice extends for over 250 km in every direction from the ice sheet's highest point at 3,250 m a.s.l (Howat et al., 2017). The structure of the atmospheric boundary layer over the ice sheet is driven by large-scale circulation, including atmospheric rivers associated with extratropical storms (Mattingly et al., 2018; Gallagher et al., 2018) and blocking anticyclones (Pettersen et al., 2022), and is modulated locally by strong radiative cooling at the ice sheet surface (Hoch et al., 2007). Under quiescent conditions (clear skies, light winds), surface radiative cooling frequently drives the formation of supercooled radiation fog through the condensation of water onto aerosol particles that act as cloud condensation nuclei (CCN) (Bergin et al., 1994; Cox et al., 2019).

At Summit Station (Summit), a research base located at the highest point on the Greenland Ice Sheet (72.57°N, -38.47°E), fogs comprised of supercooled droplets occur year-round even when the surface temperature falls below -30°C (Cox et al., 2019). These fogs can have a strong effect on the ice sheet surface energy budget, contributing on average an additional 27 W m^{-2} of total net downwelling radiation relative to clear sky conditions (Cox et al., 2019). In the summer months (May to September) solar heating of the ice sheet surface during the day results in a diurnal cycle of net surface radiation. Radiation fog forms during the period of the diurnal cycle when the sun elevation is lowest and the net radiative cooling at the surface is strongest, and the associated increase in net downwelling longwave radiation acts to damp the diurnal temperature cycle, which has been hypothesised to precondition the ice sheet surface for melt (Cox et al., 2019). These fogs can also increase the rate of aerosol deposition to the surface (Bergin et al.,

1994, 1995) and reduce ice sheet mass loss by recondensing sublimated water onto fog particles that then settle out under gravity (Berkelhammer et al., 2016).

Understanding the controls on the processes that modify the surface mass balance of the Greenland Ice Sheet is becoming increasingly important as melt events become more common and widespread (Tedesco & Fettweis, 2020; Hanna et al., 2021). The radiative impact of fog at the ice sheet surface depends on fog occurrence, duration, and optical depth, which itself is determined by the fog liquid water path (LWP), and microphysical properties such as fog particle phase and size distribution. The representation of fog microphysical properties is one of the largest sources of uncertainty in fog forecast models and Large-eddy simulations (Boutle et al., 2022), and the representation of cloud microphysical properties in general is one of the largest sources of uncertainty in projections of future Greenland Ice Sheet melt (Hofer et al., 2019). One of the reasons for these uncertainties is that there are very limited observations available to constrain model parameterisations. This is particularly true for fog over Greenland, which often occurs in shallow layers (< 100 m) below the lowest range gate of most ground-based active remote sensing instruments (such as radar or lidar). These very shallow fog layers are often subgrid-scale for most climate and weather models.

Important controls on fog (and cloud) lifetime, microphysical, and radiative properties are the number concentration, size distribution, and composition of aerosol particles on which droplets or ice crystals can form. Droplets form on CCN, so the number concentration of CCN determines the number concentration of droplets at a given supersaturation. When the CCN concentration is increased, a fog will contain a greater number of smaller droplets than an equivalent fog (with the same liquid water content) forming under a reduced CCN concentration, resulting in a relatively high fog optical depth and solar reflectivity, and hence impacting the net downwelling radiation at the surface (Twomey, 1977). Increased fog droplet number concentration also leads to enhanced longwave radiative cooling at fog top (e.g. Garrett, Radke, & Hobbs, 2002), encouraging further droplet activation, and smaller droplets that are not removed as quickly by sedimentation, with both processes working to extend fog lifetime (Maalick et al., 2016; Boutle et al., 2018; Yan et al., 2021). Increased fog top cooling can also enhance mixing and entrainment that, depending on the humidity of the overlying air, can either reduce or increase cloud/fog water content (Ackerman et al., 2004; Small et al., 2009; Williams & Igel, 2021).

In very clean environments, low CCN concentrations can limit fog (and cloud) formation and lifetime, because the few activated CCN will grow to relatively large sizes and precipitate out, removing CCN and preventing further droplet formation (Mauritsen et al., 2011; Stevens et al., 2018). Evidence suggests that this situation can occur in the Arctic, where naturally low concentrations of CCN (1 to 100 cm^{-3}) have the potential to control cloud radiative properties (Mauritsen et al., 2011; Sterzinger et al., 2022). At Summit, the annual mean aerosol particle concentration is low even compared to other Arctic sites (Schmeisser et al., 2018); the mean annual total surface aerosol particle number concentration (> 20 nm) at Summit in 2019-2020 was just 129 cm^{-3}, and fell to less than 10 cm^{-3} on occasions in all seasons (Guy et al., 2021). Given that only some of these aerosol particles act as CCN, these numbers are an upper limit on the number of CCN available near the surface where fog forms.

When the temperature is below freezing, which is the case almost all the time in central Greenland (Shupe et al., 2013), the phase partitioning of the fog is also important for fog lifetime and the radiative effect of the fog at the surface. Ice fogs usually form through the direct deposition of vapour onto ice-nucleating particles (INPs, a subset of the aerosol population that can catalyse freezing) when the air is supersaturated with respect to ice (Gultepe et al., 2015). Ice nucleation can also occur in supercooled liquid fogs by either immersion freezing (INPs are activated within a droplet) or contact freezing (droplets freeze upon contact with an INP) (Kanji et al., 2017). Once primary ice

is present, further ice can form through several different multiplicative mechanisms, collectively known as secondary ice production (Field et al., 2017). If the air becomes supersaturated with respect to ice but subsaturated with respect to water, ice crystals will grow at the expense of liquid water droplets, causing the liquid droplets to evaporate and the ice crystals to grow to relatively large sizes and settle out, removing moisture from the surface layer and acting to reduce fog lifetime; this is known as the Wegener-Bergeron-Findeisen process (e.g. Korolev, 2007).

In addition to the aerosol population having the potential to control fog lifetime and radiatively important microphysical properties, fog formation may also be an important control on the lifecycle of aerosol particles in the boundary layer over central Greenland. Fog can act as an aerosol sink, because the fog droplet deposition flux exceeds that of aerosol dry deposition (Bergin et al., 1994, 1995). Through this mechanism, fog may act to 'clean' the boundary layer of CCN and INP, which may in turn impact fog and/or cloud formation later in time. Conversely, fog could act to increase aerosol particles in the boundary layer by enhancing the transport of aerosol particles from above the fog top into the surface layer, either by buoyancy or windshear driven turbulent entrainment at fog top, or by aerosol activation at fog top followed by droplet evaporation closer to the surface. Observational and model studies have demonstrated that the latter process can be important in low-level Arctic stratocumulus (Solomon et al., 2014; Igel et al., 2017).

The relative importance of each of these fog-aerosol interactions over central Greenland is unknown, and our ability to model these processes is hindered by a lack of observations of both fog microphysical properties and surface aerosol number concentration and size distribution. Using in-situ measurements collected at Summit in 2013-2014, Cox et al. (2019) completed a comprehensive assessment of the occurrence, microphysical characteristics, and radiative properties of fogs at Summit, but there were no aerosol particle measurements available during this period. This study builds on the findings of Cox et al. (2019), and has two main objectives: (1) to explore the possibility of using spectral measurements of downwelling longwave radiation to generate retrievals of fog microphysical properties, and (2) to use these results alongside measurements of surface aerosol particle number concentration to look for observational evidence of fog-aerosol interactions over central Greenland.

The spectral signature of downwelling longwave radiation is sensitive to the radiative properties of fog that are important for the ice sheet surface energy budget and can be measured continuously by passive ground-based instrumentation that, unlike many active remote sensing instruments, are not limited by the height of their lowest range gate and so do not have a 'blind' spot close the surface. Such measurements have been used to study the microphysical properties of mixed-phase polar clouds (Mahesh et al., 2001; Rathke et al., 2002; Turner, 2005; Garrett & Zhao, 2013; Cox et al., 2014; Shupe et al., 2015; Lubin et al., 2020; Richter et al., 2022); however, these studies did not specifically focus on fog.

Here, we use a case-study based approach to examine the advantages and limitations of retrieving the microphysical properties of fog from downwelling longwave radiation measurements. Such measurements have the greatest sensitivity to the microphysical properties of clouds when the atmosphere is dry and the clouds are low and optically thin. In addition, retrieval accuracy relies on a well-constrained cloud temperature. Taken together, this makes such measurements ideal for studying fog over central Greenland.

For objective (2), we combine the results of the fog microphysical retrievals with measurements of surface aerosol particle number concentrations and supplementary observations of atmospheric state to look for observational evidence to support (or negate) the following hypotheses:

(a) That low aerosol particle number concentration can be a critical control on fog liquid water path and lifetime.
(b) That fogs can act to increase surface aerosol particle number concentration by enhancing mixing of air from above into near-surface stable layer.
(c) That multiple fog events during quiescent conditions act to deplete near surface aerosol particle number concentration, impacting fog development later in time.

The results of this analysis may be used as the basis of future modelling studies to systematically distinguish the importance of different fog-aerosol interaction processes, and to identify instrumentation requirements for future observational campaigns to study fog-aerosol interactions over central Greenland or in similar environments.

2 Measurements and instrumentation

We make use of measurements from the ICECAPS project (the Integrated Characterisation of Energy, Clouds, Atmospheric state, and Precipitation at Summit; Shupe et al., 2013) which consists of a suite of instrumentation for monitoring atmospheric processes at Summit. To generate the microphysical retrievals of fog properties we use data from the Atmospheric Emitted Radiance Interferometer (AERI), which measures spectrally resolved downwelling infrared radiance between 3 and 19 μm at $\sim$0.48 cm^{-1} resolution (Knuteson et al., 2004b, 2004a). At Summit, the AERI measures downwelling radiation continuously, alternating between views of the sky at zenith and two calibration sources, resulting in sky measurements every 15-20 s. The AERI data are quality controlled as described in Guy et al. (2022) and subjected to noise filtering using the technique described by Antonelli et al. (2004) and Turner et al. (2006). Section 3 describes the retrieval algorithm.

To explore individual fog cases in more depth we examine data from the ceilometer (CT25K, Münkel, 2006), sodar (Neff et al., 2008), total sky imager, and near-surface temperature profiles and sensible heat flux estimates from tower-mounted in-situ sensors (Guy et al., 2020). Data from the millimetre cloud radar and precipitation occurrence sensor system were used to help identify fog cases during the summer of 2019, and radiosonde data were used to help constrain retrievals of continuous thermodynamic profiles from the AERI that are required as an input to the microphysical retrieval algorithm; both steps are described in detail in Guy et al. (2022). See Shupe et al. (2013) for further information about the overall ICECAPS instrumentation suite.

2.1 Aerosol particle measurements

During the summer of 2019 there were two instruments at Summit measuring surface aerosol particle number concentration in different size ranges: a butanol-based condensation particle counter (CPC, GRIMM 5.400) that measured the total concentration of condensation nuclei every second, and an optical particle counter (SKYOPC, GRIMM 1.129) that measured size-resolved concentrations of 250 to 4500 nm diameter particles every six seconds. Guy et al. (2021) describe the CPC data in more detail, including the estimation of particle loss in the inlet line, which resulted in the CPC measuring the number concentration of condensation nuclei with diameters between 20 and 230 nm with greater than 50% efficiency. For this reason, measurements from the CPC are henceforth referred to as N_{20}, indicating the number concentration of particles $>$ 20 nm diameter.

The SKYOPC had an identical inlet to the CPC but a higher flow rate (1.2 L min^{-1}), and as a result larger particles could pass through the SKYOPC inlet. After accounting for particle losses in the inlet (using the Particle Loss Calculator, Von der Weiden, Drewnick, & Borrmann, 2009), the SKYOPC measured the number concentration of particles with diameters between 250 and 4500 nm with greater than 50% efficiency. For the SKYOPC, the measurements were corrected for particle loss in the inlet by multiplying

the particle number concentration by a correction factor based on the modelled inlet efficiency as a function of particle size (which varied from 1.02 to 1.97 in the 250 to 4500 nm size range). The total particle number concentration between 250 and 4500 nm (henceforth N_{250}) was calculated by summing the corrected size resolved SKYOPC data.

Particles larger than 6 μm in diameter, which is smaller than the typical size of fog droplets (e.g. Mazoyer, Burnet, & Denjean, 2022), could not pass through either inlet, and the instruments were located in a heated building that was always >15°C warmer than the outside air. Thus, during fog events, we assume that N_{20} and N_{250} are measurements of the dried interstitial aerosol particle number concentration. Both N_{20} and N_{250} were resampled to five-minute medians for the purpose of this study, and quality controlled to remove any instances of contamination from station pollution as in Guy et al. (2021). Note that this quality control does not impact any of the data presented here, because none of the fog cases coincide with local pollution events (which was part of the original event selection criteria).

Figure 1 shows how the measurements from the SKYOPC (N_{250}) and CPC (N_{20}) intersect with the 'typical' size range of CCN and INP from past literature, although the proportion of aerosol particles that can act as a CCN depends on the aerosol type and degree of supersaturation, and our knowledge of the typical size range of INP particles is limited by sparse observations (particularly of small INP particles < 250 nm diameter). Supersaturations can reach higher values when the aerosol particle number concentration is low, and particles as small as 20 nm have been observed to act as CCN in clean Arctic environments (Leaitch et al., 2016; Baccarini et al., 2020). Several studies indicate that the INP population is mostly made up of coarse-mode particles > 250 nm diameter (Mason et al., 2016; Creamean et al., 2018; Si et al., 2018), however recent studies of size-resolved INP concentration over the central Arctic suggest that particles as small as 150 nm diameter can be an important source of INP (Creamean et al., 2022; Porter et al., 2022). Figure 1 also shows how measurements during the summer of 2019 compare to those collected between 15 May and 16 June 2007 using a scanning mobility particle sizer to detect particles with diameters from 5.5 to 195 nm diameter (Ziemba et al., 2010), and how they compare to the 'typical' size distribution of near-surface aerosol particles in the Arctic summer, which is mostly based on measurements from coastal and low elevation Arctic sites (Carslaw & Pringle, 2022).

2.2 Fog events

We focus on the twelve radiation fog events identified by Guy et al. (2022) that occurred during the summer of 2019 (Table 1). Each fog event occurred under otherwise clear skies and had a detectable longwave radiative impact at the surface; the duration of each fog event was defined as when the 962 cm^{-1} downwelling radiance measured by the AERI is greater than a threshold of 1.7 RU (1 RU = 1 mW m^{-2} sr^{-1} cm^{-1}), which is three standard deviations above the mean clear sky radiance between June and September 2019. The 962 cm^{-1} microwindow is almost completely transparent under clear skies for conditions at Summit, and is therefore particularly sensitive to the presence of clouds (e.g. Cox, Walden, & Rowe, 2012). Note that this radiative definition of fog is distinct from the traditional definition of fog (a reduction of horizontal visibility to < 1,000 m) but is appropriate for this study because we are concerned with the radiative impact of fog on the surface energy budget. See Guy et al. (2022) for further details about the selection criteria for each of these case studies.

Table 1 details each case study and indicates where aerosol particle number concentration measurements are available. The SKYOPC vacuum pump experienced intermittent faults resulting in missing N_{250} data for some of the fog cases, and an issue with the CPC power supply resulted in incomplete N_{20} data for case 3.

Table 1. Details of fog events and data availability. Adapted from table 3 in Guy et al. (2022) and includes the mean temperature (T) and water vapor mixing ratio (wv) during each event. The minimum visibility comes from observer reports at 00, 12 and 18 UTC and may not represent the minimum visibility outside of these times. NA indicates where no data are available. Local time is UTC-3h.

ID	Case start Date Time. UTC, 2019	Case end Date Time UTC, 2019	Duration (h)	Mean surface T (°C)	Mean surface wv (g kg^{-1})	Min. visibility observer log	Min. ceilometer vertical visibility	Particle conc. available
1	08 Jun 03:30	08 Jun 05:50	2.3	-17	1.3	NA	30 m	N_{20} only
2	12 Jun 02:55	12 Jun 10:30	7.6	-8.9	2.7	NA	30 m	N_{20} only
3	13 Jul 23:25	14 Jul 04:30	5.1	-21	0.93	1,600 m	30 m	N_{250} only
4	15 Jul 23:10	16 Jul 10:30	11	-19	1.0	400 m	30 m	Yes
5	31 Jul 23:25	01 Aug 04:35	5.2	-8.6	2.7	400 m	25 m	N_{20} only
6	01 Aug 22:00	02 Aug 14:40	17	-12	2.0	800 m	20 m	N_{20} only
7	04 Aug 06:35	04 Aug 08:15	1.7	-17	1.2	NA	NA	Yes
8	04 Aug 22:40	05 Aug 11:50	13	-18	1.2	400 m	15 m	Yes
9	06 Aug 01:05	06 Aug 10:00	8.9	-21	0.82	NA	30 m	N_{20} only
10	14 Aug 23:05	15 Aug 08:00	8.9	-27	0.49	3,200 m	43 m	Yes
11	05 Sep 04:30	05 Sep 08:35	4.1	-25	0.61	NA	30 m	Yes
12	30 Sep 03:30	30 Sep 11:05	7.6	-28	0.46	NA	NA	Yes

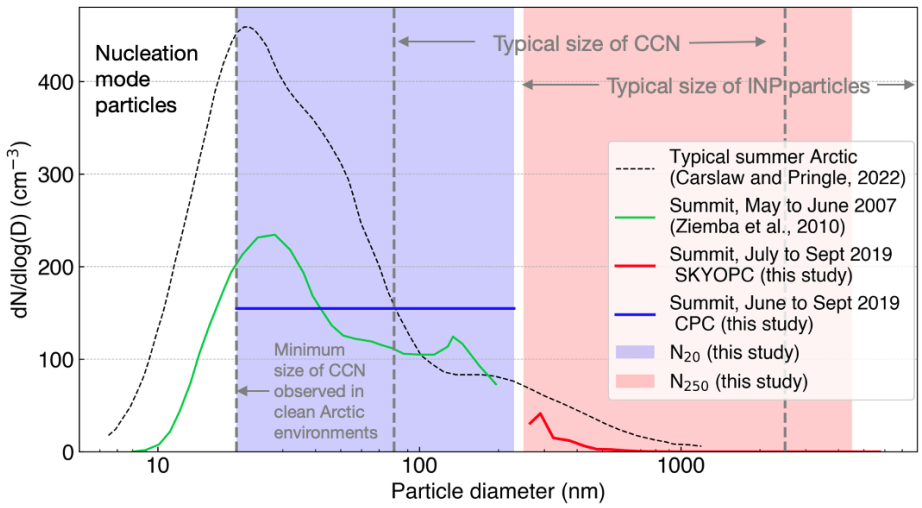

Figure 1. The portion of the aerosol particle size distribution measured in this study, N_{20} shaded in blue and N_{250} in red, overlaid on the typical size distribution of the near-surface Arctic atmosphere in summer (Carslaw & Pringle, 2022, black dashed line), and the observed size distribution of surface aerosol particles at Summit between May and June 2007 from Ziemba et al. (2010) (green line). The blue and red lines indicate the mean values from the CPC (a single value in the range 20 to 230 nm) and the SKYOPC (size resolved measurements in 20 bins between 250 and 4500 nm) observed between June (or July for the SKYOPC) and September 2019.

3 Retrieval of fog microphysical properties

We use the mixed-phase cloud property retrieval algorithm (MIXCRA, Turner, 2005), which uses optimal estimation to retrieve fog microphysical properties at 5-min intervals from the spectral longwave radiation measured by the AERI (note that we did not apply temporal averaging to the AERI spectra). The longwave radiation is sensitive to changes in cloud/fog phase, particle size, and optical depth when the optical depth is between ∼0.25 and 6, allowing the retrieval of these properties using optimal estimation (Turner, 2005; Cox et al., 2014). As the optical depth approaches the upper end of this range, the longwave spectral signature of the cloud/fog approaches that of a black body and contains little information about microphysical properties. As the optical depth approaches the lower end of this range, the signal to noise ratio of the AERI becomes too low for meaningful retrievals. Figure 2 shows how the mean spectral signature from the AERI during the fog events varied, spanning much of the dynamical range between clear sky conditions and optically thick stratus in the atmospheric window region (where the cloud-free atmosphere is mostly transparent to longwave gaseous absorption ∼800 to 1200 cm^{-1}).

MIXCRA models each fog event as two collocated 'clouds', one consisting of ice crystals and the other of water droplets. Starting from user input a priori values of optical depth (τ) and particle effective radius (R) for each cloud (τ_{liq} and R_{liq} for the liquid cloud and τ_{ice} and R_{ice} for the ice cloud), as well as vertical profiles of atmospheric temperature and water vapor content, the algorithm uses a forward model to calculate the expected spectral signature of the combined cloud and atmosphere, and then iterates using optimal estimation to determine the values [τ_{liq}, R_{liq}, τ_{ice}, R_{ice}] that optimally match the spectral signature observed by the AERI, given the a priori and the measurement uncertainty.

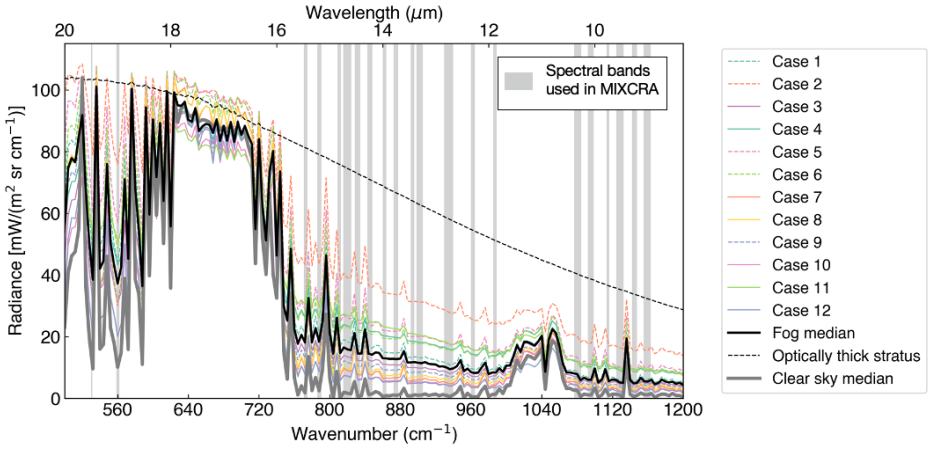

Figure 2. AERI radiance measurements averaged over each fog case (colored lines, see legend inset). The thick black line shows the median for all fog cases, which can be contrasted to the median over all confirmed clear sky hours (thick grey line), and an example of an optically thick stratus cloud (from 01 to 02 UTC on 08 June 2019, dashed black line). Spectral radiance is resampled to 4 cm^{-1} for clarity (native resolution is 0.5 cm^{-1}). Vertical grey lines show the spectral bands used in the MIXCRA retrievals (between major gaseous absorption bands). Note the two spectral bands at wavenumbers below 570 cm^{-1}; these are critical for ascertaining the phase of the fog layers (?, ?; Turner, 2005).

Note that throughout this study τ refers to the visible optical depth (where extinction efficiency is 2), transformed from the optical depth at 11 μm as described in Turner (2005). See Turner (2005) for further information about the implementation of the optimal estimation. After the retrieval of [τ_{liq}, R_{liq}, τ_{ice}, R_{ice}], fog LWP is determined from equation (1), where ρ is the bulk density of water.

$$LWP = \frac{2\rho R_{liq}\tau_{liq}}{3} \tag{1}$$

MIXCRA uses the Line-by-Line Radiative Transfer Model (LBLRTM) version 12.1 (Clough et al., 1992; Clough & Iacono, 1995) as a forward model to calculate the gaseous clear sky optical depth spectra as a function of height, and the DISORT algorithm (Stamnes et al., 1988) to simulate radiance from the ice and liquid cloud (which accounts for both scattering and absorption); the combined LBLRTM and DISORT code is referred to as LBLDIS. The HITRAN 2008 database (Rothman et al., 2009) provides the molecular absorption properties used by the LBLRTM. The single-scattering properties used by DISORT are discussed in section 3.1.1. The radiative transfer calculation also requires information about the thermodynamic structure of the atmosphere and profiles of atmospheric gases. Trace gas concentrations are supplied by the U.S. standard atmosphere (1976), and CO_2 concentrations are scaled to mimic the seasonal and yearly increase in atmospheric CO_2 observed at the Mauna Loa observatory. Uncertainties related to the distribution and concentration of these gases are mitigated in MIXCRA by only including narrow spectral bands (micro-windows) from the AERI in the optimal estimation process, and hence avoiding major gaseous absorption bands (the micro-windows used in this study are highlighted on fig. 2).

Thermodynamic profiles (temperature and water vapor) used within MIXCRA were retrieved using the TROPoe algorithm, which also uses an optimal estimation approach

based on AERI observations, taking advantage of the fact that the AERI is also highly sensitive to the thermodynamic structure of the atmosphere (Turner & Blumberg, 2019; Turner & Löhnert, 2021). The accuracy of the TROPoe thermodynamic profile retrievals during the 12 fog case studies is $\pm 1.0°$C for temperature and ± 0.39 g kg^{-1} for water vapor in the lowest 1,000 m a.g.l (Guy et al., 2022). We assume that any impact of aerosols on the radiative transfer calculation is negligible, because the absorption and scattering coefficients of aerosol particles in the infrared at Summit are generally small (Schmeisser et al., 2018) and there are no local sources of aerosol particles near Summit after instances of local pollution from the station are excluded.

The a priori value of τ_{liq} used as starting point for the optimal estimation is based on the LWP retrieved by the TROPoe algorithm (Guy et al., 2022) with a standard deviation of 6. Note that TROPoe does not account for scattering processes and assumes only liquid droplets are present; MIXCRA adjusts this first guess value to account for the possible presence of ice particles and accounts for multiple scattering. The a priori value for R_{liq} is set to 11 ± 6 μm, based on in-situ measurements of the size distribution of fog droplets at Summit in 2013 and 2014 (Cox et al., 2019). The a priori ice optical depth is set to 0 with a standard deviation of 6, which gives the algorithm flexibility to retrieve ice properties. The choice to initiate the retrieval with a liquid-only cloud is based on the fact that liquid phase fogs are more commonly detected than ice fogs during the summer at Summit (Cox et al., 2019). The a priori ice particle effective radius is set to 18 ± 15 μm based on the distribution of ice crystal effective radius retrieved from mixed-phase clouds over the Arctic Ocean in 1998 (Turner, 2005).

3.1 Uncertainty quantification and quality control

As an initial quality control, we omit any retrievals where the root mean squared error (RMSE) between the final forward radiance calculation (that is, the calculation of expected radiance using the retrieved cloud properties) and the measured AERI radiance is > 1.2 RU. The goal of this quality control is to omit any retrievals for which the retrieval is unable to bring the calculated radiance into agreement with the measured radiance to within the expected instrument uncertainty level (a threshold of 1.2 RU is selected because in 90% of all retrievals the RMSE corresponding to a 3σ uncertainty in the AERI measurements due to noise and calibration uncertainty falls below this value). For rejected retrievals, we assume that additional unknown sources of error exist (e.g. large errors in temperature), hindering accurate cloud property retrievals. Cox et al. (2019) also used a threshold of 1.2 RU for the retrieval of cloud microphysical properties from AERI measurements in northern Canada.

MIXCRA calculates the uncertainties in [τ_{liq}, R_{liq}, τ_{ice}, R_{ice}] by propagating the calibration uncertainty of the AERI ($< 1\%$ of ambient radiance, described in Knuteson et al., 2004a) and the uncertainty associated with the sensitivity of the forward model (i.e. how much the spectral cloud emissivity changes with small perturbations in [τ_{liq}, R_{liq}, τ_{ice}, R_{ice}]) through the optimal estimation algorithm (Turner, 2005). Figure 3 shows how the 2σ percentage uncertainty (as output by the MIXCRA algorithm) varies as a function of τ_{liq} (for τ_{liq} and R_{liq}) and τ_{ice} (for τ_{ice} and R_{ice}) for all the retrievals during the fog events. For all retrieved properties, the minimum percentage uncertainties occur when the fog optical depth is $\sim$1, consistent with the findings of Turner (2005).

The percentage uncertainties in all properties increase when the fog is mixed phase (i.e. when both τ_{liq} and $\tau_{ice} > 0.02$, light blue and pink colours in fig. 3), which is related to the additional degrees of freedom when retrieving properties for a mixed-phase cloud compared to a single-phase cloud as well as the challenges of separating the two phases cleanly (because the liquid and ice signals are correlated). The higher percentage uncertainties in R_{ice} compared to R_{liq} are related to the fact that the retrieval is more sensitive to small particles, and ice particles are generally larger than liquid droplets.

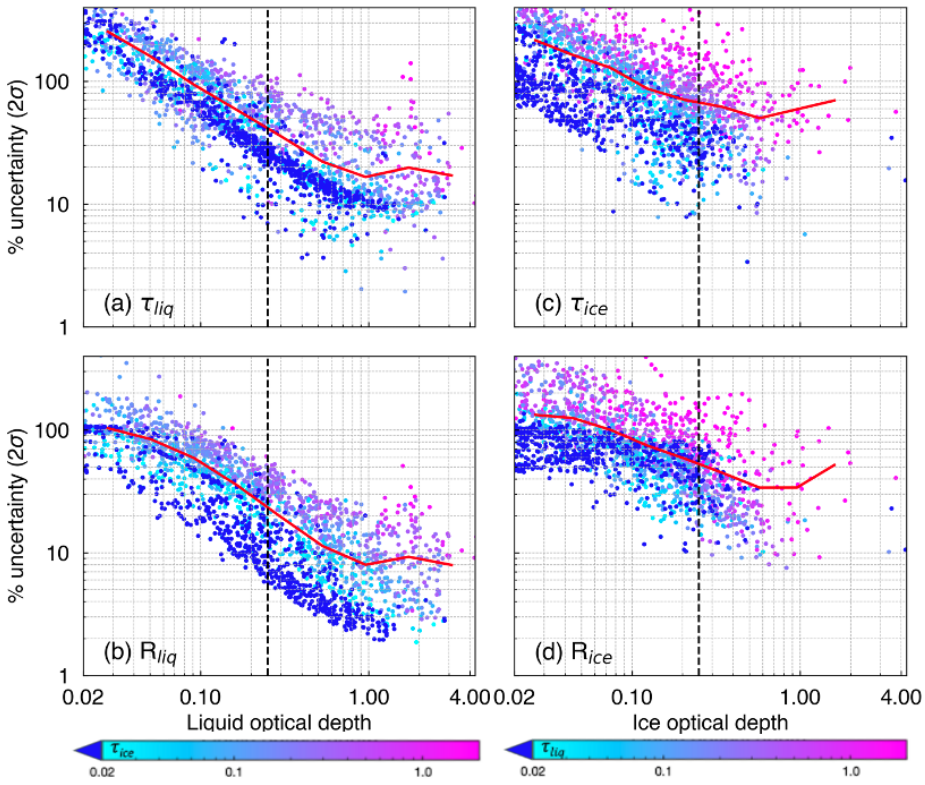

Figure 3. Percentage uncertainty (2σ) in (a) τ_{liq} and (b) R_{liq} as a function of τ_{liq} , and in (c) τ_{ice} and (d) R_{ice} as a function of τ_{ice}, for every retrieval used in this study. The red line is the mean value (in nine logarithmically spaced bins). Points are coloured based on the magnitude of τ_{ice} (a and b) or τ_{liq} (c and d). The black vertical dashed line highlights an optical depth of 0.25 used as a minimum required optical depth for valid retrievals in this study.

As the fog optical depth approaches zero, the percentage uncertainties in all retrieved properties become very large due to the decreasing signal-to-noise ratio, necessitating the selection of a minimum optical depth above which fog microphysical properties can be retrieved with an acceptable level of uncertainty. For this study we choose to use an optical depth threshold of $\tau_{liq} > 0.25$ (for τ_{liq}, R_{liq} and LWP) and $\tau_{ice} > 0.25$ (for τ_{ice}, R_{ice}), consistent with Cox et al. (2014), resulting in a mean 2σ percentage uncertainty of $< 40\%$ for τ_{liq} and $< 20\%$ for R_{liq} (fig. 3). This corresponds to a minimum detectable liquid water path of 2.0-3.0 g m^{-2} (for R_{liq} 12 to 18 μm) with a 2σ uncertainty of 0.9-1.5 g m^{-2}. For ice properties, $\tau_{ice} > 0.25$ corresponds to when the mean percentage uncertainties in τ_{ice} and R_{ice} are below $\sim$60% (fig. 3).

We do not need to be concerned about a loss of sensitivity due to saturation in the infrared, because none of the fog cases have a spectral signature approaching that of a black body (fig. 2). Furthermore, because the maximum precipitable water vapor (PWV) during the 12 fog events is only 0.78 cm (with a mean value of 0.35 cm across all events), the ability of MIXCRA to determine fog phase is not impacted by excessive water vapor ($>$ 1 cm PWV can lead to signal saturation in the 16 to 20 μm region, Turner, 2005; Cox et al., 2014). Figure 4 shows the percentage of retrievals during each case study that meet the quality control criteria of RMSE < 1.2 RU and $\tau_{liq} > 0.25$ (for liquid phase retrievals) or $\tau_{ice} > 0.25$ (for ice phase retrievals). Less than 8% of all retrievals are discarded due to poor RMSE, but the optical depth threshold severely limits the percentage of valid retrievals in each fog case, and in case 7, the optical depth is too low for any valid retrievals.

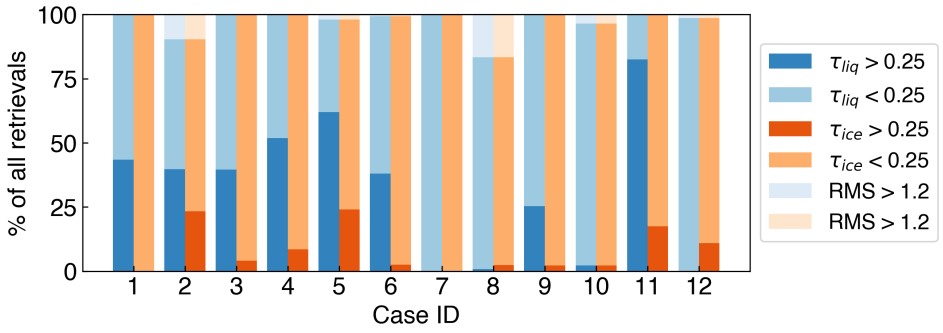

Figure 4. The percentage of all retrievals from each case study that meet the quality control criteria of RMSE < 1.2 and optical depth > 0.25 for liquid properties (blue) and ice properties (orange). The percentage of good retrievals used in the remainder of this study are shown by the dark blue and orange colours.

The MIXCRA algorithm does not account for uncertainties in the atmospheric state (gas and temperature profiles) or for uncertainties related to the choice of single-scattering properties (SSPs) for liquid droplets and ice crystals. As mentioned above, uncertainties related to the concentrations of atmospheric gases are minimised through the selection of micro-windows used by MIXCRA. The atmospheric temperature profile has a mean RMSE (compared to radiosonde profiles) of ± 1°C in the lowest 1,000 m above ground level (a.g.l.) during these case studies (Guy et al., 2022), and the difference in the retrieved values of [τ_{liq}, R_{liq}, τ_{ice}, R_{ice}] if the temperature profile is uniformly increased or decreased by 1°C are small, resulting in a mean difference in τ_{liq} of 0.2 and R_{liq} of 0.8 μm based on sensitivity tests with 38 retrievals.

404 ### *3.1.1 Uncertainties related to the choice of SSPs*

405 The choice of single-scattering properties (SSPs) to use in the retrievals is non-trivial.
406 There is emerging evidence that the SSPs of supercooled water droplets are tempera-
407 ture dependent, and that the use of SSPs that assume a warmer temperature than re-
408 ality can result in overestimations of ice fraction and underestimations of liquid droplet
409 effective radius (Rowe et al., 2013, 2022). Although the temperature profile during the
410 fog events is well characterised, the temperature during a single event can vary by up
411 to 13°C both temporally and vertically within the lowest 15 m a.g.l due to radiative cool-
412 ing and changes in boundary layer mixing (fig. S1, supporting information). Further-
413 more, the SSPs of ice crystals depend on the ice crystal habit (e.g. Yang et al., 2005),
414 but there is very little information about ice crystal habit at Summit during fog events.
415 Isolated plates and bullets are often reported by observers, but whether any of these crys-
416 tals are associated with fog events (as opposed to snow, blowing snow, or diamond dust)
417 is unclear. A multi-angled snowflake camera operational at Summit in 2019, which pho-
418 tographed particles with a maximum dimension > 30 μm (Garrett et al., 2012), did not
419 detect any identifiable ice crystals during the fog events. This suggests that any ice par-
420 ticles that were present during the fog were unlikely to be bullets or columns, which are
421 typically > 30 μm along their major axis (Walden et al., 2003). Schmitt et al. (2013) found
422 that ice fog particles in the interior of Alaska are generally droxtals or plates, although
423 these fogs are not necessarily comparable to Summit because they were heavily polluted.

424 To account for the additional uncertainty related to the choice of SSPs, we ran MIX-
425 CRA in three configurations (P_w, P_c, and D_w; Table 2). We choose from four databases
426 of liquid droplet SSPs corresponding to temperatures of 240, 253, 263, and 273 K (Rowe
427 et al., 2013, 2020). For P_w and D_w, we use the liquid SSPs that correspond to the warmest
428 temperature measured in the lowest 15 m a.g.l during each fog event, and for P_c we use
429 the liquid SSPs that correspond to the coldest temperature measured during the fog (fig.
430 S1). For ice crystals, we use SSPs associated with hexagonal plates (for P_w and P_c) and
431 droxtals (for D_w) (Yang et al., 2005). We choose these three configurations as a com-
432 promise between reducing the computational time of running multiple configurations and
433 representing the uncertainty associated with the SSPs well. Results from individual test
434 cases indicated that changing the liquid SSPs between the warmest and coolest temper-
435 atures had a larger impact on the results than changing the ice SSPs.

Table 2. The three configurations of single-scattering properties (SSPs) for ice and liquid particles used in the MIXCRA retrievals. Liquid SSPs at temperatures of either 240, 253, 263, or 273 K were used, corresponding to the warmest (or coldest, per table) measured temperature in the lowest 15 m a.g.l. during each fog event.

	Ice habit	Liquid SSP temperature
P_w	Plates	warmest
P_c	Plates	coldest
D_w	Droxtals	warmest

436 For the rest of this study, the microphysical retrievals shown are the mean values
437 of the three configurations in Table 2, and we account for the additional uncertainty in-
438 troduced by the SSPs assumption using equation (2), where 2σ is the combined uncer-
439 tainty of each retrieved parameter (i.e. τ_{liq}, R_{liq}, τ_{ice}, and R_{ice}), $2\sigma_a$ is the 2σ uncer-
440 tainty output by the MIXCRA algorithm, ΔS_i is the maximum difference in the retrieved
441 parameter resulting from varying the ice crystal SSPs, and ΔS_L is the maximum differ-
442 ence in the retrieved parameter resulting from varying the liquid SSPs.

$$2\sigma = \sqrt{2\sigma_a^2 + \Delta S_i^2 + \Delta S_L^2} \tag{2}$$

3.2 Validation against in-situ measurements

The ability of the MIXCRA algorithm to accurately determine simultaneous ice and liquid optical depths of single-layer mixed-phase Arctic clouds is well established through comparisons with depolarisation lidars (Turner et al., 2003; Turner & Eloranta, 2008), but assessments of the accuracy of MIXCRA retrievals of cloud droplet effective radius are limited to two comparisons with in-situ aircraft measurements of liquid-phase stratus clouds over the south-central US (Vogelmann et al., 2012) and off the west coast of California (Turner, 2007). Vogelmann et al. (2012) found that MIXCRA captured the primary mode of the cloud droplet distribution well; the mean and standard deviation of the MIXCRA size distribution was 5.3 ± 1.6 μm compared to 4.9 ± 0.7 μm for the aircraft probe. Turner (2007) found a mean bias of 0.1 μm between the aircraft measurements and MIXCRA, with an interquartile spread of 1.9 μm. In both cases, the aircraft measurements represent just one level in the cloud whereas the MIXCRA retrievals are representative of a column value (weighted by optical depth). To date, there have been no assessments of the accuracy of MIXCRA in determining the microphysical properties of fog.

Here, we assess the ability of MIXCRA to retrieve R_{liq} during fog at Summit by comparing MIXCRA R_{liq} retrievals with droplet effective radius determined from FM100 single-particle light scattering spectrometers installed at 2 m and 10 m a.g.l during a supercooled liquid fog event at Summit on 16 June 2013 (fig. 5). Note that the FM100 instruments were installed on a tower approximately 480 m from the AERI instrument. This case is described further in Cox et al. (2019) and is a near-idealised example of radiation fog formation at Summit, the development of which is particularly similar to case 4 in 2019.

The FM100 probes made size-resolved measurements of particles with radii (r) of 1-25 μm based on individual particle scattering characteristics, under the assumption that the particles are liquid spheres. The effective radius (R) was calculated from the FM100 particle size distribution [n(r)] using equation (3).

$$R = \frac{\int_0^\infty \pi r^3 n(r) dr}{\int_0^\infty \pi r^2 n(r) dr} \tag{3}$$

To estimate the uncertainty in R determined from the FM100 measurements, we recalculated the FM100 particle size distribution 100 times, each time randomly selecting errors from uniform distributions of five possible sources of uncertainty: (1) probe air speed (±5%), (2) wind speed (±0.5 m s^{-1}), (3) wind direction (±5°), (4) whether or not overlapping bins were combined (as described in Cox et al., 2019) (binary), and (5) the uncertainty in bin sizing (randomised shifts to neighbouring bins). For more details on the uncertainties associated with the FM100 probe, see Cox et al. (2019) and supplement. Bin sizing ambiguities were dominant over sampling errors for this case because the latter were small due to the ambient wind direction and speed being optimally aligned with the probe inlet geometry and the speed of the pumped air through the probe (see also Spiegel et al., 2012). The 2σ uncertainty in R is then determined from the standard deviation of R across all the perturbed calculations.

MIXCRA R_{liq} is not directly comparable to R determined from the FM100 probes, because the downwelling radiance measured by the AERI is sensitive to the bulk infrared signal from the entire population of particles in the scene view of the AERI instrument (the height of which varies with accumulation but is typically around 3 m a.g.l), whereas R determined from the FM100 is based on the forward scattering of light in the visible

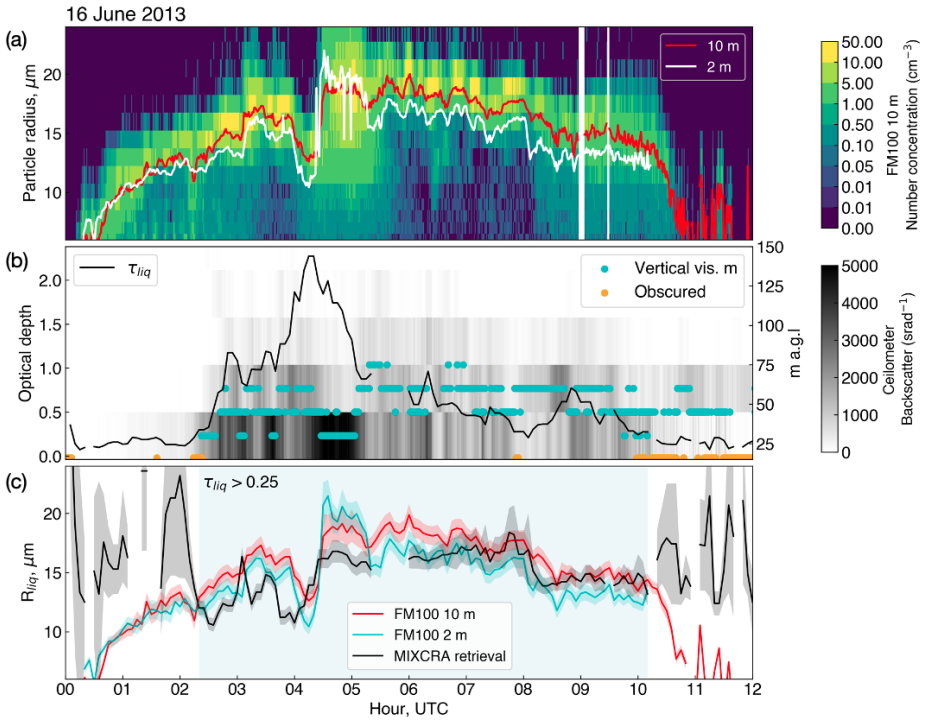

Figure 5. Fog event on 16 June 2013. (a) Calculated effective radius (R) from FM100 measurements at 10 m a.g.l (red line) and 2 m a.g.l (white line) overlaid on the FM100 particle size distribution at 10 m a.g.l. (coloured shading). (b) Retrieved liquid optical depth (black line), raw ceilometer backscatter (grey shading), and ceilometer vertical visibility values (blue markers, and orange for 'obscured'). (c) Cross validation of fog droplet R_{liq} retrieved from the MIXCRA algorithm (black) and determined from in-situ measurements (FM100 probes at 2 m, cyan, and 10 m, red). Shading represents 2 σ uncertainties, and the light blue region shows where the retrieved optical depth was greater than 0.25.

range from individual particles passed across the detector at a set height above the surface (2 m or 10 m). Therefore, we would only expect these values to compare well if the size distribution of the particle population at the height of the FM100 instrument was representative of the vertical distribution of the particle population. Cox et al. (2019) show that the fog droplet size distribution varies with height, with the 2 m probe generally measuring larger particles than the 10 m probe, consistent with particles preferentially forming higher up before settling out. However, on 16 June 2013, after the initial fog formation, the R at 2 m was consistently smaller than at 10 m (fig. 5), the particle number concentration at 2 m was also consistently higher than at 10 m (Cox et al., 2019), possibly indicating partial evaporation of droplets and a reduction in settling velocity at 2 m.

Despite this caveat, the MIXCRA R_{liq} compares very well to the R calculated from both FM100 probes when $\tau_{liq} > 0.25$ (fig. 5c) over a range of R from 12.5 to 20 μm. The RMSE between the MIXCRA R_{liq} and FM100 R is 2.0 μm at both 2 m and 10 m, with a Pearson's correlation coefficient of 0.57 and 0.69 respectively. However, the strength of this correlation is not consistent over the fog lifetime. During the initial stage of the fog (02:20 to 04:00) the MIXCRA R_{liq} was consistently smaller than R from both FM100 instruments (by an average of 1.5 μm at 2 m and 2.7 μm at 10m). Between 04:00 and 05:00 there was an initial reduction in R in the FM100 measurements (and a reduction in particle number concentration, Cox et al., 2019) followed by a sharp increase in R at 04:15. This coincided with a sharp increase in optical depth (fig. 5b), erosion of the surface temperature inversion, and evidence of wind-shear driven mixing in sodar observations (Cox et al., 2019). The increase in R was also apparent in the MIXCRA R_{liq}, but started earlier (at 04:00), and the maximum R_{liq} between 04:30 and 05:00 (17 μm) was lower than the maximum R measured by the FM100 probes during this interval (21 μm at 2 m and 19 μm at 10 m). This could be explained by an increase in altitude of the main layer of droplet formation; when the optical depth increases and the surface-based temperature inversion is eroded, new droplet formation would be initiated by radiative cooling at the fog top (Haeffelin et al., 2013). If the droplet formation layer height increased to greater than 10 m a.g.l, these droplets would have then grown and settled, resulting in larger particles at 10 m and even larger particles at 2 m (as observed between 04:30 and 05:15). After 05:15, the fog LWP decreased (Cox et al., 2019) suggesting no further droplet growth, and the optical depth gradually decreased. Between 06:00 and 10:00, the boundary layer was well-mixed (Cox et al., 2019), R varied consistently at 2 m and 10 m, and the MIXCRA R_{liq} captured these variations well. Overall, the MIXCRA R_{liq} is slightly better correlated with the measurements at 10 m, although this is largely due to detection of large (> 20 μm) particles detected at 2 m that are not reflected in the MIXCRA retrieval.

In summary, this cross-validation demonstrates that the MIXCRA algorithm can accurately retrieve R_{liq} during fog events at Summit with the following caveats:

1. Due to the threshold optical depth of 0.25, below which signal to noise ratio in the AERI measurements is insufficient to accurately retrieve fog microphysical properties, MIXCRA is not able to capture the initial growth period of the fog droplets (between 00:10 and 02:20 in fig. 5).
2. These results are based off a single case study and cover an effective radius range of 12.5 to 20 μm. More observations of R at a variety of heights and over a larger range of fog conditions are necessary to fully characterise the ability of MIXCRA to accurately retrieve fog droplet effective radius.

4 Results

4.1 Summary of microphysical retrievals during the 2019 fog cases

Figure 6 summarises the retrieved fog microphysical properties from the twelve case studies, and figures S2 and S3 in the supporting information show the temporal evolution of the microphysical properties during each case. Retrievals were calculated every five minutes during each fog event, so the number of valid retrievals indicated on fig. 6a is the number of five-minute intervals during which there was sufficient optical depth for the retrieval ($\tau_{liq} > 0.25$ for liquid, or $\tau_{ice} > 0.25$ for ice properties).

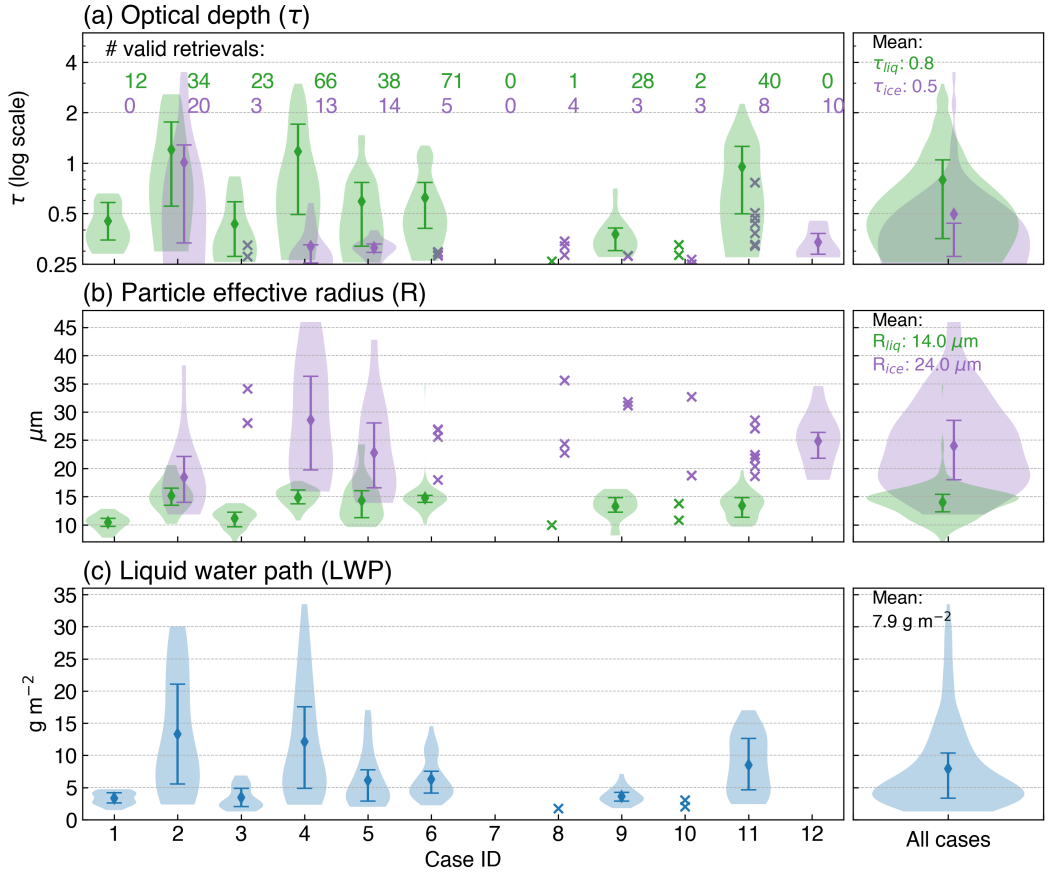

Figure 6. Relative probability distribution of fog microphysical properties retrieved during each individual case study listed in table 1 and for all cases (right hand side). The mean and interquartile range of each distribution is shown by the diamond shaped point and associated error bars when the number of valid retrievals is > 10, otherwise crosses show values from individual retrievals. (a) Liquid (τ_{liq}, green) and ice (τ_{ice}, purple) optical depth, (b) liquid (R_{liq}, green) and ice (R_{ice}, purple) particle effective radius, and (c) liquid water path (LWP). Only retrievals where the optical depth is sufficient are shown ($\tau_{ice} > 0.25$ for ice properties, or $\tau_{liq} > 0.25$ for liquid properties).

For the cases when there was sufficient ice optical depth for a retrieval, the mean R_{ice} was 24.0 μm (fig. 6b) and the range was 18.5 to 31.4 μm. This is in broad agreement with the mean effective radii of ice crystals measured in low-level Arctic clouds (~21-25 μm, Lawson, Baker, Schmitt, & Jensen, 2001; Turner et al., 2003; McFarquhar et al.,

2007). The mean R_{liq} was 14.0 μm and the mean during individual events varied from 10.0 to 15.1 μm (fig. 6b). The overall mean R_{liq} is slightly larger than the mean R determined from the summertime FM100 measurements at 10 m in 2013/14 from Cox et al. (2019), which was 11.4 $\pm$ 3 μm. However, it is important to note that the MIXCRA retrievals are only valid when $\tau_{liq} > 0.25$, and hence they do not include the initial phase of fog formation when there are a lot of very small droplets that can be detected by the FM100 (for example, see fig. 5). The range in R_{liq} across all retrievals was 6.6 μm (at the beginning of case 3) to 34.8 μm (just prior to fog dispersal in case 6).

Most of the fog cases have a mean LWP < 10 g m^{-2} (fig. 6c), but for cases 2 and 4 the maximum LWP exceeds 30 g m^{-2}, which can result in an increase in downwelling longwave radiation of > 50 W m^{-2} relative to clear sky conditions (Miller et al., 2015; Cox et al., 2019). The minimum LWP retrieved by MIXCRA was 1.3 g m^{-2} at the beginning of event 3, associated with the smallest retrieved droplet size (R_{liq} 6.6 μm). In cases 7, 8, and 10, the fog is so optically thin that the LWP is below the limit of detection for most of the event despite a reduction in horizontal visibility at the surface (to just 400 m in case 8) and observations of fog bows confirming the presence of liquid water on all three occasions. No optics were reported by onsite observers during the ice-phase fog (case 12), although the sun was below the horizon most of the time.

4.2 Aerosol particle measurements during fog events

The mean N_{250} across all fog events was 1.7 cm^{-3} (with the mean during individual events ranging from 0.4 to 2.2 cm^{-3}, fig. 7a), and the mean N_{20} across all fog events was 187 cm^{-3} (ranging from 41.9 to 448 cm^{-3}, fig. 7b), these values represent the interstitial aerosol particle number concentration during fog. The temporal evolution of N_{20} and N_{250} during each event is shown in fig. S4 in the supporting information. The mean N_{250} during fog events is slightly lower than the overall mean value (including clear and foggy periods) from June to September 2019 (2.4 cm^{-3}), whereas the mean value of N_{20} during fog is slightly higher than the seasonal mean (170 cm^{-3}). However, the mean N_{250} and N_{20} over the 2 hours prior to fog onset are 8.2 and 191 cm^{-3} respectively, both of which are higher than the mean values over the entire period. In all but case 7, N_{250} drops below 0.5 cm^{-3} during the fog event, suggesting that almost all particles in the N_{250} size range are activated into (or scavenged by) fog particles. This is not the case for N_{20}; an order of magnitude decrease in N_{20} during fog is only apparent in case 10, when N_{20} falls below 10 cm^{-3}.

Figure 8 illustrates the temporal evolution of N_{250} and N_{20} during each fog event, where fog onset is defined as when the downwelling radiance measured by the AERI increases above the clear sky threshold (see section 2.2), and the percentage change in N is relative to the mean value during the two hours prior to fog onset. On average, both N_{250} and N_{20} decrease during the first 300 minutes after fog onset, consistent with the growth and activation of aerosol particles into fog particles that are too large for either instrument to detect (> 6 μm). Note that this does not necessarily mean that these particles are removed from the atmosphere; they may sediment out or they may be released back into the atmosphere after the fog evaporates, either in the same form or after processing within the fog particle.

For N_{250} there is a reduction in number concentration after fog onset in all events (of 72 $\pm$ 26% after 300 minutes). For case 12, the magnitude of the percentage decrease is small compared to the other events, which is related to the fact that the absolute values of N_{250} during case 12 are exceptionally low, with an initial mean N_{250} in the two hours prior to fog onset of only 0.2 cm^{-3}. The initial N_{250} in the 2 hours prior to fog onset is consistent in time for all cases apart from case 11, where it varies between 1.2 and 6.8 cm^{-3}. In cases 8 and 10, a sharp reduction in N_{250} of 80% begins 30 minutes prior to the radiative detection of fog onset, whereas in cases 3 and 7, there is a slight

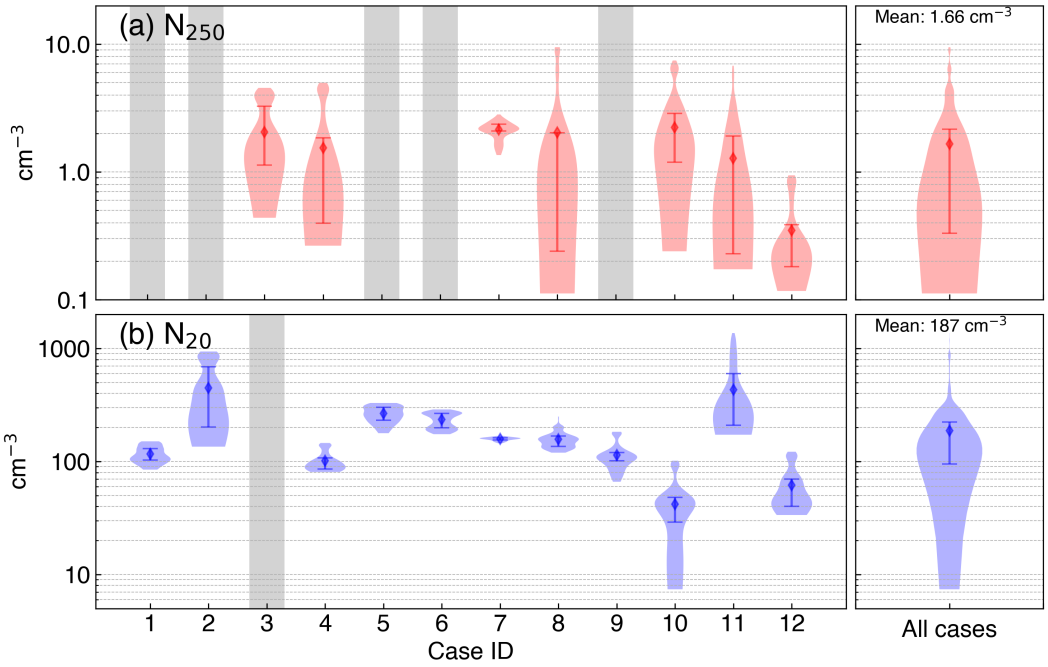

Figure 7. Relative probability distribution of aerosol particle number concentrations [(a) N_{250} and (b) N_{20}] measured during each individual case study listed in table 1 (left) and for all cases (right). The mean and interquartile range of each distribution is shown by the diamond shaped point and associated error bars. Grey bars indicate missing data (< 80% complete during fog event).

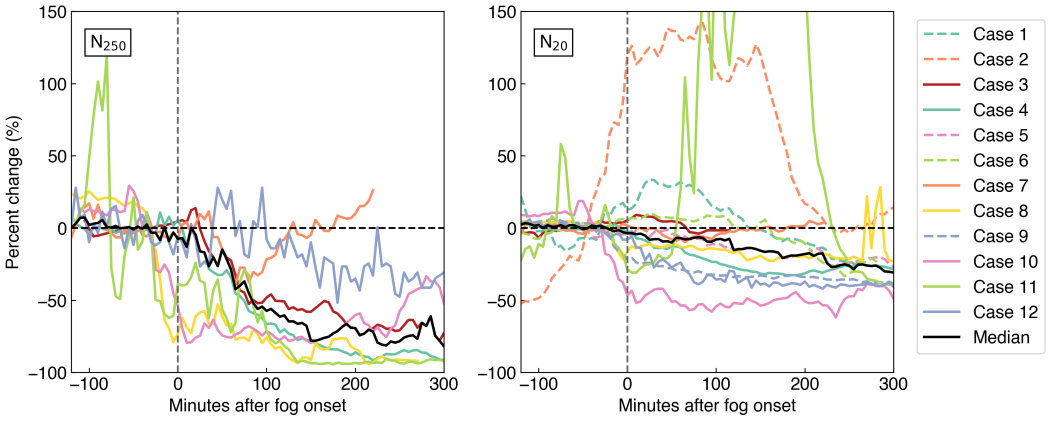

Figure 8. Percent change in N_{250} (left) and N_{20} (right) during the first 300 minutes of each fog event (coloured lines, see legend inset), compared to the average value in the two hours prior to fog onset. Thick black line is the median across all events.

increase in N_{250} at fog onset followed by a reduction in N_{250} that starts 20-30 minutes later. The duration of case 7 is only 102 minutes in total, and 80 minutes into the event N_{250} begins to increase, returning to the concentration prior to fog formation 10 minutes after the fog is no longer detected, suggesting that on this occasion, 100% of the particles that were incorporated into the fog were re-released after the fog dissipated.

In contrast to N_{250}, the change in N_{20} is highly variable between different fog events (fig. 8). In cases 2 and 11, there was more than a 100% increase in N_{20} during the event. For case 2, this increase started two hours before the fog was detected, meaning that the 'initial' N_{20} concentration is not a good representation over average conditions prior to the fog. In case 11 there was an initial decrease in N_{20} followed by a sharp increase 60 minutes into the fog event, during which N_{20} reached 1370 cm^{-3} (> 99th percentile of N_{20} measured between June and September 2019), but 240 minutes later, after the fog was no longer detected, N_{20} returned to values close to those prior to fog onset. This anomalous case is discussed further in section 5. In cases 8, 9, and 10, there was a reduction in N_{20} that started 30-40 minutes prior to fog onset (of 20%, 30%, and 50% respectively).

Note that some of the variability in evolution of N_{20} during fog events could be related to the size distribution of N_{20} particles; for example, if most of the N_{20} particles are closer to 30 nm diameter (i.e. the first mode in the Ziemba et al., 2010 measurements, fig. 1) these particles might be subject to different processes during a fog event than to N_{20} particles closer to 150 nm (the second mode in the Ziemba et al., 2010 measurements, fig. 1). Particles closer to 150 nm in size more readily act as CCN, whereas smaller particles would require larger supersaturations before activation. Size resolved measurements of particles < 250 nm diameter would be required to investigate these details further.

For five of the six cases when both N_{250} and N_{20} are available, the two measurements are positively correlated (fig. 9). The exception is case 11, during which N_{250} decreases to < 0.2 cm^{-3}, but there was an anomalous spike in N_{20} in the middle of the fog event (discussed further in section 5). In cases 4 and 8, N_{250} was almost completely depleted, but there is only a small reduction (< 35%) in N_{20}. This suggests that during these two cases, the supersaturations were not high enough to activate many particles with diameters < 250 nm. In cases 10 and 12, N_{250} was almost completely depleted, and N_{20} was also depleted by 73 and 41% respectively. During case 10, the reduction in N_{20} occurred simultaneously with the reduction in N_{250} (fig. 9) even though the initial N_{250} concentration was above average. The reduction in N_{20} and N_{250} started 30 minutes prior to fog detection, and then both concentrations remained steady after fog onset, suggesting that supersaturations during this event were high enough to activate smaller particles (or that the N_{20} concentration in this case was dominated by larger particles). In case 12 the initial concentration of N_{250} was only 0.24 cm^{-3}, and there was a gradual decrease in N_{20} after fog onset.

5 Discussion: Observational evidence of fog-aerosol interactions

The results described in section 4 suggest that there are a variety of different ways in which fog interacts with the surface aerosol particle population across the twelve case studies. Of the seven cases for which N_{250} measurements are available, only cases 4 and 11 develop a LWP > 10 g m^{-2}. The longwave radiative forcing for a LWP of 5 to 30 g m^{-2} compared to that of an equivalent clear sky day is very sensitive to small changes in LWP, and the difference between a LWP of 5 g m^{-2} and a LWP of 10 g m^{-2} can equate to > 20 W m^{-2} difference in longwave radiation at the surface (Miller et al., 2015). For this reason, understanding why some fogs develop a LWP > 10 g m^{-2} while others do not is important for understanding the radiative impact of fog over the GrIS. One of the factors that can influence LWP in liquid and mixed-phase fogs is the properties of the aerosol population. In this section, we use the observations presented in section 4 to discuss the role of fog-aerosol interactions over central Greenland. Throughout this discus-

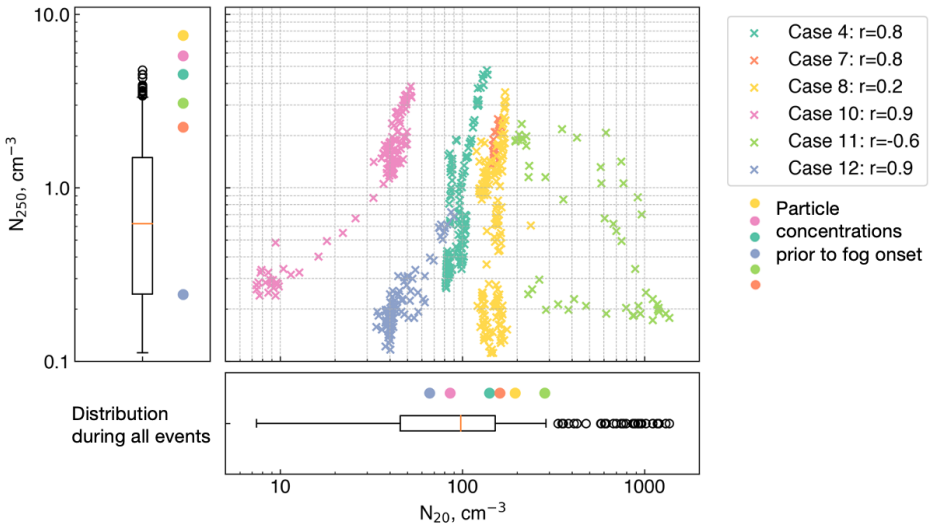

Figure 9. The relationship between N_{20} and N_{250} during the fog events for which both measurements are available. Boxplots show the aggregated distribution of N_{250} and N_{20} during all events. Coloured circles on the boxplots indicate the initial N_{20} and N_{250} concentration averaged over the 2 hours prior to each event. Pearson's-r correlation coefficients (r) in the legend inset are for the correlation between log(N_{20}) and log(N_{250}), all r values are significant at the 99% confidence level.

sion we make the assumption that changes in the fog and aerosol population were occurring in-situ (i.e. not related to advective processes). We justify this assumption based on the fact that (a) most of the fog events are likely to be radiation fogs due to the fact that they form in the evening on days with clear skies, and (b) that the wind speeds (2 to 14 m a.g.l) during all events are relatively low (3.5 ± 0.3 m s^{-1}). Despite the low wind speeds, for some of the longer events (> 8 hours) the horizontal length scale can be $\sim$100 km, and we acknowledge that advective process may have played a role in some of the observed changes in fog and aerosol properties.

5.1 Aerosol particle controls on fog microphysics

The goal of this section is to identify whether there is observational evidence that low aerosol particle number concentrations is a critical control on fog liquid water path and lifetime. To do this, we focus on the cases of liquid and mixed-phase fog when N_{250} measurements are available (cases 3, 4, 7, 8, 10, and 11).

In radiation fog, liquid droplets form when the surface cools radiatively until the air becomes saturated with respect to water, after which water condenses on CCN particles, growing them into fog droplets (e.g. Gultepe et al., 2007). Whether or not ice is present, liquid droplets will continue to grow as long as supersaturation with respect to water is maintained (either by continued radiative cooling or moisture influx) until they are large enough to settle out, and new droplet formation will continue as long as there are CCN particles present that may be activated for the given degree of supersaturation. In the initial stages of radiation fog development, when the atmosphere is stable and close to saturation, the degree of supersaturation is determined by the cooling rate, and by the properties of the aerosol particle population, which determine the number concentration of CCN for a given supersaturation. The air mass specific humidity also plays a role in determining the amount of cooling required to reach a given supersaturation,

but this effect is small because the saturation mixing ratio does not change much at cold temperatures (< 0.1 g kg^{-1} $°C^{-1}$ for temperatures <-8 °C). Based on this, and assuming an absence of advective processes and limited turbulent mixing, the initial formation of liquid droplets in a supercooled radiation fog development might either be 'aerosol-limited' or 'cooling-rate limited' (similar to how a convective cloud might be 'aerosol-limited' or 'updraft limited', i.e. Reutter et al., 2009).

In a 'cooling-rate limited' scenario, the initial supersaturation would increase slowly. Using the observations available in this study, this situation would be characterised by relatively low activated fractions of N_{250} at fog onset, because particles that can act as CCN at low supersaturations will be a subsample of N_{250} (McFiggans et al., 2006), followed by a gradual droplet growth and continual activation while cooling continues, and higher supersaturations allow the activation of further particles. In contrast, an 'aerosol-limited' fog would be characterised by high initial activation ratios of N_{250} and N_{20} at fog onset, as all particles that can act as CCN are activated. With continued cooling, and in the absence of new droplet formation due to a lack of CCN, the existing fog droplets would grow to relatively large sizes, ultimately settling out and preventing an increase in fog LWP despite continued cooling (as described by Mauritsen et al., 2011). The presence of 'aerosol-limited' fogs would support the hypothesis that the low aerosol particle number concentrations can be a critical control on fog liquid water path and lifetime.

To identify whether there are any cases of 'aerosol-limited' fogs, we calculate cooling rates during each fog event from temperature measurements at 2 m, 4 m, 9 m and 14 m a.g.l. The development of the near surface temperature profile during each fog event is shown in the supporting information (fig. S1). The cooling rate is calculated from the 60-minute rolling mean of the mean temperature across these four heights. Of the six cases for which N_{250} measurements are available and liquid water is detected, case 7 has an extremely low cooling rate (< 0.5 K h^{-1}, fig. 10a) and a low activated fraction of N_{250} at fog onset (fig. 8), suggesting that this event is more likely to be limited by the low cooling rate than by the aerosol population.

For the remaining five cases, the maximum cooling rate ranges from 2.4 K h^{-1} (case 11) to 4.0 K h^{-1} (case 10) and occurs 30 to 50 minutes after fog onset, except in case 3, when the maximum cooling rate occurs 140 minutes after fog onset (fig. 10a). These cooling rates are within the range of those observed in mid-latitude radiation fogs (∼1 to 4 K h^{-1}, e.g. Price, 2011; Haeffelin et al., 2013). In cases 3 and 4, N_{250} decreases gradually as the surface layer continues to cool, which suggests that neither of these two cases were in the 'aerosol-limited' regime, and that aerosol number concentrations were not the main reason why case 4 developed into an optically thick fog with LWP > 10 g m^{-2} but case 3 did not. The near-surface specific humidity and temperature profiles in both cases were similar (see table 1), and so the difference in fog development was likely due to differences in dynamics: In case 3, 110 minutes into the event, a burst of turbulent kinetic energy (0.3 m^2 s^{-2}, not shown) at 14 m is followed by warmer temperatures propagating downwards towards the surface (fig. S1), this mixing of warm air downwards could have limited the fog development.

In cases 8 and 10, there is a high activated fraction of N_{250} at fog onset (68 and 62% respectively) as well as a relatively high activated fraction of N_{20} (15 and 45% respectively). Case 10 had the highest activated fraction of N_{20} out of all fog cases. In both cases, there is little further change in N_{250} or N_{20} after fog onset despite continued cooling (figs. 8 and 10). This suggests that the aerosol particle number concentration could have limited fog development (lifetime and LWP) in these cases. Unfortunately, the low fog optical depths limit the ability of the MIXCRA retrieval algorithm to provide information about fog phase and particle sizes for both cases. Finally, in case 11, there is greater variability in N_{250} both prior to and after fog onset compared to the other cases, and in this case the fog develops much more rapidly than in case 4, with LWP increasing to > 10 g m^{-2} 80 minutes after fog onset (as opposed to 180 minutes in case 4). The warm-

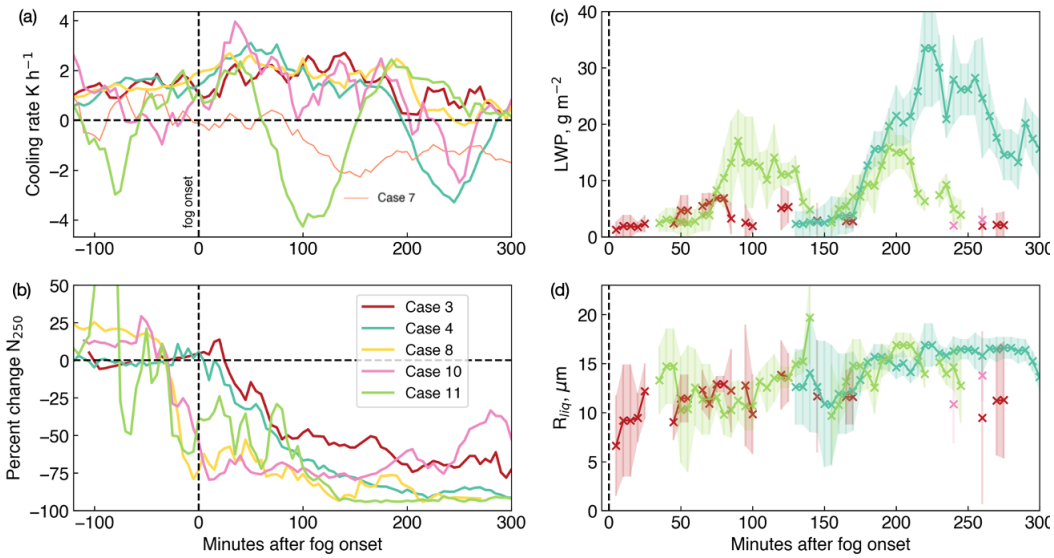

Figure 10. Time series of (a) cooling rate (2 to 14 m a.g.l), (b) percentage change in N_{250}, (c) liquid water path (LWP), and (d) Liquid droplet effective radius (R_{liq}) during the case studies for which N_{250} measurements are available. Note that cases 7 and 12, identified as 'cooling-rate limited' fogs are only included on panel (a). The error bars on panels (c) and (d) show the 2σ uncertainties in the MIXCRA retrievals.

ing of the surface layer that coincides with the sharp increase in LWP is indicative of a transition from near-surface radiative cooling to radiative cooling at fog top maintaining the fog. This case is discussed further in section 5.2.

5.2 Increase in N_{20} associated with fog

We focus on case 11 to look for evidence to support the hypothesis that fog can act to increase surface aerosol particle number concentrations by enhancing mixing of air from above into the near-surface stable layer. Case 11 was anomalous out of the 12 cases because of the exceptionally high N_{20} that occurred during the fog event (1370 cm^{-3}, $>$ 99th percentile of all N_{20} measurements made between June and September 2019), and because it consisted of two distinct phases; the LWP increased from 2.4 g m^{-2} to 17.0 g m^{-2} between 05:05 and 06:00, then decreased to 2.6 g m^{-2} at 07:05 before increasing again to 15.9 g m^{-2} at a 07:45.

The fog formed initially as the near surface temperature cooled after the dissipation of a mixed-phase cloud (with a base height of approximately 1.3 km) at 04:30. But only 80 minutes after fog onset, near surface air temperatures started to increase, and the fog optical depth and LWP started to increase rapidly (fig. 11). Because the surface temperature was no longer decreasing, the increase in fog optical depth and LWP after 05:15 must have been due to a transition from surface radiative cooling to cooling higher in the atmosphere (i.e., radiative cooling at fog top).

If the increase in near-surface air temperature was radiatively driven, we would expect the temperature increase to start closest to the surface first (for example, as in case 2 and 4, fig. S1). The fact that the near-surface air temperature increased simultaneously at each of the four heights (fig. 11d) suggests that another mechanism was responsible. This could have been the advection of a warmer air mass, but the consistent wind direction (90% of all winds measured at 2, 4, 9, and 14 m come from 156° to 222°) and

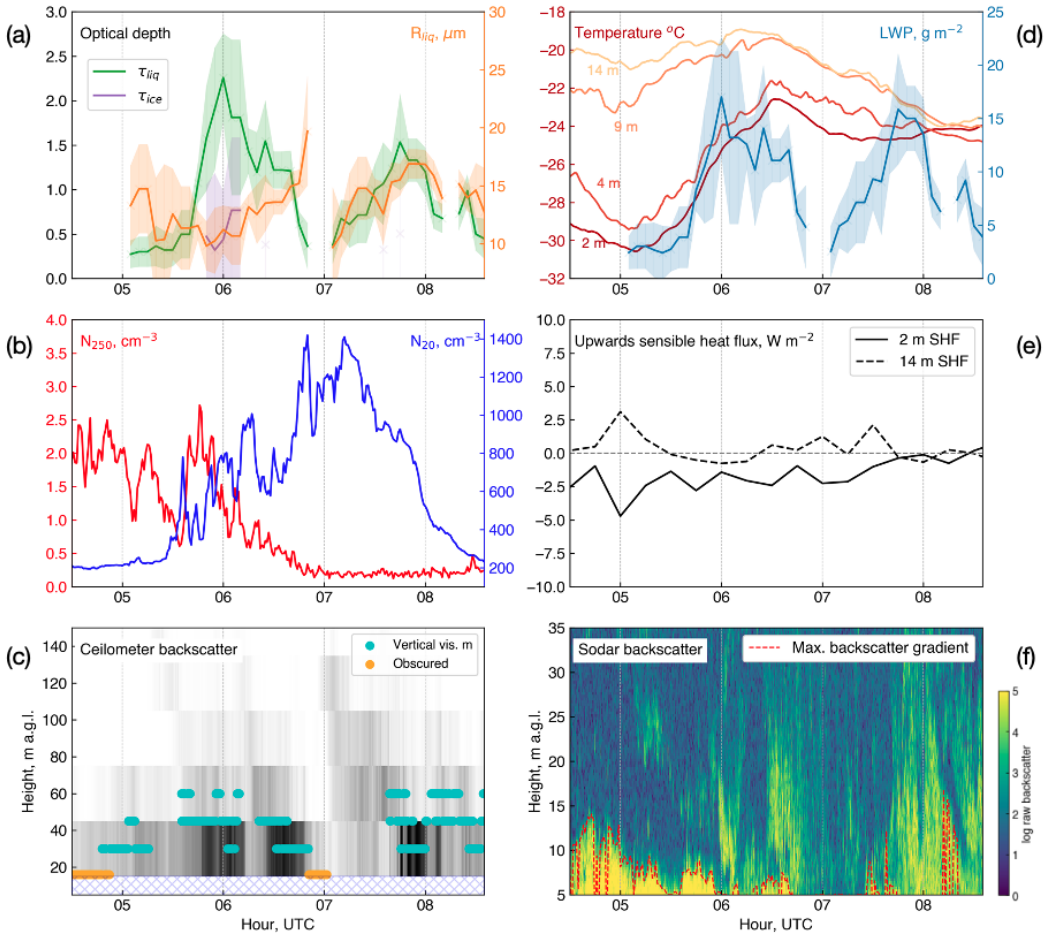

Figure 11. Atmospheric conditions during Case 11 (05 September 2019). (a) Fog optical depth (τ_{liq}, green, and τ_{ice}, purple) and droplet effective radius (R_{liq}, orange) from MIX-CRA, shading indicates 2σ uncertainties. (b) Surface aerosol particle number concentrations (1-min mean), N_{250} (red) and N_{20} (blue). (c) Backscatter (grey shading), vertical visibility (cyan points), and obscured flag (orange) from the ceilometer. (d) Near surface temperature profile (reds) and fog liquid water path (LWP, blue, shading indicates 2σ uncertainties). (e) Upwards sensible heat fluxes at 2 m (solid) and 14 m (dashed). (f) Sodar backscatter, red dashed line indicates the height of strongest negative backscatter gradient (when Δlog(backscatter) $<$ -0.8 m^{-1}).

low winds speeds (90 % of which range from 1.65 to 3.86 m s^{-1}) throughout the event indicates that advection at the surface is unlikely to be an important process on the timescale of this event. Alternatively, this near-surface heating could result from the mixing of warm air down from above. The sensible heat fluxes at 2 m and 14 m are small (mostly < 2.5 W m^{-2}, fig. 11e) suggesting that this mixing was not driven by changes in thermodynamic stability at the surface. However, there is evidence both in the ceilometer backscatter (fig. 11c) and the sodar acoustic backscatter (fig. 11f) of features propagating downwards towards the surface. These could be remnants of mesoscale dynamical features, such as buoyancy waves, mixing warmer air down from higher in the atmosphere, or entrainment driven by radiative cooling at fog top. In either case, propagation of these features down to the surface coincide with the sudden increase in N_{20}, suggesting this is related to the mixing of more polluted air down to the surface from above into what was previously an isolated stable surface layer.

The top of the strong surface echo in the sodar backscatter, identified by the maximum negative gradient (fig. 11f), is associated with the top of the stable near-surface layer which is isolated from above by a strong surface-based temperature inversion (fig. 11d). The top of this layer decreases intermittently with height between 05:00 and 07:00, and these variations are strongly anti-correlated with N_{20} (Pearson's r = -0.69, p-value < 0.001). For example, the top of the strong sodar echo falls to 5 m a.g.l at 05:20, coinciding with the initial sharp increase in N_{20} and an increase in surface temperature. Between 05:35 and 05:55, the height of the sodar echo increases again to 8 m a.g.l and N_{20} decreases, before increasing again once the sodar echo height lowers at 05:55. This pattern continues until 06:50 after which the surface temperature inversion is completely eroded at 9 m a.g.l and the near-surface echo in the sodar disappears. The erosion of the isolated surface layer from above indicated by the sodar echo, and the anti-correlation between the surface layer height and N_{20}, is consistent with the hypothesis that the increase in N_{20} is related to the mixing of air down from above.

During the most optically thick part of the fog there was also detectable ice that increased between 05:50 and 06:10. The increase in ice optical depth is coincident with a decrease in liquid optical depth, which could be indicative of ice growing at the expense of liquid water droplets (i.e. via the Wegener-Bergeron-Findeisen process). This would result in the evaporation of liquid droplets and the release of any aerosol particles they contain within the surface layer. In this situation, liquid droplets could form due to radiative cooling at fog top in a layer of the atmosphere where aerosol particle concentrations might be higher than at the surface, these droplets could then settle and mix towards the surface, eventually reaching a lower level that is sub-saturated with respect to water but supersaturated with respect to ice. The droplets would then evaporate, releasing aerosol particles into the surface layer. This process has been observed in Arctic mixed-phase stratocumulus clouds (Igel et al., 2017), and could also contribute to an increase in N_{20}, but it is unlikely to be the sole process driving the (~ 1000 cm^{-3}) increase in N_{20} because the typical number concentration of fog droplets at Summit is only $\sim$10 to 50 cm^{-3} (Cox et al., 2019).

When the surface temperature inversion was completely eroded above 9 m a.g.l at 06:50, the fog dissipated, and the surface began to cool again (fig. 11d). At this time, N_{250} had decreased to near-zero, suggesting that there were no further particles > 250 nm diameter available to act as CCN or INP. The cooling of the near-surface air would have increased saturation near the surface, potentially initiating the second phase of the fog. The increase in LWP during the second phase of the fog coincided with a sharp depletion of N_{20} and given that there were no particles > 250 nm left to activate, the decrease in N_{20} during the second phase of the fog was likely associated with the activation of N_{20} particles into fog droplets and the scavenging of particles by fog droplets close to the surface.

This case illustrates some of the complexities of the relationship between dynamics, thermodynamics, and aerosol properties during mixed-phase fog events, and it is not possible to say definitively what processes were involved from looking at the available observations alone. The observational evidence supports the hypothesis that the sharp increase in N_{20} associated with this fog event resulted from the mixing of higher N_{20} concentrations down to the surface, which was either driven by the fog itself (i.e. radiative cooling at fog top), or both the fog and changes in N_{20} were forced by the same external mixing event (e.g. buoyancy waves).

5.3 The impact of multiple fog events on the surface aerosol particle number concentration.

In this section we look for evidence that multiple consecutive fog events in quiescent conditions can act to deplete the near surface aerosol particle number concentration with the potential to impact fog development later in time. Fog with an observable radiative impact at the surface formed on four out of the five evenings between 01 and 06 August 2019 (fog case numbers 6 to 9, table 1), with skies otherwise clear throughout the day; associated with a persistent (weakening) high-pressure system over central Greenland (fig. S5, supporting information). Although this persistent anticyclone contributed to the unprecedented GrIS surface melt in 2019 (Tedesco & Fettweis, 2020), similar events are common over Greenland in the summer (occurring 30% of the time in JJA 1981-2010; Tedesco & Fettweis, 2020). During this event, the near-surface winds were consistently from the south-east, with 90% of measured 1-minute averaged wind speeds ranging from 1.26 to 4.81 m s^{-1}. There was a strong diurnal cycle, with radiative cooling in the near-surface layer beginning in the evening when the sun dropped below ~25° and lasting until the sun rose above ~15° the following morning (fig. 12b).

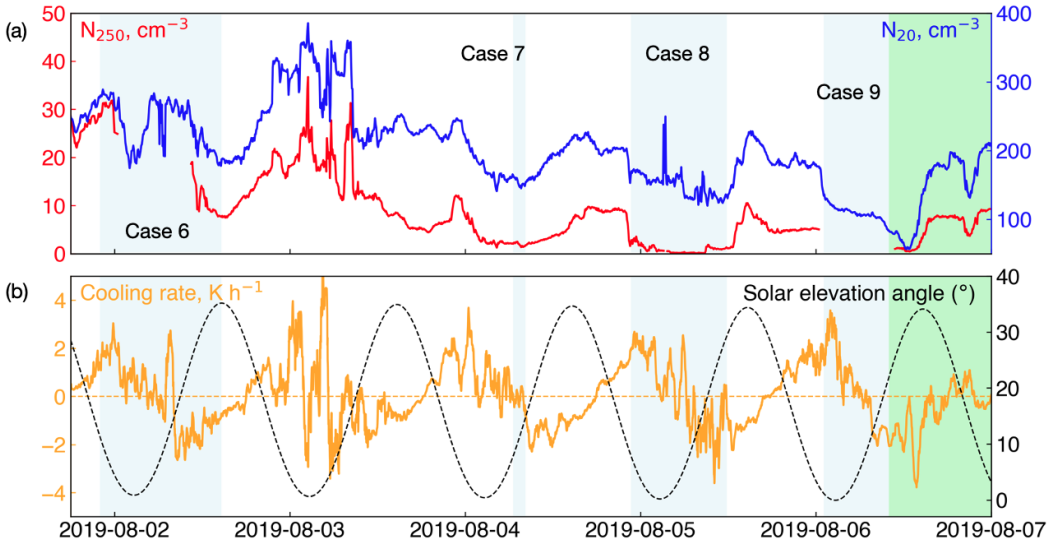

Figure 12. Surface aerosol particle number concentrations (a) and cooling rate (b) during a five day clear sky period in August 2019. Radiation fog events are highlighted in light blue, and the solar elevation angle is shown by the black dashed line on panel (b). The green highlighted region at the end of the period indicates the start of a cloudy period.

The initial N_{250} averaged over the two hours prior to case 6 was 27.7 cm^{-3}, and N_{20} was 262 cm^{-3}. Both concentrations are higher than the seasonal average, associated

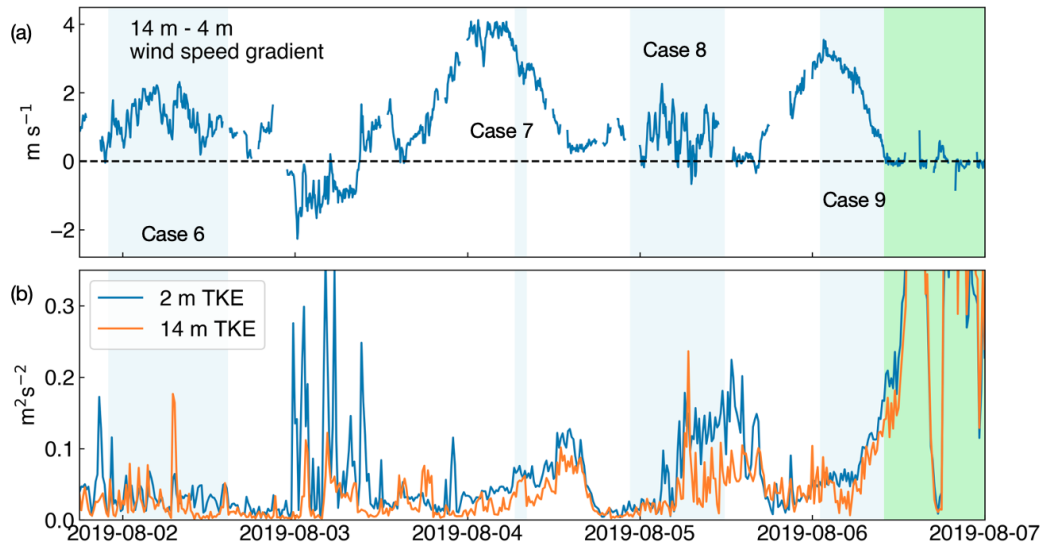

Figure 13. (a) Near surface wind shear (14 m minus 4 m wind speed, 5-minute mean) during the first week of August 2019. (b) Turbulent kinetic energy (TKE) at 2 m a.s.l (blue) and 14 m a.s.l (orange) over the same period. Radiation fog events are highlighted in blue shading as in fig. 12.

with the descent of free tropospheric air down to the surface during the high-pressure event (Guy et al., 2021). Both concentrations decrease gradually throughout the period, with daily minima generally occurring during fog events (fig. 12a). The minimum N_{250} was 0.11 cm^{-3} towards the end of case 8 (5 Aug 2019), and the minimum N_{20} was 56.5 cm^{-3}, at the end of case 9. After the end of case 9, the fog lifted from the surface, forming a low-level stratus cloud (base ∼200 m) that persisted through 7 August. Both N_{20} and N_{250} increased after the fog lifted, N_{20} to 177 cm^{-3}, and N_{250} to 7.63 cm^{-3}, but even after this recovery, both concentrations were 30% lower than the initial concentrations at the beginning of the quiescent cloud-free period.

Despite similar maximum near-surface cooling rates on the evenings with fog (2.7 to 3.7 K h^{-1}), only the first case (case 6) develops a LWP $>$ 10 g m^{-2} (fig. 6), and there is some evidence presented in section 5.1 that the development of case 8 might be limited by low aerosol particle concentration. One explanation for the gradual decrease in surface aerosol particle concentrations throughout this period (01 to 06 August) is that the scavenging of particles by fog droplets exceeds the rate of particle influx (presumably due to descent via sedimentation and/or turbulent entrainment from the free troposphere). Without measurements of vertical aerosol profiles and subsidence rates we cannot determine the relative importance of fog scavenging in this process compared to changes in particle influx (i.e. particle influx may also be decreasing with time as the anticyclonic circulation over Greenland weakens, fig. S5). However, the fact that the mean deposition flux of particles to the surface during fog events (on average 0.62 ng cm^{-2} for SO_4^{2-}, Bergin et al., 1994) is twice that of the mean dry deposition flux during the summer at Summit (0.29 ng cm^{-2} for SO_4^{2-}, Bergin et al., 1994), supports the hypothesis that multiple fog events during quiescent conditions act to deplete near surface aerosol particle concentrations, which in this case may have contributed to the latter fog cases approaching the aerosol-limited regime.

Another interesting question is why the nocturnal fog did not form on 03 August. Both near-surface temperature and aerosol concentration were highly variable early on

03 August, the maximum near-surface cooling rate reached 5.70 K h^{-1} and both N_{20} and N_{250} remained higher than the seasonal average (fig. 12), suggesting that fog formation was neither 'cooling-rate limited' nor 'aerosol limited'. Photographs from the total sky imager and observer reports of unlimited visibility confirm that the sky remained clear throughout the day. One difference between the early morning period on 03 Aug and the other mornings when fog did form is in the near-surface wind profile (fig. 13a), during the morning of 03 Aug there was a wind speed maximum close to the surface: The 4 m wind speed (mean: 3.2 m s^{-1}) was consistently 1-2 m s^{-1} faster than the 14 m wind speed (mean: 2.2 m s^{-1}). The shear generated by this near-surface wind-speed jet modified the turbulent properties of the surface layer, increasing mixing (indicated by the coincident increase in turbulent kinetic energy, fig. 13b), which may have been sufficient to prevent the formation of fog droplets and likely contributed to the high variability in the near-surface aerosol concentrations and temperature profile.

6 Summary and conclusions

The first goal of this study was to highlight the advantages and limitations of using spectral ground-based measurements of downwelling longwave radiation (measured by the AERI) to examine fog microphysical properties. Unlike active remote sensing instruments, which have a blind range close to the instrument, the AERI is most sensitive to the near-surface atmosphere, making it particularly suitable for the study of shallow fogs. Measurements of shallow fog with an AERI at Summit Station, in central Greenland, also benefit from the extreme dryness of the atmosphere and the improved ability to characterize temperature and humidity near the surface. The 8-19 μm spectral range of the AERI is most sensitive to fog (or cloud) microphysical properties when the fog visible optical depth is close to 1. This is particularly advantageous for the study of optically thin clouds in polar regions (particularly fogs), which can be responsible for the maximum cloud radiative forcing at the surface during summer months (e.g. Miller et al., 2015). At Summit, optically thin fogs are common (the maximum mixed-phase optical depth retrieved from the 12 fog cases in this study is 4.8, and the mean is 0.8) so the sensitivity of the AERI instrument (which can detect LWP as low as 3 g m^{-2}) is particularly suited for the study of these fogs. However, the loss of sensitivity to fog microphysical properties for optical depths > 6 means that this technique is not appropriate for studying the microphysical properties of optically thick fogs/clouds.

The MIXCRA algorithm is designed to retrieve the optical depth of liquid droplets, the optical depth of ice crystals, and the effective radius of the liquid and ice particles from the measured spectral radiance. Although MIXCRA retrievals of cloud properties have been validated against independent measurements in multiple previous studies, this is the first validation of the MIXCRA algorithm for fog events. A cross-validation of droplet effective radius retrieved using the MIXCRA algorithm with in-situ measurements from an FM100 forward scattering probe demonstrates that MIXCRA can capture variations in R_{liq} with a RMSE of 2.0 μm when the fog optical depth is sufficient ($0.25 < \tau < 6.0$).

The loss of sensitivity of the spectral infrared signature to changes in fog microphysical properties as the fog optical depth approaches zero means that MIXCRA is unable to retrieve fog microphysical properties during the initial growth phase of fog. This also means that MIXCRA is unable to retrieve microphysical properties associated with tenuous fogs (or higher clouds) that are potentially limited by low aerosol particle number concentration. We would expect such events to be characterised by large droplet effective radius and low optical depths, but for the two potential examples shown in this study, the optical depths are too low for MIXCRA to determine the fog phase or particle effective radius.

For the 12 fog cases studied, 92% of retrievals passed the initial quality control (radiances calculated using retrieved cloud properties matched measured radiances to within

an RMSE of 1.2 RU). Where there was sufficient optical depth for the retrieval ($\tau > 0.25$), the mean total (liquid plus ice) optical depth across all fog events was 0.78 ± 0.71 (one standard deviation). Nine of the twelve cases were mixed-phase fogs, one consisted of only ice particles, one of only liquid droplets, and one case was too optically thin for any valid retrievals. The mean ice particle effective radius was 24.0 ± 7.8 μm, and the mean liquid droplet effective radius was 14.0 ± 2.8 μm. The sensitivity of the AERI allows for the detection of LWP as small as 2.0-3.0 g m^{-2} (for R_{liq} 12 to 18 μm) with a 2σ uncertainty of 0.9-1.5 g m^{-2}. The mean LWP across all fog events was 7.9 ± 6.6 g m^{-2}, and in two cases the maximum LWP exceeded 30 g m^{-2}.

The second objective of this study was to use the MIXCRA microphysical retrievals alongside measurements of surface aerosol number concentration to look for observational evidence of fog-aerosol interactions at Summit. In all cases apart from one, the concentration of aerosol particles > 250 nm (N_{250}) decreased to < 0.5 cm^{-3} during the fog event (with a median decrease of 82% after 300 minutes), suggesting that almost all particles in this size range are activated into (or scavenged by) fog droplets, consistent with past studies (Bergin et al., 1994, 1995). Changes in the concentration of 20 to 230 nm diameter particles (N_{20}) were more variable; in some cases, N_{20} was found to be well correlated with N_{250} and decreased by up to 50% during fog, whereas in others, the two populations were decoupled, and on two occasions there was a > 100% increase in N_{20} during fog.

In two case studies, there is observational evidence that the near-surface aerosol particle number concentration might be a critical control on fog LWP and lifetime, but in other cases there is evidence that dynamical processes (i.e. turbulent mixing, subsidence, or the near-surface wind profile) are more important. Large-eddy simulations based on these detailed case studies are necessary to determine why some cases developed into well-mixed optically thick fogs and others did not, which is important for the resulting net radiative forcing of the fog at the ice sheet surface. In one case study there is evidence that fog can act to increase the near-surface aerosol particle number concentration by enhancing mixing of air from above into the near-surface stable layer. During a separate period of clear skies and low winds, when nocturnal radiation fog formed on four out of five consecutive nights, a gradual reduction in N_{20} and N_{250} supports the hypothesis that multiple fog events in quiescent periods act to clean the near-surface layer of aerosol particles.

The examples presented in this study demonstrate that there are multiple pathways through which the surface aerosol population may (or may not) impact fog development, and through which fog itself can modify the surface aerosol population. Correlations between aerosol properties and fog (or cloud) microphysics should not be considered in isolation, because there are other completing processes that can impact fog development, such as the thermodynamic and turbulent structure of the boundary layer. A larger dataset of fog cases studies is necessary to investigate the competing effects of the scavenging of surface aerosol particles by fog versus increases in aerosol particles during fog events, and the importance of both processes for fog and cloud formation later in time.

Open Research Section

AERI data and the thermodynamic profiles used to drive the MIXCRA algorithm are in the process of being submitted to the Arctic Data Center at `https://doi.org/10.5439/1880028`. The temperature dependent single scattering property databases are available online at `https://people.nwra.com/rowe/refractive_indices.shtml`. The FM100 data from Cox et al. (2019) are archived at `https://doi.org/10.18739/A28K74W5W` (Noone & Cox, 2019). Aerosol particle number concentration measurements, near surface temperature and wind profiles from the 15 m tower, and sensible heat flux measure-

ments are available from CEDA data archive (Guy et al., 2020). ICECAPS ceilometer data (`https://doi.org/10.18739/A27659G3R`) and sodar data (`https://doi.org/10.18739/A2HM52K68`) are archived at the Arctic Data Center (Shupe, 2020a, 2020b). The MIXCRA retrievals used in this study are in the process of being submitted to the Arctic Data Center and are available upon request.

Acknowledgments

The efforts of technicians at Summit Station and science support provided by Polar Field Services were crucial to maintaining data quality and continuity at Summit. ICECAPS is a long-term research program with many collaborators, and we are grateful for all their efforts in developing and maintaining the various instruments and data products used in this study. Thank you also to Professor Ken S. Carslaw for proof-reading and providing valuable feedback on this publication. Financial support for ICECAPS was provided by NSFGEO-NERC grants 1801477 and 2137083. HG was funded by the NERC SPHERES DTP grant number NE/L002574/1. MDS was supported by the National Science Foundation (OPP-1801477, OPP-2137091) and the NOAA cooperative agreement (NA22OAR4320151). PMR was supported by the National Science Foundation OPP Grant 2127632. Ceilometer data were provided by the Atmospheric Radiation Measurement (ARM) User Facility, a U. S. Department of Energy (DOE) Office of Science User Facility managed by the Biological and Environmental Research Program. This work used JASMIN, the UK collaborative data analysis facility.

References

Ackerman, A. S., Kirkpatrick, M. P., Stevens, D. E., & Toon, O. B. (2004). The impact of humidity above stratiform clouds on indirect aerosol climate forcing. *Nature*, *432*(7020), 1014–1017.

Antonelli, P., Revercomb, H., Sromovsky, L., Smith, W., Knuteson, R., Tobin, D., ... Best, F. (2004). A principal component noise filter for high spectral resolution infrared measurements. *Journal of Geophysical Research: Atmospheres*, *109*(D23).

Baccarini, A., Karlsson, L., Dommen, J., Duplessis, P., Vüllers, J., Brooks, I. M., ... Baltensperger, U. (2020). Frequent new particle formation over the high Arctic pack ice by enhanced iodine emissions. *Nature communications*, *11*(1), 1–11.

Bergin, M., Jaffrezo, J., Davidson, C., Caldow, R., & Dibb, J. (1994). Fluxes of chemical species to the Greenland Ice Sheet at Summit by fog and dry deposition. *Geochimica et cosmochimica acta*, *58*(15), 3207–3215.

Bergin, M., Jaffrezo, J.-L., Davidson, C., Dibb, J. E., Pandis, S., Hillamo, R., ... Makela, T. (1995). The contributions of snow, fog, and dry deposition to the summer flux of anions and cations at Summit, Greenland. *Journal of Geophysical Research: Atmospheres*, *100*(D8), 16275–16288.

Berkelhammer, M., Noone, D. C., Steen-Larsen, H. C., Bailey, A., Cox, C. J., O'Neill, M. S., ... White, J. W. (2016). Surface-atmosphere decoupling limits accumulation at Summit, Greenland. *Science Advances*, *2*(4).

Boutle, I., Angevine, W., Bao, J.-W., Bergot, T., Bhattacharya, R., Bott, A., ... Grell, E. (2022). Demistify: a large-eddy simulation (LES) and single-column model (SCM) intercomparison of radiation fog. *Atmospheric Chemistry and Physics*, *22*(1), 319-333.

Boutle, I., Price, J., Kudzotsa, I., Kokkola, H., & Romakkaniemi, S. (2018). Aerosol–fog interaction and the transition to well-mixed radiation fog. *Atmospheric Chemistry and Physics*, *18*(11), 7827–7840.

Carslaw, K. S., & Pringle, K. (2022). Global aerosol properties. In *Aerosols and climate* (pp. 101–133). Elsevier.

Clough, S. A., & Iacono, M. J. (1995). Line-by-line calculation of atmospheric fluxes

and cooling rates: 2. application to carbon dioxide, ozone, methane, nitrous oxide and the halocarbons. *Journal of Geophysical Research: Atmospheres*, *100*(D8), 16519–16535.

Clough, S. A., Iacono, M. J., & Moncet, J.-L. (1992). Line-by-line calculations of atmospheric fluxes and cooling rates: Application to water vapor. *Journal of Geophysical Research: Atmospheres*, *97*(D14), 15761–15785.

Cox, C. J., Noone, D. C., Berkelhammer, M., Shupe, M. D., Neff, W. D., Miller, N. B., ... Steffen, K. (2019). Supercooled liquid fogs over the central Greenland Ice Sheet. *Atmospheric Chemistry and Physics*, *19*(11), 7467–7485.

Cox, C. J., Walden, V. P., Compo, G. P., Rowe, P. M., Shupe, M. D., & Steffen, K. (2014). Downwelling longwave flux over Summit, Greenland, 2010–2012: Analysis of surface-based observations and evaluation of ERA-Interim using wavelets. *Journal of Geophysical Research: Atmospheres*, *119*(21), 12–317.

Cox, C. J., Walden, V. P., & Rowe, P. M. (2012). A comparison of the atmospheric conditions at Eureka, Canada, and Barrow, Alaska (2006–2008). *Journal of Geophysical Research: Atmospheres*, *117*(D12).

Creamean, J. M., Barry, K., Hill, T. C., Hume, C., DeMott, P. J., Shupe, M. D., ... Beck, I. (2022). Annual cycle observations of aerosols capable of ice formation in central Arctic clouds. *Nature communications*, *13*(1), 1–12.

Creamean, J. M., Kirpes, R. M., Pratt, K. A., Spada, N. J., Maahn, M., De Boer, G., ... China, S. (2018). Marine and terrestrial influences on ice nucleating particles during continuous springtime measurements in an Arctic oilfield location. *Atmospheric Chemistry and Physics*, *18*(24), 18023–18042.

Field, P. R., Lawson, R. P., Brown, P. R., Lloyd, G., Westbrook, C., Moisseev, D., ... Choularton, T. (2017). Secondary ice production: Current state of the science and recommendations for the future. *Meteorological Monographs*, *58*, 7–1.

Gallagher, M. R., Shupe, M. D., & Miller, N. B. (2018). Impact of atmospheric circulation on temperature, clouds, and radiation at Summit station, Greenland, with self-organizing maps. *Journal of Climate*, *31*(21), 8895–8915.

Garrett, Fallgatter, C., Shkurko, K., & Howlett, D. (2012). Fall speed measurement and high-resolution multi-angle photography of hydrometeors in free fall. *Atmospheric Measurement Techniques*, *5*(11), 2625–2633.

Garrett, Radke, L. F., & Hobbs, P. V. (2002). Aerosol effects on cloud emissivity and surface longwave heating in the Arctic. *Journal of the Atmospheric Sciences*, *59*(3), 769-778.

Garrett, & Zhao, C. (2013). Ground-based remote sensing of thin clouds in the Arctic. *Atmospheric Measurement Techniques*, *6*(5), 1227–1243.

Gultepe, I., Tardif, R., Michaelides, S. C., Cermak, J., Bott, A., Bendix, J., ... Ellrod, G. (2007). Fog research: A review of past achievements and future perspectives. *Pure and applied geophysics*, *164*(6), 1121–1159.

Gultepe, I., Zhou, B., Milbrandt, J., Bott, A., Li, Y., Heymsfield, A. J., ... Kuhn, T. (2015). A review on ice fog measurements and modeling. *Atmospheric Research*, *151*, 2–19.

Guy, H., Brooks, I., Carslaw, K., Murray, B., Walden, V., Shupe, M., ... Neff, W. (2021). Controls on surface aerosol number concentrations and aerosol-limited cloud regimes over the central Greenland Ice Sheet. *Atmospheric Chemistry and Physics*, *21*(19), 1–36.

Guy, H., Neely III, R. R., & Brooks, I. (2020). ICECAPS-ACE: Integrated Characterization of Energy, Clouds, Atmospheric state, and Precipitation at Summit, Greenland - Aerosol Cloud Experiment measurements. *Centre for Environmental Data Analysis*. Retrieved from `http://catalogue.ceda.ac.uk/uuid/f06c6aa727404ca788ee3dd0515ea61a` ([Dataset] Last accessed: 23 November 2022)

Guy, H., Turner, D. D., Walden, V. P., Brooks, I. M., & Neely, R. R. (2022). Passive

ground-based remote sensing of radiation fog. *Atmospheric Measurement Techniques*, *15*, 5095–5115.

Haeffelin, M., Dupont, J.-C., Boyouk, N., Baumgardner, D., Gomes, L., Roberts, G., & Elias, T. (2013). A comparative study of radiation fog and quasi-fog formation processes during the ParisFog field experiment 2007. *Pure and Applied Geophysics*, *170*(12), 2283–2303.

Hanna, E., Cappelen, J., Fettweis, X., Mernild, S. H., Mote, T. L., Mottram, R., ... Hall, R. J. (2021). Greenland surface air temperature changes from 1981 to 2019 and implications for ice-sheet melt and mass-balance change. *International Journal of Climatology*, *41*, E1336–E1352.

Hoch, S., Calanca, P., Philipona, R., & Ohmura, A. (2007). Year-round observation of longwave radiative flux divergence in Greenland. *Journal of Applied Meteorology and Climatology*, *46*(9), 1469–1479.

Hofer, S., Tedstone, A. J., Fettweis, X., & Bamber, J. L. (2019). Cloud microphysics and circulation anomalies control differences in future Greenland melt. *Nature Climate Change*, *9*(7), 523–528.

Howat, I., Negrete, A., & Smith, B. (2017). The Greenland ice mapping project (GIMP) land ice and ocean classification mask, version 1. *NASA National Snow and Ice Data Center Distributed Active Archive Center.*. doi: https://doi.org/10.5067/B8X58MQBFUPA

Igel, A. L., Ekman, A. M., Leck, C., Tjernström, M., Savre, J., & Sedlar, J. (2017). The free troposphere as a potential source of Arctic boundary layer aerosol particles. *Geophysical Research Letters*, *44*(13), 7053–7060.

Kanji, Z. A., Ladino, L. A., Wex, H., Boose, Y., Burkert-Kohn, M., Cziczo, D. J., & Krämer, M. (2017). Overview of ice nucleating particles. *Meteorological Monographs*, *58*, 1–1.

Knuteson, R., Revercomb, H., Best, F., Ciganovich, N., Dedecker, R., Dirkx, T., ... Howell, H. (2004a). Atmospheric emitted radiance interferometer. Part II: Instrument performance. *Journal of Atmospheric and Oceanic Technology*, *21*(12), 1777–1789.

Knuteson, R., Revercomb, H., Best, F., Ciganovich, N., Dedecker, R., Dirkx, T., ... Howell, H. (2004b). Atmospheric emitted radiance interferometer. Part I: Instrument design. *Journal of Atmospheric and Oceanic Technology*, *21*(12), 1763–1776.

Korolev, A. (2007). Limitations of the Wegener–Bergeron–Findeisen mechanism in the evolution of mixed-phase clouds. *Journal of the Atmospheric Sciences*, *64*(9), 3372–3375.

Lawson, R. P., Baker, B. A., Schmitt, C. G., & Jensen, T. (2001). An overview of microphysical properties of Arctic clouds observed in May and July 1998 during FIRE ACE. *Journal of Geophysical Research: Atmospheres*, *106*(D14), 14989–15014.

Leaitch, W. R., Korolev, A., Aliabadi, A. A., Burkart, J., Willis, M. D., Abbatt, J. P., ... Schneider, J. (2016). Effects of 20–100 nm particles on liquid clouds in the clean summertime Arctic. *Atmospheric Chemistry and Physics*, *16*(17), 11107–11124.

Lubin, D., Zhang, D., Silber, I., Scott, R. C., Kalogeras, P., Battaglia, A., ... Fridlind, A. (2020). AWARE: The atmospheric radiation measurement (ARM) west Antarctic radiation experiment. *Bulletin of the American Meteorological Society*, *101*(7), E1069–E1091.

Maalick, Z., Kühn, T., Korhonen, H., Kokkola, H., Laaksonen, A., & Romakkaniemi, S. (2016). Effect of aerosol concentration and absorbing aerosol on the radiation fog life cycle. *Atmospheric Environment*, *133*, 26–33.

Mahesh, A., Walden, V. P., & Warren, S. G. (2001). Ground-based infrared remote sensing of cloud properties over the Antarctic plateau. Part II: Cloud optical depths and particle sizes. *Journal of Applied Meteorology and Climatology*,

40(7), 1279–1294.

Mason, R., Si, M., Chou, C., Irish, V., Dickie, R., Elizondo, P., ... Lassar, W. (2016). Size-resolved measurements of ice-nucleating particles at six locations in North America and one in Europe. *Atmospheric Chemistry and Physics*, *16*(3), 1637–1651.

Mattingly, K., Mote, T., & Fettweis, X. (2018). Atmospheric river impacts on Greenland Ice Sheet surface mass balance. *Journal of Geophysical Research: Atmospheres*, *123*(16), 8538–8560.

Mauritsen, T., Sedlar, J., Tjernström, M., Leck, C., Martin, M., Shupe, M., ... Brooks, I. (2011). An Arctic CCN-limited cloud-aerosol regime. *Atmospheric Chemistry and Physics*, *11*(1), 165–173.

Mazoyer, M., Burnet, F., & Denjean, C. (2022). Experimental study on the evolution of droplet size distribution during the fog life cycle. *Atmospheric Chemistry and Physics*, *22*(17), 11305–11321.

McFarquhar, G. M., Zhang, G., Poellot, M. R., Kok, G. L., McCoy, R., Tooman, T., ... Heymsfield, A. J. (2007). Ice properties of single-layer stratocumulus during the Mixed-Phase Arctic Cloud Experiment: 1. Observations. *Journal of Geophysical Research: Atmospheres*, *112*(D24).

McFiggans, G., Artaxo, P., Baltensperger, U., Coe, H., Facchini, M. C., Feingold, G., ... Lohmann, U. (2006). The effect of physical and chemical aerosol properties on warm cloud droplet activation. *Atmospheric Chemistry and Physics*, *6*(9), 2593–2649.

Miller, N. B., Shupe, M. D., Cox, C. J., Walden, V. P., Turner, D. D., & Steffen, K. (2015). Cloud radiative forcing at Summit, Greenland. *Journal of Climate*, *28*(15), 6267–6280.

Münkel, C. (2006). Boundary layer and air quality monitoring with a commercial lidar ceilometer. In *Lidar technologies, techniques, and measurements for atmospheric remote sensing ii* (Vol. 6367, pp. 188–194).

Neff, W., Helmig, D., Grachev, A., & Davis, D. (2008). A study of boundary layer behavior associated with high NO concentrations at the South Pole using a minisodar, tethered balloon, and sonic anemometer. *Atmospheric Environment*, *42*(12), 2762–2779.

Noone, D., & Cox, C. (2019). Closing the isotope hydrology at Summit: Measurements of source regions, precipitation and post-deposition processes, Greenland, 2011-2014. *Arctic Data Center*.

Pettersen, C., Henderson, S. A., Mattingly, K. S., Bennartz, R., & Breeden, M. L. (2022). The critical role of euro-atlantic blocking in promoting snowfall in central Greenland. *Journal of Geophysical Research: Atmospheres*, *127*(6).

Porter, G. C., Adams, M. P., Brooks, I. M., Ickes, L., Karlsson, L., Leck, C., ... Sikora, S. N. (2022). Highly active ice-nucleating particles at the summer North Pole. *Journal of Geophysical Research: Atmospheres*, *127*(6), e2021JD036059.

Price, J. (2011). Radiation fog. Part I: observations of stability and drop size distributions. *Boundary-layer meteorology*, *139*(2), 167–191.

Rathke, C., Neshyba, S., Shupe, M. D., Rowe, P., & Rivers, A. (2002). Radiative and microphysical properties of Arctic stratus clouds from multiangle downwelling infrared radiances. *Journal of Geophysical Research: Atmospheres*, *107*(D23), AAC–12.

Reutter, P., Su, H., Trentmann, J., Simmel, M., Rose, D., Gunthe, S., ... Pöschl, U. (2009). Aerosol-and updraft-limited regimes of cloud droplet formation: influence of particle number, size and hygroscopicity on the activation of cloud condensation nuclei (CCN). *Atmospheric Chemistry and Physics*, *9*(18), 7067–7080.

Richter, P., Palm, M., Weinzierl, C., Griesche, H., Rowe, P. M., & Notholt, J. (2022). A dataset of microphysical cloud parameters, retrieved from Fourier-

transform infrared (FTIR) emission spectra measured in Arctic summer 2017. *Earth System Science Data*, *14*(6), 2767–2784.

Rothman, L. S., Gordon, I. E., Barbe, A., Benner, D. C., Bernath, P. F., Birk, M., ... Champion, J.-P. (2009). The HITRAN 2008 molecular spectroscopic database. *Journal of Quantitative Spectroscopy and Radiative Transfer*, *110*(9-10), 533–572.

Rowe, Fergoda, M., & Neshyba, S. (2020). Temperature-dependent optical properties of liquid water from 240 to 298 K. *Journal of Geophysical Research: Atmospheres*, *125*(17), e2020JD032624.

Rowe, Neshyba, S., & Walden, V. (2013). Radiative consequences of low-temperature infrared refractive indices for supercooled water clouds. *Atmospheric Chemistry and Physics*, *13*(23), 11925–11933.

Rowe, Walden, V. P., Brandt, R. E., Town, M. S., Hudson, S. R., & Neshyba, S. (2022). Evaluation of temperature-dependent complex refractive indices of supercooled liquid water using downwelling radiance and in-situ cloud measurements at South Pole. *Journal of Geophysical Research: Atmospheres*, *127*(1), e2021JD035182.

Schmeisser, L., Backman, J., Ogren, J. A., Andrews, E., Asmi, E., Starkweather, S., ... Eleftheriadis, K. (2018). Seasonality of aerosol optical properties in the Arctic. *Atmospheric Chemistry and Physics*, *18*(16), 11599–11622.

Schmitt, C. G., Stuefer, M., Heymsfield, A. J., & Kim, C. K. (2013). The microphysical properties of ice fog measured in urban environments of interior alaska. *Journal of Geophysical Research: Atmospheres*, *118*(19), 11–136.

Shupe. (2020a). Ceilometer cloud base height measurements at Summit Station, Greenland, 2019. *Arctic Data Center*.

Shupe. (2020b). SOnic Detection And Ranging (SODAR) measurements taken at Summit Station, Greenland, 2019. *Arctic Data Center*.

Shupe, Turner, D. D., Walden, V. P., Bennartz, R., Cadeddu, M. P., Castellani, B. B., ... Miller, N. B. (2013). High and dry: New observations of tropospheric and cloud properties above the Greenland Ice Sheet. *Bulletin of the American Meteorological Society*, *94*(2), 169–186.

Shupe, Turner, D. D., Zwink, A., Thieman, M. M., Mlawer, E. J., & Shippert, T. (2015). Deriving Arctic cloud microphysics at Barrow, Alaska: Algorithms, results, and radiative closure. *Journal of Applied Meteorology and Climatology*, *54*(7), 1675–1689.

Si, M., Irish, V. E., Mason, R. H., Vergara-Temprado, J., Hanna, S. J., Ladino, L. A., ... Abbatt, J. P. (2018). Ice-nucleating ability of aerosol particles and possible sources at three coastal marine sites. *Atmospheric Chemistry and Physics*, *18*(21), 15669–15685.

Small, J. D., Chuang, P. Y., Feingold, G., & Jiang, H. (2009). Can aerosol decrease cloud lifetime? *Geophysical Research Letters*, *36*(16).

Solomon, A., Shupe, M. D., Persson, O., Morrison, H., Yamaguchi, T., Caldwell, P. M., & de Boer, G. (2014). The sensitivity of springtime Arctic mixed-phase stratocumulus clouds to surface-layer and cloud-top inversion-layer moisture sources. *Journal of the Atmospheric Sciences*, *71*(2), 574–595.

Spiegel, J., Zieger, P., Bukowiecki, N., Hammer, E., Weingartner, E., & Eugster, W. (2012). Evaluating the capabilities and uncertainties of droplet measurements for the fog droplet spectrometer (FM-100). *Atmospheric Measurement Techniques*, *5*(9), 2237–2260.

Stamnes, K., Tsay, S.-C., Wiscombe, W., & Jayaweera, K. (1988). Numerically stable algorithm for discrete-ordinate-method radiative transfer in multiple scattering and emitting layered media. *Applied optics*, *27*(12), 2502–2509.

Sterzinger, L. J., Sedlar, J., Guy, H., Neely III, R. R., & Igel, A. L. (2022). Do Arctic mixed-phase clouds sometimes dissipate due to insufficient aerosol? evidence from comparisons between observations and idealized simulations.

Atmospheric Chemistry and Physics, *22*(13), 8973–8988.

Stevens, R. G., Loewe, K., Dearden, C., Dimitrelos, A., Possner, A., Eirund, G. K., ... Wilkinson, J. (2018). A model intercomparison of CCN-limited tenuous clouds in the high Arctic. *Atmospheric Chemistry and Physics*, *18*(15), 11041–11071.

Tedesco, M., & Fettweis, X. (2020). Unprecedented atmospheric conditions (1948–2019) drive the 2019 exceptional melting season over the Greenland Ice Sheet. *The Cryosphere*, *14*(4), 1209–1223.

Turner. (2005). Arctic mixed-phase cloud properties from AERI lidar observations: Algorithm and results from SHEBA. *Journal of Applied Meteorology*, *44*(4), 427–444.

Turner. (2007). Improved ground-based liquid water path retrievals using a combined infrared and microwave approach. *Journal of Geophysical Research: Atmospheres*, *112*(D15).

Turner, Ackerman, S., Baum, B., Revercomb, H. E., & Yang, P. (2003). Cloud phase determination using ground-based AERI observations at SHEBA. *Journal of Applied Meteorology*, *42*(6), 701–715.

Turner, & Blumberg, W. G. (2019). Improvements to the AERIoe thermodynamic profile retrieval algorithm. *IEEE Journal of Selected Topics in Applied Earth Observations and Remote Sensing*, *12*(5), 1339–1354.

Turner, & Eloranta, E. W. (2008). Validating mixed-phase cloud optical depth retrieved from infrared observations with high spectral resolution lidar. *IEEE Geoscience and Remote Sensing Letters*, *5*(2), 285–288.

Turner, Knuteson, R., Revercomb, H., Lo, C., & Dedecker, R. (2006). Noise reduction of atmospheric emitted radiance interferometer (AERI) observations using principal component analysis. *Journal of Atmospheric and Oceanic Technology*, *23*(9), 1223–1238.

Turner, & Löhnert, U. (2021). Ground-based temperature and humidity profiling: combining active and passive remote sensors. *Atmospheric Measurement Techniques*, *14*(4), 3033–3048.

Twomey, S. (1977). The influence of pollution on the shortwave albedo of clouds. *Journal of the atmospheric sciences*, *34*(7), 1149–1152.

Vogelmann, A. M., McFarquhar, G. M., Ogren, J. A., Turner, D. D., Comstock, J. M., Feingold, G., ... Collins, D. R. (2012). RACORO extended-term aircraft observations of boundary layer clouds. *Bulletin of the American Meteorological Society*, *93*(6), 861–878.

Von der Weiden, S.-L., Drewnick, F., & Borrmann, S. (2009). Particle Loss Calculator–a new software tool for the assessment of the performance of aerosol inlet systems. *Atmospheric Measurement Techniques*, *2*(2), 479–494.

Walden, V. P., Warren, S. G., & Tuttle, E. (2003). Atmospheric ice crystals over the Antarctic plateau in winter. *Journal of Applied Meteorology*, *42*(10), 1391–1405.

Williams, A. S., & Igel, A. L. (2021). Cloud top radiative cooling rate drives nonprecipitating stratiform cloud responses to aerosol concentration. *Geophysical Research Letters*, *48*(18).

Yan, S., Zhu, B., Zhu, T., Shi, C., Liu, D., Kang, H., ... Lu, C. (2021). The effect of aerosols on fog lifetime: observational evidence and model simulations. *Geophysical Research Letters*, *48*(2), e2020GL61803.

Yang, P., Wei, H., Huang, H.-L., Baum, B. A., Hu, Y. X., Kattawar, G. W., ... Fu, Q. (2005). Scattering and absorption property database for nonspherical ice particles in the near-through far-infrared spectral region. *Applied optics*, *44*(26), 5512–5523.

Ziemba, L. D., Dibb, J. E., Griffin, R. J., Huey, L. G., & Beckman, P. (2010). Observations of particle growth at a remote, Arctic site. *Atmospheric Environment*, *44*(13), 1649–1657.

Chapter 5.

Discussion and Conclusions

1. Overview and key findings

This thesis presents new in-situ measurements of aerosol particle number concentrations and boundary layer meteorology at Summit Station in central Greenland, from instrumentation installed in 2019 as part of the ICECAPS- Aerosol Cloud Experiment (ICECAPS-ACE) project, with the overarching goal of improving our understanding of the controls on the near-surface aerosol population and the interactions between fog and aerosol particles over the central Greenland Ice Sheet (GrIS). Chapter 2 focuses on the first full annual cycle of surface aerosol particle number concentration measurements recorded at Summit and explores the local and synoptic controls on the intra-annual and intra-seasonal variability. Chapter 3 is a measurements technique study that explores the advantages and limitations of using ground based infrared remote sensing to retrieve near-surface temperature and water vapor profiles and to detect radiatively important fog events over central Greenland. Finally, Chapter 4 uses the temperature profiles from Chapter 3 to drive the mixed-phase cloud property retrieval algorithm (MIXCRA) to determine particle phase and effective radius during twelve fog case studies, and explores these results alongside the aerosol measurements to discuss evidence for fog-aerosol interactions. The key findings of this thesis and outstanding questions are summarised in Table 5.1 and discussed below.

The seasonal cycle in near-surface aerosol particle number concentrations at Summit is distinct from that observed at sea-level Arctic sites, which typically experience minimum aerosol particle number concentrations in the late summer and autumn, followed by an increase in accumulation mode particles ($>$ 100 nm diameter) in the winter associated with Arctic haze (e.g. Freud et al. 2017; Schmeisser et al. 2018). At Summit, the minimum monthly mean N_{20} occurred in February in 2019 (18 cm^{-3}), followed by

Table 5.1.: A summary of key findings and limitations/outstanding questions.

Key findings	Limitations / Outstanding questions	Chapter reference
The seasonal cycle in surface aerosol concentration at Summit is distinct from that of sea-level Arctic sites that experience maximum concentrations in early spring and minimum in late summer. In 2019 the minimum monthly mean N_{20} at Summit occurred in February (18 cm^{-3}) and the maximum in April (247 cm^{-3}).	- The seasonal cycle in aerosol particle size distributions (< 250 nm diameter) is unknown. - The contribution of new particle formation to the aerosol population over central Greenland is unknown.	Chapter 2
High N_{20} events at Summit are associated with anticyclonic conditions and the descent of free tropospheric air to the surface. Low N_{20} events are associated with low pressure systems that drive upslope flow.	- How does precipitation (amount and phase) along the aerosol transport pathway impact N_{20} over central Greenland? - Is this also true higher in the atmosphere? Or does this reflect changes in the sources/sinks of aerosol particles in the surface layer?	Chapter 2
N_{20} falls below 10 cm^{-3} on multiple occasions and in all seasons at Summit in 2019, implying that N_{CCN} falls low enough to limit cloud/fog formation.	- Is this also true at cloud level? How does N_{20} vary with height over the ice sheet? - There are no directly measurements of N_{CCN} or aerosol particle hygroscopicity at Summit.	Chapter 2
Fog significantly modifies the surface aerosol population: - Almost all particles > 250 nm are scavenged during fog. - There is an average reduction of 20% in N_{20} during fog but, on some occasions, fog is associated with significant increases in N_{20}.	- Fog case studies are limited in number due to a lack of dedicated and validated instrumentation for fog detection. - Size resolved measurements of particles < 250 nm diameter and measurements of fog droplet number concentrations would help improve our understanding of changes in N_{20} during fog.	Chapter 2, Chapter 4
Ground-based measurements of spectrally resolved longwave radiation are particularly sensitive to the shallow surface-based temperature inversions and small amounts of LWP associated with radiation fogs at Summit, and can detect fogs which other remote-sensing instruments (lidar, MWR) cannot.	- Fog case studies are limited in number due to a lack of dedicated and validated instrumentation for fog detection. - Thermodynamic profile retrievals are not possible above optically thick fog/ cloud. - Thermodynamic profile and LWP retrievals require accurate measurements of cloud base height.	Chapter 3
Ground-based measurements of spectrally resolved longwave radiation can be used to retrieve fog microphysical properties (phase portioning and particle size).	- Fog case studies are limited in number due to a lack of dedicated and validated instrumentation for fog detection. - Thorough validation requires in-situ vertical profile measurements of fog particle size and phase. - Retrievals are only possible when the fog optical depth is between ~0.25 to 6, and when the fog occurs under otherwise clear skies. - Due to the minimum optical depth requirement these retrievals cannot be used to study initial fog formation or tenuous aerosol-limited fog events.	Chapter 4

a rapid increase to the maximum monthly mean of 247 cm^{-3} in April. Throughout the summer, N_{20} remained close to the annual mean (129 cm^{-3}) and then began to decrease again in October. The seasonal cycle in N_{20} at Summit in 2019 is consistent with multi-year observations of surface aerosol optical properties (scattering and absorption coefficients), and total aerosol optical depth measurements at Summit (Tomasi et al. 2015; Schmeisser et al. 2018).

Anomalously high N_{20} events at Summit in 2019 were associated with anticyclonic circulation and the descent of free tropospheric air to the ice sheet surface, whereas anomalously low N_{20} events were associated with cyclonic circulation over south-east Greenland driving up slope flow (Chapter 2). This supports the hypotheses of Dibb (2007), and Hirdman et al. (2010), that the main source of aerosol particles over central Greenland is the well-mixed free troposphere, and suggests that wet deposition during transport is an important control on N_{20} over central Greenland, since up slope flow is strongly linked to increases in precipitation and anomalously warm temperatures (resulting in more liquid versus ice precipitation) on route to Summit (Schuenemann et al. 2009; Pettersen et al. 2022; Gallagher et al. 2022). Overall, these findings demonstrate that the synoptic controls on the near-surface aerosol population over central Greenland are unique in the Arctic, in agreement with previous studies (Hirdman et al. 2010; Schmeisser et al. 2018; Schmale et al. 2021), and therefore aerosol parameterisations developed for the central Arctic region should not be generalised over the central GrIS.

N_{20} fell to exceptionally low values (below 10 cm^{-3}) on multiple occasions and in all seasons in 2019 (Chapter 2). Since the number concentration of cloud condensation nuclei (CCN), cm^{-3} (N_{CCN}) and the number concentration of ice nucleating particles (INP), cm^{-3} (N_{INP}) are a subset of N_{20}, this suggests that fog and low-level clouds at Summit sometimes exists in the aerosol-limited regime described by Mauritsen et al. (2011), where aerosol number concentrations are a critical control on fog/cloud lifetime and radiative forcing (i.e. small changes in aerosol particle number concentrations can be the difference between cloud/fog presence or absence). Sterzinger et al. (2022) recently used one of the case studies of extremely low N_{20} at Summit presented in Chapter 2 to drive large eddy simulations which demonstrated that the coincident cloud dissipation was plausibly controlled by the low aerosol particle concentration in this case.

A critical limitation of this study is that surface measurements of aerosol particle number concentrations are rarely likely to be representative of the aerosol population at cloud height, since the near-surface layer is almost always isolated from above by a strong surface-based temperature inversion (Miller et al. 2013, and Chapter 2). The

median cloud base height at Summit [for clouds below 3 km above ground level (a.g.l)] ranges from 260 to 780 m a.g.l annually (Shupe et al. 2013), which is above the median depth of the surface-based temperature inversion (< 200 m a.g.l year-round, Shupe et al. 2013). This, combined with the fact that the primary source of aerosol particles appears to be descent from the free troposphere (Hirdman et al. 2010, and Chapter 2), and that there is evidence of increases in the near-surface aerosol particle concentrations associated with mixing down from above (Dibb 2007, and chapter 4), implies that the aerosol population interacting with low-level tropospheric clouds is likely to be different to that measured at the surface. This highlights a critical need for measurements of the vertical profile of aerosol particle number concentrations up to 1,000 m a.g.l over central Greenland in order to understand the role of aerosol-cloud interactions on the GrIS surface energy budget (SEB). Specific recommendations for future studies are discussed further in section 2.

Unlike clouds, fogs form within the isolated near-surface layer and interact with the near-surface aerosol population. Almost all particles > 250 nm diameter are incorporated into fog particles (Chapter 4), and there is 20% reduction in N_{20} on average during fog (Chapter 2). However, changes in N_{20} associated with fog are highly variable between events, and N_{20} can also sometimes increase during fog, by over 100% on some occasions (Chapter 4). Some of this variability in the modification of N_{20} during fog could be related to differences in the particle size distribution; for example, N_{20} particles with diameters > 100 nm are more likely to act as CCN than smaller particles. Measurements of the particle size distribution between 20 and 230 nm are required to investigate these processes further. Some of the differences in the N_{20} response during fog events can be explained by differences in vertical mixing; some fogs remain in an isolated stable layer throughout their lifetime, whereas others generate mixing through radiative cooling at fog top, and there is evidence in at least one case that a large increase in N_{20} is associated with the mixing of air down to the surface (Chapter 4). Differences in aerosol composition could also be important, since more soluble particles can be activated at smaller diameters; measurements of aerosol particle composition, hygroscopicity, or direct measurements of N_{CCN} are necessary to investigate this further.

Even though fog is common and clearly modifies the near-surface aerosol population, there are no instruments specifically dedicated to fog detection at Summit. This is surprising given the importance of visibility for station operations, and the fact that fog increases net downwelling radiation at the surface by 26.1 W m^{-2} on average compared to equivalent clear sky days (Cox et al. 2019). This motivated the novel application of measurements of spectrally resolved downwelling longwave radiation (from the

Atmospheric Emitted Radiance Interferometer (AERI)) for the detection and characterisation of radiation fog events at Summit (Chapters 3 and 4). Chapter 3 introduced a radiative definition of fog that is more appropriate for studying the impact of fog on the SEB than traditional visibility-based definitions and demonstrated that AERI measurements can be used to generate continuous accurate retrievals of near-surface temperature and water vapor profiles even in the presence of the exceptionally strong surface-based temperature inversions (lapse rates up to -1.2°C m^{-1}) associated with radiation fog at Summit.

Chapter 3 also demonstrated that the AERI is particularly sensitive to small (< 5 g m^{-2}) changes in liquid water path (LWP) and can therefore detect the initial increases in LWP associated with radiation fog formation on average 90 minutes before the microwave radiometer and 30 minutes before the ceilometer – two instruments that have already been incorporated into fog detection and early warning systems (Haeffelin et al. 2016; Martinet et al. 2020). The wider applicability of these results for fog detection are discussed in section 3.c. For investigating fog-aerosol interactions at Summit, continuous accurate retrievals of boundary layer temperature profiles are required as input to MIXCRA to retrieve fog microphysical properties. Chapter 3 demonstrated that the uncertainties in the temperature profiles retrieved from AERI data were ±1°C in the lowest 1,000 m a.g.l, which was small enough that the contribution of this uncertainty to the total uncertainty in MIXCRA was negligible compared to the uncertainties related to the forward-model sensitivity (Chapter 4). This was a critical step for retrieving fog microphysical properties at Summit, especially given how steep the temporal and vertical gradients in temperature can be (e.g. Appendix A).

The goal of Chapter 4 was to explore the possibility of using MIXCRA to generate retrievals of fog microphysical properties from spectrally resolved measurements of downwelling longwave radiation from the AERI, and to use the results alongside measurements of near-surface aerosol particle number concentration to look for observational evidence of fog-aerosol interactions. This is the first time that MIXCRA has been applied to cases of fog (rather than cloud). A cross-validation with in-situ measurements of fog droplet effective radius demonstrated that MIXCRA retrievals can capture variations in fog droplet effective radius (root mean squared error (RMSE) 2.0 μm) when the fog optical depth is sufficient ($\tau > 0.25$). However, the small signal-to-noise ratio when $\tau < 0.25$ means that it is not possible to use MIXCRA retrievals of fog microphysical properties to study the initial formation stage of the fog or tenuous fogs that could be in the aerosol-limited regime.

The case studies presented in Chapter 4 demonstrate that there are multiple pathways

through which the surface aerosol population may (or may not) impact fog development, and through which fog itself can modify the surface aerosol population. The relative importance of these different pathways cannot be determined from the small number of case studies; however, this study provides a proof of concept for the use of MIXCRA to determine fog microphysical properties. The AERI has been operating continuously at Summit since 2010 (Shupe et al. 2013), so the methodologies applied in Chapters 3 and 4 to detect fog and retrieve thermodynamic profiles, liquid water path, and fog microphysical properties can now be applied to the full 12-year dataset, which would allow investigations into the trends in fog and low cloud occurrence and microphysical properties over time as well as the generation of a much larger dataset of fog events.

2. Recommendations for future work

Many of the conclusions of this thesis are limited by measurement and instrument constraints, and by a limited number of suitable case studies. The lack of fog case studies at Summit can be addressed in the future by applying the fog detection procedure demonstrated in Chapter 3 to the full 12-year Integrated Characterization of Energy, Clouds, Atmospheric state and Precipitation at Summit (ICECAPS) dataset as mentioned above. However, continuous monitoring of near-surface aerosol particle number concentrations only began in 2019, and a longer-term dataset of aerosol properties is necessary to understand the relative importance of some of the fog-aerosol interactions identified in Chapter 4, and how these will change in a changing climate; for example, whether changes in synoptic circulation around Greenland will lead to changes in the aerosol population or changes in fog frequency. As well as maintaining the existing instrumentation at Summit, additional measurements are necessary to address many of the outstanding limitations and questions, these measurement and instrumentation requirements are summarised in Table 5.2.

Two key measurements of aerosol properties at Summit are missing: (1) size resolved measurements of particles < 250 nm diameter, and (2) vertical profiles of aerosol particle number concentrations and size distributions up to the top of boundary layer and to heights where they are relevant for cloud formation (up to ∼1,000 m a.g.l). Size resolved measurements of smaller particles will enable straightforward comparisons between Summit and other measurement sites that report particle size distributions. For example, many Arctic sites (including along the north coast of Greenland) experience maximum number concentrations of larger particles (> 100 nm diameter) in the spring and maximum number concentrations of smaller particles (< 100 nm diameter) in the

Table 5.2.: Measurement and instrument requirements to address outstanding science objectives. Instruments in bold are currently not available at Summit, instruments in bold italics have recently been installed at Summit as a result of the findings in this thesis.

Science objective	Measurement requirements	Instrument requirements
• Understand the seasonal variations in surface aerosol particle size distributions over the central GrIS. • Determine the contribution of new particle formation to the aerosol population over the central GrIS.	Size resolved measurements of particles 5 to 250 nm diameter.	Condensation particle counter (CPC)
		Scanning mobility particle sizer (SMPS) or equivalent.
	Measurements of precursor vapor concentrations (e.g., NH_3, H_2SO_4, VOCs)	**Atmospheric ion mass spectrometer, e.g., CI-APi-TOF (Jokinen et al., 2012)**
• Determine how precipitation (amount and phase) along the aerosol transport pathway impacts aerosol particle number concentrations over the central GrIS.	Measurements of aerosol particle number concentrations.	Condensation particle counter (CPC)
	Aerosol transport back trajectories and spatial distribution of precipitation amount and phase.	e.g., from reanalysis data and dispersion modelling tools.
• Understand how the aerosol population varies with height over the central GrIS	Continuous vertical profiles of aerosol particle concentrations and size distributions. 1-min sampling resolution, surface to 1,000 m a.g.l (above boundary layer)	Lightweight, battery powered, optical particle spectrometer.
		Platform to vary instrument height (e.g., drone, helikite)
		Ground-based high spectral resolution lidar, (e.g., Reid et al., 2017) or a Raman lidar (e.g., Ansmann et al., 1990)
• Determine when and how often low-level clouds and fog over central Greenland are critically limited by CCN concentrations.	Continuous measurements of aerosol particle size distribution at cloud height.	Lightweight, battery powered, optical particle spectrometer.
		Platform to vary instrument height (e.g., drone, helikite)
	Measurements of N_{CCN}	**Cloud condensation nuclei counter (e.g., Paramonov et al., 2015)**
• Understand the role of nocturnal radiation fog in pre-conditioning the ice sheet surface for melt. • Understand how fog microphysical properties and fog-aerosol-SEB interactions vary seasonally over the GrIS.	Continuous fog detection.	***Visibility sensor or fog monitor (e.g., forward scattering spectroscopy probe).***
	Continuous measurements of SEB components (upwelling and downwelling LW/SW radiation, sensible and latent heat fluxes, ground heat flux).	Radiometer suite (upwelling and downwelling pyranometers, pyrgeometers).
		3D sonic anemometer, temperature and water vapor measurements.
		Sub-surface thermistor string / ground heat flux plates.
	Fog microphysical properties (phase and size distribution)	Measurements of spectrally resolved downwelling longwave radiation (e.g., AERI)
• Validate MIXCRA retrievals of phase partitioning and particle size during mixed-phase fogs.	Vertical profiles of fog particle phase and size distribution	**Fog droplet monitor/ forward scattering spectroscopy probe. At multiple levels (e.g., tower based)**
		Cloud imaging probe/ cloud particle imager. At multiple levels (e.g., tower based)

summer associated with new-particle formation (e.g. Croft et al. 2016; Freud et al. 2017; Dall'Osto et al. 2019). Currently the only measurements of particle size distributions < 250 nm diameter at Summit were collected in May and June 2007 (Ziemba et al. 2010). During this time the majority of the particle number concentration was in the 30 to 110 nm range, but there were four events when the number concentration of 9 to 30 nm particles increased to > 500 cm^{-3}. Although there was no evidence of direct new particle formation at Summit (i.e. no particles < 9 nm diameter), the authors attribute the particle growth events to the condensation of photochemically produced organic material from the snowpack (Ziemba et al. 2010). Year-round measurements of the aerosol particle size distribution < 250 nm will provide a better understanding of the processes controlling cloud relevant aerosols in different seasons. Simultaneous measurements of precursor vapor concentrations (i.e. H_2SO_4 and volatile organic compounds) would also be useful to determine the sources of secondary aerosol and particle growth at Summit.

The importance of understanding how the aerosol particle number concentration and size distribution varies with height throughout the boundary layer and up to cloud level at Summit is critical for determining the role of aerosol-cloud interactions in modulating the ice sheet surface energy budget (for reasons outlined in section 1). These measurements do not currently exist and should be a priority for future measurement campaigns at Summit. Lightweight, battery powered, optical particle spectrometers that can measure size-resolved particle number concentrations > 140 nm (e.g. the Portable Optical Particle Counter (POPS), Gao et al. 2016; Mei et al. 2020), are small enough to mount on unmanned aerial vehicles or balloon platforms to collect vertical profiles from the surface up to 2,000 m a.g.l (e.g. Kezoudi et al. 2021; Creamean et al. 2021). These measurements, alongside simultaneous measurements of surface aerosol particle properties, will help improve our understanding of the how aerosol particles are transported within the boundary layer and interact with clouds above the GrIS. Ground-based lidars can also detect continuous vertical profiles of aerosol optical depth (e.g. Ansmann et al. 1990; Reid et al. 2017; Zhang et al. 2022), but due to the low total aerosol optical depths at Summit (∼0.05, Tomasi et al. 2015), such a system would require careful calibration and validation against in-situ measurements to extract a sufficient signal-to-noise ratio. This has not previously been attempted in an environment as clean as Summit and is an important area for future research.

Direct measurements of N_{CCN} would also help to determine when and how often fog is critically limited by CCN concentrations. Current cloud condensation nuclei counters are not small enough to fly on (drone or heli-kite) aerial platforms, so continuous measurements of N_{CCN} at cloud height (∼ 200 to 1,000 m a.g.l at Summit) are not possible.

However, the relationship between N_{CCN} and the aerosol particle size distribution at the surface can be used to estimate the critical dry diameter for CCN activation at a particular supersaturation using κ–Köhler theory (as long as polydisperse measurements of N_{CCN} are available, e.g. Schmale et al. 2018). Assuming that the chemical composition of the aerosol particles at cloud height are similar to those at the surface, the critical diameter derived using the surface observations can then be used to calculate N_{CCN} at cloud height based on vertical profiles of aerosol particle size distribution from lightweight optical particle counters.

Direct measurements of N_{INP} were collected throughout 2019 (currently unpublished), but the temporal resolution of 56-hours (due to low concentrations and the requirements of the filter sampling technique), is too coarse to investigate how fog interacts with surface N_{INP}. Despite recent and ongoing improvements in online N_{INP} measurements (e.g. Möhler et al. 2021), it is not currently possible to measure low concentrations of INP particles such as those observed in the Arctic (< 0.01 L^{-1}, e.g. Wex et al. 2019) at a temporal resolution of < 24 hours. Further research into measurement techniques is needed to enable direct observations of the interaction between fog/clouds and N_{INP} in clean environments.

Continuous in-situ fog monitoring alongside measurements of the SEB components (upwelling and downwelling radiation, sensible and latent heat fluxes, and ground heat flux) are necessary to understand how fog impacts the GrIS SEB, and the role of nocturnal radiation fog in pre-conditioning the ice sheet surface for melt. Measurements of ground heat flux are currently unavailable at Summit and are important for determining how repeated events result in modification of the snowpack temperature over time. Although this thesis has demonstrated the skill of the AERI for the detection of optically thin but radiatively important fogs at Summit, in-situ measurements of visibility and/or fog particles would be a useful addition, both for the detection of fogs when there are other cloud layers present, and for the detection and characterisation of tenuous fogs that are below the detection limit of the AERI but might still interact significantly with the surface aerosol population (i.e. in aerosol-limited fogs). In-situ measurements of fog particle phase and size distribution at multiple heights (i.e. fog droplet monitors and cloud imaging probes at different levels on a tower) would enable a complete validation of the MIXCRA retrieval and investigation of the vertical structure and development of mixed-phase fogs over the ice sheet, which has not been measured before.

The additional measurement recommendations detailed above will help to improve our understanding of fog-aerosol interactions and their importance for the GrIS SEB,

but to fully address the science objectives listed in Table 5.2 these must be combined with modelling studies that can help to isolate the individual processes involved. For example, the results of Chapter 2 led to the hypothesis that precipitation (both amount and phase) along transport pathways is an important control on aerosol particle number concentrations at Summit. Testing this hypothesis would require combining in-situ aerosol particle measurements at Summit with back-trajectory information, for example modelled using the flexible particle dispersion model (FLEXPART) (Chapter 2), and spatially interpolated measurements of precipitation amount and phase (for example from satellite products or reanalysis data) using a Lagrangian approach (e.g. Sodemann et al. 2008), or implemented into a model that incorporates all of the relevant processes (e.g. Browse et al. 2012). This is an important area for future study given that precipitation amount and phase over the GrIS are likely to change in a changing climate (e.g. Lenaerts et al. 2020).

Modelling studies, such as large-eddy simulations (LES) that explicitly resolve the turbulent motions important for fog and cloud development, can provide information about the relative importance of different physical processes that cannot be determined from observations alone. For example, by artificially removing all aerosol particles in idealised LES simulations of case studies when cloud dissipation coincided with extremely low aerosol particle number concentrations, Sterzinger et al. (2022), was able to show that in two cases (including one of the cases from Summit that was discussed in Chapter 2) a lack of CCN could have been responsible for the cloud dissipation, whereas in another case (observed in the North Slope of Alaska) other processes were more likely to have been the main drivers. Through making controlled changes to individual parameters (such as the initial aerosol number concentration) or how the model represents certain processes (e.g. the details of the microphysics scheme), the sensitivity of the simulation to particular parameters or parameterisations can be determined. The results of such studies can be used to prioritise improvements to aerosol and cloud/fog microphysical parameterisations in larger scale climate models, where the value of increasing complexity must be balanced against increases in computational expense. LES studies based on the detailed fog case studies presented in this thesis are necessary to answer some of the outstanding questions that cannot be addressed through observations, for example why some fog cases developed into well-mixed optically thick fogs and others did not, which is important for the resulting net radiative forcing of the fog at the ice sheet surface.

Finally, to completely quantify the impact of fog, aerosols, and fog-aerosol interactions on the GrIS SEB, we need to integrate impacts across different regions of the GrIS. This thesis focuses on the central accumulation zone of the ice sheet using measurements

from a single location (Summit Station). The frequency and impact of fog in the ablation zone around the margin of the GrIS is currently unknown. The interaction between clouds and the GrIS SEB is different in the ablation zone (see fig. 1.1), and clouds usually cool the surface during daylight hours. The ablation zone features strong elevation gradients, a wide range of ice surface albedo (0.2 to 0.9, e.g. Moustafa et al. 2015) and has a stronger coastal influence; this means that different types of fog (such as advection or orographically forced fog) might be more prevalent, and that aerosol transport pathways and source regions are likely to be different. Therefore understanding how the impact of fog and fog-aerosol interactions changes between the ice sheet margin and the central plateau is another important area for future study.

3. Wider implications

3.a. For the Greenland Ice Sheet

This thesis highlights how difficult the detection of optically thin fog over the central GrIS can be; there are occasions when the ground-based radar, lidar (ceilometer), and microwave radiometer at Summit indicate clear sky conditions, but photographs of fog bows confirm the presence of liquid water droplets, and the AERI detects the associated increase in downwelling radiation at the surface. This identifies a need for dedicated instrumentation for continuous fog monitoring over the GrIS and illustrates the value of having human observers on the ground. Currently, climate models underestimate longwave cloud radiative forcing at the surface at Summit by 13.6 to 35.7 W m^{-2} (Lacour et al. 2018) and generate too few optically thin low-level clouds over the GrIS (Lacour et al. 2018; Taylor et al. 2019). Fog under otherwise clear skies occurs commonly at Summit, is usually optically thin, and contributes an average net longwave radiative forcing at the surface during individual events that is similar in magnitude to the climate model deficiency (19.8 to 26.1 W m^{-2}, Cox et al. 2019). Plausibly, an underestimation of fog occurrence in climate models over the GrIS could be contributing to the model bias in longwave cloud radiative forcing. Since radiation fog forms under quite different conditions to clouds, determining how well climate models represent fog over the ice sheet is an important next step.

3.b. For Antarctica

Aside from the central Greenland, the only other place on Earth where there is a high elevation ice covered continental plateau with an area of > 1 x 10^5 km^2 is Antarctica. Measurements of cloud/fog microphysical properties and their interaction with aerosol particles over the Antarctic plateau are even more sparse and difficult to obtain than those over the GrIS (Lachlan-Cope 2010; Bromwich et al. 2012). Past studies have assumed that fog and cloud over the Antarctic Plateau are ice phase (e.g. Lubin and Harper 1996; Mahesh et al. 2001), but more recently, the existence of supercooled liquid droplets and the importance of their radiative effects on at the surface have been recognised (e.g. Bromwich et al. 2012; Ricaud et al. 2017, 2020, 2022).

The Concordia Research Station at Dome-C is especially similar to Summit; located at a topographic peak with shallow relief at 3,233 m above sea level (a.s.l) and 74°S. Dome C experiences surface temperatures ranging from -50 to -20°C (Argentini et al. 2005) and surface-based temperature inversions that are of a comparable frequency and magnitude to those at Summit (with near-surface temperature gradients as high as 1°C m^{-1}, Genthon et al. 2013). Supercooled liquid droplets can have an important radiative impact at the surface at Dome-C (Ricaud et al. 2022), and optically thin fog is observed on summer evenings (Genthon et al. 2022). This suggests that the observations of fog and fog-aerosol interactions at Summit could also be relevant at Dome-C and over the Antarctic plateau more broadly. Also, due to similar atmospheric conditions between the Antarctic plateau and Summit, the techniques demonstrated in Chapters 3 and 4 to detect fog and to retrieve thermodynamic profiles and fog/cloud microphysical properties from AERI measurements can be effectively applied to AERI measurements that are already available from both Dome-C (Walden et al. 2005) and South Pole Station (Town et al. 2005).

3.c. For fog forecasting and nowcasting

The accurate characterisation of shallow surface-based temperature inversions, and the detection of small increases in LWP using AERI measurements, has broader implications for fog detection and nowcasting both within polar regions, and in the more densely populated mid-latitudes. The reduction in horizontal visibility caused by fog can disrupt ground and air transportation and present a serious safety hazard (Gultepe et al. 2007, 2019; Panahi et al. 2020), and the build-up of rime ice associated with supercooled fog can damage structures and power transmission lines and poses a safety hazard in shipping and aviation (Ducloux and Nygaard 2018; Cao et al. 2018; Panahi

et al. 2020). Despite this, fog forecasting remains a significant challenge for numerical weather prediction models (Steeneveld et al. 2015; Philip et al. 2016; Westerhuis and Fuhrer 2021). Part of the reason for this is that fog formation is particularly sensitive to the thermodynamic structure of the boundary layer (e.g. Steeneveld et al. 2015), and numerical weather prediction (NWP) models often fail to reproduce the steep and shallow temperature gradients associated with radiation fog formation (Martinet et al. 2020; Westerhuis and Fuhrer 2021). Recent studies have demonstrated that assimilating measurements of boundary later thermodynamic structure into NWP models can improve fog forecasts by correcting errors in the temperature profile in the lowest 500 m a.g.l (Martinet et al. 2017, 2020). These studies used temperature profile retrievals from ground-based microwave radiometers, that have a maximum vertical resolution of 50 m at the surface, decreasing to 1.7 km at 1 km a.g.l (Rose et al. 2005; Cadeddu et al. 2013).

Chapter 3 demonstrates that retrievals of temperature profiles from AERI measurements are better able to capture the steep shallow surface-based temperature inversions associated with radiation fog formation than retrievals from the microwave radiometer, due to the higher sensitivity of the AERI to the near-surface temperature profile. In addition, the high sensitivity of the AERI to small changes in LWP means that the AERI can detect small increases in LWP associated with radiation fog formation and the reduction in horizontal visibility at the surface up to 185 minutes before the microwave radiometer. Together this suggests that the AERI could be a useful tool for improving forecasting and nowcasting of fog in NWP models, and the results of Chapter 3 present a case for future observing-system experiments (or observing-system simulation experiments, as in Otkin et al. 2011; Hartung et al. 2011) to quantify the impact of the operational use of AERI observations in terms of improvements to fog forecasting skill in NWP models.

Although the AERI is especially useful for the detection of radiation fog at Summit, it has several key limitations for the detection of fog more generally. The AERI is unable to retrieve thermodynamic profiles above optically thick clouds or fog and requires separate accurate measurements of cloud base height (i.e., from a ceilometer). Retrievals from the AERI are less sensitive to small changes in LWP in moist atmospheres (precipitable water content > 1 cm) where the clear sky infrared emission is greater and so the signal-to-noise ratio is smaller. Overall, the results presented in this thesis emphasize that a multi-instrument approach will provide the most accurate boundary layer thermodynamic profiles and LWP detection with the potential to improve fog forecasting and nowcasting in operational models, and that the inclusion of the AERI or an equivalent instrument could add significant value in certain situations.

4. Final remarks

The Arctic is warming up to four times faster than the global average (Rantanen et al. 2022) and the GrIS is changing rapidly in response (e.g. IMBIE 2020). In the four years that I have been working on this thesis, I have witnessed the second and third surface melt events at Summit in over a century (Tedesco and Fettweis 2020; Xu et al. 2022), the first time in the observational record that rain has been reported on the top of the ice sheet (Xu et al. 2022), and the first ever confirmed visitation of a polar bear to Summit Station (Summit Station Season Update 2018). Within the next few years Summit is likely to experience surface melt on an annual basis (McGrath et al. 2013), which will modify the surface albedo (and therefore the SEB and cloud radiative forcing) and the structure of the firn in the accumulation zone (impacting the transfer of heat and melt percolation, e.g. Van den Broeke et al. 2016). Large-scale circulation patterns such as blocking events over Greenland, and the frequency of north Atlantic cyclones are also changing as the climate warms (e.g. Rinke et al. 2017; Barrett et al. 2020), which in turn can be expected to impact cloud cover, temperature, and precipitation patterns over the GrIS (Gallagher et al. 2018, 2022), as well as the properties of atmospheric aerosol (e.g. Pernov et al. 2022). Understanding what drives the changes in the aerosol population, the frequency of cloud and fog events, and the relative impact of cloud/fog and cloud/fog-aerosol interactions on the GrIS SEB, is now more important than simply observing mean values, since all the relevant properties are in a state of change. Both remote and in-situ observations of aerosol and cloud properties are critical for improving model parameterisations of cloud-aerosol interactions (Morrison et al. 2020), and establishing consistent long-term observations are important to monitor and understand how atmospheric properties over the ice sheet are changing in time (e.g. Schmale et al. 2021), and to evaluate whether climate models are adequately capturing these changes.

This thesis has provided new observations of fog and aerosol properties over the central GrIS, where existing observations are sparse and environmental conditions are unique outside of Antarctica, and has tested novel techniques for retrieving near-surface thermodynamic profiles and fog microphysical properties in such environments based on ground-based remote sensing of spectrally resolved longwave radiation. These techniques can now be applied retrospectively to existing data in Greenland and elsewhere to develop longer term datasets of fog and fog microphysical properties. Twelve detailed case studies of fog-aerosol interactions over the central GrIS highlight key processes (such as the importance of dynamics) and measurement limitations (e.g. longwave remote sensing cannot retrieve fog microphysical properties during tenuous potentially

aerosol-limited fogs). These results, alongside the publicly available data collected as part of the ICECAPS-ACE project (Guy et al. 2020), will provide the foundation for future observational campaigns and modelling studies that will ultimately improve the representation of cloud/fog-aerosol-energy feedbacks in climate and ice sheet mass balance models and reduce model uncertainties in future projections of the GrIS.

References

Ansmann, A., Riebesell, M., and Weitkamp, C.: Measurement of atmospheric aerosol extinction profiles with a Raman lidar, Optics letters, 15, 746–748, 1990.

Argentini, S., Viola, A., Sempreviva, A., and Petenko, I.: Summer boundary-layer height at the plateau site of Dome'C, Antarctica, Boundary-Layer Meteorology, 115, 409–422, 2005.

Barrett, B. S., Henderson, G. R., McDonnell, E., Henry, M., and Mote, T.: Extreme Greenland blocking and high-latitude moisture transport, Atmospheric Science Letters, 21, e1002, 2020.

Bromwich, D. H., Nicolas, J. P., Hines, K. M., Kay, J. E., Key, E. L., Lazzara, M. A., Lubin, D., McFarquhar, G. M., Gorodetskaya, I. V., Grosvenor, D. P., et al.: Tropospheric clouds in Antarctica, Reviews of Geophysics, 50, 2012.

Browse, J., Carslaw, K., Arnold, S., Pringle, K., Boucher, O., et al.: The scavenging processes controlling the seasonal cycle in Arctic sulphate and black carbon aerosol, Atmospheric Chemistry and Physics, 12, 6775–6798, 2012.

Cadeddu, M., Liljegren, J., and Turner, D.: The Atmospheric Radiation Measurement (ARM) program network of microwave radiometers: Instrumentation, data, and retrievals, Atmospheric Measurement Techniques, 6, 2359–2372, 2013.

Cao, Y., Tan, W., and Wu, Z.: Aircraft icing: An ongoing threat to aviation safety, Aerospace science and technology, 75, 353–385, 2018.

Cox, C. J., Noone, D. C., Berkelhammer, M., Shupe, M. D., Neff, W. D., Miller, N. B., Walden, V. P., and Steffen, K.: Supercooled liquid fogs over the central Greenland Ice Sheet, Atmospheric Chemistry and Physics, 19, 7467–7485, 2019.

Creamean, J. M., de Boer, G., Telg, H., Mei, F., Dexheimer, D., Shupe, M. D., Solomon, A., and McComiskey, A.: Assessing the vertical structure of Arctic aerosols using balloon-borne measurements, Atmospheric Chemistry and Physics, 21, 1737–1757, 2021.

Croft, B., Martin, R. V., Leaitch, W. R., Tunved, P., Breider, T. J., D'Andrea, S. D., and Pierce, J. R.: Processes controlling the annual cycle of Arctic aerosol number and size distributions, Atmospheric Chemistry and Physics, 16, 3665–3682, 2016.

Dall'Osto, M., Beddows, D., Tunved, P., Harrison, R. M., Lupi, A., Vitale, V., Becagli, S., Traversi, R., Park, K.-T., Yoon, Y. J., et al.: Simultaneous measurements of aerosol size distributions at three sites in the European high Arctic, Atmospheric Chemistry and Physics, 19, 7377–7395, 2019.

Dibb, J. E.: Vertical mixing above Summit, Greenland: Insights into seasonal and high frequency variability from the radionuclide tracers 7Be and 210Pb, Atmospheric Environment, 41, 5020–5030, 2007.

Ducloux, H. and Nygaard, B.: Ice loads on overhead lines due to freezing radiation fog events in plains, Cold Regions Science and Technology, 153, 120–129, 2018.

Freud, E., Krejci, R., Tunved, P., Leaitch, R., Nguyen, Q. T., Massling, A., Skov, H., and Barrie, L.: Pan-Arctic aerosol number size distributions: seasonality and transport patterns, Atmospheric Chemistry and Physics, 17, 8101–8128, 2017.

Gallagher, M. R., Shupe, M. D., and Miller, N. B.: Impact of atmospheric circulation on temperature, clouds, and radiation at Summit Station, Greenland, with self-organizing maps, Journal of Climate, 31, 8895–8915, 2018.

Gallagher, M. R., Shupe, M. D., Chepfer, H., and L'Ecuyer, T.: Relating snowfall observations to Greenland Ice Sheet mass changes: an atmospheric circulation perspective, The Cryosphere, 16, 435–450, 2022.

Gao, R., Telg, H., McLaughlin, R., Ciciora, S., Watts, L., Richardson, M., Schwarz, J., Perring, A., Thornberry, T., Rollins, A., et al.: A light-weight, high-sensitivity particle spectrometer for PM2. 5 aerosol measurements, Aerosol Science and Technology, 50, 88–99, 2016.

Genthon, C., Six, D., Gallée, H., Grigioni, P., and Pellegrini, A.: Two years of atmospheric boundary layer observations on a 45-m tower at Dome C on the Antarctic plateau, Journal of Geophysical Research: Atmospheres, 118, 3218–3232, 2013.

Genthon, C., Veron, D. E., Vignon, E., Madeleine, J.-B., and Piard, L.: Water vapor in cold and clean atmosphere: a 3-year data set in the boundary layer of Dome C, East Antarctic Plateau, Earth System Science Data, 14, 1571–1580, 2022.

Gultepe, I., Tardif, R., Michaelides, S. C., Cermak, J., Bott, A., Bendix, J., Müller, M. D., Pagowski, M., Hansen, B., Ellrod, G., et al.: Fog research: A review of past achievements and future perspectives, Pure and applied geophysics, 164, 1121–1159, 2007.

Gultepe, I., Sharman, R., Williams, P. D., Zhou, B., Ellrod, G., Minnis, P., Trier, S., Griffin, S., Yum, S., Gharabaghi, B., et al.: A review of high impact weather for aviation meteorology, Pure and applied geophysics, 176, 1869–1921, 2019.

Guy, H., Neely III, R. R., and Brooks, I.: ICECAPS-ACE: Integrated Characterization of Energy, Clouds, Atmospheric state, and Precipitation at Summit, Greenland - Aerosol Cloud Experiment measurements., Centre for Environmental Data Analysis, URL http://catalogue.ceda.ac.uk/uuid/f06c6aa727404ca788ee3dd0515ea61a, last accessed: 23 November 2022, 2020.

Haeffelin, M., Laffineur, Q., Bravo-Aranda, J.-A., Drouin, M.-A., Casquero-Vera, J.-A., Dupont, J.-C., and De Backer, H.: Radiation fog formation alerts using attenuated backscatter power from automatic lidars and ceilometers, Atmospheric Measurement Techniques, 9, 5347–5365, 2016.

Hartung, D. C., Otkin, J. A., Petersen, R. A., Turner, D. D., and Feltz, W. F.: Assimilation of surface-based boundary layer profiler observations during a cool-season weather event using an observing system simulation experiment. Part II: Forecast assessment, Monthly weather review, 139, 2327–2346, 2011.

Hirdman, D., Burkhart, J. F., Sodemann, H., Eckhardt, S., Jefferson, A., Quinn, P. K., Sharma, S., Ström, J., and Stohl, A.: Long-term trends of black carbon and sulphate aerosol in the Arctic: changes in atmospheric transport and source region emissions, Atmospheric Chemistry and Physics, 10, 9351–9368, 2010.

IMBIE: Mass balance of the Greenland Ice Sheet from 1992 to 2018, Nature, 579, 233–239, 2020.

Kezoudi, M., Keleshis, C., Antoniou, P., Biskos, G., Bronz, M., Constantinides, C., Desservettaz, M., Gao, R.-S., Girdwood, J., Harnetiaux, J., et al.: The Unmanned Systems Research Laboratory (USRL): A New Facility for UAV-Based Atmospheric Observations, Atmosphere, 12, 1042, 2021.

Lachlan-Cope, T.: Antarctic clouds, Polar Research, 29, 150–158, 2010.

Lacour, A., Chepfer, H., Miller, N., Shupe, M., Noel, V., Fettweis, X., Gallee, H., Kay, J., Guzman, R., and Cole, J.: How well are clouds simulated over Greenland in climate models? Consequences for the surface cloud radiative effect over the ice sheet, Journal of Climate, 31, 9293–9312, 2018.

Lenaerts, J., Camron, M. D., Wyburn-Powell, C. R., and Kay, J. E.: Present-day and

future Greenland Ice Sheet precipitation frequency from CloudSat observations and the Community Earth System Model, The Cryosphere, 14, 2253–2265, 2020.

Lubin, D. and Harper, D.: Cloud radiative properties over the South Pole from AVHRR infrared data, Journal of climate, pp. 3405–3418, 1996.

Mahesh, A., Walden, V. P., and Warren, S. G.: Ground-based infrared remote sensing of cloud properties over the Antarctic Plateau. Part II: Cloud optical depths and particle sizes, Journal of Applied Meteorology and Climatology, 40, 1279–1294, 2001.

Martinet, P., Cimini, D., De Angelis, F., Canut, G., Unger, V., Guillot, R., Tzanos, D., and Paci, A.: Combining ground-based microwave radiometer and the AROME convective scale model through 1DVAR retrievals in complex terrain: An Alpine valley case study, Atmospheric Measurement Techniques, 10, 3385–3402, 2017.

Martinet, P., Cimini, D., Burnet, F., Ménétrier, B., Michel, Y., and Unger, V.: Improvement of numerical weather prediction model analysis during fog conditions through the assimilation of ground-based microwave radiometer observations: a 1D-Var study, Atmospheric Measurement Techniques, 13, 6593–6611, 2020.

Mauritsen, T., Sedlar, J., Tjernström, M., Leck, C., Martin, M., Shupe, M., Sjogren, S., Sierau, B., Persson, P., Brooks, I., et al.: An Arctic CCN-limited cloud-aerosol regime, Atmospheric Chemistry and Physics, 11, 165–173, 2011.

McGrath, D., Colgan, W., Bayou, N., Muto, A., and Steffen, K.: Recent warming at Summit, Greenland: Global context and implications, Geophysical Research Letters, 40, 2091–2096, 2013.

Mei, F., McMeeking, G., Pekour, M., Gao, R.-S., Kulkarni, G., China, S., Telg, H., Dexheimer, D., Tomlinson, J., and Schmid, B.: Performance Assessment of Portable Optical Particle Spectrometer (POPS), Sensors, 20, 6294, 2020.

Miller, N., Turner, D., Bennartz, R., Shupe, M., Kulie, M., Cadeddu, M., and Walden, V. P.: Surface-based inversions above central Greenland, Journal of Geophysical Research: Atmospheres, 118, 495–506, 2013.

Möhler, O., Adams, M., Lacher, L., Vogel, F., Nadolny, J., Ullrich, R., Boffo, C., Pfeuffer, T., Hobl, A., Weiß, M., et al.: The Portable Ice Nucleation Experiment (PINE): a new online instrument for laboratory studies and automated long-term field observations of ice-nucleating particles, Atmospheric Measurement Techniques, 14, 1143–1166, 2021.

Morrison, H., van Lier-Walqui, M., Fridlind, A. M., Grabowski, W. W., Harrington, J. Y., Hoose, C., Korolev, A., Kumjian, M. R., Milbrandt, J. A., Pawlowska, H., et al.: Confronting the challenge of modeling cloud and precipitation microphysics, Journal of advances in modeling earth systems, 12, 2020.

Moustafa, S., Rennermalm, A., Smith, L., Miller, M., Mioduszewski, J., Koenig, L., Hom, M., and Shuman, C.: Multi-modal albedo distributions in the ablation area of the southwestern Greenland Ice Sheet, The Cryosphere, 9, 905–923, 2015.

Otkin, J. A., Hartung, D. C., Turner, D. D., Petersen, R. A., Feltz, W. F., and Janzon, E.: Assimilation of surface-based boundary layer profiler observations during a cool-season weather event using an observing system simulation experiment. Part I: Analysis impact, Monthly Weather Review, 139, 2309–2326, 2011.

Panahi, R., Ng, A. K., Afenyo, M. K., and Haeri, F.: A novel approach in probabilistic quantification of risks within the context of maritime supply chain: The case of extreme weather events in the Arctic, Accident Analysis & Prevention, 144, 2020.

Paramonov, M., Kerminen, V.-M., Gysel, M., Aalto, P. P., Andreae, M. O., Asmi, E., Baltensperger, U., Bougiatioti, A., Brus, D., Frank, G., et al.: A synthesis of cloud condensation nuclei counter (CCNC) measurements within the EUCAARI network, Atmospheric Chemistry and Physics, 15, 12 211–12 229, 2015.

Pernov, J. B., Beddows, D., Thomas, D. C., Harrison, R. M., Schmale, J., Skov, H., Massling, A., et al.: Increased aerosol concentrations in the High Arctic attributable to changing atmospheric transport patterns, npj Climate and Atmospheric Science, 5, 1–13, 2022.

Pettersen, C., Henderson, S. A., Mattingly, K. S., Bennartz, R., and Breeden, M. L.: The Critical Role of Euro-Atlantic Blocking in Promoting Snowfall in Central Greenland, Journal of Geophysical Research: Atmospheres, 127, 2022.

Philip, A., Bergot, T., Bouteloup, Y., and Bouyssel, F.: The impact of vertical resolution on fog forecasting in the kilometric-scale model arome: a case study and statistics, Weather and Forecasting, 31, 1655–1671, 2016.

Rantanen, M., Karpechko, A. Y., Lipponen, A., Nordling, K., Hyvärinen, O., Ruosteenoja, K., Vihma, T., and Laaksonen, A.: The Arctic has warmed nearly four times faster than the globe since 1979, Communications Earth & Environment, 3, 1–10, 2022.

Reid, J. S., Kuehn, R. E., Holz, R. E., Eloranta, E. W., Kaku, K. C., Kuang, S., Newchurch, M. J., Thompson, A. M., Trepte, C. R., Zhang, J., et al.: Ground-based High Spectral Resolution Lidar observation of aerosol vertical distribution in the summertime Southeast United States, Journal of Geophysical Research: Atmospheres, 122, 2970–3004, 2017.

Ricaud, P., Bazile, E., del Guasta, M., Lanconelli, C., Grigioni, P., and Mahjoub, A.: Genesis of diamond dust, ice fog and thick cloud episodes observed and modelled above dome c, Antarctica, Atmospheric Chemistry and Physics, 17, 5221–5237, 2017.

Ricaud, P., Del Guasta, M., Bazile, E., Azouz, N., Lupi, A., Durand, P., Attié, J.-L., Veron, D., Guidard, V., and Grigioni, P.: Supercooled liquid water cloud observed, analysed, and modelled at the top of the planetary boundary layer above Dome C, Antarctica, Atmospheric Chemistry and Physics, 20, 4167–4191, 2020.

Ricaud, P., Del Guasta, M., Lupi, A., Roehrig, R., Bazile, E., Durand, P., Attié, J.-L., Nicosia, A., and Grigioni, P.: Supercooled liquid water clouds observed over Dome C, Antarctica: temperature sensitivity and surface radiation impact, Atmospheric Chemistry and Physics Discussions, pp. 1–38, 2022.

Rinke, A., Maturilli, M., Graham, R. M., Matthes, H., Handorf, D., Cohen, L., Hudson, S. R., and Moore, J. C.: Extreme cyclone events in the Arctic: Wintertime variability and trends, Environmental Research Letters, 12, 2017.

Rose, T., Crewell, S., Löhnert, U., and Simmer, C.: A network suitable microwave radiometer for operational monitoring of the cloudy atmosphere, Atmospheric research, 75, 183–200, 2005.

Schmale, J., Henning, S., Decesari, S., Henzing, B., Keskinen, H., Sellegri, K., Ovadnevaite, J., Pöhlker, M. L., Brito, J., Bougiatioti, A., et al.: Long-term cloud condensation nuclei number concentration, particle number size distribution and chemical composition measurements at regionally representative observatories, Atmospheric Chemistry and Physics, 18, 2853–2881, 2018.

Schmale, J., Zieger, P., and Ekman, A. M.: Aerosols in current and future Arctic climate, Nature Climate Change, 11, 95–105, 2021.

Schmeisser, L., Backman, J., Ogren, J. A., Andrews, E., Asmi, E., Starkweather, S., Uttal, T., Fiebig, M., Sharma, S., Eleftheriadis, K., et al.: Seasonality of aerosol optical properties in the Arctic, Atmospheric Chemistry and Physics, 18, 11 599–11 622, 2018.

Schuenemann, K. C., Cassano, J. J., and Finnis, J.: Synoptic forcing of precipitation over Greenland: Climatology for 1961–99, Journal of Hydrometeorology, 10, 60–78, 2009.

Shupe, M. D., Turner, D. D., Walden, V. P., Bennartz, R., Cadeddu, M. P., Castellani, B. B., Cox, C. J., Hudak, D. R., Kulie, M. S., Miller, N. B., et al.: High and dry: New observations of tropospheric and cloud properties above the Greenland Ice Sheet, Bulletin of the American Meteorological Society, 94, 169–186, 2013.

Sodemann, H., Schwierz, C., and Wernli, H.: Interannual variability of Greenland winter precipitation sources: Lagrangian moisture diagnostic and North Atlantic Oscillation influence, Journal of Geophysical Research: Atmospheres, 113, 2008.

Steeneveld, G., Ronda, R., and Holtslag, A.: The challenge of forecasting the onset and development of radiation fog using mesoscale atmospheric models, Boundary-Layer Meteorology, 154, 265–289, 2015.

Sterzinger, L. J., Sedlar, J., Guy, H., Neely III, R. R., and Igel, A. L.: Do Arctic mixed-phase clouds sometimes dissipate due to insufficient aerosol? Evidence from comparisons between observations and idealized simulations, Atmospheric Chemistry and Physics, 22, 8973–8988, 2022.

Summit Station Season Update: Summit Station Season Update, summer 2018, `https://geo-summit.org/news/summit-station-season-updates-summer-2018`, accessed: 23 November 2022, 2018.

Taylor, P. C., Boeke, R. C., Li, Y., and Thompson, D. W.: Arctic cloud annual cycle biases in climate models, Atmospheric Chemistry and Physics, 19, 8759–8782, 2019.

Tedesco, M. and Fettweis, X.: Unprecedented atmospheric conditions (1948–2019) drive the 2019 exceptional melting season over the Greenland Ice Sheet, The Cryosphere, 14, 1209–1223, 2020.

Tomasi, C., Kokhanovsky, A. A., Lupi, A., Ritter, C., Smirnov, A., O'Neill, N. T., Stone, R. S., Holben, B. N., Nyeki, S., Wehrli, C., et al.: Aerosol remote sensing in polar regions, Earth-Science Reviews, 140, 108–157, 2015.

Town, M. S., Walden, V. P., and Warren, S. G.: Spectral and broadband longwave downwelling radiative fluxes, cloud radiative forcing, and fractional cloud cover over the South Pole, Journal of climate, 18, 4235–4252, 2005.

Van den Broeke, M. R., Enderlin, E. M., Howat, I. M., Kuipers Munneke, P., Noël, B. P., Van De Berg, W. J., Van Meijgaard, E., and Wouters, B.: On the recent contribution of the Greenland Ice Sheet to sea level change, The Cryosphere, 10, 1933–1946, 2016.

Walden, V., Town, M., Halter, B., and Storey, J.: First measurements of the infrared sky brightness at Dome C, Antarctica, Publications of the Astronomical Society of the Pacific, 117, 300, 2005.

Westerhuis, S. and Fuhrer, O.: A Locally Smoothed Terrain-Following Vertical Coordinate to Improve the Simulation of Fog and Low Stratus in Numerical Weather Prediction Models, Journal of Advances in Modeling Earth Systems, 13, 2021.

Wex, H., Huang, L., Zhang, W., Hung, H., Traversi, R., Becagli, S., Sheesley, R. J., Moffett, C. E., Barrett, T. E., Bossi, R., et al.: Annual variability of ice-nucleating particle concentrations at different Arctic locations, Atmospheric Chemistry and Physics, 19, 5293–5311, 2019.

Xu, M., Yang, Q., Hu, X., Liang, K., and Vihma, T.: Record-breaking rain falls at Greenland summit controlled by warm moist-air intrusion, Environmental Research Letters, 17, 044 061, 2022.

Zhang, D., Comstock, J., Xie, H., and Wang, Z.: Polar Aerosol Vertical Structures and Characteristics Observed with a High Spectral Resolution Lidar at the ARM NSA Observatory, Remote Sensing, 14, 4638, 2022.

Ziemba, L. D., Dibb, J. E., Griffin, R. J., Huey, L. G., and Beckman, P.: Observations of particle growth at a remote, Arctic site, Atmospheric Environment, 44, 1649–1657, 2010.

Appendix A.

Supporting figures for Chapter 4

This supporting information contains additional figures that expand on and support the figures and ideas presented in chapter 4, but that are not used to generate the main conclusions.

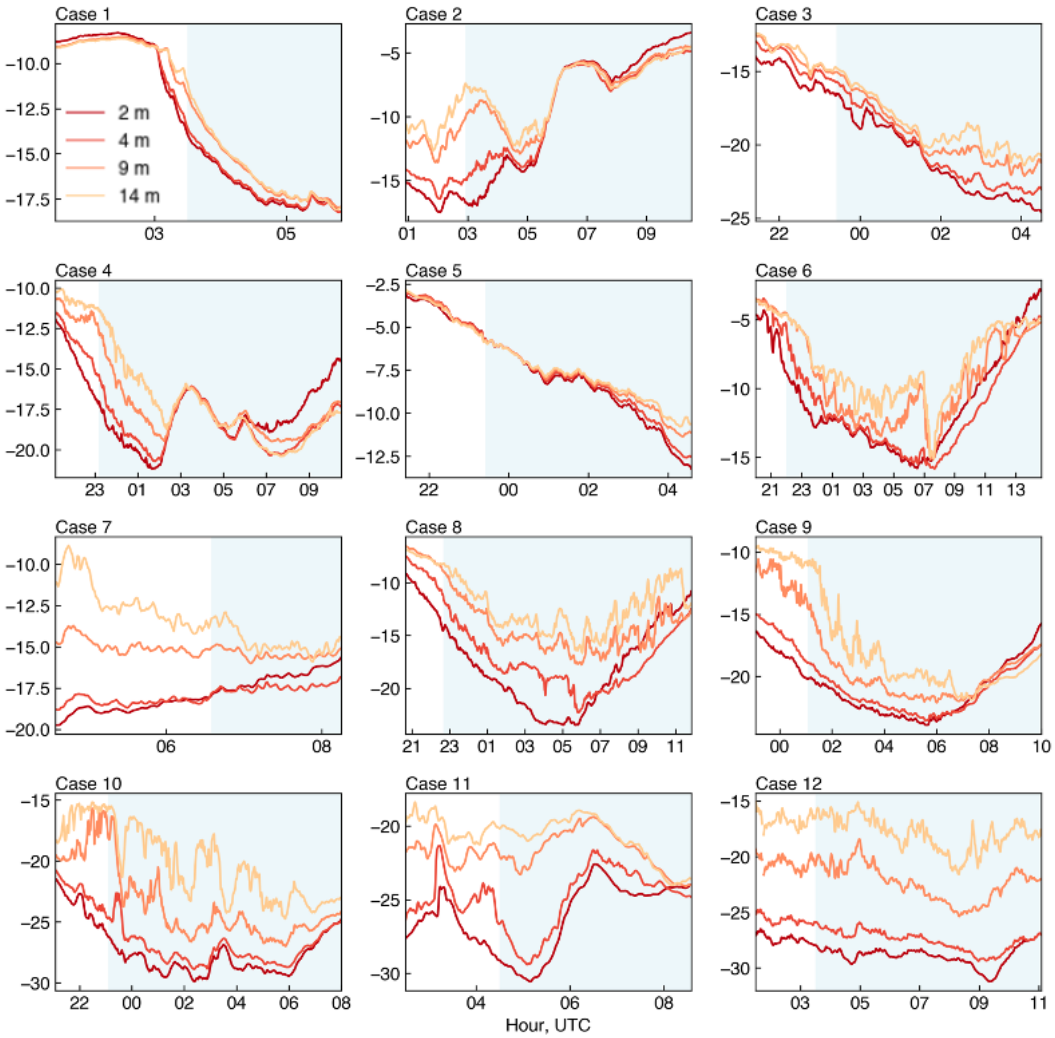

Figure A.1.: The temperature at four heights (2 m, 4 m, 9 m, and 14 m, see legend inset) measured by tower-mounted in-situ probes during each fog case. Plots include the two hours prior the event, the duration of each event (when there was a detectable radiative impact at the surface) is shaded in blue. Note the different y-scales on each plot.

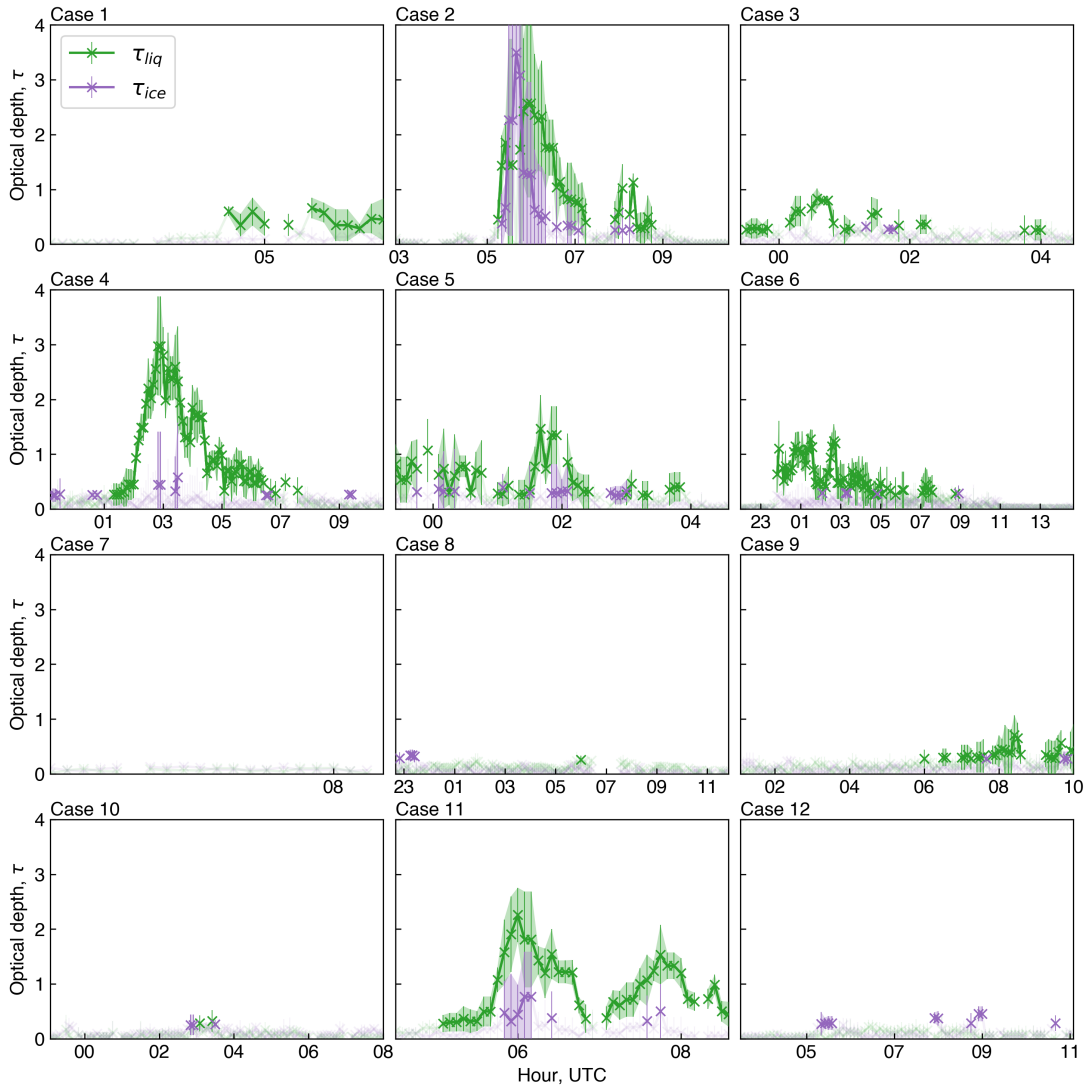

Figure A.2.: Temporal evolution of optical depth retrievals for the liquid (τ_{liq}, green) and ice (τ_{ice}, purple) phase of each fog event. Error bars show 2σ uncertainties. Retrievals for which the optical depth is insufficient ($\tau < 0.25$) are included on the plot but are faded out.

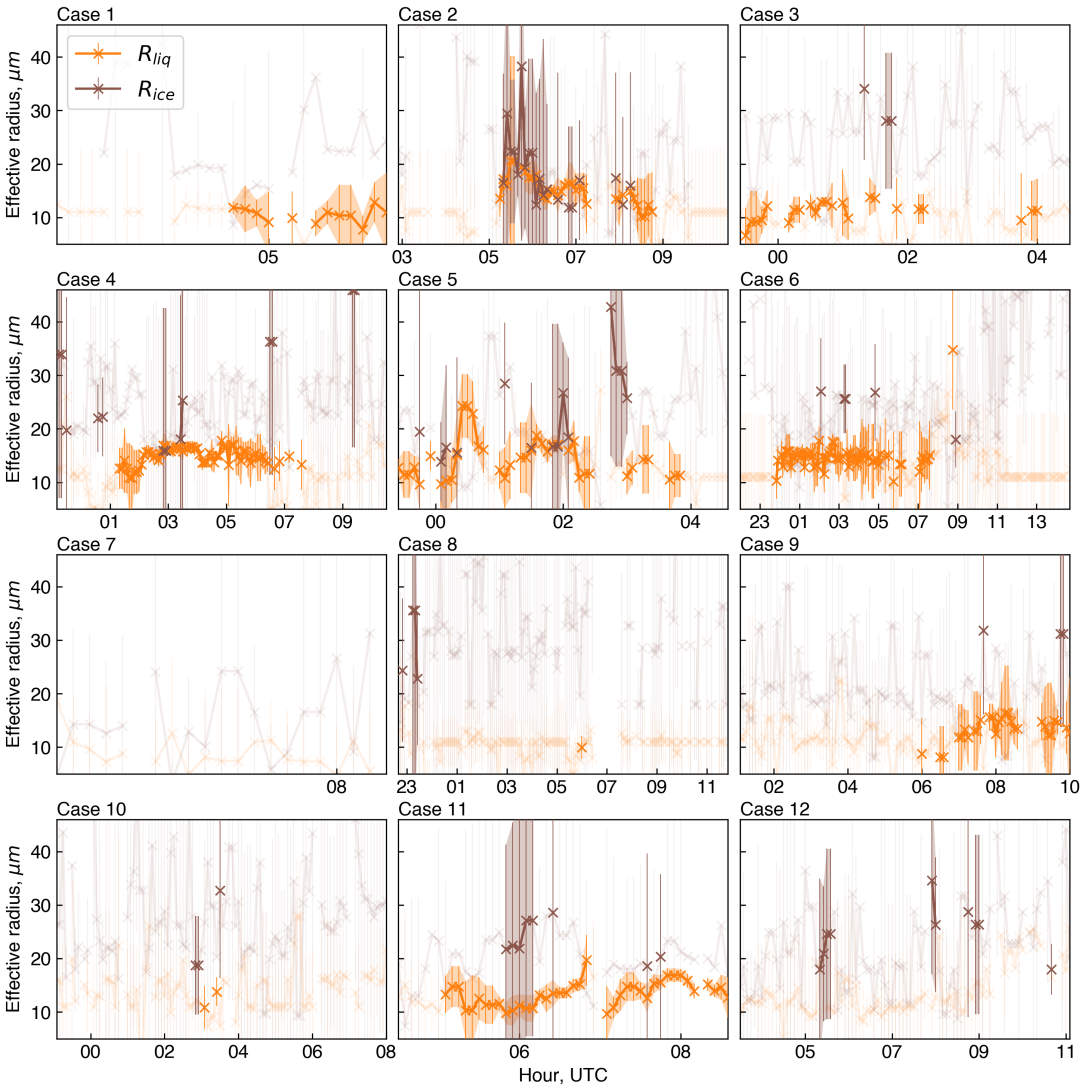

Figure A.3.: Temporal evolution of fog particle effective radius retrievals for the liquid (R_{liq}, orange) and ice (R_{ice}, brown) phase of each fog event. Error bars show 2σ uncertainties. Retrievals for which the optical depth is insufficient ($\tau < 0.25$) are included on the plot but are faded out.

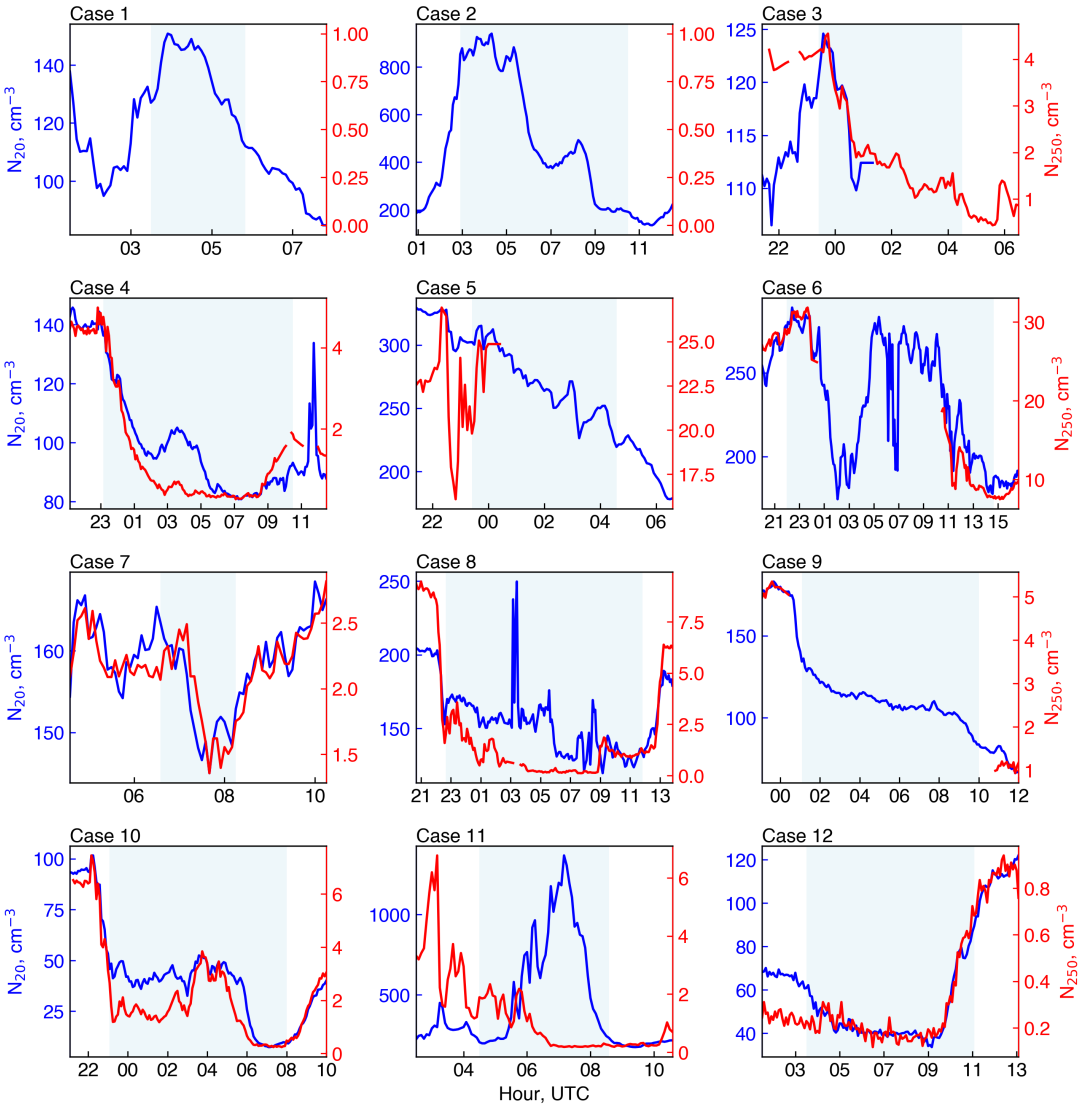

Figure A.4.: Aerosol particle number concentration measurements (N_{20}, blue, and N_{250}, red) during each fog case. Plots include the two hours prior to and after each event, the duration of each fog event (when there was a detectable radiative impact at the surface) is shaded in blue. Note the different y-scales on each plot.

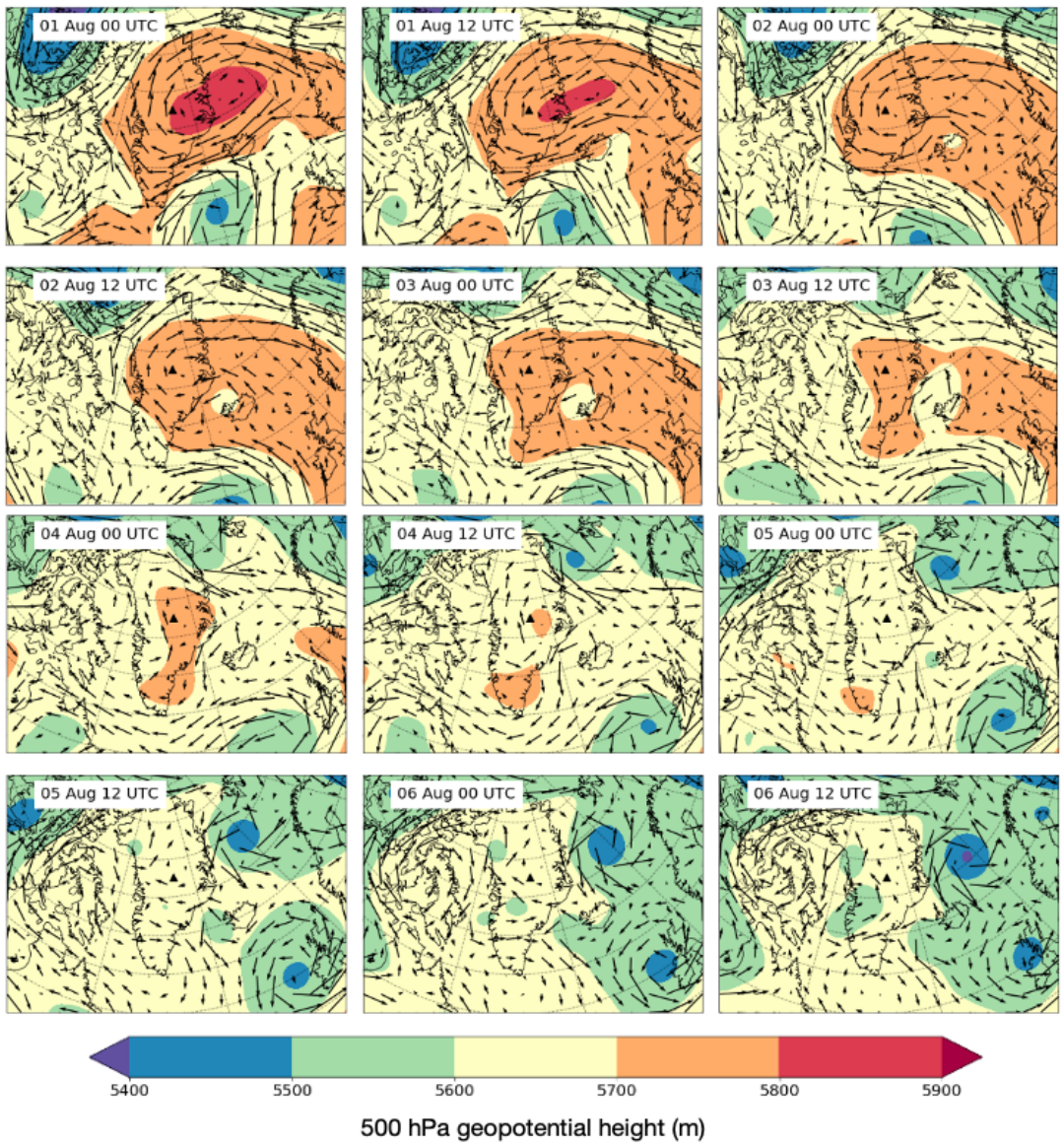

Figure A.5.: 500 hPa geopotential height (shaded) and wind (barbed) from ERA5 reanalysis during the first week of August 2019. Plots show the mean value averaged over the 12 hours centered on the time labelled in the upper left. The location of Summit Station is indicated by a black triangle.